The creation of innovative biomedical polymers by controlled polymerisation techniques

Huayang Yu

Main Supervisor: Dr Paul Thornton

Dr Terence Kee

Submitted in accordance with the requirements for the degree of Doctor of Philosophy

School of Chemistry, University of Leeds

August 2020

The candidate confirms that the work submitted is her own and that appropriate credit has been given where reference has been made to the work of others.

Acknowledgements

I want to say a big thank you to my supervisor Dr. Paul Thornton who directed my PhD research project. You are very patient to explain my questions and modify my reports and manuscripts. Only I know how great efforts that you put into my PhD research projects. Thanks a lot! To Dr. David Green, Dr. Algy Kazlauciunas and Dr. Sam Parkinson who helped me characterise my samples. Thank you! To Dr. Nicola Ingram who helped me conduct cytotoxicity study for my samples, thank you very much! To my friends, Jason Rowley, Simran Channa, David Martin, Zexi Xu, Ziyu Gao, Dong Xia and all members from lab 3.14 who provided ingenious ideas to my research and made my PhD journey cheerful and enjoyable. Thank you all!

To my parents, you are the most selfless and lovely father and mother in the world. Thank you so much for supporting my PhD journey and my whole overseas study. You are always positive and believe in me that I can overcome difficulties and homesick in my overseas school life. Thank you so much and really really love you!

Abstract

Polymer nanoparticles that are non-cytotoxic, biocompatible and water-dispersible are highly suited for use as drug delivery vehicles. Reversible addition fragmentation chain transfer (RAFT) polymerisation and *N*-carboxyanhydride ring-opening polymerisation (NCA ROP) are two controlled polymerisation techniques that enable the generation of polymers capable of forming nanoparticles by self-assembly in aqueous solution. Such nanoparticles are excellent candidates to be used as drug delivery vehicles.

One single block polymer (fucose-poly(2-hydroxypropyl methacrylate) (fucose-PHPMA)) and two types of diblock copolymers (polysarcosine-*b*-PHPMA (PSar-*b*-PHPMA), and poly(benzyl glutamate)-*b*-poly(ethylene glycol) (PBLG-*b*-PEG)) were synthesised via RAFT polymerisation and NCA ROP which were thermoresponsive and pH-responsive. Nanoparticles were formed from the produced polymers in the presence, and absence of doxorubicin (Dox) in aqueous solution via polymer induced self-assembly (PISA) and/or coacervation. Dox release from the nanoparticles was actuated by changes in environmental temperature and pH, which may be exploited for controlled release *in vivo*. The rigorous assessment of the anti-cancer behaviour of the Dox-loaded polymer nanoparticles was made against MCF-7 breast cancer cells, triple-negative breast cancer cells (MDA-MB-231), and Her2-enriched (ER and PR negative) breast cancer cells (MDA-MB-453).

Chapter 3, thermoresponsive PSar-*b*-PHPMA was created by NCA ROP and RAFT polymerisation. Grafting 3.5 % of HPMA to PSar of the copolymer with respect to the number of repeat units, producing thermoresponsive nanoparticles. PSar cannot form nanoparticles by itself. Significant amounts (74 %) of Dox were released from the nanoparticles at 41 °C compared to 37 °C (4 %) in phosphate-buffered saline (PBS) solution which proved that PSar-*b*-PHPMA nanoparticles are thermoresponsive.

Chapter 4, NCA ROP was employed to synthesise pH-responsive PBLG-*b*-PEG. Dox was efficiently released as the central ester linkage in the PBLG-*b*-PEG nanoparticles was broken under weakly acid pH (6.5), but not at normal physiological pH 7.4. Negligible amounts of Dox were released when the PBLG-*b*-PEG nanoparticles were stored at 37 °C in PBS buffer solution (pH 7.4). In pH 6.5 buffer solution, a quarter of the loaded Dox was

released from the PBLG-*b*-PEG nanoparticles at 37 °C over a month. $PHPMA_{200}$ (200 chain length), an injectable, self-healing, thermoresponsive gel depot was produced by RAFT polymerisation, loading Dox-loaded PBLG-*b*-PEG nanoparticles into the gel showed greater Dox release at 37 °C compared to at room temperature. An injectable Dox delivery system was formed by combining the PHPMA gel and the Dox loaded PBLG-*b*-PEG nanoparticles, with near-complete Dox release being realised when stored at 37 °C in pH 6.5 environment over 16 days. Therefore, PBLG-*b*-PEG_{113} nanoparticles are pH-responsive and the $PHPMA_{200}$ gel depot is thermoresponsive.

Chapter 5, fucose-modified thermoresponsive PHPMA was synthesised by RAFT polymerisation and the resultant nanoparticles showed extensive Dox release upon the solution temperature being increased to 41 °C. Fucose-PHPMA nanoparticles were produced as a result of fucose conjugation to the PHPMA chain, PHPMA cannot form nanoparticles by itself. Fucose-PHPMA nanoparticles are useful for pancreatic cells targeting because of their enhanced fucose uptake. Dox-loaded fucose-PHPMA nanoparticles encapsulated in the $PHPMA_{200}$ gel depot showed greater Dox release at 37 °C compared to at room temperature, approximately half of the loaded Dox was released at 37 °C in PBS buffer solution over a week. Therefore, both of fucose-PHPMA nanoparticle and $PHPMA_{200}$ gel depot are thermoresponsive.

Chapter 6, pH-responsive poly(ρ-hydroxystyrene-sulfanilamide) and poly(ρ-hydroxystyrene-sulfanilamide)-*b*-poly(acrylamide) were synthesised via RAFT polymerisation, acid hydrolysis and azo coupling with sulfanilamide. Both of the polymers were pH-reversible (indicated by reversible colour change) due to the protonation/deprotonation of the sulfonamide and deprotonation of the phenol groups, resulting in changes in the related resonance. Sulfanilamide has antimicrobial activity which may render the polymers useful as antibacterial agents.

List of Contents

List of Figures

List of Tables

List of Schemes

List of Abbreviations

ABA - 4-(*N*-acrylamido)benzenesulfonamide

ACS - 4-acetoxystyrene

AAPH - 2,2'-Azobis(2-amidinopropane) dihydrochloride

AM - Acrylamide

AC - Acrylic acid

AN - acrylonitrile

ADC - Antibody drug conjugates

APC- Advanced polymer chromatography

Ar - Aromatic

AFM - Atomic force microscopy

ATR - Attenuated total reflection

APD - Avalanche photodiode

AIBN - Azobisisobutyronitrile

BSA - Bovine serum albumin

CTA - Chain transfer agent

CS-PVA - Chitosan-polyvinyl alcohol

DCM - Dichloromethane

DSC - Differential scanning colorimetry

DMF - Dimethyl formamide

DMSO - Dimethyl sulfoxide

Dox - Doxorubicin

DP - Degree of polymerisation

DLS - Dynamic light scattering

EPC - Egg phosphocholine

EDX - Energy dispersive x-ray

FTIR - Fourier transform infrared

BLG - γ-Benzyl-L-glutamate

G'- Loss or viscous modulus

G'' - Elastic or storage modulus

GPC - Gel permeation chromatography

Glu - L-Glutamic acid

HPMA - 2-Hydroxypropyl methacrylate

HSA - Human serum albumin

HOBt - Hydroxybenzotriazole

IC_{50} -Half maximal inhibitory concentration

Ala - L-Alanine

λ_{max} - Wavelength of maximum absorbance

LCST - Lower critical solution temperature

MIC - Minimum inhibitory concentration

MTT - 3-(4, 5-Dimethylthiazolyl-2)-2,5-diphenyltetrazoliumbromide

MS - Mesoporous silica

TA - *N*-(Thiazol-2-yl)acrylamide

M - Monomer

HEMM - *N*-Hydroxyethyl methacrylamide

M_W - Weight average molecular weight

NMR - Nuclear magnetic resonance

NCA - *N*-Carboxyanhydride

DIPEA - *N,N'*-Diisopropylethylamine

BLS - O-Benzyl-L-serine

PMMA - Poly(methyl methacrylate)

PACS - Poly(acetoxystyrene)

PEG - Poly(ethylene glycol)

PGA - Poly(*L*-glutamic acid)

PHEMM - Poly(*N*-hydroxyethyl methacrylamide)

PρHS - Poly(ρ-hydroxystyrene)

PDI - Polydispersity index

RAFT - Reversible addition fragmentation chain transfer

ROP - Ring-opening polymerisation

SEM - Scanning electron microscopy

SAXS - Small-angle x-ray scattering

t-Boc - Tert-Butyloxycarbonyl

TEM - Transmission Electron Microscopy

TMS - Trimethylsilane

UCST - Upper critical solution temperature

EDC.HCL - 1-(3-Dimethylaminopropyl)-3-ethylcarbodiimide hydrochloride

HEA - 2-Hydroxyethyl acrylate

PBS - Phosphate-buffered saline

PHPMA - Poly(2-hydroxypropyl methacrylate)

PAM - Poly(acrylamide)

PGMA - Poly(glycerol monomethacrylate)

PISA - Polymer induced self-assembly

PSVPh - Poly(styrene-*ran*-vinyl phenol)

PCL - Polycaprolactone

PSar - Polysarcosine

RDRP - Reversible-deactivation radical polymerisation

Sar - Sarcosine

SSD - Silver sulfadiazine

SA - Sulfanilamide

THF - Tetrahydrofuran

TFA - Trifluoroacetic acid

UV-Vis - Ultraviolet-visible

SCPDB - (4-Cyano-4-(phenylcarbonothioylthio) pentanoic acid *N*-succinimidyl ester

DOPE - 1,2-Dioleoyl-sn-glycero-3-phosphoethanolamine

DPPH - 2,2-Diphenyl-1-picrylhydrazyl

EPR - Enhanced Permeability and Retention

Chapter 1. Introduction

Polymers for biomedical applications such as drug delivery vehicles and antimicrobial agents are introduced initially in this chapter. For drug delivery vehicles, polymers can be synthesised by reversible addition fragmentation chain transfer polymerisation and *N*-carboxyanhydride ring-opening polymerisation. Using the polymerisation methods above, diblock copolymers can self-assemble in aqueous solution to form nanoparticles. An anti-cancer drug, doxorubicin was loaded into the stimuli-responsive polymeric nanoparticles, for instance poly(ethylene glycol) modified copolymers with a central ester linkage enables pH-responsive property, and thermoresponsive poly(2-hydroxypropyl methacrylate) related copolymers making drug release at certain temperature. Sulfanilamide has antimicrobial activity which modifies polymers and make them as antibacterial agents. The reaction mechanisms, examples of synthesised polymers and the biomedical applications are also discussed in this chapter.

1.1. Polymers for biomedical applications

Polymers which are biocompatible [1-2], biodegradable [3-4], non-toxic [5-6], non-immunogenic [7-8], non-antigenic [9-10] and antibacterial [11-12] can be applied to biomedical applications such as drug carriers with controlled release profiles [13-14], implants in bones and joints [15-16], tissue engineering [17-18] and dental materials [19-20]. Drug molecules can be delivered to cancer tissue directly by polymer nanoparticles with minimal damage of healthy tissues in human body which maximise efficiency of drug [21-22]. Antimicrobial agents can modify polymers, giving polymer antibacterial property [23-24] which can be applied to antibiotics delivery [25-26], antibacterial coating on medical devices [27-28], antimicrobial plastics [29-30], and antimicrobial textile [31-32].

1.1.1. Polymers for drug delivery

The design of effective delivery of anti-cancer drugs for the treatment of cancer (chemotherapy) remains a key goal of contemporary medicinal chemistry [33-35]. In

order to deliver drug molecules to target cancer tissues, polymeric nanoparticles may be used that absorb the anti-cancer drug, or covalently conjugate to the therapeutic [36]. Drug loaded polymer nanoparticles may accumulate on cancer cells due to enhanced permeability and retention (EPR) effect [37]. This principle was first reported by Maeda and co-workers in 1986 [38]. Cancer cells divide faster than normal cells [38]. In order to support cancer cell growth, more blood vessels are produced, more nutrition and oxygen are required [39]. During this process, angiogenesis ("leaky" blood vessel) is involved [39]. Angiogenesis means new blood vessels form from original vessels [39]. Cancer cells are not aligned and lacking of smooth surface [39]. Therefore, drug loaded polymer nanoparticles (macromolecules) may accumulate into tumours due to the hyper-permeable vasculature and the lack of a lymphatic drainage system within tumours [39]. In 1995, the first approved nanomedicine Doxil/Caelyx was launched which was used to treat breast cancer [40]. Then Abraxane and Vyxeos were published and applied to metastatic breast cancer, pancreatic adenocarcinoma and leukaemia treatments [41-42]. Recently, Andresen and co-workers reported that liposome retention in different kinds of tumours has heterogeneity in nanoparticle accumulation which demonstrated EPR effect cannot be considered as a general principle [43]. Chan and co-workers reported that 97 % of nanoparticles were transported into solid tumours by endothelial cells through an active process of transcytosis, also the frequency of gaps on the endothelial lining is too low to account for the accumulation of nanoparticles in tumours [44]. Therefore, the mechanism of drug delivery by nanoparticles to tumours is still researching.

There are only ten nanoparticle-based nanomedicines on the market [45]. For the nanomedicines that reached phase III clinical trials, only 14 % of the nanomedicine proved the drug delivery efficiency to solid tumour [45]. This was caused by poor efficiency of accumulating nanoparticles on tumour and poor pharmacokinetics [45]. Recently, it was reported that an average of 0.7 % of nanoparticles that can reach the target tumour according to the published literature over a decade [46]. Therefore, high efficiency drug loading into, and release from nanoparticles needs to be developed which is essential for effective cancer treatment.

1.1.2. Polymers for antimicrobial applications

Antibiotic-resistant infection is the main concern of using antimicrobial agents in human body. Antimicrobial agents inhibit microorganisms' growth or kill them so the toxicity of the antimicrobial agents directly influence human health. Antimicrobial polymers can inhibit the infection because the action mechanisms are different from the antimicrobial agents [47-53] including the surface-activity properties, adsorption/absorption abilities and the bonding affinity between the polymer/copolymer and the bacterial cells [48]. Antimicrobial agents modified polymer can be achieved by chemical conjugation of antibiotics to polymers [54]. General antibiotics are beta lactams, fluoroquinolones, aminoglycosides and sulfonamides [55]. For antibiotics delivery by polymers, the release rate can be controlled by conjugated bonds (ester bond, pH-responsive), and intrinsic property of the polymers (thermoresponsive) [56-57]. Antimicrobial coating is utilised extensively on medical devices, especially on dental restorative materials [58-62]. Antibacterial agents limit the activity of cariogenic bacteria, reducing the activity of secondary caries. Therefore, the lifetime of composite restorations can be prolonged [59]. Antibacterial plastic was produced by adding antimicrobial additives during the plastics manufacturing process which can be utilised in water filters, food containers and coolers [63]. Antimicrobial textiles can inhibit propagation of germs, reducing the rate of cross infection and the risk of human pathogens which can be applied to wound healing, surgical masks and medical clothing [64]. Antimicrobial agents were widely developed in the medical field. In the area of daily supplies, antimicrobial agents are used in hand wash and laundry detergent. Salicylic acid, n-xylene chloride, ethyl alcohol, triclosan and o-phenylphenol are general antibacterial agents added in hand wash [65]. In laundry detergent, triclocarban, triclosan, diclosan and chlorohydroquinone are the common antibacterial additives [66]. Most of the antibacterial agents in hand wash and laundry detergent have chlorine, resulting in irritation to human skin and eyes potentially. Therefore, a new antimicrobial agent with no irritation to human body needs to be developed which can be applied in hand wash and laundry detergent.

1.2. Nanoparticle for controlled drug delivery

Amphiphilic poly(amino acid)(PAA)-based nanoparticles are cited to be suitable for use as drug delivery vehicles, owing to the versatile chemical structures and self-assembly properties [67] for instance poly(*N*-isopropylacrylamide)-*b*-poly(*L*-alanine) [68] and biotin-PEG-*b*-poly[(lysine-*co*-leucine)-*graft*-(gemcitabine-*co*-rhodamine B)] [69]. Various stimuli may be utilised to trigger controlled drug release from the PAA carriers, for instance changes in environmental temperature [70], pH [71], the presence of a particular enzyme [72], light irradiation [73] and the presence of a magnetic field [74]. Changes in environmental pH is particularly relevant as an actuator in chemotherapy, and attracts widespread attention [71, 75-79]. The pH varies in different tissues in human bodies [71], with cancerous tissue (pH 5-pH 6.8) being more acidic than healthy tissue and blood, which possesses a pH of 7.4 [80].

Nanoparticles can have various size, morphology and chemical properties which depend on the starting materials and the reaction conditions [81-86]. The particle size influences the biodistribution of the nanoparticles [82]. It is reported that the diameter of the particles smaller than 10 nm can be removed from the bloodstream through renal clearance [87]. The particle size less than 100 nm is considered suitable for brain drug delivery [88-89]. For the particle size greater than 200 nm, the nanoparticles often accumulate in the bone marrow [87]. The shape of the nanoparticles also has an impact on the biological side in human bodies. For the nanoparticles larger than 100 nm, rod-shaped particles have more efficiency in cellular uptake compared to spheres, cylinders, and cubes [90]. However, for the nanoparticles smaller than 100 nm, spheres have the highest cellular intake than that of the shapes discussed above [91]. This might because the smaller the nanoparticles resulting in weaker attachment to the endothelium and larger surface-to-volume ratio [92]. Therefore, nanoparticles with size below 200 nm might be suitable for drug delivery in the human body [87]. Examples of nanoparticles with different chemical properties which are suitable for drug delivery are discussed below.

A hydrophilic polymer (with residues of sodium salicylate attached) coupled to the backbone of polysulfonilamine via an azo bond has been shown to release 5-aminosalicyclic acid [93]. The 5-aminosalicyclic acid can be used to treat inflammatory bowel disease in human bodies [93-94]. The conjugation of ρ-aminosalicyclic chloride to poly(vinyl alcohol) was published by Ushakov and co-workers [93]. Excellent anti-tubercular effect was performed by applying the synthesised polymeric derivatives [95]. The theory of the reaction was applying esterification partially via the hydroxyl group and the carboxylic acid group from the poly(vinyl alcohol) and the aminosalicyclic acid, respectively [95]. The polymeric drug of 5-aminosalicyclic acid attached to hydrophilic polymeric materials by azo bonds which were discussed previously [95]. Callant and Schacht found that the cleavage of azo bonds can be used to release the 5-aminosalicyclic acid which can be realised by anaerobic bacteria (for instance colon has azo reductase activity) from the lower bowel in human bodies [95]. Therefore, drug modified polymers via an azo bond might be suitable for drug delivery in the human body.

1.2.1. Poly(glutamic acid) based nanoparticles for drug delivery

Glutamic acid belongs to the family of amino acids. Poly(*L*-glutamic acid) (PGA) is non-toxic, non-immunogenic and stable in plasma and can be degraded by lysosomal enzyme cathepsin B [96-98]. Tukappa and co-workers synthesised enzyme-responsive drug delivery vehicles. Anti-cancer drug doxorubicin (Dox) was loaded into the mesoporous silica (MS) nanoparticles followed by grafting PGA (M_W= 6300 g mol^{-1}) on the surface to produce PGA-capped MS nanoparticles [99]. The particle size of the Dox loaded nanoparticles were ≈ 100 nm [99]. In presence of pronase, the peptide bonds in PGA from the nanoparticles were hydrolysed and 90 % of Dox was released in 5 hours. In the cytotoxicity study, PGA-capped MS nanoparticles without Dox loaded were non-toxic against SK-BR-3 breast cancer cells, but showed toxicity for Dox-loaded PGA-capped MS nanoparticles, over 90 % of the cancer cells died at a concentration of 100 μg mL^{-1} after 48 hours [99]. Therefore, enzyme-responsive PGA based nanoparticles can be used as drug carriers potentially.

1.2.2. Poly(ethylene glycol) related nanoparticles for drug delivery and medical applications

PEG is biocompatible, non-fouling, non-toxic, non-antigenic and non-immunogenic and so is widely exploited within a biomedical context [100-104]. Since PEG has these properties, intravenous and dermal pharmaceutical applications have been demonstrated in human bodies [105]. The tests and the characteristics of PEG were approved by Food and Drug Administration U.S. [105]. Therefore, PEG is a promising candidate as the hydrophilic block in the design copolymer. Modification of PEG with thiol functional group and biotin was employed to create surface-grafted polydopamine shells, increasing colloidal stability and biocompatibility of fluorescent nanodiamonds (Figure 1.1) [106]. Fluorescent nanodiamonds were coated with polydopamine then functionalised by biotin-PEG with thiol terminated groups [106]. The modified nanodiamonds can be used as fluorescent probes in cell imaging since the biotin decorated nanodiamonds can attach to DNA via biotin-streptavidin interaction [106]. Hak-Sung and co-workers discovered that the functionalised fluorescent nanodiamonds decreased non-specific membrane adhesion since mouse bone marrow dendritic cells and HeLa cells interact with the modified fluorescent nanodiamonds [106]. PEG has been widely utilised to modify polymer nanoparticles in the pharmaceutical industry. The benefits of the modification are enhancing steric stabilisation of nanoparticles, improving circulation time and enzymatic degradation [107]. Ali Pourjavadi and co-workers synthesised PEG-polycaprolactone-PEG pH-responsive polymers that coated magnetic nanoparticles iron oxide [107]. Paclitaxel was loaded into the magnetic polymer nanoparticles via solvent-evaporation and drug release was performed in pH 7.4 and pH 5.5 environments [107]. In acidic environment, paclitaxel was released more efficiently since ester and imine bonds break apart the nanoparticles [107]. The pH environment of cancer tumour tissue in human bodies is around pH 6.8 which lower than the healthy sites (pH 7.4) [107]. It has been found the pH is approximately 5 to pH 6 in endosomal and lysosomal in human bodies during the cell internalising process so anti-cancer drug release analysis may be conducted in pH 5 potentially [107-108].

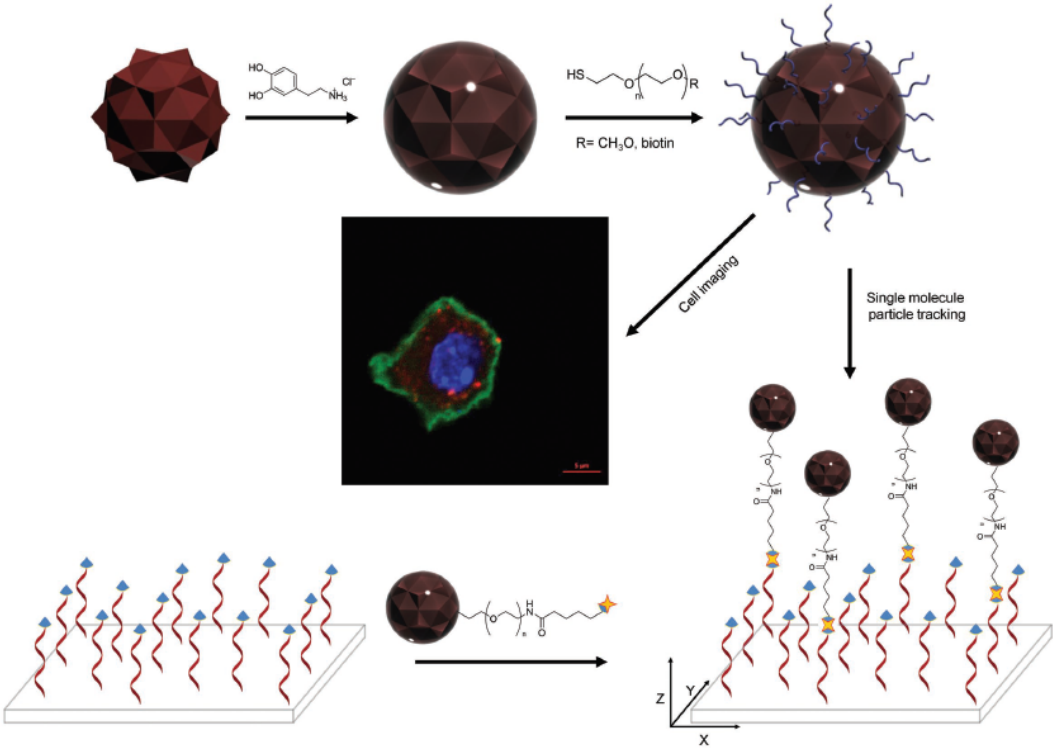

Figure 1. 1 Encapsulation outline of functionalised fluorescent nanodiamonds [106].

Polydopamine was coated on fluorescent nanodiamonds and then the polydopamine shell was functionalised by biotin-PEG with thiol terminated groups via Michael addition or Schiff base reactions [106].

1.2.3. Poly(2-hydroxypropyl methacrylate) related nanoparticles for drug delivery

PHPMA and PHPMA based drug delivery systems are widely investigated for use in biomedical field since PHPMA is hydrophilic, synthetic, non-immunogenic, non-toxic, biocompatible and stable in blood circulation [109-111]. The hydroxyl groups from the PHPMA side chains offer opportunities for conjugation to a large diversity of functional groups so cell-uptake (proteins), bioimaging (fluorescent tags) and biorecognition (carbohydrates) features can be developed [111]. It has been reported that drug carrier systems that contain PHPMA allow specific site drug delivery and controlled drug release [112]. Xiaohan and co-workers has reported self-assembled nanoparticles of PHPMA with cholesterol side groups are anti-cancer drug (Dox) delivery vehicles potentially, human serum albumin (HSA) does not affect the drug carry efficiency [112]. Chao and co-workers employed photoinitiated Reversible Addition Fragmentation Chain Transfer

(RAFT) polymerisation and Polymer Induced Self-Assembly (PISA) methods to synthesise BSA based PHPMA nanoparticles which can encapsulate hydrophilic or hydrophobic substances for instance DNA and Dox [113]. Therefore, modified PHPMA is suitable for nanoparticle synthesis which can potentially be utilised as drug delivery vehicles.

1.2.4. Fucose

Fucose is a sugar with a 6-deoxy hexose chemical structure (Figure 1.2). It can be found in different kinds of organs in mammals in the L-configuration (Figure 1.2) [114]. In cancer tumour sites, a significant change of fucosylated proteins can be detected compared to healthy tissues which gives evidence of cancer diagnosis and prognosis [114]. Immunological reactions, blood group determination and signal transduction pathways all employ fucosylation [115]. One of the most aggressive malignancies with a dismal prognosis is pancreatic ductal adenocarcinoma, which is the eighth in cancer-related deaths worldwide [115]. Systemic chemotherapy of human bodies resulting in hypovascularity of pancreatic ductal which makes it very hard to deliver anticancer drug to cancer tumours [115]. Makoto Yoshida and his co-workers have reported cisplatin loaded liposomes with L-fucose-bound delivered successfully to pancreatic cancer cells emphasising that fucose may be used for target cell binding [115].

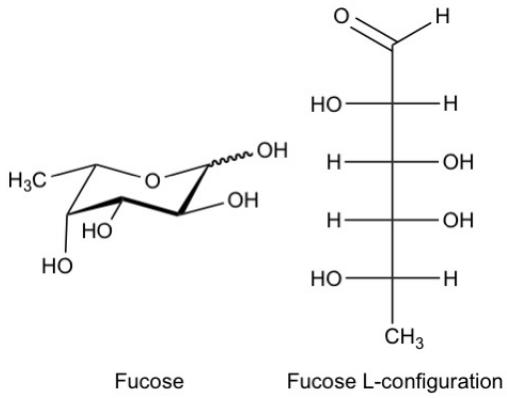

Figure 1. 2. Chemical structures of fucose and fucose L-configuration [114].

1.2.5. Fucose modified polymer for anti-cancer applications

Nednaldo and co-workers reported an amphiphilic nanogel, structuring hexadecylamine as the hydrophobic inner core and sulfated fucan as the hydrophilic outer core [116].

Sulfated fucan is a fucose containing sulfated polysaccharides which can be extracted from the class phaeophycese-brown seaweed [117]. With the concentration 0.05-0.5 mg mL^{-1} of the nanogel, 2.0%-43.7% of HepG2, 786, and H-S5 tumour cells proliferation were inhibited but improving Chinese hamster ovary and monocyte macrophage cell non-tutor cell line proliferation [116]. In the light of the flow cytometric analysis, 786 tumour cell proliferation was inhibited by inducing apoptosis and blocking 786 cell passways in the S and G2/M phases of the cell cycle [116]. Fucan modified nanogel has antiproliferative property against tumour cells which can be applied along with anti-cancer drugs in forms of drug carriers, showing candidates of cancer tumour treatment potentially [116].

1.2.6. pH-Stimulated drug release from polymeric nanoparticles

pH-Responsive nanoparticles were widely explored in past decade [80, 118-122] and an example is in Scheme 1.1. Initially, *N*-hydroxyethyl methacrylamide (HEMM) reacted with *N*-Boc ethylenediamine, in the presence of *N,N'*-diisopropylethylamine (DIPEA), hydroxybenzotriazole (HOBt) and 1-(3-dimethylaminopropyl)-3-ethylcarbodiimide hydrochloride (EDC.HCL) to produce Boc protected HEMM [123]. Then the Boc protected poly(*N*-hydroxyethyl methacrylamide) (PHEMM) was formed by free radical polymerisation using azobisisobutyronitrile (AIBN) as an initiator in dimethyl sulfoxide (DMSO) [123-124]. The Boc group from the polymer was removed by trifluoroacetic acid (TFA), followed by Dox conjugation (Scheme 1.1). It is pH-sensitive due to the acid-cleavable hydrazine bonds that link the PHEMM to Dox [124]. During 12 hours of incubation, Dox release occurred more efficiently in solution of pH 5.4 (>75 %) compared to release in solution of pH 7.4 (<20%) [124].

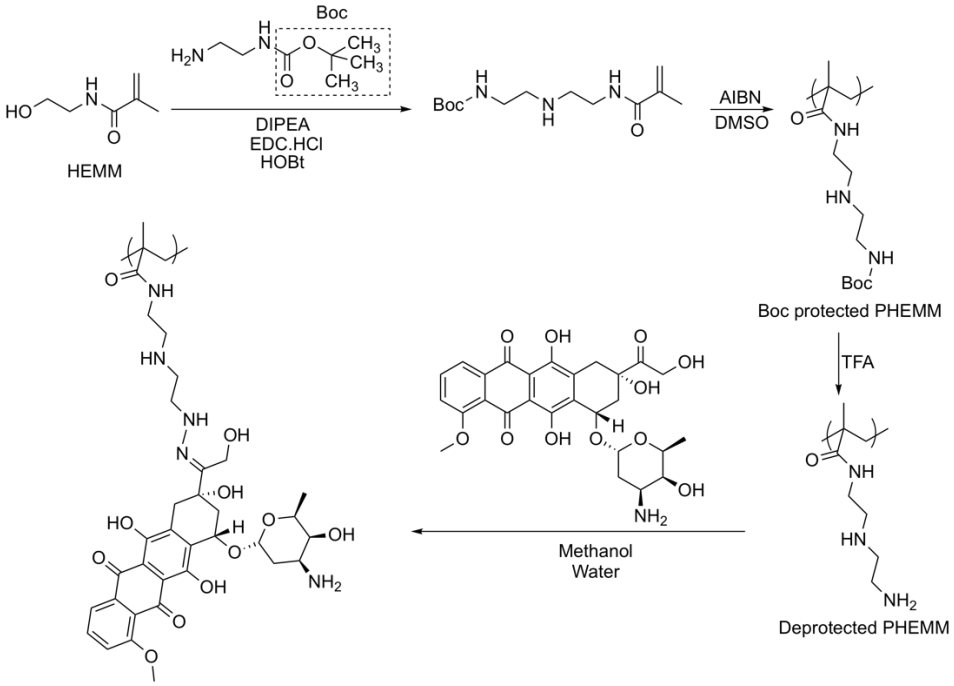

Scheme 1. 1. Synthesis of PHEMM-Dox [123-124].

1.2.7. Thermal-controlled drug release

Polyvinylethers and poly(*N*-isopropylacrylamide) are examples of thermoresponsive polymers which are potential candidates for temperature induced drug release [80]. At certain temperature, thermoresponsive polymers show a volume phase transition, resulting in a change in the solvation state. The temperature of a polymer becomes insoluble upon heating is called Lower Critical Solution Temperature (LCST). The Upper Critical Solution Temperature (UCST) is the polymer becomes soluble upon heating. The LCST and UCST of a polymer is not restricted to aqueous solution but for biomedical studies water as the solvent is more important for research compared to organic solvents. The hydration state changed causes the volume phase transition, reflecting where intra- and intermolecular hydrogen bonding of the polymers are favoured compared to a solubilisation by water [125-132]. In addition, poly(HPMA mono/dilactate) coated 1,2-dioleoyl-sn-glycero-3-phosphoethanolamine(DOPE)/ egg phosphocholine (EPC) liposomes have thermosensitive characteristics, as disclosed by Hennink and co-workers [70]. DOPE/EPC Liposomes can be prepared via mixing cholesterol or phosphocholines (stabilising agents) with DOPE followed by extrusion through 50 nm-100 nm filters [70]. EPC is a natural substance which is a mixture of saturated and unsaturated

phosphocholines [70]. Pure DOPE/EPC liposomes that were loaded with calcein did not demonstrate fluorescent marker release as the temperature increased from 37 °C to 46 °C [70]. However, when the calcein-loaded liposomes were coated with the polymer, payload release was observed as the solution temperature increased from 37 °C to 42 °C [70]. As the temperature increased to 46 °C, 90 % of calcein had been released from the polymer-coated liposomes [70]. Therefore, poly(HPMA mono/dilactate) is thermoresponsive with stimulated calcein release upon increasing temperature.

1.2.8. Anticancer drug—Dox

Dox is widely used to treat a large variety of cancer types [36, 133-136]. However, bone marrow suppression and cardiotoxicity side effects from Dox limit daily clinical practice [137]. Polymer nanoparticles (drug delivery system) with Dox-loaded largely suppress the side effects but modify Dox specific site release profile, absorption and distribution resulting in more targeted therapy [137]. Dox intercalates with the DNA base pair preventing DNA replication, delivering a series of cytotoxic effects [36] with targeting molecules which result in cell apoptosis [33]. According to Figure 1.3, amino and carbonyl groups are present in Dox [71]. Therefore, hydrogen bonding interactions can be formed between Dox and other substances which have amino groups, for instance particular polymeric nanoparticles [71]. It is difficult to break hydrogen bonding interactions which slows the release of Dox into the target cells of cancer tissues [71]. If Dox releases too fast, patients may get maladjustment which may cause increased damage of the healthy cells in human body [71]. Dox is also water miscible [71].

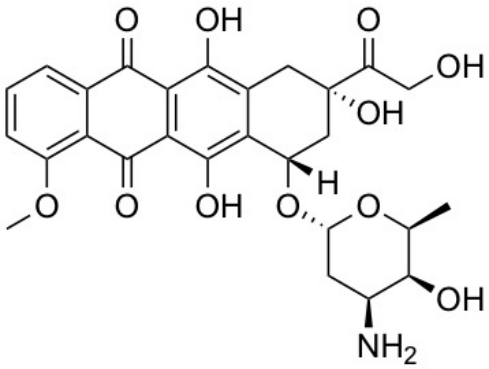

Figure 1. 3. Chemical structure of Dox [100].

1.3. Antibacterial drug—Sulfanilamide

Sulfanilamide (SA) has a core skeleton of para-aminobenzene sulfoamide which has properties of antimicrobial and bacteriostatic and used widely in sulfa drugs [138-139]. Due to the aromatic ring and heteroatoms, SA has a stable chemical structure [140]. It is reported that gram-positive and gram-negative bacteria can be inhibited effectively by SA [138]. Suppressing the bacterial growth, SA is competing with ρ–aminobenzoic acid in dihydrofolate biosynthesis, hindering the synthesis of dihydrofolate, inhibiting the synthesis of nucleic acids and proteins and preventing the growth of various microorganisms [138-139, 141]. In the prevention and bacterial infection therapy, SA is commonly used in human and veterinary medicine [138]. SA is also employed in herbicides in agriculture area [140]. The core antibacterial skeleton SA is hybridised with five-membered thiazole and oxazole and six-membered pyrimidine and diazine, producing a range of SA types of antibacterial drugs, for instance sulfamoxole, sulfathiazole, sulfadiazine and sulfamethoxypyridazine (Figure 1.4) [139].

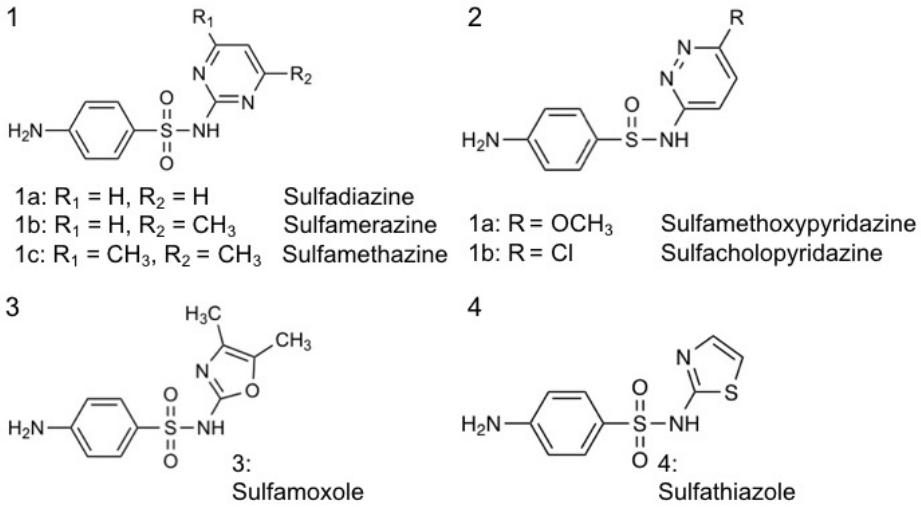

Figure 1. 4. Hybridised SA and heterocycles as clinical antibacterial drugs [139].

1.3.1. Sulfanilamide based polymers

SA was used to modified polymers and providing antimicrobial property to the synthesised polymer. Seham's group synthesised 4-(*N*-acrylamido)benzenesulfonamide (ABA) (Scheme 1.2) which reacted with *N*-(thiazol-2-yl)acrylamide (TA), AM and

acrylonitrile (AN), respectively to produce PABA-*co*-PTA, PABA-*co*-PAM and PABA-*co*-PAN by copolymerisation at 75 °C using AIBN as the initiator (Scheme 1.3) [142]. The antimicrobial activities of the synthesised copolymers were tested against *Staphylococcus aureus (S. aureus), Escherichia coli (E. coli) and Bacillus subtilis (B. subtilis)* and the Minimum Inhibitory Concentration (MIC) (average of triplicates) were determined [142]. The MIC values measured the minimum concentration of the antimicrobial polymer that prevented the visible growth of test organisms [142]. PABA-*co*-PTA has the most severe effect for all of the microorganisms compared to PABA-*co*-PAM and PABA-*co*-PAN [142]. This might due to the thiaozle group from the PABA-*b*-PTA which also has anti-inflammatory property [143]. Therefore, SA modified polymers can potentially inhibit bacterial growth.

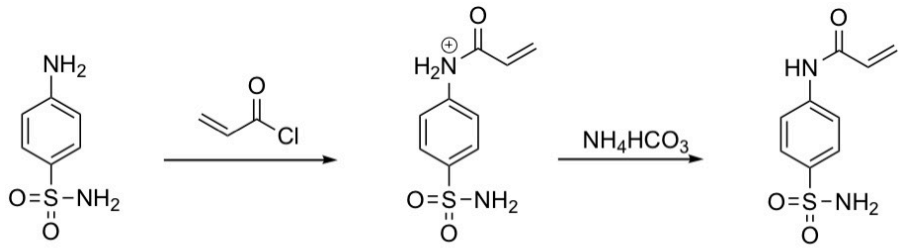

Scheme 1. 2. Synthesis of 4-(*N*-acrylamido)benzenesulfonamide [142].

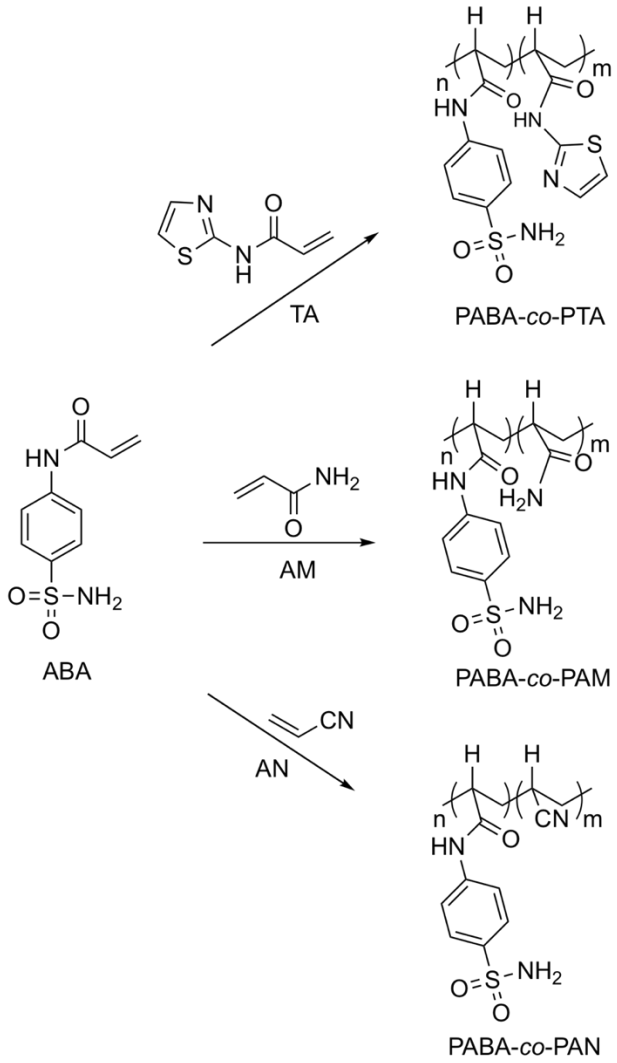

Scheme 1. 3. Synthesis of PABA-*co*-PTA, PABA-*co*-PAM and PABA-*co*-PAN [142].

1.3.2. Sulfanilamide applied in fibres

SA and SA based molecules can be used in wound healing applications. Fereshteh and co-workers synthesised a wound healing membrane with 500 μm thickness, using 0.3 % (w/v) silver sulfadiazine (SSD) polycaprolactone (PCL) composite [144]. PCL has good mechanical property but its hydrophobicity lowered the wound healing process [145]. Applying the SSD in the PCL, the hydrophilicity was increased and the antibacterial and antifungal properties also contributed to the wound healing [146]. The PCL (80KDa) and SSD were dissolved in acetic acid and the nanofibrous membrane was produced by electrospinning technique [144]. The membrane was tested against gram-positive *S. aureus* and gram-negative *Pseudomonas aeruginosa*, clear inhibition areas were seen around the membrane over 20 days which showed the antibacterial activity [144]. For

the PCL/SSD membrane, 80 % wound closure was observed after 14 days which was greater than the PCL membrane (40 % wound closure) [144]. The results indicated the PCL/SSD membrane has antimicrobial activity and shortened the wound healing time [144].

1.4. Reversible Addition Fragmentation Chain Transfer Polymerisation

An amphiphilic diblock copolymer for drug delivery application can be synthesised by RAFT polymerisation [147]. RAFT polymerisation belongs to the family of Reversible-Deactivation Radical Polymerisation (RDRP) [148]. Various vinyl monomers can be polymerised by RAFT polymerisation under different reaction conditions, using a large variety of RAFT agents (Chain Transfer Agents (CTAs)) [148-151]. RAFT agents (labelled in green in Scheme 1.4) play the crucial role in the reaction process as the reactive radicals are limited by their reversible transfer to the CTA [152]. According to Scheme 1.4, the CTA reacts with the propagating species (produced from initiation) resulting in the substitution of the RAFT agent R group with the incoming radical, yielding a new free radical is produced ($R^{\cdot}$) in the pre-equilibrium step [152]. In the re-initiation step, the reactive free radical reacts with another monomer and the CTA by producing a macro-RAFT agent [152]. Finally, the polymer can be synthesised [152].

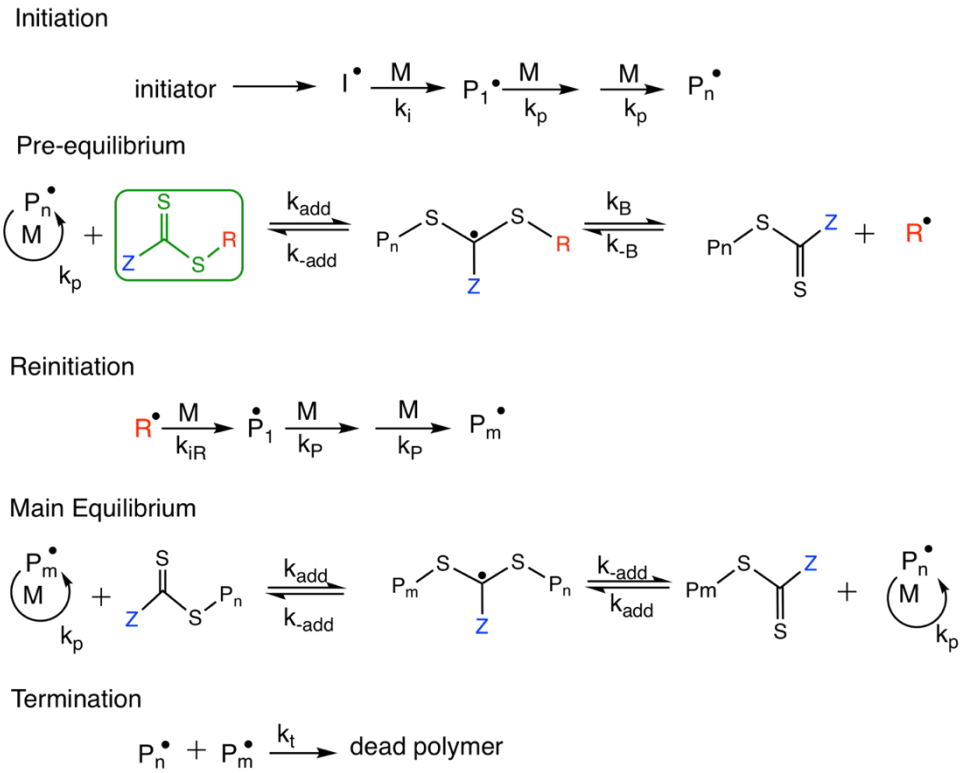

Scheme 1. 4. Mechanism of RAFT polymerisation where I: initiator; M: monomer; k_i: rate of initiation; k_p: rate of propagation; k_{add}: rate of fragmentation of the RAFT agent intermediate in the pre-equilibrium step; k_B: rate of fragmentation of the RAFT agent with P_n group attached [153].

1.4.1. RAFT agents

The reaction of radical addition fragmentation was published in the 1970s [148] and the details are covered in reference [154-155]. The Keck asymmetric allylation and the Barton-McCombie reaction are prominent examples [148]. In the 1980s, the use of irreversible CTAs to control the molecular weight and the end group functionalities of polymers was highlighted [148]. The first CTA which enabled living polymerisation was discovered in the 1990s [148]. For compounds A and B (Figure 1.5), the R-C and R-S bonds are easy to break so free radical leaving groups R (electron donating group) are able to reinitiate polymerisations. The reactivity of C=C or C=S bonds are controlled by Z groups which affect the rate of radical addition and fragmentation in the polymerisation process. Examples of R and Z groups are shown in Figure 1.6. The compound A was used before 1998 then compound B was introduced in 1998 and used until now because the C=S

bond (compound B) is more reactive than the C=C bond (compound A), favouring forward fragmentation and achieving 100 % monomer conversion [148, 153].

Common structures of R and Z are discussed below.

Figure 1. 5. Chemical structures of compound A and compound B [148].

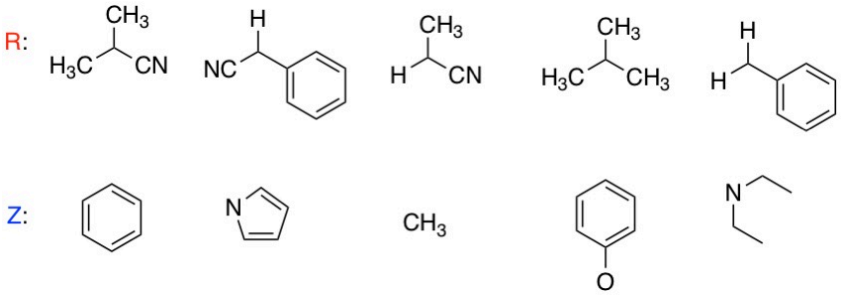

Figure 1. 6. Examples of R and Z groups [148].

1.4.2. Synthesis of Macro-RAFT agent

RAFT agent modification of a polymer may be done to create macro-RAFT agents [148]. Proteins, polysaccharides and peptides are examples of biopolymers which may be employed in RAFT polymerisation as macroinitiators in order to achieve targeted drug delivery in human body [156-159]. This is because different proteins, polysaccharides and peptides are found in different parts of the body such as trypsinogen in pancreas [160] and cell-penetrating peptides in the small intestine [161]. Reactions of the macroinitiators with hydroxyl or amino functional groups and RAFT agents that possess carboxyl groups are major strategies for producing macro-RAFT agents [148]. The RAFT agent precursors that contain carboxyl functionality are illustrated in Figure 1.7.

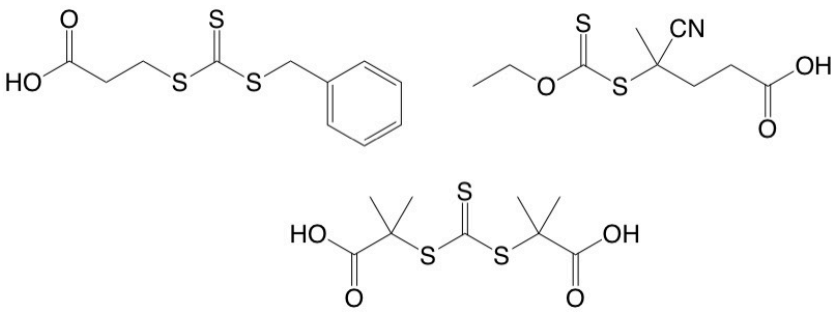

Figure 1. 7. Chemical structures of the RAFT agent precursors with carboxyl functionality [148].

The RAFT agents which have activated ester functionality can be synthesised via reaction between molecules that have ester or amine functional groups [162]. An example is illustrated in Scheme 1.5.

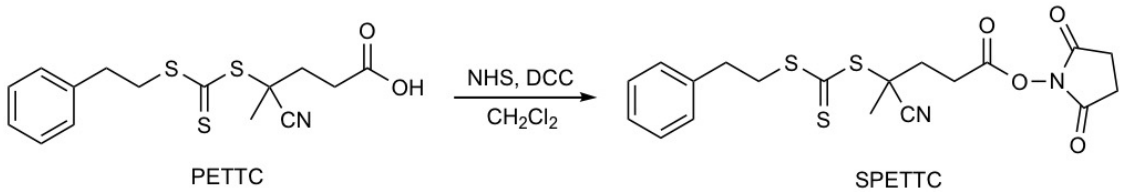

Scheme 1. 5. Synthesising SPETTC RAFT agent which has ester functionality; NHS: *N*-hydroxysuccinimide; DCC: *N,N'*-dicyclohexylcarbodiimide; reaction conditions: at 20 °C and overnight [162].

Modification of RAFT agents (R groups) can be performed via the strategy of thiol-ene click reactions [163]. From the point of view of synthesising macro-RAFT agents, this method provides a high yield of modified RAFT agents, with an example being the reactions of the cysteine functional groups in Bovine Serum Albumin (BSA) with a maleimide [164-165]. The key reaction condition is that the RAFT agent (reactant) must be involved in excess [164]. An example of the RAFT agent modification is shown in Scheme 1.6.

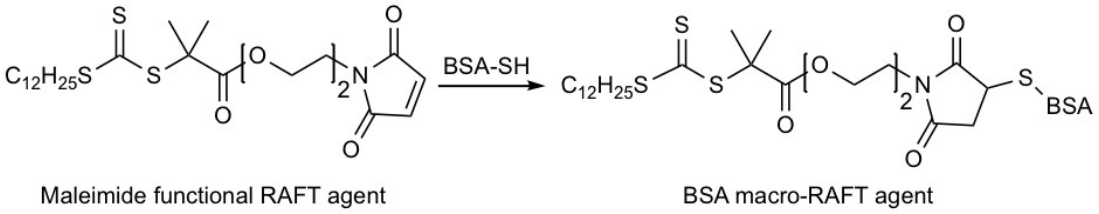

Scheme 1. 6. An example of RAFT agent modification reaction by thiol-ene click chemistry. The reaction is conducted in phosphate buffer pH 7.2 solution with 5% of DMF [164-165].

1.4.3. Copolymer synthesis via RAFT polymerisation

High yield of polymers is produced by RAFT polymerisation and the chain lengths of each block can also be controlled [166-167]. Lee and co-workers reported thiol-terminated poly(styrene-*ran*-vinyl phenol) (PSVPh) copolymers and PSVPh-coated gold nanoparticles, aiming for creating stable ligands for nanoparticles with controlled hydrophilicity [168]. Dithioester-terminated poly(styrene-*ran*-acetoxystyrene) was produced by RAFT

polymerisation employing cumyl dithiobenzoate as a chain transfer agent [168]. The acetoxy-pendant groups were hydrazinolysised to thiol-terminal hydroxyl-pendant groups by hydrazine hydrate [168]. PSVPh-coated nanoparticles with an average diameter of 7.2 nm were produced in a mixture of thiol-terminated PSVPh and PSVPh copolymer with disulfides in a water/toluene, two-phase system [168]. The hydrophilicity of the metal nanoparticle surface can be controlled which can be applied in biological and hierarchically ordered system (diblock copolymers) [168].

1.4.4. Acrylamide segmental copolymers synthesised via RAFT polymerisation

Acrylamide (AM) can be generated in carbohydrated-rich food by using high temperature cooking methods, for instance roasting, baking and frying [169]. The carbonyl group of fructose and glucose reacts with the amino group of asparagine in a condensation reaction to produce AM [169]. The U.S. Environmental Protection Agency cancer potency reported the no significant risk level of AM is 4.5 $(mg/kg\text{-}day)^{-1}$ for human body [169]. The analysis and results were determined from a linearised multistage procedure and using the remarkably increased incidences of central nervous system, uterus, mammary and thyroid glands and oral cavity tumors in female Fischer 344 rats [169]. Therefore, AM should be safe to utilise as one of the blocks of the synthesised copolymer which can potentially be used as drug carriers in human body.

AM and various other monomers were employed to synthesise copolymer nanoparticles and modify of metal nanoparticles in cancer treatment applications. Joseph and co-workers synthesised amphiphilic diblock copolymer nanoparticles poly[(propylene sulfide)-*b*-(alendronate acrylamide-*co*-*N,N*-dimethylacrylamide)] [170]. Small molecules GANT58 inhibitor were loaded into the nanoparticles (≈ 40 nm) to achieve bone-targeted property and achieved significant reduction in tumor-induced bone destruction using an intracardiac mouse model of bone metastasis [170]. Sujittra and co-workers reported poly(poly(ethylene glycol) monomethyl ether methacrylate)-*b*-(poly(*N*-isopropyl acrylamide)-*stat*-poly(thiolactone acrylamide)) diblock copolymer which was produced by RAFT polymerisation (Scheme 1.7) [171]. This copolymer modified the surface of amino-coated iron (II,III) oxide (Fe_3O_4) magnetic nanoparticle by reacting the thiolactone

part of the copolymer with the amino group on the metal nanoparticle surface (Figure 1.7) [171]. The modified Fe_3O_4 nanoparticle achieved water dispersible and thermoresponsible properties and can be potentially used as controlled release drug carrier in human body [171].

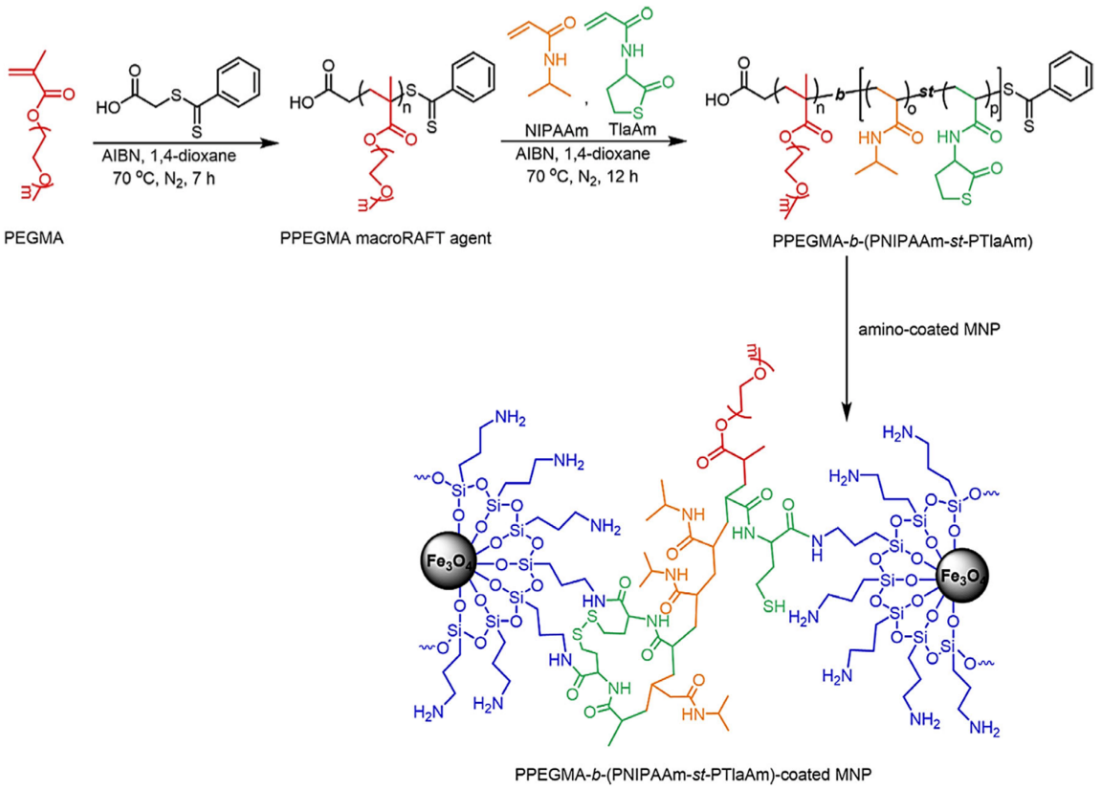

Scheme 1. 7. Reaction outline of PPEGMA-b-(PNIPAAm-*st*-PTlaAm)-coated magnetic nanoparticle [171].

1.5. Polymer Induced Self-Assembly

Macro-RAFT agents can be used in-conjunction with Polymer Induced Self-Assembly (PISA) [172-178]. PISA can be applied to dispersion polymerisation for synthesising biodegradable and biocompatible diblock copolymers [179-180]. The bio-copolymers form nanoparticles which show changes of morphology during polymerisation, including spherical vesicles, ellipsoidal vesicles, short nanotubes to nanotubes [172]. The RAFT agent precursor is used to produce a solvent soluble polymer which is a macro-RAFT agent [172]. A second type of monomer (solvent soluble) is responsible for the production of the second block of the copolymer, which becomes increasingly solvent insoluble upon an increased degree of polymerisation [172]. Alcohols, water or a mixture

of water and alcohol [172], *n*-alkanes, and ionic liquids can be used as solvents [172]. According to the basic theory of PISA, it can be performed with many kinds of living polymerisation [181-182]. However, a large number of reports show that RAFT polymerisation is highly suitable for PISA [181, 183-190]. Generally, the second block of the copolymer has a greater number of repeat units than that of the first block [172, 181]. Therefore, the copolymer cannot molecularly dissolve in the solvent by producing macromolecular nanoassemblies during the polymerisation [172]. By applying this strategy, a high concentration of copolymer nanoparticles can be prepared in "one pot" reaction [172, 181]. Polymer nanoparticles are not only restricted to spheres, but also have other shapes such as worms, vesicles, lamellae, framboidal vesicles, oligolamellar vesicles, jellyfish, and yolk/shell particles (Tables 1.1-1.2). The morphology of nanoparticles can be controlled by changing the number of repeat units of the two blocks, the actual polymer of each block, and the polymerisation medium (Figure 1.8) [181].

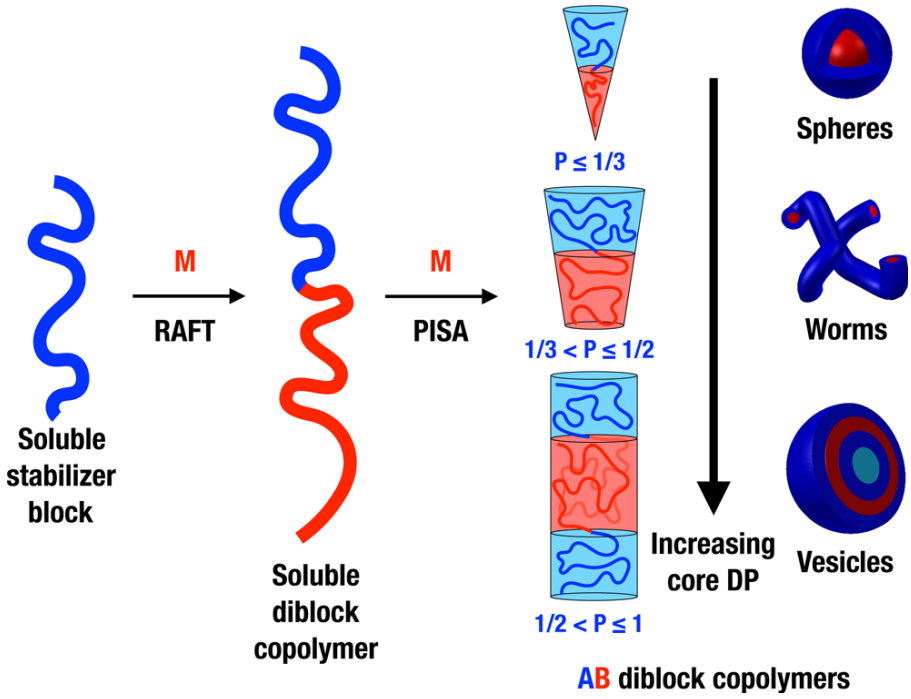

Figure 1. 8. Schematic of synthesising diblock copolymers by using RAFT polymerisation and PISA [181].

M: monomer; DP: degree of polymerisation. Hydrophilic and hydrophobic chain lengths affect shape of synthesised diblock copolymer nanoparticles.

Table 1. 1. Common morphologies of copolymers and chemical examples [181].

Usual morphologies	Examples of copolymers
Spheres [183]	Poly(2-(dimethylamino) ethylmethacrylate$_{11}$-*stat*-glycerol monomethacrylate)$_{116}$-*b*-poly(2-hydroxypropyl methacrylate)$_{900}$ [191]
Worms [192]	Poly(glycerol monomethacrylate)$_{47}$-*b*-poly(2-hydroxypropyl methacrylate)$_{130}$ [193]
Vesicles [194]	Poly(glycerol monomethacrylate)$_{47}$-*b*-poly(2-hydroxypropyl methacrylate)$_{200}$ [181]

Table 1. 2. Unusual morphologies of copolymers and chemical examples [181].

Unusual morphologies	Examples of copolymers
Lamellae [195]	Poly(methacrylic acid)$_{79}$-*b*-poly(styrene-*alt*-*N*-phenylmaleimide)$_{650}$ [181]
Framboidal vesicles [196]	Poly(glycerol monomethacrylate)$_{63}$-*b*-poly(2-hydroxypropyl methacrylate)$_{350}$-*b*-poly(benzyl methacrylate)$_{125}$ [181]
Oligolamellar vesicles [181]	Poly(4-vinyl-pyridine)$_{73}$-*b*-polystyrene$_{654}$ [181]
Jellyfish [197]	Poly(glycerol monomethacrylate)$_{47}$-*b*-poly(2-hydroxypropyl methacrylate)$_{156}$ (at 78% HPMA conversion) [181]
Yolk/shell particles [181]	Poly(4-vinylpyridine)-*b*-polystyrene [181]

1.5.1. Diblock copolymer nanoparticles synthesis by RAFT polymerisation and PISA

Diblock copolymers synthesised by RAFT polymerisation can be used in drug delivery and cell imaging [198-199]. The copolymer must have minimal toxicity and high biocompatibility [200]. High solid content (>20 % w/w) of nanoparticles can be produced by applying a macro-RAFT agent as a steric stabiliser [181]. Longer macro-RAFT agents

provides greater steric stabilisation [181]. The production of diblock copolymers (RAFT polymerisation) that form nanoparticles via PISA in an aqueous environment is shown in Schemes 1.8-1.9. Both of the Schemes 1.8 dispersion and 1.9 emulsion RAFT polymerisations use the same macro-RAFT agent, poly(glycerol monomethacrylate) (PGMA) [181].

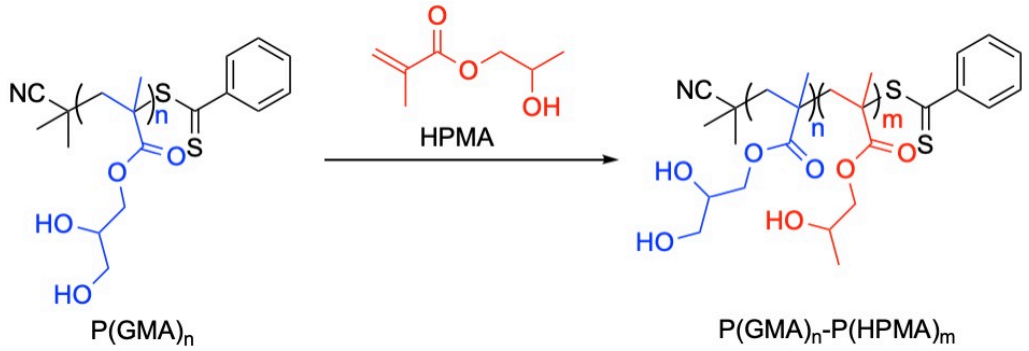

Scheme 1. 8. RAFT dispersion polymerisation mediated PISA in aqueous environment.

The reaction is conducted in water at 70 °C [181]; HPMA: 2-hydroxypropyl methacrylate.

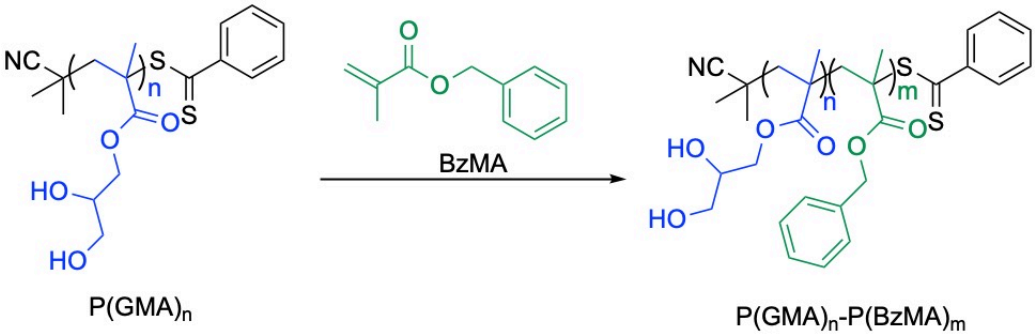

Scheme 1. 9. RAFT emulsion polymerisation mediated PISA in aqueous environment.

The reaction is conducted in water at 70 °C [181]; BzMA: benzyl methacrylate.

Poly(2-hydroxypropyl methacrylate) (PHPMA) attracts interest due to its thermoresponsive characteristics [201]. The block copolymer poly(ethylene glycol)-*b*-PHPMA (PEG-*b*-PHPMA) has various morphologies at different reaction temperatures [201]. With increasing the repeat units of the PHPMA, the copolymer becomes more linear which can be detected by the nanoparticle shape changing from spheres to vesicles [201]. The scheme for linking PEG to a RAFT agent and the copolymerisation is illustrated in Scheme 1.10.

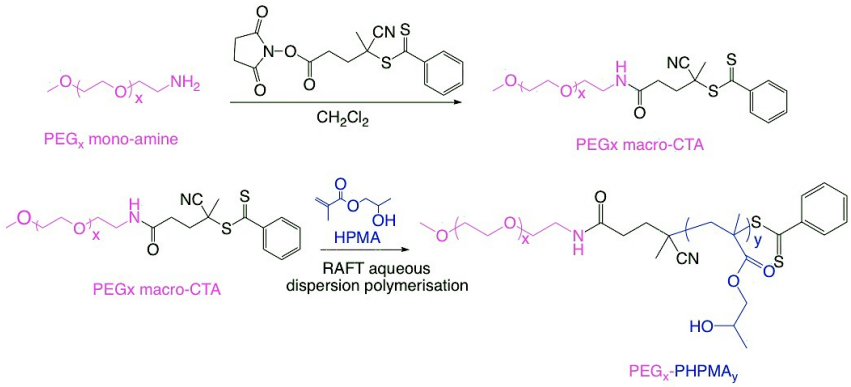

Scheme 1. 10. Preparation of PEG-macro-CTA and subsequent the copolymer PEG-*b*-PHPMA [201].

The reaction is conducted in dichloromethane at 20 °C for 18 hours.

The PEG-*b*-PHPMA copolymer is successfully produced with efficient conversions, low polydispersity index (PDI) and high rate of blocking properties (concentration of solid state in produced copolymer nanoparticles) [201]. Therefore, nanoparticles of this copolymer can be produced. Modification of PHPMA can be further studied due to the thermoresponsive property and different shapes of nanoparticle formed by varying the PHPMA chain length. It is interesting to point out that a unique morphology—oligolamellar vesicles are discovered by Small-Angle X-ray Scattering (SAXS) and Transmission Electron Microscopy (TEM) [201]. The changing of the morphologies of the PEG-*b*-PHPMA copolymer nanoparticles is shown in Figure 1.9.

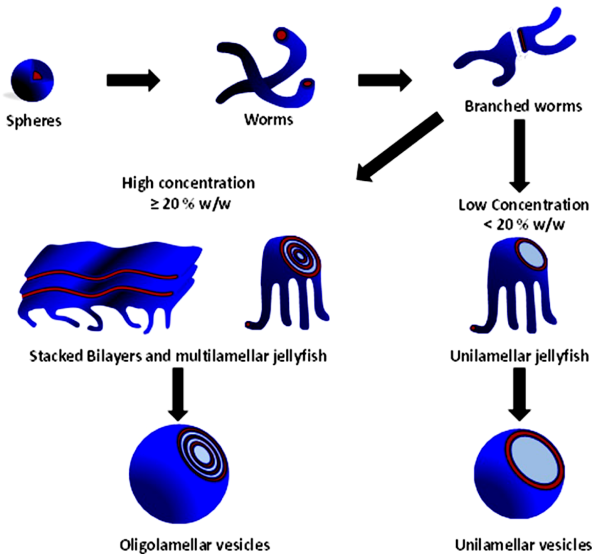

Figure 1. 9. Various morphologies of the PEG-*b*-PHPMA copolymer nanoparticles.

% w/w: percentage weight per weight of the solid contents in each nanoparticle [201].

1.6. *N*-Carboxyanhydride Ring-Opening Polymerisation

A diblock copolymer for drug delivery application can be synthesised by NCA ROP. *N*-Carboxyanhydrides (NCA)s derived from amino acids were published in 1906 by Leuchs [202]. In the 1950s, the Ring–Opening Polymerisation (ROP) of various NCAs by employing primary amines as the initiators was successfully performed [202]. Scheme 1.11 shows the general mechanism of NCA ROP [202]. It is meaningful to point out that the characteristics of the synthesised poly(amino acid)s (PAAs) are the same as the original amino acids [202].

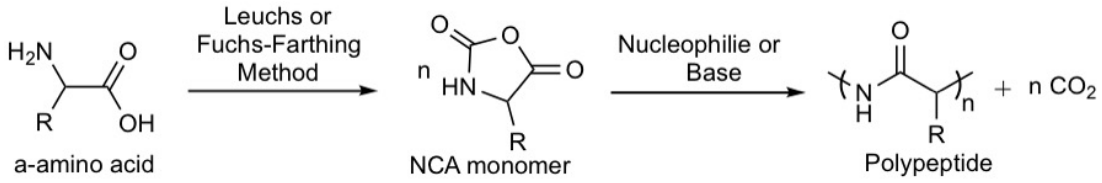

Scheme 1. 11. General mechanism of NCA ROP [202].

There are two strategies by which the NCA can be synthesised; the Leuchs [203] method and the Fuchs-Farthing method [202]. Leuchs method utilises reactions between *N*-alkyloxycarbonylamino acids and molecules that contain halogen functionality [202]. Compared to the Leuchs technique, the Fuchs-Farthing method uses more harmful reactants [202]. In the Fuchs-Farthing strategy, phosgene compounds (for example diphosgene, triphosgene and di-*tert*-butyltricarbonate) are used as the carbonyl source that reacts with the chosen amino acid [202]. One of the safety issues of the Fuchs-Farthing method is that toxic phosgene gas is produced during the reaction which needs to be handled carefully [202]. The desired NCAs can be collected via recrystallisation [202]. Flash column chromatography can also be used for the products isolation but an inert atmosphere must to be maintained [202]. However, the final products can be contaminated by side products for instance hydrochloride, salts of hydrochloride-amino acid and 2-isocyanatoacyl chlorides [202].

The first living polymerisation of α-amino acid NCA via the theory of NCA ROP with organonickel catalysts was reported by Deming in 1997 [202, 204]. By applying the techniques reported, the large molecular mass copolymers (co-polypeptides) with desired end functional groups can be synthesised [202]. Subsequently, controlled NCA

ROP under strict reaction conditions were published [202]. Table 1.3 illustrates various reaction conditions that have been utilised for the production of PAAs by NCA ROP. The efficiency of NCA ROP can be affected by temperature and pressure. Both of silazane derivatives and primary amine hydrochlorides have lone pairs of electrons on nitrogen atoms which react with carbonyl group on the NCA (carbon-5, C=O, not close to secondary amine), initiating NCA ROP.

Table 1. 3. NCA ROP with various reaction conditions.

Novel initiators	Polymerisation techniques	Optimised reaction conditions
Silazane derivatives [205]	High vacuum polymerisation [206]	Temperature [202]
Primary amine hydrochlorides [207]		Pressure [202]

1.6.1. Monodisperse poly(amino acid) synthesis

Monodisperse PAAs can be synthesised via NCA ROP, which has the benefits of desired molecular weight control and minimal side reactions [208-210]. Popular amino acid NCAs are shown in Figure 1.10. With the application of this strategy, copoly(amino acid)s may be synthesised which have various chemical structures, properties and functions depending on each PAA repeat unit [208, 211-212]. Since the copoly(amino acid)s can have a large variety of characteristics, they have the potential use in many areas for instance, drug delivery [213-214], cell adhesion [215-216] and oncology [208].

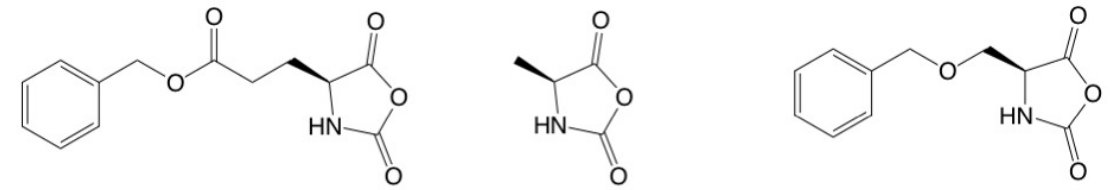

Figure 1. 10. Examples of popular amino acid NCA. [208, 217].

A common ROP mechanism which is initiated by a nucleophile (benzyl amine) is shown in Scheme 1.12. Carbamic acid or anions are formed when the fifth carbon atom on a

NCA molecule is attacked by a primary amine [208]. Then the primary amine is produced by releasing carbon dioxide [208]. Therefore, the reactions repeat as a polymerisation. At the same time, side reactions can be minimised (low temperature, for instance 0 °C, and/or high vacuum), such as the termination of the unreacted chains and the production of cyclic substances [208]. The side reactions take place due to the transfer of hydrogen atoms from the NCA and the presence of water molecules that may initiate NCA ROP [208]. Therefore, NCA ROP must be carried out in anhydrous solvents and glassware needs to be dried.

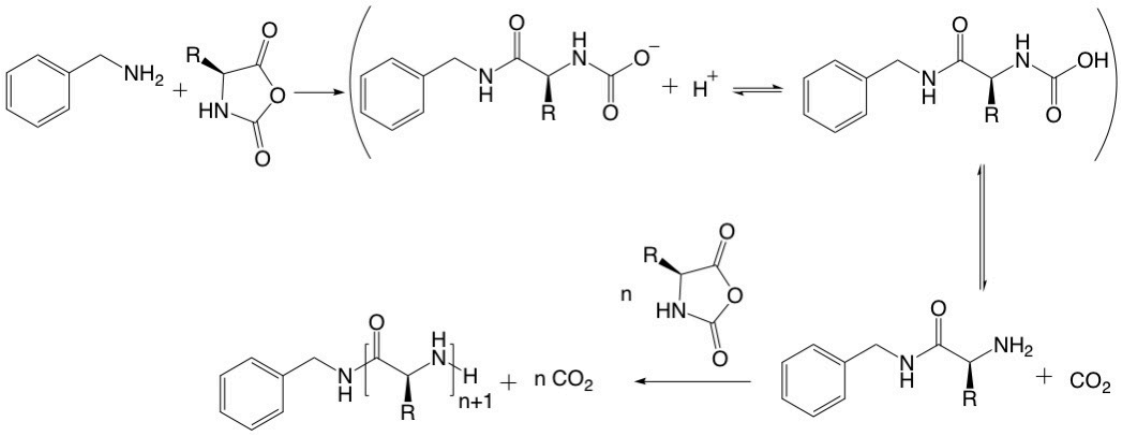

Scheme 1. 12. Mechanism of ROP which is initiated by benzyl amine [208, 217-218].

1.7. Azo compounds

Azo compounds are widely used as food additives, radical reaction initiators, pigments, indicators, therapeutic agents, potentially in electronics and drug carriers [219-222]. Aromatic azo compounds have efficient *cis-trans* iosomerisation under appropriate radiation so they also be employed as molecular switches [222]. A molecule contains azobenzene, the motion of the azobenzene influences and controls the movement of the complementary substrate which is non-covalently bound to the azobenzene fragment [223].

1.7.1. Azo coupling

The mechanism of azo coupling reaction is the diazotisation of an aromatic primary amine at low temperature and then reacting with an electron rich aromatic nucleophile, which usually gives short reaction time and high yields [222]. An example of the reaction

and its mechanism are provided in Schemes 1.13 and 1.14. Weak electrophilic diazonium salts react with aromatic hydrocarbon (arenes) that possess electron donor functional groups such as amine, hydroxyl and acrylamido to produce azobenzenes [222]. In accordance with the mechanism in Scheme 1.14, this reaction is pH dependent. Acid (e.g. HCl) is necessary to provide *in situ* nitrous acid from sodium nitrite ($NaNO_2$) [222]. The nitrosating agent ($^{+}N=O$) is produced by continuing protonation and water elimination. Reaction of the amine and the nitrosating agent gives the *N*-nitroso derivative 5, and a tautomer of the diazohydroxide 6. After further protonation and water elimination, the diazonium salt 1 is synthesised which is stabilised by resonance [222]. The Scheme 1.14 is the most accepted mechanism currently involving the electrophilic aromatic substitution of the phenol and the aniline and the electrophilic nitrogen of the diazonium salt [222].

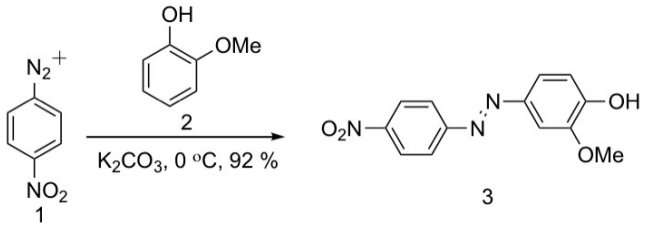

Scheme 1. 13. An example of synthesising azo benzene with high yields at low temperature [224].

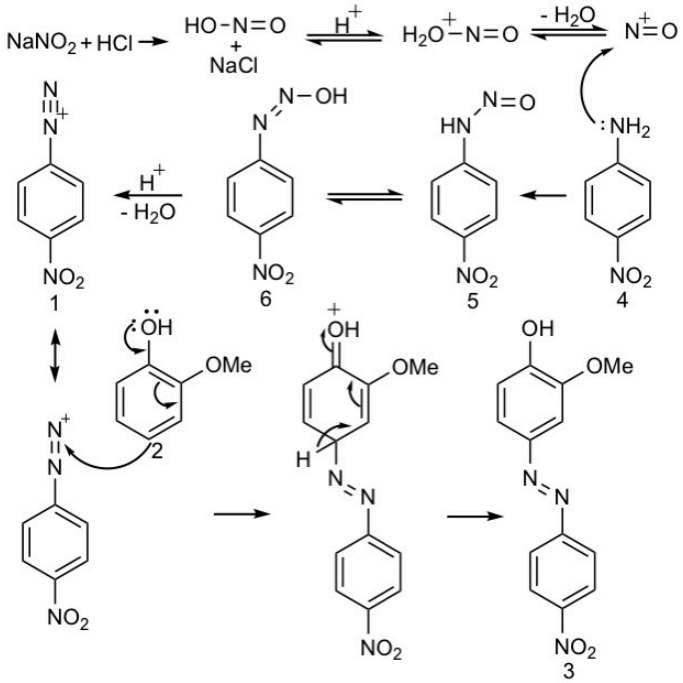

Scheme 1. 14. Mechanism of the reaction in Scheme 1.13 [224].

1.7.2. Compounds produced via azo coupling reaction

Enzyme triggered fluorescent nanoparticles can be produced by azo coupling reaction and RAFT polymerisation. Shang and co-workers synthesised nanoparticles with an average diameter of 196 nm by azo coupling reaction induced macromolecular self-assembly in aqueous environment [225]. A diblock copolymer poly(ethylene glycol)$_{43}$-*b*-poly(ρ-*N*-Boc-vinylaniline)$_{10}$ (PEG$_{43}$-*b*-PSNH$_{10}$Boc) was produced by RAFT polymerisation [225]. The PEG$_{43}$-*b*-PSN$_2^+{}_{10}$ diazonium salt was synthesised via deprotected of PEG$_{43}$-*b*-PSNH$_{10}$Boc using dichloromethane (DCM), TFA, concentrated hydrochloric acid and sodium nitrite in water [225]. Then tetraphenylethene and *N,N*-dimethylaniline were added in the reaction, reacting with the PEG$_{43}$-*b*-PSN$_2^+{}_{10}$ diazonium salt in aqueous acidic media to generate the azobenzene [225]. The fluorescent self-assembly nanoparticles were formed due to the hydrophobicity of the azobenzene fragment and the fluorescent group in aniline in aqueous solution [225]. By adding azoreductase enzyme, the fluorescent self-assembled nanoparticles changed from yellow (UV-vis λ_{max}= 415 nm) to pale yellow (UV-vis spectrum decreased to nearly zero), suggested the nanoparticles have enzyme-triggered fluorescent and can be applied in imaging of hypoxic tumor potentially [225-228].

New azo dyes based on 4-aminostilbene via azo coupling which have antioxidant and antibacterial properties were produced by Esmail's group [229]. 4-aminostilbene was synthesised from 4-nitrobenzyl bromide by Wittig and reduction reactions (Scheme 1.15) [229]. Five different phenols were reacted with the 4-aminostilbene, respectively under azo coupling reaction and producing five azobenzene dyes (Scheme 1.16) [229]. The antioxidant and antimicrobial activities all of the synthesised azo compounds were tested against radical scavenging assay using 2,2-diphenyl-1-picrylhydrazyl (DPPH) radical and one gram-positive and eight gram-negative strains based on the inhibition zone using disc diffusion assay [229]. All the azo compounds can scavenge free radical of DPPH, compounds 2c and 2d (Scheme 1.16) performed better scavenging property than that of butylated hydroxytoluene (an antioxidant agent in food industry) [229]. Additionally, the compounds 2c and 2d (Scheme 1.16) can inhibit the growth of *S. pneumonia* and *P. aeruginosa* [229]. Compounds 2c and 2d inhibited the growth of microorganisms might

due to the two hydroxyl groups on the phenolic ring [229]. Therefore, azo coupling and RAFT polymerization can be performed in the synthesis of fluorescent nanoparticles. 4-Aminostilbene modified azo dyes have antioxidant and antibacterial properties. Sufanilamide (antimicrobial agent) modified polymers via azo coupling reaction can be developed, which may be applied to hand wash and laundry detergent.

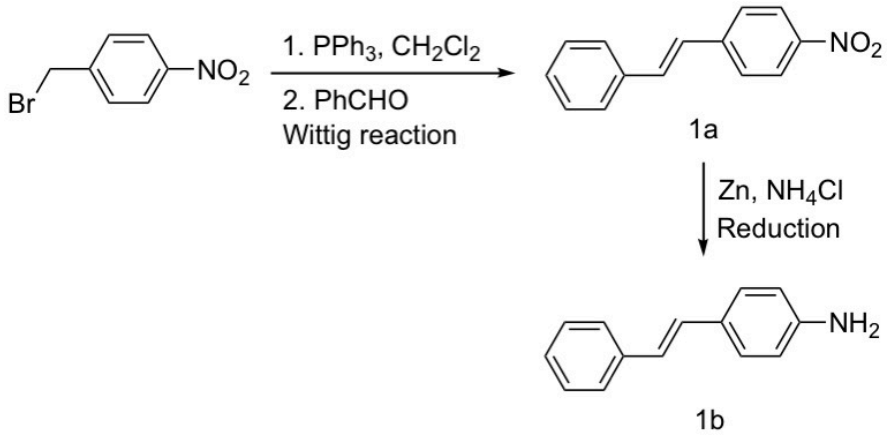

Scheme 1. 15. Synthesis of 4-aminostilbene [229].

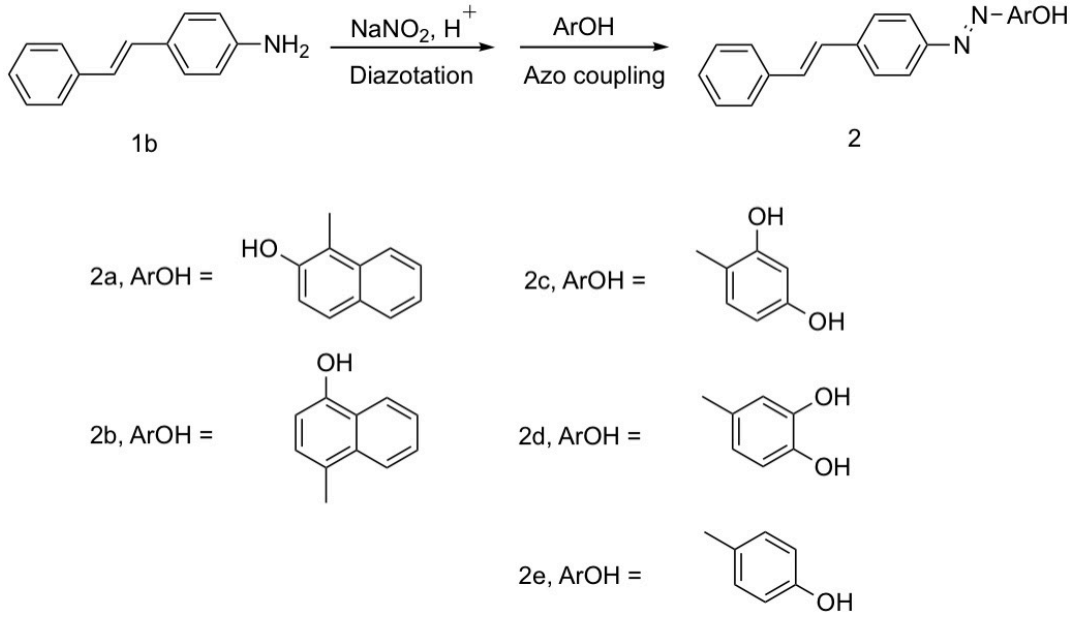

Scheme 1. 16. Synthesis of five azo compounds via azo coupling reaction [229].

1.8. Research aims and thesis outline

Challenges: Conjugation of fucose to RAFT agent (SCPDB) because polarity of the two compounds are very different.

New contributions: For fucose and RAFT agent conjugation, acetic acid was used to dissolve the mentioned substances and the conjugation progressed successfully. PSar-*b*-PHPMA, PBLG-*b*-PEG and fucose-PHPMA nanoparticles were utilised as drug delivery vehicles and published. Sulfanilamide modified P(ρHS)-*b*-PAM nanoparticles as antimicrobial agents were first time synthesised.

RAFT polymerisation has been widely used to create a wide range of polymers capable of forming nanoparticles in aqueous environments which can be used as drug delivery vehicles in human body. During polymerisation, nanoparticles form, potentially in the presence of drug molecules. Therefore, the drug can be encapsulated within the nanoparticles that may potentially be used to transport the drug to target disease sites. In order for the drug molecules to be released, and the polymer nanoparticles to be cleared from the body post-deployment, it is essential that non-toxic and biocompatible polymers are used for nanoparticle creation. Such polymers can be synthesised via ROP NCA. Using RAFT polymerisation, PISA and NCA ROP, stable amphiphilic nanoparticles synthesised can be used as drug carriers potentially.

The initial research is introduced in Chapter 3, generating a range of amphiphilic and thermoresponsive nanoparticles from sarcosine (Sar) NCA and HPMA via NCA ROP, RAFT polymerisation and PISA. The toxicity of the nanoparticles was tested against three breast cancer cell lines (MCF-7, MDA-MB-231 and MDA-MB-453). Pure PSar-*b*-PHPMA nanoparticles were non-toxic but showed toxicity with enhanced Dox-loaded PSar-*b*-PHPMA nanoparticle concentration. In Chapter 4, hydroxyl initiation of benzyl glutamate (BLG) NCA by PEG yields PEG-*b*-poly(benzyl glutamate) (PEG-*b*-PBLG), that crucially presents an acid labile ester link. This link renders the diblock polymer pH-responsive, and susceptible to acid-mediated-degradation. The formation of non-cytotoxic PEG-*b*-PBLG nanoparticles, and their assessment against three breast cancer cell lines, was achieved. The pH-responsive PBLG-*b*-PEG nanoparticles may be applied as anti-cancer drug carriers for controlled release applications. A PHPMA material was produced by RAFT polymerisation. An injectable, self-healing and thermoresponsive gel depot was formed by dissolving PHPMA in DMSO then injecting the PHPMA solution in an aqueous media. Combining the PBLG-*b*-PEG nanoparticles and PHPMA gel depot, an injectable drug delivery system was produced. Modification of PHPMA with fucose to yield a

polymer able to form thermoresponsive nanoparticles that may have enhanced binding to pancreatic cancer cells is illustrated in Chapter 5. Fucose-PHPMA nanoparticles were synthesised via RAFT polymerisation followed by coacervation in aqueous solution. The thermoresponsive PHPMA gel depot also applied to the fucose-PHPMA nanoparticles. An injectable drug carrier can be formed and specific to pancreatic cancer cells. In Chapter 6, poly(ρ-hydroxystyrene-sulfanilamide) (PρHS-SA) and poly(ρ-hydroxystyrene-SA)-*b*-poly(acrylamide) (P(ρHS-SA)-*b*-PAM) were synthesised via RAFT polymerisation, acid hydrolysis and azo coupling reaction. SA has antimicrobial activity. The nanoparticles produced from PρHS-SA and P(ρHS-SA)-*b*-PAM were considered suitable for antimicrobial applications.

1.9. References

1. Balachandra, A., Chan, E.C., Paul, J.P., Ng, S., Chrysostomou, V., Ngo, S., Mayadunne, R. and van Wijngaarden, P. A biocompatible reverse thermoresponsive polymer for ocular drug delivery. *Drug Delivery.* 2019, **26**(1), pp.343-353.
2. Zabihi, F., Graff, P., Schumacher, F., Kleuser, B., Hedtrich, S. and Haag, R. Synthesis of poly(lactide-co-glycerol) as a biodegradable and biocompatible polymer with high loading capacity for dermal drug delivery. *Nanoscale.* 2018, **10**(35), pp.16848-16856.
3. Liu, S.D., Huang, Z.P., Li, F., Yan, T.F., Fu, S., Tian, R.Z., Hou, C.X., Luo, Q., Xu, J.Y. and Liu, J.Q. Supramolecular polymer nanocapsules by enzymatic covalent condensation: biocompatible and biodegradable drug-delivery systems for chemo-photothermal anticancer therapy. *Polymer Chemistry.* 2019, **10**(26), pp.3566-3570.
4. George, A., Shah, P.A. and Shrivastav, P.S. Natural biodegradable polymers based nano-formulations for drug delivery: A review. *International Journal of Pharmaceutics.* 2019, **561**, pp.244-264.
5. George, A., Shah, P.A. and Shrivastav, P.S. Natural biodegradable polymers based nano-formulations for drug delivery: A review. *International Journal of Pharmaceutics.* 2019, **561**, pp.244-264.
6. Da, L.C., Gong, M., Chen, A.J., Zhang, Y., Huang, Y.Z., Guo, Z.J., Li, S.F., Li-Ling, J., Zhang, L. and Xie, H.Q. Composite elastomeric polyurethane scaffolds incorporating small intestinal submucosa for soft tissue engineering. *Acta Biomaterialia.* 2017, **59**, pp.45-57.
7. Rosello, A.P., da Silva, R.T., Castro, C., Bardallo, R.G., Calvo, M., Folch-Puy, E., Carbonell, T., Palmeira, C., Catafau, J.R. and Adam, R. Polyethylene Glycol 35 as a Perfusate Additive for Mitochondrial and Glycocalyx Protection in HOPE Liver Preservation. *International Journal of Molecular Sciences.* 2020, **21**(16), p.16.
8. Zhang, Z., Zhang, Y.Y., Song, S.W., Yin, L., Sun, D. and Gu, J.K. Recent advances in the bioanalytical methods of polyethylene glycols and PEGylated pharmaceuticals. *Journal of Separation Science.* 2020, **43**(9-10), pp.1978-1997.
9. Bayram, B., Ozgur, A., Tutar, L. and Tutar, Y. Tumor Targeting of Polymeric Nanoparticles Conjugated with Peptides, Saccharides, and Small Molecules for Anticancer Drugs. *Current Pharmaceutical Design.* 2017, **23**(35), pp.5349-5357.
10. Wagner, E. and Kloeckner, J. Gene delivery using polymer therapeutics. In: SatchiFainaro, R. and Duncan, R. eds. *Polymer Therapeutics I: Polymers as Drugs, Conjugates and Gene Delivery Systems*. Berlin: Springer-Verlag Berlin, 2006, pp.135-173.

11. Liu, T.W., Yan, S.J., Zhou, R.T., Zhang, X., Yang, H.W., Yan, Q.Y., Yang, R. and Luan, S.F. Self-Adaptive Antibacterial Coating for Universal Polymeric Substrates Based on a Micrometer-Scale Hierarchical Polymer Brush System. *Acs Applied Materials & Interfaces.* 2020, **12**(38), pp.42576-42585.
12. Zhang, Y.J., Kang, K., Zhu, N.H., Li, G.H., Zhou, X.X., Zhang, A.M., Yi, Q.Y. and Wu, Y. Bottlebrush-like highly efficient antibacterial coating constructed using alpha-helical peptide dendritic polymers on the poly(styrene-b-(ethylene-co-butylene)-b-styrene) surface. *Journal of Materials Chemistry B.* 2020, **8**(33), pp.7428-7437.
13. Yang, F., Zhang, X.X., Song, L.N., Cui, H.T., Myers, J.N., Bai, T.T., Zhou, Y., Chen, Z. and Gu, N. Controlled Drug Release and Hydrolysis Mechanism of Polymer-Magnetic Nanoparticle Composite. *Acs Applied Materials & Interfaces.* 2015, **7**(18), pp.9410-9419.
14. Asadi, E., Azodi-Deilami, S., Abdouss, M., Kordestani, D., Rahimi, A. and Asadi, S. Synthesis, recognition and evaluation of molecularly imprinted polymer nanoparticle using miniemulsion polymerization for controlled release and analysis of risperidone in human plasma samples. *Korean Journal of Chemical Engineering.* 2014, **31**(6), pp.1028-1035.
15. Gut, G., Ambroziak, M., Bojar, W., Szaraniec, B., Chlopek, J., Flis, S., Koronkiewicz, M. and Jastrzebski, Z. In Vitro and In Vivo (Rabbit, Guinea Pig, Mouse) Properties of a Novel Resorbable Polymer and Allogenic Bone Composite for Guided Bone Regeneration and Orthopedic Implants. *Transplantation Proceedings.* 2018, **50**(7), pp.2223-2228.
16. Kettunen, J., Makela, A., Miettinen, H., Nevalainen, T., Pohjonen, T., Suokas, E. and Rokkanen, P. The fixation properties of carbon fiber-reinforced liquid crystalline polymer implant in bone: An experimental study in rabbits. *Journal of Biomedical Materials Research.* 2001, **56**(1), pp.137-143.
17. Mishra, R., Varshneya, R., Das, N., Sircar, D. and Roy, P. Synthesis and characterization of gelatin-PVP polymer composite scaffold for potential application in bone tissue engineering. *European Polymer Journal.* 2019, **119**, pp.155-168.
18. Sponchioni, M., Palmiero, U.C. and Moscatelli, D. Thermo-responsive polymers: Applications of smart materials in drug delivery and tissue engineering. *Materials Science & Engineering C-Materials for Biological Applications.* 2019, **102**, pp.589-605.
19. Berge, T.L.L., Lygre, G.B., Lie, S.A., Lindh, C.H. and Bjorkman, L. Bisphenol A in human saliva and urine before and after treatment with dental polymer-based restorative materials. *European Journal of Oral Sciences.* 2019, **127**(5), pp.435-444.
20. Nilsen, B.W., Ortengren, U., Simon-Santamaria, J., Sorensen, K.K. and Michelsen, V.B. Methods and terminology used in cell-culture studies of low-dose effects of matrix constituents of polymer resin-based dental materials. *European Journal of Oral Sciences.* 2016, **124**(6), pp.511-525.
21. Kabanov, A.V., Batrakova, E.V. and Alakhov, V.Y. Pluronic (R) block copolymers as novel polymer therapeutics for drug and gene delivery. *Journal of Controlled Release.* 2002, **82**(2-3), pp.189-212.
22. Du, J.Z., Du, X.J., Mao, C.Q. and Wang, J. Tailor-Made Dual pH-Sensitive Polymer-Doxorubicin Nanoparticles for Efficient Anticancer Drug Delivery. *Journal of the American Chemical Society.* 2011, **133**(44), pp.17560-17563.
23. Mi, L. and Jiang, S.Y. Integrated Antimicrobial and Nonfouling Zwitterionic Polymers. *Angewandte Chemie-International Edition.* 2014, **53**(7), pp.1746-1754.
24. Lam, S.J., O'Brien-Simpson, N.M., Pantarat, N., Sulistio, A., Wong, E.H.H., Chen, Y.Y., Lenzo, J.C., Holden, J.A., Blencowe, A., Reynolds, E.C. and Qiao, G.G. Combating multidrug-resistant Gram-negative bacteria with structurally nanoengineered antimicrobial peptide polymers. *Nature Microbiology.* 2016, **1**(11), p.11.
25. Ungaro, F., d'Angelo, I., Coletta, C., Bianca, R.D.D., Sorrentino, R., Perfetto, B., Tufano, M.A., Miro, A., La Rotonda, M.I. and Quaglia, F. Dry powders based on PLGA

nanoparticles for pulmonary delivery of antibiotics: Modulation of encapsulation efficiency, release rate and lung deposition pattern by hydrophilic polymers. *Journal of Controlled Release.* 2012, **157**(1), pp.149-159.
26. Lepretre, S., Chai, F., Hornez, J.C., Vermet, G., Neut, C., Descamps, M., Hildebrand, H.F. and Martel, B. Prolonged local antibiotics delivery from hydroxyapatite functionalised with cyclodextrin polymers. *Biomaterials.* 2009, **30**(30), pp.6086-6093.
27. Monteiro, D.R., Gorup, L.F., Takamiya, A.S., Ruvollo, A.C., Camargo, E.R. and Barbosa, D.B. The growing importance of materials that prevent microbial adhesion: antimicrobial effect of medical devices containing silver. *International Journal of Antimicrobial Agents.* 2009, **34**(2), pp.103-110.
28. Guo, L.Y., Yuan, W.Y., Lu, Z.S. and Li, C.M. Polymer/nanosilver composite coatings for antibacterial applications. *Colloids and Surfaces a-Physicochemical and Engineering Aspects.* 2013, **439**, pp.69-83.
29. Roe, D., Karandikar, B., Bonn-Savage, N., Gibbins, B. and Roullet, J.B. Antimicrobial surface functionalization of plastic catheters by silver nanoparticles. *Journal of Antimicrobial Chemotherapy.* 2008, **61**(4), pp.869-876.
30. Dhende, V.P., Samanta, S., Jones, D.M., Hardin, I.R. and Locklin, J. One-Step Photochemical Synthesis of Permanent, Nonleaching, Ultrathin Antimicrobial Coatings for Textiles and Plastics. *Acs Applied Materials & Interfaces.* 2011, **3**(8), pp.2830-2837.
31. Gao, Y. and Cranston, R. Recent advances in antimicrobial treatments of textiles. *Textile Research Journal.* 2008, **78**(1), pp.60-72.
32. Dubas, S.T., Kumlangdudsana, P. and Potiyaraj, P. Layer-by-layer deposition of antimicrobial silver nanoparticles on textile fibers. *Colloids and Surfaces a-Physicochemical and Engineering Aspects.* 2006, **289**(1-3), pp.105-109.
33. Chao, Y.H., Liang, Y.H., Fang, G.H., He, H.B., Yao, Q., Xu, H., Chen, Y.R. and Tang, X. Biodegradable Polymersomes as Nanocarriers for Doxorubicin Hydrochloride: Enhanced Cytotoxicity in MCF-7/ADR Cells and Prolonged Blood Circulation. *Pharmaceutical Research*. 2017, **34**(3), pp.610-618.
34. Xu, Y.B., Zi, Y.X., Lei, J.F., Mo, X.Y., Shao, Z.L., Wu, Y.Y., Tian, Y., Li, D.F. and Mu, C.D. pH-Responsive nanoparticles based on cholesterol/imidazole modified oxidized-starch for targeted anticancer drug delivery. *Carbohydrate Polymers*. 2020, **233**, 115858.
35. Rahbar, M., Morsali, A., Bozorgmehr, M.R. and Beyramabadi, S.A. Quantum chemical studies of chitosan nanoparticles as effective drug delivery systems for 5-fluorouracil anticancer drug. *Journal of Molecular Liquids*. 2020, **302**, 112495.
36. Zayed, G.M., Kamal, I., Abdelhafez, W.A., Alsharif, F.M., Amin, M.A., Shaykoon, M.S.A., Sarhan, H.A. and Abdelsalam, A.M. Effect of Chemical Binding of Doxorubicin Hydrochloride to Gold Nanoparticles, Versus Electrostatic Adsorption, on the In Vitro Drug Release and Cytotoxicity to Breast Cancer Cells. *Pharmaceutical Research*. 2018, **35**(6) 112.
37. Challenging paradigms in tumour drug delivery. *Nature Materials.* 2020, **19**(5), pp.477-477.
38. Maeda, H., Tsukigawa, K. and Fang, J. A Retrospective 30Years After Discovery of the Enhanced Permeability and Retention Effect of Solid Tumors: Next-Generation Chemotherapeutics and Photodynamic TherapyProblems, Solutions, and Prospects. *Microcirculation.* 2016, **23**(3), pp.173-182.
39. Folkman, J. Angiogenesis in cancer, vascular, rheumatoid and other disease. *Nature Medicine.* 1995, **1**(1), pp.27-31.
40. Hubert, A., Lyass, O., Pode, D. and Gabizon, A. Doxil (Caelyx): an exploratory study with pharmacokinetics in patients with hormone-refractory prostate cancer. *Anti-Cancer Drugs.* 2000, **11**(2), pp.123-127.

41. Miele, E., Spinelli, G.P., Miele, E., Tomao, F. and Tomao, S. Albumin-bound formulation of paclitaxel (Abraxane (R) ABI-007) in the treatment of breast cancer. *International Journal of Nanomedicine.* 2009, **4**(1), pp.99-105.
42. Alfayez, M., Kantarjian, H., Kadia, T., Ravandi-Kashani, F. and Daver, N. Emerging drug profile: CPX-351 (vyxeos) in AML. *Leukemia & Lymphoma.* 2020, **61**(2), pp.288-297.
43. Hansen, A.E., Petersen, A.L., Henriksen, J.R., Boerresen, B., Rasmussen, P., Elema, D.R., af Rosenschold, P.M., Kristensen, A.T., Kjaer, A. and Andresen, T.L. Positron Emission Tomography Based Elucidation of the Enhanced Permeability and Retention Effect in Dogs with Cancer Using Copper-64 Liposomes. *Acs Nano.* 2015, **9**(7), pp.6985-6995.
44. Sindhwani, S., Syed, A.M., Ngai, J., Kingston, B.R., Maiorino, L., Rothschild, J., MacMillan, P., Zhang, Y.W., Rajesh, N.U., Hoang, T., Wu, J.L.Y., Wilhelm, S., Zilman, A., Gadde, S., Sulaiman, A., Ouyang, B., Lin, Z., Wang, L.S., Egeblad, M. and Chan, W.C.W. The entry of nanoparticles into solid tumours. *Nature Materials.* 2020, **19**(5), pp.566-575.
45. He, H.L., Liu, L.S., Morin, E.E., Liu, M. and Schwendeman, A. Survey of Clinical Translation of Cancer Nanomedicines-Lessons Learned from Successes and Failures. *Accounts of Chemical Research.* 2019, **52**(9), pp.2445-2461.
46. Wilhelm, S., Tavares, A.J., Dai, Q., Ohta, S., Audet, J., Dvorak, H.F. and Chan, W.C.W. Analysis of nanoparticle delivery to tumours. *Nature Reviews Materials.* 2016, **1**(5), pp.1-12.
47. Alvarez-Paino, M., Munoz-Bonilla, A. and Fernandez-Garcia, M. Antimicrobial Polymers in the Nano-World. *Nanomaterials.* 2017, **7**(2), 48.
48. Timofeeva, L. and Kleshcheva, N. Antimicrobial polymers: mechanism of action, factors of activity, and applications. *Applied Microbiology and Biotechnology.* 2011, **89**(3), pp.475-492.
49. Siedenbiedel, F. and Tiller, J.C. Antimicrobial Polymers in Solution and on Surfaces: Overview and Functional Principles. *Polymers.* 2012, **4**(1), pp.46-71.
50. Engler, A.C., Wiradharma, N., Ong, Z.Y., Coady, D.J., Hedrick, J.L. and Yang, Y.Y. Emerging trends in macromolecular antimicrobials to fight multi-drug-resistant infections. *Nano Today.* 2012, **7**(3), pp.201-222.
51. Krumm, C., Harmuth, S., Hijazi, M., Neugebauer, B., Kampmann, A.L., Geltenpoth, H., Sickmann, A. and Tiller, J.C. Antimicrobial Poly(2-methyloxazoline) s with Bioswitchable Activity through Satellite Group Modification. *Angewandte Chemie-International Edition.* 2014, **53**(15), pp.3830-3834.
52. Al-Ahmad, A., Laird, D., Zou, P., Tomakidi, P., Steinberg, T. and Lienkamp, K. Nature-Inspired Antimicrobial Polymers - Assessment of Their Potential for Biomedical Applications. *Plos One.* 2013, **8**(9), 73812.
53. Santos, M.R.E., Fonseca, A.C., Mendona, P.V., Branco, R., Serra, A.C., Morais, P.V. and Coelho, J.F.J. Recent Developments in Antimicrobial Polymers: A Review. *Materials.* 2016, **9**(7), 599.
54. Lim, K.Y., Chua, R.R.Y., Bow, H., Tambyah, P.A., Hadinoto, K. and Leong, S.S.J. Development of a catheter functionalized by a polydopamine peptide coating with antimicrobial and antibiofilm properties. *Acta Biomaterialia.* 2015, **15**, pp.127-138.
55. McKeever, T.M., Lewis, S.A., Smith, C., Collins, J., Heatlie, H., Frischer, M. and Hubbard, R. Early exposure to infections and antibiotics and the incidence of allergic disease: A birth cohort study with the West Midlands General Practice Research Database. *Journal of Allergy and Clinical Immunology.* 2002, **109**(1), pp.43-50.
56. Risbud, M.V., Hardikar, A.A., Bhat, S.V. and Bhonde, R.R. pH-sensitive freeze-dried chitosan-polyvinyl pyrrolidone hydrogels as controlled release system for antibiotic delivery. *Journal of Controlled Release.* 2000, **68**(1), pp.23-30.

57. Kelly, H.M., Deasy, P.B., Ziaka, E. and Claffey, N. Formulation and preliminary in vivo dog studies of a novel drug delivery system for the treatment of periodontitis. *International Journal of Pharmaceutics.* 2004, **274**(1-2), pp.167-183.
58. Busscher, H.J., Rinastiti, M., Siswomihardjo, W. and van der Mei, H.C. Biofilm Formation on Dental Restorative and Implant Materials. *Journal of Dental Research.* 2010, **89**(7), pp.657-665.
59. Moussa, D.G., Fok, A. and Aparicio, C. Hydrophobic and antimicrobial dentin: A peptide-based 2-tier protective system for dental resin composite restorations. *Acta Biomaterialia.* 2019, **88**, pp.251-265.
60. Rokaya, D., Srimaneepong, V., Sapkota, J., Qin, J.Q., Siraleartmukul, K. and Siriwongrungson, V. Polymeric materials and films in dentistry: An overview. *Journal of Advanced Research.* 2018, **14**, pp.25-34.
61. Salehi, S., Davis, H.B., Ferracane, J.L. and Mitchell, J.C. Sol-gel-derived bioactive glasses demonstrate antimicrobial effects on common oral bacteria. *American Journal of Dentistry.* 2015, **28**(2), pp.111-115.
62. Paula, A.J. and Koo, H. Nanosized Building Blocks for Customizing Novel Antibiofilm Approaches. *Journal of Dental Research.* 2017, **96**(2), pp.128-136.
63. Freschauf, L.R., McLane, J., Sharma, H. and Khine, M. Shrink-Induced Superhydrophobic and Antibacterial Surfaces in Consumer Plastics. *Plos One.* 2012, **7**(8), 40987.
64. Duran, N., Marcato, P.D., De Souza, G.I.H., Alves, O.L. and Esposito, E. Antibacterial effect of silver nanoparticles produced by fungal process on textile fabrics and their effluent treatment. *Journal of Biomedical Nanotechnology.* 2007, **3**(2), pp.203-208.
65. Loeb, M.B., Craven, S., McGeer, A.J., Simor, A.E., Bradley, S.F., Low, D.E., Armstrong-Evans, M., Moss, L.A. and Walter, S.D. Risk factors for resistance to antimicrobial agents among nursing home residents. *American Journal of Epidemiology.* 2003, **157**(1), pp.40-47.
66. Tandon, V.K., Maurya, H.K., Mishra, N.N. and Shukla, P.K. Micelles catalyzed chemoselective synthesis 'in water' and biological evaluation of oxygen containing hetero-1,4-naphthoquinones as potential antifungal agents. *Bioorganic & Medicinal Chemistry Letters.* 2011, **21**(21), pp.6398-6403.
67. Shen, W., He, P., Xiao, C.S. and Chen, X.S. From Antimicrobial Peptides to Antimicrobial Poly(alpha-amino acid)s. *Advanced Healthcare Materials*. 2018, **7**(20) 1800354.
68. Liu, N., Li, B.Q., Gong, C., Liu, Y., Wang, Y.M. and Wu, G.L. A pH- and thermo-responsive poly(amino acid)-based drug delivery system. *Colloids and Surfaces B-Biointerfaces*. 2015, **136**, pp.562-569.
69. Teng, W.Z., Jia, F., Han, H.J., Qin, Z.H., Jin, Q. and Ji, J. Polyamino acid-based gemcitabine nanocarriers for targeted intracellular drug delivery. *Polymer Chemistry.* 2017, **8**(16), pp.2490-2498.
70. Paasonen, L., Romberg, B., Storm, G., Yliperttula, M., Urtti, A. and Hennink, W.E. Temperature-sensitive poly(N-(2-hydroxypropyl)methacrylamide mono/dilactate)-coated liposomes for triggered contents release. *Bioconjugate Chemistry*. 2007, **18**(6), pp.2131-2136.
71. Wang, X., Li, C., Fan, N., Li, J., He, Z.G. and Sun, J. Multimodal nanoporous silica nanoparticles functionalized with aminopropyl groups for improving loading and controlled release of doxorubicin hydrochloride. *Materials Science & Engineering C-Materials for Biological Applications*. 2017, **78**, pp.370-375.
72. Kalafatovic, D., Nobis, M., Son, J.Y., Anderson, K.I. and Ulijn, R.V. MMP-9 triggered self-assembly of doxorubicin nanofiber depots halts tumor growth. *Biomaterials*. 2016, **98**, pp.192-202.

73. Li, Y., Sun, J., Chen, Q.P., Chen, Z.P. and Zhu, L. Fast Drug Release of Liposome-Gold Conjugation Under Light Irradiation and the Comparison with Liposome-Gold Hybrid. *Nanoscience and Nanotechnology Letters*. 2017, **9**(6), pp.982-987.
74. Rafiee, E., Nobakht, N. and Behbood, L. Influence of pH, temperature, and alternating magnetic field on drug release from Keggin-type heteropoly acid encapsulated in iron-carboxylate nanoscale metal-organic framework. *Research on Chemical Intermediates*. 2017, **43**(2), pp.951-969.
75. Zhou, M.L., Tang, M.L., Zhang, H., Luo, K. and Huang, Y. HPMA Polymeric Nanocarriers for Anticancer Drugs with Tumor Microenvironment-Responsive Extracellular Biodegradation and Intracellular Drug Release. *Journal of Biomedical Nanotechnology*. 2019, **15**(8), pp.1688-1700.
76. Ray, P., Confeld, M., Borowicz, P., Wang, T., Mallik, S. and Quadir, M. PEG-b-poly (carbonate)-derived nanocarrier platform with pH-responsive properties for pancreatic cancer combination therapy. *Colloids and Surfaces B-Biointerfaces*. 2019, **174**, pp.126-135.
77. Pola, C.C., Moraes, A.R.F., Medeiros, E.A.A., Teofilo, R.F., Soares, N.F.F. and Gomes, C.L. Development and optimization of pH-responsive PLGA-chitosan nanoparticles for triggered release of antimicrobials. *Food Chemistry*. 2019, **295**, pp.671-679.
78. Chen, X.J., Niu, T.Y., Gao, Y.Z., Liang, X., Li, S.N., Zhang, L.Y., Li, L., Wang, T.T., Su, Z.M. and Wang, C.G. Tunable synthesis of pH-responsive biodegradable ZnO nanospheres assembled from ultrasmall particles for cancer chemotherapy. *Chemical Engineering Journal*. 2019, **371**, pp.443-451.
79. Gao, G., Jiang, Y.W., Sun, W., Guo, Y.X., Jia, H.R., Yu, X.W., Pan, G.Y. and Wu, F.G. Molecular Targeting-Mediated Mild-Temperature Photothermal Therapy with a Smart Albumin-Based Nanodrug. *Small*. 2019, **15**(33), 1900501
80. Haktaniyan, M., Atilla, S., Cagli, E. and Erel-Goktepe, I. pH- and temperature-induced release of doxorubicin from multilayers of poly(2-isopropyl-2-oxazoline) and tannic acid. *Polymer International*. 2017, **66**(12), pp.1851-1863.
81. Gholami, A., Mousavi, S.M., Hashemi, S.A., Ghasemi, Y., Chiang, W.H. and Parvin, N. Current trends in chemical modifications of magnetic nanoparticles for targeted drug delivery in cancer chemotherapy. *Drug Metabolism Reviews*. pp.205-224.
82. Luo, Y., Yang, H., Zhou, Y.F. and Hu, B. Dual and multi-targeted nanoparticles for site-specific brain drug delivery. *Journal of Controlled Release*. 2020, **317**, pp.195-215.
83. Pearce, A.K. and O'Reilly, R.K. Insights into Active Targeting of Nanoparticles in Drug Delivery: Advances in Clinical Studies and Design Considerations for Cancer Nanomedicine. *Bioconjugate Chemistry*. 2019, **30**(9), pp.2300-2311.
84. Calzoni, E., Cesaretti, A., Polchi, A., Di Michele, A., Tancini, B. and Emiliani, C. Biocompatible Polymer Nanoparticles for Drug Delivery Applications in Cancer and Neurodegenerative Disorder Therapies. *Journal of Functional Biomaterials*. 2019, **10**(1), 4.
85. Sun, Y.Z., Chen, D.M., Pan, Y.H., Qu, W., Hao, H.H., Wang, X., Liu, Z.L. and Xie, S.Y. Nanoparticles for antiparasitic drug delivery. *Drug Delivery*. 2019, **26**(1), pp.1206-1221.
86. Lombardo, D., Kiselev, M.A. and Caccamo, M.T. Smart Nanoparticles for Drug Delivery Application: Development of Versatile Nanocarrier Platforms in Biotechnology and Nanomedicine. *Journal of Nanomaterials*. 2019.
87. Hoshyar, N., Gray, S., Han, H.B. and Bao, G. The effect of nanoparticle size on in vivo pharmacokinetics and cellular interaction. *Nanomedicine*. 2016, **11**(6), pp.673-692.
88. Kreuter, J. Drug delivery to the central nervous system by polymeric nanoparticles: What do we know? *Advanced Drug Delivery Reviews*. 2014, **71**, pp.2-14.
89. Wang, B.Y., Lv, L.Y., Wang, Z.Y., Zhao, Y., Wu, L., Fang, X.L., Xu, Q.W. and Xin, H.L. Nanoparticles functionalized with Pep-1 as potential glioma targeting delivery system via

interleukin 13 receptor alpha 2-mediated endocytosis. *Biomaterials*. 2014, **35**(22), pp.5897-5907.
90. Gratton, S.E.A., Ropp, P.A., Pohlhaus, P.D., Luft, J.C., Madden, V.J., Napier, M.E. and DeSimone, J.M. The effect of particle design on cellular internalization pathways. Proceedings of the National Academy of Sciences of the United States of America. 2008, **105**(33), pp.11613-11618.
91. Qiu, Y., Liu, Y., Wang, L.M., Xu, L.G., Bai, R., Ji, Y.L., Wu, X.C., Zhao, Y.L., Li, Y.F. and Chen, C.Y. Surface chemistry and aspect ratio mediated cellular uptake of Au nanorods. *Biomaterials.* 2010, **31**(30), pp.7606-7619.
92. Moghimi, S.M., Hunter, A.C. and Andresen, T.L. Factors Controlling Nanoparticle Pharmacokinetics: An Integrated Analysis and Perspective. In: Insel, P.A. et al. eds. Annual Review of Pharmacology and Toxicology, Vol 52. Palo Alto: Annual Reviews, 2012, pp.481-503.
93. Elvira, C. and SanRoman, J. Synthesis and stereochemistry of isomeric methacrylic polymers derived from 4- and 5-aminosalicylic acids. *Polymer*. 1997, **38**(18), pp.4743-4750.
94. Brown, J.P., McGarraugh, G.V., Parkinson, T.M., Wingard, R.E. and Onderdonk, A.B. SOLUBLE FUNCTIONAL POLYMERS .3. A POLYMERIC DRUG FOR TREATMENT OF INFLAMMATORY BOWEL-DISEASE. *Journal of Medicinal Chemistry*. 1983, **26**(9), pp.1300-1307.
95. Callant, D. and Schacht, E. Macromolecular prodrugs of 5-aminosalycylic acid, 1-azo-conjugates. *Makromolekulare Chemie-Macromolecular Chemistry and Physics.* 1990, **191**(3), pp.529-536.
96. Akagi, T., Higashi, M., Kaneko, T., Kida, T. and Akashi, M. Hydrolytic and enzymatic degradation of nanoparticles based on amphiphilic poly(gamma-glutamic acid)-graft-L-phenylalanine copolymers. *Biomacromolecules*. 2006, **7**(1), pp.297-303.
97. Eldar-Boock, A., Miller, K., Sanchis, J., Lupu, R., Vicent, M.J. and Satchi-Fainaro, R. Integrin-assisted drug delivery of nano-scaled polymer therapeutics bearing paclitaxel. *Biomaterials*. 2011, **32**(15), pp.3862-3874.
98. Talelli, M. and Vicent, M.J. Reduction Sensitive Poly(L-glutamic acid) (PGA)-Protein Conjugates Designed for Polymer Masked-Unmasked Protein Therapy. *Biomacromolecules*. 2014, **15**(11), pp.4168-4177.
99. Tukappa, A., Ultimo, A., de la Torre, C., Pardo, T., Sancenon, F. and Martinez-Manez, R. Polyglutamic Acid-Gated Mesoporous Silica Nanoparticles for Enzyme-Controlled Drug Delivery. *Langmuir*. 2016, **32**(33), pp.8507-8515.
100. Ulbrich, K., Subr, V., Pechar, M., Strohalm, J., Jelinkova, M. and Rihova, B. Hydrophilic polymers for drug delivery. *Macromolecular Symposia*. 2000, **152**, pp.151-162.
101. Pal, N., Banerjee, S., Roy, P. and Pal, K. Reduced graphene oxide and PEG-grafted TEMPO-oxidized cellulose nanocrystal reinforced poly-lactic acid nanocomposite film for biomedical application. *Materials Science & Engineering C-Materials for Biological Applications*. 2019, **104**, 109956.
102. Figueiredo, P., Almeida, B.C. and Carvalho, A.T.P. Enzymatic Polymerization of PCL-PEG Co-polymers for Biomedical Applications. *Frontiers in Molecular Biosciences*. 2019, **6**, 109.
103. Wang, C.Y., Zolotarskaya, O., Ashraf, K.M., Wen, X.J., Ohman, D.E. and Wynne, K.J. Surface Characterization, Antimicrobial Effectiveness, and Human Cell Response for a Biomedical Grade Polyurethane Blended with a Mixed Soft Block PTMO-Quat/PEG Copolyoxetane Polyurethane. *Acs Applied Materials & Interfaces*. 2019, **11**(23), pp.20699-20714.

104. Liu, X.L., Xia, Y.R., Liu, L.L., Zhang, D.M. and Hou, Z.S. Synthesis of a novel biomedical poly(ester urethane) based on aliphatic uniform-size diisocyanate and the blood compatibility of PEG-grafted surfaces. *Journal of Biomaterials Applications*. 2018, **32**(10), pp.1329-1342.
105. Gu, Z.C., Gao, D.Y., Al-Zubaydi, F., Li, S.K., Singh, Y., Rivera, K., Holloway, J., Szekely, Z., Love, S. and Sinko, P.J. The effect of size and polymer architecture of doxorubicin-poly(ethylene) glycol conjugate nanocarriers on breast duct retention, potency and toxicity. *European Journal of Pharmaceutical Sciences*. 2018, **121**, pp.118-125.
106. Jung, H.S., Cho, K.J., Seol, Y., Takagi, Y., Dittmore, A., Roche, P.A. and Neuman, K.C. Polydopamine Encapsulation of Fluorescent Nanodiamonds for Biomedical Applications. *Advanced Functional Materials*. 2018, **28**(33), 1801252.
107. Pourjavadi, A., Dastanpour, L. and Tehrani, Z.M. Magnetic micellar nanocarrier based on pH-sensitive PEG-PCL-PEG triblock copolymer: a potential carrier for hydrophobic anticancer drugs. *Journal of Nanoparticle Research*. 2018, **20**(10), 282.
108. Yoshida, T., Lai, T.C., Kwon, G.S. and Sako, K. pH- and ion-sensitive polymers for drug delivery. *Expert Opinion on Drug Delivery*. 2013, **10**(11), pp.1497-1513.
109. Li, Q.M., Yang, S.N., Zhu, L.J., Kang, H.L., Qu, X.Z., Liu, R.G. and Huang, Y. Dual-stimuli sensitive keratin graft PHPMA as physiological trigger responsive drug carriers. *Polymer Chemistry*. 2015, **6**(15), pp.2869-2878.
110. Petrova, S., Klepac, D., Konefal, R., Kereiche, S., Kovacik, L. and Filippov, S.K. Synthesis and Solution Properties of PCL-b-PHPMA Diblock Copolymers Containing Stable Nitroxyl Radicals. *Macromolecules*. 2016, **49**(15), pp.5407-5417.
111. Yan, X.B., Ramos, R., Hoibian, E., Soulage, C., Alcouffe, P., Ganachaud, F. and Bernard, J. Nanoprecipitation of PHPMA (Co)Polymers into Nanocapsules Displaying Tunable Compositions, Dimensions, and Surface Properties. *Acs Macro Letters*. 2017, **6**(4), pp.447-451.
112. Zhang, X.H., Niebuur, B.J., Chytil, P., Etrych, T., Filippov, S.K., Kikhney, A., Wieland, D.C.F., Svergun, D.I. and Papadakis, C.M. Macromolecular pHPMA-Based Nanoparticles with Cholesterol for Solid Tumor Targeting: Behavior in HSA Protein Environment. *Biomacromolecules*. 2018, **19**(2), pp.470-480.
113. Ma, C., Liu, X.M., Wu, G.Y., Zhou, P., Zhou, Y.T., Wang, L. and Huang, X. Efficient Way to Generate Protein-Based Nanoparticles by in-Situ Photoinitiated Polymerization-Induced Self-Assembly. *Acs Macro Letters*. 2017, **6**(7), pp.689-694.
114. Schneider, M., Al-Shareffi, E. and Haltiwanger, R.S. Biological functions of fucose in mammals. *Glycobiology*. 2017, **27**(7), pp.601-618.
115. Yoshida, M., Takimoto, R., Murase, K., Sato, Y., Hirakawa, M., Tamura, F., Sato, T., Iyama, S., Osuga, T., Miyanishi, K., Takada, K., Hayashi, T., Kobune, M. and Kato, J. Targeting Anticancer Drug Delivery to Pancreatic Cancer Cells Using a Fucose-Bound Nanoparticle Approach. *Plos One*. 2012, **7**(7), 39545.
116. Dantas-Santos, N., Almeida-Lima, J., Vidal, A.A.J., Gomes, D.L., Oliveira, R.M., Pedrosa, S.S., Pereira, P., Gama, F.M. and Rocha, H.A.O. Antiproliferative Activity of Fucan Nanogel. *Marine Drugs*. 2012, **10**(9), pp.2002-2022.
117. Ale, M.T., Maruyama, H., Tamauchi, H., Mikkelsen, J.D. and Meyer, A.S. Fucose-Containing Sulfated Polysaccharides from Brown Seaweeds Inhibit Proliferation of Melanoma Cells and Induce Apoptosis by Activation of Caspase-3 in Vitro. *Marine Drugs*. 2011, **9**(12), pp.2605-2621.
118. Zhao, J.Y., Zheng, D., Tao, Y.H., Li, Y.C., Wang, L.Y., Liu, J., He, J. and Lei, J.D. Self-assembled pH-responsive polymeric nanoparticles based on lignin-histidine conjugate with small particle size for efficient delivery of anti-tumor drugs. Biochemical Engineering Journal. 2020, **156**, 107526.

119. Feng, Y., Li, N.X., Yin, H.L., Chen, T.Y., Yang, Q. and Wu, M. Thermo- and pH-responsive, Lipid-coated, Mesoporous Silica Nanoparticle-based Dual Drug Delivery System To Improve the Antitumor Effect of Hydrophobic Drugs. *Molecular Pharmaceutics.* 2019, **16**(1), pp.422-436.
120. Xu, C., Zhang, C., Wang, Y.X., Li, L., Li, L. and Whittaker, A.K. Controllable synthesis of a novel magnetic core-shell nanoparticle for dual-modal imaging and pH-responsive drug delivery. *Nanotechnology.* 2017, **28**(49), 495101.
121. Zhang, Y., Lu, Y.F., Wang, F., An, S., Zhang, Y.J., Sun, T., Zhu, J.H. and Jiang, C. ATP/pH Dual Responsive Nanoparticle with D- des-Arg(10) Kallidin Mediated Efficient In Vivo Targeting Drug Delivery. *Small.* 2017, **13**(3), 1602494.
122. Wen, H., Guo, J., Chang, B.S. and Yang, W.L. pH-responsive composite microspheres based on magnetic mesoporous silica nanoparticle for drug delivery. *European Journal of Pharmaceutics and Biopharmaceutics.* 2013, **84**(1), pp.91-98.
123. Zhang, C.Y., Pan, D.Y., Luo, K., Li, N., Guo, C.H., Zheng, X.L. and Gu, Z.W. Dendrimer-doxorubicin conjugate as enzyme-sensitive and polymeric nanoscale drug delivery vehicle for ovarian cancer therapy. *Polymer Chemistry.* 2014, **5**(18), pp.5227-5235.
124. Wei, X.L., Luo, Q., Sun, L., Li, X., Zhu, H.Y., Guan, P.J., Wu, M., Luo, K. and Gong, Q.Y. Enzyme- and pH-Sensitive Branched Polymer-Doxorubicin Conjugate-Based Nanoscale Drug Delivery System for Cancer Therapy. *Acs Applied Materials & Interfaces*. 2016, **8**(18), pp.11765-11778.
125. Gandhi, A., Paul, A., Sen, S.O. and Sen, K.K. Studies on thermoresponsive polymers: Phase behaviour, drug delivery and biomedical applications. *Asian Journal of Pharmaceutical Sciences.* 2015, **10**(2), pp.99-107.
126. Feil, H., Bae, Y.H., Feijen, J. and Kim, S.W. EFFECT OF COMONOMER HYDROPHILICITY AND IONIZATION ON THE LOWER CRITICAL SOLUTION TEMPERATURE OF N-ISOPROPYLACRYLAMIDE COPOLYMERS. *Macromolecules.* 1993, **26**(10), pp.2496-2500.
127. Vihola, H., Laukkanen, A., Tenhu, H. and Hirvonen, J. Drug Release Characteristics of Physically Cross-Linked Thermosensitive Poly(N-vinylcaprolactam) Hydrogel Particles. *Journal of Pharmaceutical Sciences.* 2008, **97**(11), pp.4783-4793.
128. Vihola, H., Marttila, A.K., Pakkanen, J.S., Andersson, M., Laukkanen, A., Kaukonen, A.M., Tenhu, H. and Hirvonen, J. Cell-polymer interactions of fluorescent polystyrene latex particles coated with thermosensitive poly (N-isopropylacrylamide) and poly (N-vinylcaprolactam) or grafted with poly(ethylene oxide)-macromonomer. *International Journal of Pharmaceutics.* 2007, **343**(1-2), pp.238-246.
129. Klouda, L. and Mikos, A.G. Thermoresponsive hydrogels in biomedical applications. *European Journal of Pharmaceutics and Biopharmaceutics.* 2008, **68**(1), pp.34-45.
130. Lutz, J.F. Polymerization of oligo(ethylene glycol) (meth)acrylates: Toward new generations of smart biocompatible materials. *Journal of Polymer Science Part a-Polymer Chemistry.* 2008, **46**(11), pp.3459-3470.
131. Pasparakis, G. and Vamvakaki, M. Multiresponsive polymers: nano-sized assemblies, stimuli-sensitive gels and smart surfaces. *Polymer Chemistry.* 2011, **2**(6), pp.1234-1248.
132. Liu, F. and Urban, M.W. Recent advances and challenges in designing stimuli-responsive polymers. *Progress in Polymer Science.* 2010, **35**(1-2), pp.3-23.
133. Fan, Y.W., Ma, K., Jing, J.Y., Wang, C.Y., Hu, Y., Shi, Y., Li, E.X. and Geng, Q.Q. Recombinant Dual-target MDM2/MDMX Inhibitor Reverses Doxorubicin Resistance through Activation of the TAB1/TAK1/p38 MAPK Pathway in Wild-type p53 Multidrug-resistant Breast Cancer Cells. *Journal of Cancer.* 2020, **11**(1), pp.25-40.

134. Steffensen, K.D., Waldstrom, M., Pallisgard, N., Lund, B., Bergfeldt, K., Wihl, J., Keldsen, N., Marth, C., Vergote, I. and Jakobsen, A. Panitumumab and Pegylated Liposomal Doxorubicin in Platinum-Resistant Epithelial Ovarian Cancer With KRAS Wild-Type The PaLiDo Study, a Phase II Nonrandomized Multicenter Study. *International Journal of Gynecological Cancer.* 2013, **23**(1), pp.73-80.
135. Matsui, Y., Watanabe, J., Ding, S., Nishizawa, K., Kajita, Y., Ichioka, K., Saito, R., Kobayashi, T., Ogawa, O. and Nishiyama, H. Dicoumarol enhances doxorubicin-induced cytotoxicity in p53 wild-type urothelial cancer cells through p38 activation. *Bju International.* 2010, **105**(4), pp.558-564.
136. Serova, M., Ghoul, A., Benhadji, K.A., Cvitkovic, E., Chiao, J., Rombotis, S., Lokiec, F., Calvo, F. and Raymond, E. CYC682, a novel 2 '-deoxycytidine-type antimetabolite, enhances the anti proliferative effects of oxaliplatin, doxorubicin, docetaxel, and gemcitabine in human colon cancer cells. *Clinical Cancer Research.* 2005, **11**(24), pp.9014-9015.
137. Betka, J., Hovorka, O., Boucek, J., Ulbrich, K., Etrych, T. and Rihova, B. Fine needle aspiration biopsy proves increased T-lymphocyte proliferation in tumor and decreased metastatic infiltration after treatment with doxorubicin bound to PHPMA copolymer carrier. *Journal of Drug Targeting*. 2013, **21**(7), pp.648-661.
138. Feng, T.Y., Ren, F., Fang, Q., Dai, G.C., Li, Y., Li, Q., Xi, H.M., Li, H., Hao, Y.Y. and Hu, J.H. Effects of sulfanilamide on boar sperm quality, bacterial composition, and fertility during liquid storage at 17 degrees C. *Animal Science Journal*. 2019, **90**(9), pp.1161-1169.
139. Sui, Y.F., Li, D., Wang, J., Bheemanaboina, R.R.Y., Ansari, M.F., Gan, L.L. and Zhou, C.H. Design and biological evaluation of a novel type of potential multi-targeting antimicrobial sulfanilamide hybrids in combination of pyrimidine and azoles. *Bioorganic & Medicinal Chemistry Letters*. 2020, **30**(6), 126982.
140. Wang, R.X., Tang, J.H., Zhang, X.Y., Wang, D., Wang, X., Xue, S., Zhang, Z.H. and Dionysiou, D.D. Construction of novel Z-scheme Ag/ZnFe2O4/Ag/BiTa1-xVxO4 system with enhanced electron transfer capacity for visible light photocatalytic degradation of sulfanilamide. *Journal of Hazardous Materials*. 2019, **375**, pp.161-173.
141. Miller, R.G., Vazquez-Hernandez, M., Prochnow, P., Bandow, J.E. and Metzler-Nolte, N. A CuAAC Click Approach for the Introduction of Bidentate Metal Complexes to a Sulfanilamide-Derived Antibiotic Fragment. *Inorganic Chemistry*. 2019, **58**(14), pp.9404-9413.
142. Alsughayer, A., Elassar, A.Z.A., Al Sagheer, F. and Mustafa, S. Synthesis and characterization of polysulfanilamide and its copolymers: bioactivity and drug release. *Pharmaceutical Chemistry Journal.* 2012, **46**(7), pp.418-428.
143. Khamees, H.A., Mohammed, Y.H.E., Ananda, S., Al-Ostoot, F.H., Sangappa, Y., Alghamdi, S., Khanum, S.A. and Madegowda, M. Effect of o-difluoro and p-methyl substituents on the structure, optical properties and anti-inflammatory activity of phenoxy thiazole acetamide derivatives: Theoretical and experimental studies. *Journal of Molecular Structure.* 2020, **1199**, 127024.
144. Nejaddehbashi, F., Hashemitabar, M., Bayati, V., Moghimipour, E., Movaffagh, J., Orazizadeh, M. and Abbaspour, M. Incorporation of Silver Sulfadiazine into An Electrospun Composite of Polycaprolactone as An Antibacterial Scaffold for Wound Healing in Rats. *Cell Journal.* 2020, **21**(4), pp.379-390.
145. Gholipour-Kanani, A., Bahrami, S.H., Joghataie, M.T., Samadikuchaksaraei, A., Ahmadi-Taftie, H., Rabbani, S., Kororian, A. and Erfani, E. Tissue engineered poly(caprolactone)-chitosan-poly (vinyl alcohol) nanofibrous scaffolds for burn and cutting wound healing. *Iet Nanobiotechnology.* 2014, **8**(2), pp.123-131.

146. Shafiee, A., Soleimani, M., Chamheidari, G.A., Seyedjafari, E., Dodel, M., Atashi, A. and Gheisari, Y. Electrospun nanofiber-based regeneration of cartilage enhanced by mesenchymal stem cells. *Journal of Biomedical Materials Research Part A.* 2011, **99A**(3), pp.467-478
147. York, A.W., Kirkland, S.E. and McCormick, C.L. Advances in the synthesis of amphiphilic block copolymers via RAFT polymerization: Stimuli-responsive drug and gene delivery. *Advanced Drug Delivery Reviews.* 2008, **60**(9), pp.1018-1036.
148. Keddie, D.J., Moad, G., Rizzardo, E. and Thang, S.H. RAFT Agent Design and Synthesis. *Macromolecules*. 2012, **45**(13), pp.5321-5342.
149. Klimkevicius, V., Steponaviciute, M. and Makuska, R. Kinetics of RAFT polymerization and copolymerization of vinyl monomers by size exclusion chromatography. *European Polymer Journal.* 2020, **122**, 109356.
150. Lopez-Dominguez, P., Jaramillo-Soto, G. and Vivaldo-Lima, E. A Modeling Study on the RAFT Polymerization of Vinyl Monomers in Supercritical Carbon Dioxide. *Macromolecular Reaction Engineering.* 2018, **12**(4), 1800011.
151. Huang, Z.C., Peng, Y., Chen, H.B., Xue, Q. and Li, H.M. Synthesis and RAFT polymerization of a novel vinyl monomer containing both triarylimidazole and triazole moieties. *Designed Monomers and Polymers.* 2014, **17**(7), pp.601-609.
152. Pearson, S., St Thomas, C., Guerrero-Santos, R. and D'Agosto, F. Opportunities for dual RDRP agents in synthesizing novel polymeric materials. *Polymer Chemistry*. 2017, **8**(34), pp.4916-4946.
153. Keddie, D.J. A guide to the synthesis of block copolymers using reversible-addition fragmentation chain transfer (RAFT) polymerization. *Chemical Society Reviews.* 2014, **43**(2), pp.496-505.
154. Iqbal, J., Bhatia, B. and Nayyar, N.K. Tranisition-metal promoted radical reactions in organic-synthesis - the formation of carbon-carbon bonds (vol 94, pp. 519, 1994). *Chemical Reviews.* 1994, **94**(8), pp.2549-2549.
155. Curran, D.P. The design and application of free-radical chain reactions in organic-synthesis.2. *Synthesis-Stuttgart.* 1988, (7), pp.489-513.
156. Boyer, C., Bulmus, V., Davis, T.P., Ladmiral, V., Liu, J.Q. and Perrier, S. Bioapplications of RAFT Polymerization. *Chemical Reviews.* 2009, **109**(11), pp.5402-5436.
157. Broyer, R.M., Grover, G.N. and Maynard, H.D. Emerging synthetic approaches for protein-polymer conjugations. *Chemical Communications.* 2011, **47**(8), pp.2212-2226.
158. Dehn, S., Chapman, R., Jolliffe, K.A. and Perrier, S. Synthetic Strategies for the Design of Peptide/Polymer Conjugates. *Polymer Reviews.* 2011, **51**(2), pp.214-234.
159. Chu, D.S.H., Schellinger, J.G., Shi, J.L., Convertine, A.J., Stayton, P.S. and Pun, S.H. Application of Living Free Radical Polymerization for Nucleic Acid Delivery. *Accounts of Chemical Research.* 2012, **45**(7), pp.1089-1099.
160. Bhagat, L., Singh, V.P., Hietaranta, A.J., Agrawal, S., Steer, M.L. and Saluja, A.K. Heat shock protein 70 prevents secretagogue-induced cell injury in the pancreas by preventing intracellular trypsinogen activation. *Journal of Clinical Investigation.* 2000, **106**(1), pp.81-89.
161. Wu, J.W., Zheng, Y.X., Liu, M., Shan, W., Zhang, Z.R. and Huang, Y. Biomimetic Viruslike and Charge Reversible Nanoparticles to Sequentially Overcome Mucus and Epithelial Barriers for Oral Insulin Delivery. *Acs Applied Materials & Interfaces.* 2018, **10**(12), pp.9916-9928.
162. Penfold, N.J.W., Lovett, J.R., Warren, N.J., Verstraete, P., Smets, J. and Armes, S.P. pH-Responsive non-ionic diblock copolymers: protonation of a morpholine end-group induces an order-order transition. *Polymer Chemistry.* 2016, **7**(1), pp.79-88.

163. Hoyle, C.E., Lowe, A.B. and Bowman, C.N. Thiol-click chemistry: a multifaceted toolbox for small molecule and polymer synthesis. *Chemical Society Reviews*. 2010, **39**(4), pp.1355-1387.
164. De, P., Li, M., Gondi, S.R. and Sumerlin, B.S. Temperature-regulated activity of responsive polymer-protein conjugates prepared by grafting-from via RAFT polymerization. *Journal of the American Chemical Society*. 2008, **130**(34), pp.11288-11289.
165. Li, M., Li, H.M., De, P. and Sumerlin, B.S. Thermoresponsive Block Copolymer-Protein Conjugates Prepared by Grafting-from via RAFT Polymerization. *Macromolecular Rapid Communications*. 2011, **32**(4), pp.354-359.
166. Yu, W., Foster, J.C., Dove, A.P. and O'Reilly, R.K. Length Control of Biodegradable Fiber-Like Micelles via Tuning Solubility: A Self-Seeding Crystallization-Driven Self-Assembly of Poly(epsilon-caprolactone)-Containing Triblock Copolymers. *Macromolecules.* 2020, **53**(4), pp.1514-1521.
167. Yang, H.C., Cai, Z.N., Liu, H.T., Cao, Z., Xia, Y.P., Ma, W.Z., Gong, F.H., Tao, G.L. and Liu, C.L. Tailoring the surface of attapulgite by combining redox-initiated RAFT polymerization with alkynyl-thiol click reaction for polycarbonate nanocomposites:Effect of polymer brush chain length on mechanical, thermal and rheological properties. *Materials Chemistry and Physics.* 2020, **241**, 122334.
168. Lee, C.U., Roy, D., Sumerlin, B.S. and Dadmun, M.D. Facile synthesis of thiol-terminated poly(styrene-ran-vinyl phenol) (PSVPh) copolymers via reversible addition-fragmentation chain transfer (RAFT) polymerization and their use in the synthesis of gold nanoparticles with controllable hydrophilicity. *Polymer*. 2010, **51**(6), pp.1244-1251.
169. Wang, B.X., Guerrette, Z., Whittaker, M.H. and Ator, J. Derivation of a No significant risk level (NSRL) for acrylamide. *Toxicology Letters*. 2020, *320*, pp.103-108.
170. Vanderburgh, J., Hill, J.L., Gupta, M.K., Kwakwa, K.A., Wang, S.K., Moyer, K., Bedingfield, S.K., Merkel, A.R., d'Arcy, R., Guelcher, S.A., Rhoades, J.A. and Duvall, C.L. Tuning Ligand Density To Optimize Pharmacokinetics of Targeted Nanoparticles for Dual Protection against Tumor-Induced Bone Destruction. *Acs Nano*. 2020, **14**(1), pp.311-327.
171. Paenkaew, S., Kajornprai, T. and Rutnakornpituk, M. Water dispersible magnetite nanocluster coated with thermo-responsive thiolactone-containing copolymer. *Polymers for Advanced Technologies*. pp.1349-1355.
172. Gao, C.Q., Zhou, H., Qu, Y.Q., Wang, W., Khan, H. and Zhang, W.Q. In Situ Synthesis of Block Copolymer Nanoassemblies via Polymerization-Induced Self-Assembly in Poly(ethylene glycol). *Macromolecules*. 2016, **49**(10), pp.3789-3798.
173. Rahman, M.A., Cha, Y.J., Yuan, L., Pageni, P., Zhu, T.Y., Jui, M.S. and Tang, C.B. Polymerization-Induced Self-Assembly of Metallo-Polyelectrolyte Block Copolymers. *Journal of Polymer Science*. 2020, **58**(1), pp.77-83.
174. Man, S.K., Wang, X., Zheng, J.W. and An, Z.S. Effect of Butyl alpha-Hydroxymethyl Acrylate Monomer Structure on the Morphology Produced via Aqueous Emulsion Polymerization-induced Self-assembly. *Chinese Journal of Polymer Science*. 2020, **38**(1), pp.9-16.
175. Shi, B.Y., Zhang, H., Liu, Y., Wang, J., Zhou, P., Cao, M.Y. and Wang, G.W. Development of ICAR ATRP-Based Polymerization-Induced Self-Assembly and Its Application in the Preparation of Organic-Inorganic Nanoparticles. *Macromolecular Rapid Communications*. 2019, **40**(24), 1900547.
176. Samanta, S., Banerjee, S.L., Ghosh, S.K. and Singha, N.K. Smart Polyacrylate Emulsion Based on a New ABC-Type Triblock Copolymer via RAFT-Mediated Surfactant-Free Miniemulsion Polymerization: Its Multifunctional Properties. *Acs Applied Materials & Interfaces*. 2019, **11**(47), pp.44722-44734.

177. Qiu, L., Xu, C.R., Zhong, F., Hong, C.Y. and Pan, C.Y. Fabrication of Functional Nano-objects through RAFT Dispersion Polymerization and Influences of Morphology on Drug Delivery. *Acs Applied Materials & Interfaces*. 2016, **8**(28), pp.18347-18359.
178. Fielding, L.A., Derry, M.J., Ladmiral, V., Rosselgong, J., Rodrigues, A.M., Ratcliffe, L.P.D., Sugihara, S. and Armes, S.P. RAFT dispersion polymerization in non-polar solvents: facile production of block copolymer spheres, worms and vesicles in n-alkanes. *Chemical Science*. 2013, **4**(5), pp.2081-2087.
179. Wang, M.Z., Zhou, C.C., Chen, J., Xiao, Y.F. and Du, J.Z. Multifunctional Biocompatible and Biodegradable Folic Acid Conjugated Poly(epsilon-caprolactone)-Polypeptide Copolymer Vesicles with Excellent Antibacterial Activities. *Bioconjugate Chemistry*. 2015, **26**(4), pp.725-734.
180. Chen, M., Zhang, W.G., Li, J.W., Hong, C.Y., Zhang, W.J. and You, Y.Z. Preparation of pH- and reductive-responsive prodrug nanoparticles via polymerization-induced self-assembly. *Science China-Chemistry*. 2018, **61**(9), pp.1159-1166.
181. Canning, S.L., Smith, G.N. and Armes, S.P. A Critical Appraisal of RAFT-Mediated Polymerization-Induced Self Assembly. *Macromolecules*. 2016, **49**(6), pp.1985-2001.
182. Sugihara, S., Armes, S.P. and Lewis, A.L. One-Pot Synthesis of Biomimetic Shell Cross-Linked Micelles and Nanocages by ATRP in Alcohol/Water Mixtures. *Angewandte Chemie-International Edition*. 2010, **49**(20), pp.3500-3503.
183. Li, Y.T. and Armes, S.P. RAFT Synthesis of Sterically Stabilized Methacrylic Nanolatexes and Vesicles by Aqueous Dispersion Polymerization. *Angewandte Chemie-International Edition.* 2010, **49**(24), pp.4042-4046.
184. He, J., Xu, Q., Tan, J.B. and Zhang, L. Ketone-Functionalized Polymer Nano-Objects Prepared via Photoinitiated Polymerization-Induced Self-Assembly (Photo-PISA) Using a Poly(diacetone acrylamide)-Based Macro-RAFT Agent. *Macromolecular Rapid Communications*. 2019, **40**(2), 1800296.
185. Wang, K., Wang, Y.X. and Zhang, W.Q. Synthesis of diblock copolymer nano-assemblies by PISA under dispersion polymerization: comparison between ATRP and RAFT. *Polymer Chemistry*. 2017, **8**(41), pp.6407-6415
186. Tan, J.B., Bai, Y.H., Zhang, X.C., Huang, C.D., Liu, D.D. and Zhang, L. Low-Temperature Synthesis of Thermoresponsive Diblock Copolymer Nano-Objects via Aqueous Photoinitiated Polymerization-Induced Self-Assembly (Photo-PISA) using Thermoresponsive Macro-RAFT Agents. *Macromolecular Rapid Communications*. 2016, **37**(17), pp.1434-1440.
187. Das, D., Gerboth, D., Postma, A., Srinivasan, S., Kern, H., Chen, J., Ratner, D.M., Stayton, P.S. and Convertine, A.J. Synthesis of zwitterionic, hydrophobic, and amphiphilic polymers via RAFT polymerization induced self-assembly (PISA) in acetic acid. *Polymer Chemistry*. 2016, **7**(39), pp.6133-6143.
188. Yu, M.G., Tan, J.B., Yang, J.W. and Zeng, Z.H. Z-type and R-type macro-RAFT agents in RAFT dispersion polymerization - another mechanism perspective on PISA. *Polymer Chemistry*. 2016, **7**(22), pp.3756-3765.
189. Jones, E.R. and Armes, S.P. Addition of water to an alcoholic RAFT PISA formulation affects both polymerization kinetics and copolymer morphology. *Abstracts of Papers of the American Chemical Society*. 2014, **248**.
190. Perrier, S. Polymer nanoparticles for drug delivery by PISA RAFT polymerization. *Abstracts of Papers of the American Chemical Society*. 2018, **255**.
191. Semsarilar, M., Ladmiral, V., Blanazs, A. and Armes, S.P. Cationic Polyelectrolyte-Stabilized Nanoparticles via RAFT Aqueous Dispersion Polymerization. *Langmuir*. 2013, **29**(24), pp.7416-7424.

192. Blanazs, A., Ryan, A.J. and Armes, S.P. Predictive Phase Diagrams for RAFT Aqueous Dispersion Polymerization: Effect of Block Copolymer Composition, Molecular Weight, and Copolymer Concentration. *Macromolecules*. 2012, **45**(12), pp.5099-5107.
193. Blanazs, A., Madsen, J., Battaglia, G., Ryan, A.J. and Armes, S.P. Mechanistic Insights for Block Copolymer Morphologies: How Do Worms Form Vesicles? *Journal of the American Chemical Society.* 2011, **133**(41), pp.16581-16587.
194. Yang, J.Y., Hu, Y., Wang, R. and Xie, D.Q. Nanoparticle encapsulation in vesicles formed by amphiphilic diblock copolymers. *Soft Matter*. 2017, **13**(43), pp.7840-7847.
195. Wang, X., Zhou, J.M., Lv, X.Q., Zhang, B.H. and An, Z.S. Temperature-Induced Morphological Transitions of Poly(dimethylacrylamide)-Poly(diacetone acrylamide) Block Copolymer Lamellae Synthesized via Aqueous Polymerization-Induced Self-Assembly. *Macromolecules*. 2017, **50**(18), pp.7222-7232.
196. Mable, C.J., Warren, N.J., Thompson, K.L., Mykhaylyk, O.O. and Armes, S.P. Framboidal ABC triblock copolymer vesicles: a new class of efficient Pickering emulsifier. *Chemical Science*. 2015, **6**(11), pp.6179-6188.
197. Cai, T., Yang, W.J., Neoh, K.G. and Kang, E.T. Preparation of jellyfish-shaped amphiphilic block-graft copolymers consisting of a poly(epsilon-caprolactone)-block-poly(pentafluorostyrene) ring and poly(ethylene glycol) lateral brushes. *Polymer Chemistry*. 2012, **3**(4), pp.1061-1068.
198. Huang, Z.F., Chen, Y.L., Wang, R.Z., Zhou, C.Y., Liu, X.B., Mao, L.C., Yuan, J.Y., Tao, L. and Wei, Y. An acrylate AIE-active dye with a two-photon fluorescent switch for fluorescent nanoparticles by RAFT polymerization: synthesis, molecular structure and application in cell imaging. *Rsc Advances*. 2020, **10**(10), pp.5704-5711.
199. Lu, L., Yuan, L., Yan, J., Tang, C.B. and Wang, Q. Development of Core-Shell Nanostructures by In Situ Assembly of Pyridine-Grafted Diblock Copolymer and Transferrin for Drug Delivery Applications. *Biomacromolecules*. 2016, **17**(7), pp.2321-2328.
200. Peng, S.M., Chen, Y., Hua, C. and Dong, C.M. Dendron-like Polypeptide/Linear Poly(ethylene oxide) Biohybrids with Both Asymmetrical and Symmetrical Topologies Synthesized via the Combination of Click Chemistry and Ring-Opening Polymerization. *Macromolecules.* 2009, **42**(1), pp.104-113.
201. Warren, N.J., Mykhaylyk, O.O., Mahmood, D., Ryan, A.J. and Armes, S.P. RAFT Aqueous Dispersion Polymerization Yields Poly(ethylene glycol)-Based Diblock Copolymer Nano-Objects with Predictable Single Phase Morphologies. *Journal of the American Chemical Society.* 2014, **136**(3), pp.1023-1033.
202. Wibowo, S.H., Sulistio, A., Wong, E.H.H., Blencowe, A. and Qiao, G.G. Polypeptide films via N-carboxyanhydride ring-opening polymerization (NCA-ROP): past, present and future. *Chemical Communications*. 2014, **50**(39), pp.4971-4988.
203. Hadjichristidis, N., Iatrou, H., Pitsikalis, M. and Sakellariou, G. Synthesis of Well-Defined Polypeptide-Based Materials via the Ring-Opening Polymerization of alpha-Amino Acid N-Carboxyanhydrides. *Chemical Reviews*. 2009, **109**(11), pp.5528-5578.
204. Deming, T.J. Facile synthesis of block copolypeptides of defined architecture. *Nature*. 1997, **390**(6658), pp.386-389.
205. Lu, H. and Cheng, J.J. Hexamethyldisilazane-mediated controlled polymerization of alpha-Amino acid N-carboxyanhydrides. *Journal of the American Chemical Society.* 2007, **129**(46), pp.14114-14115.
206. Aliferis, T., Iatrou, H. and Hadjichristidis, N. Living polypeptides. *Biomacromolecules*. 2004, **5**(5), pp.1653-1656.
207. Dimitrov, I. and Schlaad, H. Synthesis of nearly monodisperse polystyrene-polypeptide block copolymers via polymerisation of N-carboxyanhydrides. *Chemical Communications*. 2003, (23), pp.2944-2945.

208. Habraken, G.J.M., Heise, A. and Thornton, P.D. Block Copolypeptides Prepared by N-Carboxyanhydride Ring-Opening Polymerization. *Macromolecular Rapid Communications.* 2012, **33**(4), pp.272-286.
209. Xu, D.Z., Zeng, S.M., Liu, M.Y., Chen, J.Y., Huang, H.Y., Deng, F.J., Tian, J.W., Wen, Y.Q., Zhang, X.Y. and Wei, Y. Preparation of PEGylated and biodegradable fluorescent organic nanoparticles with aggregation-induced emission characteristics through direct ring-opening polymerization. *Journal of the Taiwan Institute of Chemical Engineers.* 2019, **95**, pp.234-240.
210. Robin, Y. alpha-Amino acid N-Carboxy Anhydrides in pharmaceutical innovations: try them to capture new value. *Chimica Oggi-Chemistry Today.* 2015, **33**(4), pp.26-31.
211. Zheng, Z., Wang, R., Yao, H.F., Xie, S.K., Zhang, Y., Hou, J.H., Zhou, H.Q. and Tang, Z.Y. Polyamino acid interlayer facilitates electron extraction in narrow band gap fullerene-free organic solar cells with an outstanding short-circuit current. *Nano Energy.* 2018, **50**, pp.169-175.
212. Yuan, Y.L., Zhang, L., Wang, H.J., Chai, Y.Q. and Yuan, R. Self-enhanced PEI-Ru(II) complex with polyamino acid as booster to construct ultrasensitive electrochemiluminescence immunosensor for carcinoembryonic antigen detection. *Analytica Chimica Acta.* 2018, **1001**, pp.112-118.
213. Mauro, N., Scialabba, C., Puleio, R., Varvara, P., Licciardi, M., Cavalaro, G. and Giammona, G. SPIONs embedded in polyamino acid nanogels to synergistically treat tumor microenvironment and breast cancer cells. *International Journal of Pharmaceutics.* 2019, **555**, pp.207-219.
214. Gupta, B., Ruttala, H.B., Poudel, B.K., Pathak, S., Regmi, S., Gautam, M., Poudel, K., Sung, M.H., Ou, W., Jin, S.G., Jeong, J.H., Ku, S.K., Choi, H.G., Yong, C.S. and Kim, J.O. Polyamino Acid Layer-by-Layer (LbL) Constructed Silica-Supported Mesoporous Titania Nanocarriers for Stimuli-Responsive Delivery of microRNA 708 and Paclitaxel for Combined Chemotherapy. *Acs Applied Materials & Interfaces.* 2018, **10**(29), pp.24392-24405.
215. Schackel, T., Kumar, P., Gunther, M., Liu, S.W., Brunner, M., Sandner, B., Puttagunta, R., Muller, R., Weidner, N. and Blesch, A. Peptides and Astroglia Improve the Regenerative Capacity of Alginate Gels in the Injured Spinal Cord. *Tissue Engineering Part A.* 2019, **25**(7-8), pp.522-537.
216. Wang, R., Zhou, B., Xu, D.L., Xu, H., Liang, L., Feng, X.H., Ouyang, P.K. and Chi, B. Antimicrobial and biocompatible epsilon-polylysine-gamma-poly(glutamic acid)-based hydrogel system for wound healing. *Journal of Bioactive and Compatible Polymers.* 2016, **31**(3), pp.242-259.
217. Habraken, G.J.M., Wilsens, K., Koning, C.E. and Heise, A. Optimization of N-carboxyanhydride (NCA) polymerization by variation of reaction temperature and pressure. *Polymer Chemistry*. 2011, **2**(6), pp.1322-1330.
218. Deming, T.J., Cobalt and iron initiators for the controlled polymerization of alpha-amino acid-N-carboxyanhydrides. *Macromolecules*, 1999. **32**(13): p. 4500-4502.
219. Davidson, R.S. Organic-chemistry in color - Gordon, P.F., Gregory, P. *Nature*. 1984, **308**(5954), pp.90-90.
220. Cisnetti, F., Ballardini, R., Credi, A., Gandolfi, M.T., Masiero, S., Negri, F., Pieraccini, S. and Spada, G.P. Photochemical and electronic properties of conjugated bis(azo) compounds: An experimental and computational study. *Chemistry-a European Journal*. 2004, **10**(8), pp.2011-2021.
221. Jain, A., Gupta, Y. and Jain, S.K. Azo chemistry and its potential for colonic delivery. *Critical Reviews in Therapeutic Drug Carrier Systems*. 2006, **23**(5), pp.349-399.
222. Merino, E. Synthesis of azobenzenes: the coloured pieces of molecular materials. *Chemical Society Reviews*. 2011, **40**(7), pp.3835-3853.

223. Muraoka, T., Kinbara, K. and Aida, T. Mechanical twisting of a guest by a photoresponsive host. *Nature*. 2006, **440**(7083), pp.512-515.
224. Haghbeen, K. and Tan, E.W. Facile synthesis of catechol azo dyes. *Journal of Organic Chemistry*. 1998, **63**(13), pp.4503-4505.
225. Li, S., Wang, J.L., Shen, J.J., Wu, B. and He, Y.N. Azo Coupling Reaction Induced Macromolecular Self-Assembly in Aqueous Solution. *Acs Macro Letters*. 2018, **7**(4), pp.437-441.
226. Chevalier, A., Renard, P.Y. and Romieu, A. Azo-Based Fluorogenic Probes for Biosensing and Bioimaging: Recent Advances and Upcoming Challenges. *Chemistry-an Asian Journal.* 2017, **12**(16), pp.2008-2028.
227. Liu, J.N., Bu, W.B. and Shi, J.L. Chemical Design and Synthesis of Functionalized Probes for Imaging and Treating Tumor Hypoxia. *Chemical Reviews.* 2017, **117**(9), pp.6160-6224.
228. Kumari, R., Sunil, D., Ningthoujam, R.S. and Kumar, N.V.A. Azodyes as markers for tumor hypoxia imaging and therapy: An up-to-date review. *Chemico-Biological Interactions.* 2019, **307**, pp.91-104.
229. Rezaei-Seresht, E., Salimi, A. and Mahdavi, B. Synthesis, antioxidant and antibacterial activity of azo dye-stilbene hybrid compounds. *Pigment & Resin Technology*. 2019, **48**(1), pp.84-88.

Chapter 2. Instruments, Methods and Materials

2.1. Nuclear Magnetic Resonance (NMR) Spectroscopy

^{1}H and ^{13}C spectra were analysed by Bruker AV3HD 9.4 T (400 MHz ^{1}H) NMR spectrometer (AV3HD-400) and Bruker AV4 NEO 11.75 T (500 MHz ^{1}H) NMR spectrometer (500 CP). The measured chemical shifts (in ppm) were referenced to a trimethylsilane (TMS) standard with a chemical shift of 0 ppm. The NMR studies were carried out in common NMR solvents ($CDCl_3$, DMSO-d_6 and D_2O) and standard 400 MHz and 500 MHz Wilmad-LabGlass NMR tubes. MestreNova Research Lab software was used to analyse NMR spectra.

2.2. Fourier Transform Infrared (FTIR) Spectroscopy

Samples were dried under vacuum for 48 hours before FTIR analysis. FTIR spectra were analysed by Bruker Attenuated Total Reflection ALPHA-P FTIR spectrometer with 32 scans and Bruker OPUA 7.0 software. Wavenumber range was 400 cm^{-1} – 4000 cm^{-1}. Scan speed was 0.2 cm s^{-1}.

2.3. Dynamic Light Scattering (DLS)

DLS analysis was carried out by a Malvern Zetasizer Nano ZSP series instrument with a 4 mW He-Ne laser which performed at a wavelength of 633 nm, an avalanche photodiode (APD) detector and DTS software. The light was scatted at 173° and collected by a back-scatter-optic arrangement. Samples were equilibrated for 2 minutes prior to analysis at room temperature and at 37 °C in disposable polystyrene cuvettes (1.5 mL to 3.0 mL). The diameter of the particles was calculated by the diffusion coefficient and the Stokes-Einstein's equation (Equation 2.1) [1-2]. Each sample was measured in triplicate. Scattering intensity was the parameter used for size analysis. DLS measurements are based on the light scattering by the particles as they move by Brownian motion. The scattering intensity pattern is converted into a correlation function, which describes the fluctuations in the scattering light. The lighter the particles, the faster they are, so the

correlation function graph (correlogram) decays quicker. In correlation functions, time when decay starts indicates mean size, and the gradient indicates the polydispersity of sample [3]. The correlation function contains the diffusion coefficient information which is needed to be input into the Stokes-Einstein equation (Equation 2.1) [3]. The diffusion coefficients can be determined by fitting the correlation function with cumulants analysis. The cumulants analysis measures the mean size and polydispersity index of the sample [3]. The Z-average indicates the intensity weighted mean particle size, and is obtained from the fitting of the correlogram, specifically from the rate of decay of the correlation function [3]. Essentially, the rate of decay of light intensity fluctuations is proportional to the particle movement, which is inversely proportional to size. As the z-average size increases, the particle size increases [3]. Polydispersity index (PDI) is also calculated from the rate of decay of a correlogram. If the rate is fast (steep gradient) then the sample has a single size, and if the rate is slow (shallow gradient) the sample has particles of many sizes in it. The PDI estimates the width of the size distribution, so the smaller the PDI, the smaller the width and the more particles there are of one size [3]. Monodisperse systems have a PDI of approximately 0.1. A PDI value of 0.1-0.7 means the sample is nearly monodisperse and PDI value above 0.7 means polydisperse and the correlogram requires a CONTIN or NNLS (non-negative least squares) fitting procedure [3]. For intensity size distribution, size analysis is determined by the intensity of light scattered by the particle, dispersant viscosity and refractive index. Size analysis peaks are determined as a function of light intensity. The volume and number size distribution can be determined from the intensity distribution using Mie theory, size analysis can be calculated from the intensity analysis of inputting the correct refractive index and absorption for the sample [3]. Intensity particle size distribution can be used to report the size of each in the distribution. For reporting the relative amounts of each peak in the distribution, volume or number particle size distribution can be used.

$$D = \frac{k_B T}{6\pi\eta R_H}$$

Equation 2.1. The Stokes-Einstein's equation [3].

D: Diffusion coefficient ($m^2\ s^{-1}$).

k_B: Bolzmann constant ($m^2 kg\ K^{-1} s^{-2}$).

T: Temperature (K).

η: Dynamic viscosity (Pa.s).

R_H: Hydrodynamic radius.

2.4. Differential Scanning Calorimetry (DSC)

DSC analysis was carried out using a TA Instruments DSC Q20 instrument. Indium was used as the calibrant. Samples were placed on aluminium pans with a heating rate of 5 °C min^{-1} between 0 °C-100 °C and an inert flow of N_2 at a rate of 50 mL min^{-1}.

2.5. pH Measurements

pH Values were measured using a Thermo Scientific UY-58800-04 pH/mV/temperature meter. Sodium hydroxide standard solution and hydrochloric acid standard solution were used as calibrants prior to analysis.

2.6. Centrifugation and Sample-Drying

Samples were centrifuged using a Corning® LSE™ compact centrifuge, at 20 °C, 6000 rpm. Synthesised compounds were dried in a Fistreem vacuum oven with a temperature control unit from 0 °C-40 °C and a pressure gauge from 0 mbar-1020 mbar. Samples with water in were frozen initially in polystyrene falcon tubes, a Thermoelectron Heto Powderdry LLI500 freeze dryer with an Edward two stage vacuum pump was used to lyophilise the samples.

2.7. Ultraviolet-Visible (UV-Vis) Spectrophotometry

UV-vis spectra were recorded by using a VARIAN Cary 50 Probe UV-vis spectrometer with a xenon pulse lamp and Varian Cary WinUV 3.0 software. The Wavelength was set from 300 nm to 800 nm. The cuvettes used were Hellma™ Quartz Suprasil™ Micro Cuvette (10 mm, 0.7 mL) and disposable poly(methyl methacrylate) (PMMA) cuvettes (1.5 mL to 3.0 mL).

2.8. Sample Preparation, Sputter-Coating and Scanning Electron Microscopy (SEM) Energy Dispersive X-ray (EDX)

For the nanoparticles in solution state, a micropipette was used to extract 2 μL of the sample, which was then placed on a silicon wafer and air dried at room temperature in a fumehood. Conductive copper tape was applied to mount the silicon wafer on a SEM alumina stud. For lyophilised samples, mounting on SEM alumina stud by the copper tap directly was done. Then, a 2 nm of iridium film was coated on the samples to enhance the surface conductivity. The morphology and the particle size of the samples were measured by a Nova NanoSEM^{TM} scanning electron microscope, images were taken with an accelerating voltage of 3 kV. EDX mapping was performed with an accelerating voltage of 18 kV.

2.9. Advanced Polymer Chromatography

APC is a type of size exclusion chromatography. APC was conducted on a Waters Acquity APC system using three Acquity columns APC TM (200Å, 2.5 μm, 4.5 x 150 mm) packed with poly(ethylene) hybrid particles and calibrated against standard PMMA samples in THF. The temperature of the column was set at 40 °C and the flow rate was 0.5 mL/minute.

2.10. Gel Permeation Chromatography

GPC is a type of size exclusion chromatography. GPC was analysed using an Agilent 1260 instrument equipped with 2× mixed-C columns plus guard column and a refractive index detector. DMF containing lithium bromide was used as eluent at a flow rate of 1.0 mL min^{-1} and the temperature of the column oven and RI detector were set at 60 °C. PMMA calibration standards were used in conjunction with the RI detector for determining molecular weight values.

2.11. Rheology

Rheology was measured using an Anton Paar MCR 302 rheometer with a 25 mm parallel plate. Frequency sweeps were recorded at 100-0.1 rad s^{-1} with a constant amplitude (1%) at room temperature and a gap of 1.9 mm.

2.12. Preparation of Nanoparticles (Nanoprecipitation)

Nanoparticles were created by the 'dropping-in' method [4-6]. Polymers were dissolved in a particular organic solvent, for instance DMF, DMSO or acetone. The polymer solution was added dropwise into aqueous media, for example deionised water or PBS buffer solution with vigorous stirring, before the mixture was dialysed against the same aqueous solution.

2.13. Preparation of Doxorubicin Calibration Curve

Dox hydrochloride was dissolved in triethylamine and chloroform (molar ratio of Dox to triethylamine =1:26), and stirred for four hours in the dark (bright red solution). Then, the solution was mixed with PBS buffer solution, pH 6.5, pH 5 acetate buffer solutions or deionised water to obtain the desired concentrations as reported in the tables (Tables 2.1-2.2) below.

Table 2. 1. Absorbance of Dox in PBS buffer solution and pH 6. 5 acetate buffer solution at various Dox concentrations.

Concentration of Dox at pH 7.4 (mg mL^{-1})	Absorbance at 498 nm	Concentration of Dox at pH 6.5 (mg mL^{-1})	Absorbance at 504 nm
0.01	0.07282	0.05	1.1357
0.005	0.03569	0.025	0.58775
0.003	0.02024	0.02	0.49615
0.001	0.00388	0.015	0.39849
--	--	0.01	0.26351
--	--	0.0075	0.20348
--	--	0.005	0.14316
--	--	0.003	0.08961
--	--	0.001	0.04298

For R^2 value (Figure 2.1), the closer to 1, the better the curve fits the data. The R^2 values of both Dox in PBS buffer and Dox in pH 6.5 acetate buffer solution were 0.99. Therefore, both of the calibration curves fitted the data well. PBS buffer solution has disodium

hydrogen phosphate and sodium chloride. Acetate buffer solution has sodium acetate and acetic acid. There are different hydrogen bonding interactions, dipole-dipole interactions and Van der Waal forces between PBS buffer solution, pH 6.5 acetate buffer solution and Dox. Therefore, the slopes in PBS buffer and acetate solution were different. Calibration curve of Dox in PBS buffer (pH 7.4), y=0.003+7.19x, where intercept=0.003±6.7×10^{-4}; slope=7.19±0.11; R^2=0.99. Calibration curve of Dox in acetate buffer (pH 6.5), y=0.003+23.49x, where intercept=0.003±0.004; slope=23.49±0.36; R^2=0.99.

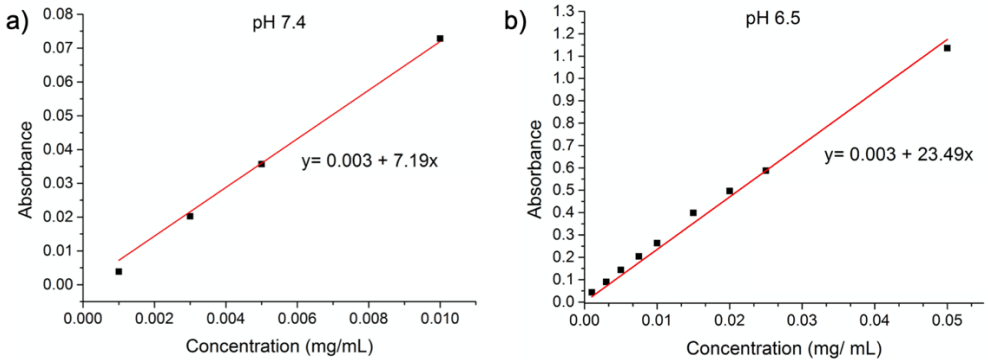

Figure 2. 1. Calibration curves and best fit lines of Dox in a) PBS buffer solution and b) pH 6.5 acetate buffer solution with different concentrations.

Table 2. 2. Absorbance of Dox in pH 5 acetate buffer solution and deionised water at various Dox concentrations.

Concentration of Dox at pH 5 (mg mL^{-1})	Absorbance at 502 nm	Concentration of Dox in deionised water (mg mL^{-1})	Absorbance at 448 nm
0.01	0.07687	0.1	1.3603
0.005	0.04287	0.075	1.00937
0.003	0.02648	0.05	0.84951
0.001	0.00689	0.03	0.62037
0.0005	0.00371	0.01	0.31803
--	--	0.005	0.22015
--	--	0.001	0.11691
--	--	0.0005	0.12517
--	--	0.0001	0.11235
--	--	0.00005	0.086655

The R^2 value of the calibration curve of Dox in pH 5 acetate buffer solution and Dox in deionised water were 0.99 and 0.98 (Figure 2.2). Therefore, both of the calibration curves fitted the data well. The pH 5 buffer solution has sodium acetate and acetic acid. There are different hydrogen bonding interactions, dipole-dipole interactions and Van der Waal forces between pH 5 acetate buffer solution, water and Dox. Therefore, the slopes in pH 5 acetate buffer solution and water were different. Calibration curve of Dox in acetate buffer (pH 5), y=0.001+7.92x, where intercept=0.001±0.002; slope=7.92±0.35; R^2=0.99. Calibration curve of Dox in water, y=0.14+12.4x, where intercept=0.14±0.03; slope=12.4±0.59; R^2=0.98.

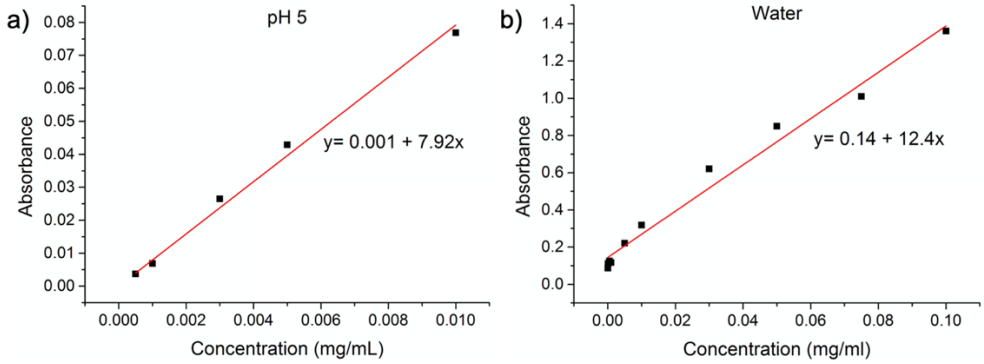

Figure 2. 2. Calibration curves and best fit lines of Dox in a) pH 5 acetate buffer solution and b) deionised water at various concentrations.

2.14. Doxorubicin Loaded Nanoparticles Preparation and Encapsulation Efficiency

The Dox solution (Dox dissolved in triethylamine and chloroform) was prepared using the same procedure as that described in 2.13. The Dox solution was added dropwise into the polymer nanoparticle solution with vigorous stirring for 24 hours to let the chloroform evaporate. Initially a two-layered solution was formed, a top layer that was bright red and a bottom layer was purple. When all the chloroform evaporated, the purple layer disappeared leaving a red solution. Then the red solution was dialysed against deionised water or PBS buffer solution for three days to remove excess (unloaded) Dox. The concentration of Dox loaded nanoparticle solution was measured by UV-vis spectrometer and calculated via the Dox calibration curve (2.13). In dialysis, solution volume in a dialysis bag does not change in an aqueous system. Dox encapsulation efficiency was calculated by Equation 2.2.

$$Dox\ Encapsulation\ Efficiency = \frac{M_E}{M_T} \times 100\ \% \qquad (2.2)$$

M_E is the mass of the Dox encapsulation in the nanoparticles, M_T is the mass of the Dox added at the beginning.

2.15. Loading of Doxorubicin Encapsulated Nanoparticles in Polymer Gel Depot

Lyophilised Dox encapsulated nanoparticles and polymer gel were dissolved in DMSO. The mixture was injected in PBS buffer solution and pH 6.5 acetate buffer solution, producing Dox loaded nanoparticles in polymer gel depot. The same procedure was applied to free Dox loaded polymer gels. The mass of Dox loaded in the polymer gel depot was calculated using Equation 2.3.

$$Mass\ of\ Dox\ loaded\ in\ gel\ depot = M_L \times E_D \qquad (2.3)$$

M_L is the mass of lyophilised Dox encapsulated nanoparticle, E_D is the Dox encapsulation efficiency.

2.16. Materials Inventory

All of the chemicals in Tables 2.3-2.4 were received from suppliers. Air sensitive chemicals were dried under nitrogen for 24 hours before use.

Table 2. 3. Chemicals that were used in the research projects.

Chemical	Supplier	Chemical	Supplier
Sarcosine (98%)	Alfa Aesar	α-Pinene (98%)	ACROS Organics
N-Boc-ethylenediamine hydrochloride (98%)	Alfa Aesar	Trifluoroacetic acid (99%, extra pure)	ACROS Organics
Chloroform (99.9%, extra dry over Molecular Sieves)	ACROS Organics	Buffer solution pH 5 (acetate buffer)	ACROS Organics
Triphosgene	Fluorochem	Triethylamine anhydrous	Fluorochem
Doxorubicin hydrochloride	Fluorochem	n-Hexane	VWR International
Ethanol absolute	VWR International	Dichloromethane (HPLC grade)	VWR International
Dimethyl sulfoxide (99.8 % D)	EURISO-TOP	Diethyl ether (analytical reagent grade)	Fisher Scientific

Table 2. 4. Chemicals that were used in the research projects (continued).

Chemical	Supplier	Chemical	Supplier
Triethylamine	Fisher Scientific	Piperidine (99%)	Alfa Aesar
Tetrahydrofuran (99.5%, Extra Dry, over Molecular Sieves)	ACROS Organics	*N,N*-Dimethylformamide (anhydrous, 99.8%)	Sigma-Aldrich
4-Cyano-4-(phenylcarbonothioylthio) pentanoic acid *N*-succinimidyl ester	Sigma-Aldrich	2,2'-Azobis(2-methyl-propionamidine) dihydrochloride (granular, 97%)	Sigma-Aldrich
Hydrobromic acid solution (33% in acetic acid)	Sigma-Aldrich	Poly(ethylene glycol) methyl ether (average M_n 5,000)	Sigma-Aldrich
Phosphate buffered saline tablet	Sigma-Aldrich	Methanesulfonic acid (98+%)	Alfa Aesar
N-ethyldiisopropylamine (99%)	Alfa Aesar	TRIS acetate 1.0 M buffer solution pH 6.5	Alfa Aesar
4-Cyano-4-((phenylcarbonothioyl)thio) pentanoic acid	Fluoroform	Chloroform-d (99.8 atom %D)	Sigma-Aldrich
Acetone	VWR chemicals	Y-Benzyl-L-glutamic acid (99%)	Alfa Aesar
L(-)-Fucose (97%)	ACROS Organic	Deuterium oxide (99.9 atom D%)	Sigma-Aldrich
Acetic acid (99-100%)	Sigma-Aldrich	Sodium cyanoborohydride (95 %)	Alfa Aesar
Ethylenediamine (99%)	Alfa Aesar	Sodium meta-periodate	Thermo Scientific
2-Hydroxypropyl methacrylate	Alfa Aesar	4-Acetoxystyrene	Fluorochem
Acrylamide	Fluka Analytical	Azobisisobutyronitrile	Sigma-Aldrich
Sodium nitrite	Sigma-Aldrich	Phosphoric acid	ACROS Organic
Sulfanilamide	Alfa Aesar	Propionic acid	Alfa Aesar
Concentrated sulphuric acid	Fisher scientific	Rhodamine B (98%)	Alfa Aesar
Poly(ethylene glycol) methyl ether (average M_n 5,000)	Sigma-Aldrich	Benzyl glutamate NCA	Dr. Mthulisi Khuphe (a previous PhD student) [4]

2.17. References

1. Hassan, P.A., Rana, S. and Verma, G. Making Sense of Brownian Motion: Colloid Characterization by Dynamic Light Scattering. *Langmuir.* 2015, **31**(1), pp.3-12.
2. Patterson, G.D. and Munozrojas, A. DYNAMIC LIGHT-SCATTERING NEAR THE GLASS-TRANSITION. *Annual Review of Physical Chemistry.* 1987, **38**, pp.191-210.
3. Murdock, R.C., Braydich-Stolle, L., Schrand, A.M., Schlager, J.J. and Hussain, S.M. Characterization of nanomaterial dispersion in solution prior to In vitro exposure using dynamic light scattering technique. *Toxicological Sciences.* 2008, **101**(2), pp.239-253.
4. Khuphe, M. and Thornton, P.D. Poly(hydroxy acid) Nanoparticles for the Encapsulation and Controlled Release of Doxorubicin. *Macromolecular Chemistry and Physics.* 2018, **219**(23), 1800352.
5. Khuphe, M., Ingram, N. and Thornton, P.D. Exploiting poly(alpha-hydroxy acids) for the acid-mediated release of doxorubicin and reversible inside-out nanoparticle self-assembly. *Nanoscale.* 2018, **10**(29), pp.14201-14206.
6. Price, D.J., Khuphe, M., Davies, R.P.W., McLaughlan, J.R., Ingram, N. and Thornton, P.D. Poly(amino acid)-polyester graft copolymer nanoparticles for the acid-mediated release of doxorubicin. *Chemical Communications.* 2017, **53**(62), pp.8687-8690.

Chapter 3. Thermoresponsive polysarcosine-based nanoparticles

Preamble

This chapter is based on work published as:

Yu H.; Ingram N.; Rowley J.; Parkinson S.; Green DC.; Warren NJ.; Thornton P.D. *Journal of Materials Chemistry B,* 2019, 26, 4217-4223.

Abstract

Polysarcosine holds great promise as an alternative to poly(ethylene glycol) for use within both biomedical and non-biomedical applications owing to its hydrophilicity and non-cytotoxicity, amongst other features. The grafting of a limited quantity of (2-hydroxypropyl methacrylate) to polysarcosine, for instance 3.5% of the total copolymer in terms of the number of repeat units, has a profound effect on the properties of the copolymer formed; polymer self-assembly to yield thermoresponsive nanoparticles can now be realised. Such nanoparticles are non-cytotoxic against a range of human breast cancer cell lines, able to withhold the therapeutic compound doxorubicin, and allow pronounced doxorubicin release in response to subtle thermal stimulation. The research in this chapter informs of how the straightforward modification of polysarcosine with a minimal molar amount of poly(2-hydroxypropyl methacrylate) can yield stimuli-responsive polymers that are suitable for use within controlled release applications.

3.1 Introduction

Amphiphilic stimuli-responsive polymers are widely utilised as drug delivery vehicles owing to their capability to form nanoparticles that can encapsulate cytotoxic therapeutic compounds [1-4]. The polymer acts to distribute the drug compound throughout an aqueous environment, preventing premature metabolism of the

compound, *in vivo* [5]. High efficiency drug loading into, and release from, nanoparticles is essential for effective treatment, and has been demonstrated by various anticancer products clinically, for instance irinotecan, anthracycline and Dox [6-7]. Various stimuli may be utilised to trigger controlled drug release from polymeric carriers, for instance changes in environmental temperature [8], pH [9], the presence of a particular enzyme [10], light irradiation [11] and the presence of a magnetic field [12] have been shown to instigate the release of drug molecules from polymeric nanoparticles. Thermoresponsive nanocarriers are of particular significance as anticancer drug delivery vehicles as it has been reported that patients may suffer fever and/ or chill after initial chemotherapy resulting in a slight increase in the temperature of diseased tissue [13]. This slight increase in temperature may be exploited to actuate drug release from thermoresponsive polymers *in vivo*.

Polypeptoids can form effective components of biomaterials owing to their variable and controllable chemical functionality, thermal stability, non-cytotoxicity, potential degradability and low immunogenicity [14]. In particular, polysarcosine (PSar) holds outstanding promise as a biomedical polymer due to its hydrophilicity, the easy of controlled synthesis [15-16], and the exclusive hydrogen bond acceptor repeat units that offer it resistance to protein fouling [17]. Consequently, PSar offers a real alternative to PEG for numerous applications [18], including its use as a non-fouling coating [19], and therapeutic protein conjugation [15]. The precise control over PSar synthesis has enabled the accurate synthesis of block copolymers that contain PSar conjugated to other polypeptoids [20-22], PCL [23-24], tertiary amine-containing molecules [25], PEG [26], and PAAs/polyamides [27-29].

There has been much recent interest in the application of PSar for the controlled release of therapeutic compounds. In such instances, PSar habitually forms the hydrophilic, and non-fouling, section of an amphiphilic block copolymer capable of forming nanoparticles in an aqueous solution [30]. Recent literature examples of PSar-based systems that have broad potential as drug delivery/controlled release vehicles include the creation of amphiphilic block copolymers composed of PSar and PCL that are capable of undergoing thermally-mediated self-assembly to bear a range of (nano)carriers [24], amphiphilic

star-like copolymers consisting of PSar and Boc-protected polylysine, that undergo degradation in response to elevated glutathione concentration [31], and very recently the creation of b-glucuronidase-responsive antibody drug conjugates (ADC) that feature PSar as a hydrophobicity masking entity within an ADC drug-linker platform [32]. Recent work reports the creation of PSar-containing block copolymers, polymerised from a therapeutic initiator, that form enzyme-responsive nanoparticles [33], and the creation of PAA–*b*-poly(ester) conjugates synthesised by glucosamine-initiated ROP, that are susceptible to acid-mediated degradation [34]. Such promising results ensure that additional investigation into the use of PSar as a component within controlled release systems is of significant value.

The good water-solubility of PSar means that polymer modification must be realised in order to create PSar-based nanoparticles in aqueous solution. RAFT polymerisation is an extensively exploited technique for the generation of amphiphilic block copolymers, and offers the opportunity to graft non-water-soluble oilgomers/ polymers to PSar, enabling the creation of thermoresponsive polymer nanoparticles [35]. Combining RAFT polymerisation and PISA may be exploited to conveniently elucidate the capability of block copolymers to form nanoparticles during the polymerisation by taking DLS measurements. Here, nanoparticle dimensions and dispersity are determined non-destructively, under normal conditions (i.e. without drying, extraction etc.), offering a convenient initial guide of the suitability of the block copolymer synthesised as a potential nanocarrier. The RAFT polymerisation of HPMA generates a non-immunogenic and non-toxic polymer [36-37], and a well-established route to PHPMA-based polymer nanoparticles is via RAFT aqueous dispersion polymerisation. Frequently, nanoparticles are produced by conducting this process in the presence of a PEG macro RAFT agent [38], although recently, O'Reilly and co-workers described the preparation of a range of PSar-*b*-PHPMA copolymers capable of forming various morphologies dependent on the copolymer composition [39]. The number of non-biodegradable PHPMA repeat units within the block copolymer typically ranged between 100 and 400, and dictated the outcome of $PSar_{59}$-*b*-$PHPMA_n$ self-assembly in aqueous solution. Although the drug delivery capabilities, and the thermoresponse of the nanoparticles created were not reported, such materials may be considered appropriate for use in drug delivery

applications if the molecular weight of the non-degradable PHPMA section within the copolymer can be reduced to enable its clearance from the body, post-deployment.

The research in this chapter reports the creation of thermoresponsive PSar-*b*-PHPMA nanoparticles designed to contain highly constrained molar amounts of PHPMA within the block copolymer composition. Nanoparticle formation was monitored *in situ*, and the polymer deemed most suitable for use a potential drug delivery vehicle was advanced to Dox loading and release studies. The thermoresponse of the polymers was demonstrated by pronounced Dox release as a consequence of a moderate increase in solution temperature. Accordingly, the efficacy of the Dox-loaded nanoparticles against a range of breast cancer cell types was evaluated, and revealed that Dox-loaded nanoparticles were lethal against all breast cancer cell types tested, in marked contrast to unloaded non-cytotoxic nanoparticles. The reported polymers are thus highly-suited to the encapsulation and thermally-triggered release of molecular cargo, which may be applied for the eradication of breast cancer cells.

3.2 Experimental

3.2.1 Synthesis of sarcosine NCA

The Polymer synthesis conditions were optimised by a previous MSc student (Ting Yao). Sarcosine NCA synthesis was conducted under a nitrogen atmosphere. Sarcosine (4.0 g, 44.9 mmol) and α-pinene (14.0 mL, 88.2 mmol) were added to anhydrous THF (60.0 mL). Triphosgene (10.0 g, 33.7 mmol) was dissolved in anhydrous THF (10.0 mL) and added dropwise to the reaction mixture. The mixture was stirred under reflux at 60 °C for 4.5 hours. The appearance of the resulting solution was brown-yellow. After rotary evaporation, brown precipitate and yellow solution were formed, before the products were stored under vacuum at 50 °C overnight. Consequently, brown solid formed that was dissolved in THF and added dropwise to cold n-hexane (recrystallisation). The recrystallisation procedure was performed two additional times before suction filtration was used to collect the products. The melting point was determined to be 104–104.6 °C, in agreement with prior studies [40]. Sarcosine NCA: 2.56 g, 49.5 wt. % (white crystalline powder). ^{1}H NMR (400 MHz, $CDCl_3$, δ, ppm): 4.13 (s, 2H, C$\underline{H_2}$), 3.06 (s, 3H, C$\underline{H_3}$). FTIR:

ν_{max}/cm^{-1} (solid): 3227 cm^{-1} (tertiary amine N-H stretch), 2948 cm^{-1} (alkyl C-H stretch), 1846 cm^{-1} and 1757 cm^{-1} (anhydride CO stretch).

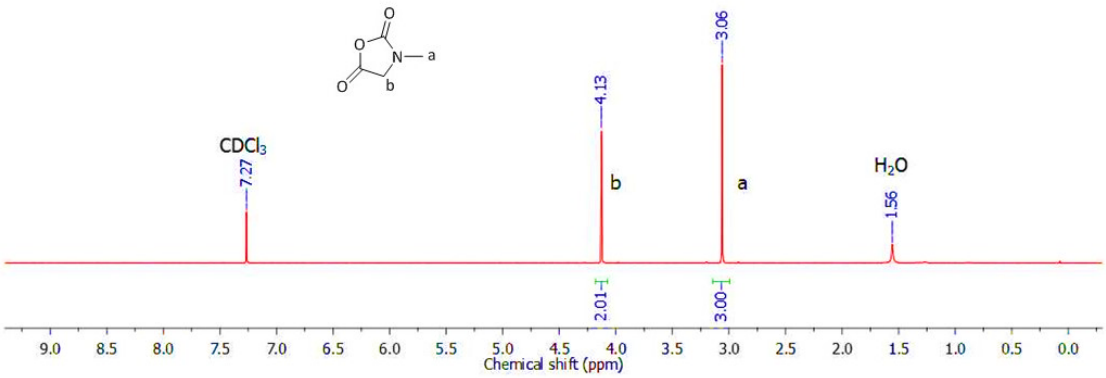

Figure 3. 1. The 400 MHz ^{1}H-NMR spectrum of sarcosine NCA in $CDCl_3$ at 25 °C.

3.2.2 Polymerisation of sarcosine NCA from *N*-Boc-ethylenediamine

Sarcosine NCA (0.80 g, 6.96 mmol) was dissolved in anhydrous DMF (3.0 mL), maintained under constant nitrogen flow. Then, *N*-Boc-ethylenediamine hydrochloride (0.01 g, 0.051 mmol) was dissolved in anhydrous DMF (3.0 mL) before being added to the monomer solution. The polymerisation proceeded for four days until the products were isolated by polymer precipitation into cold diethyl ether (35.0 mL). Polymer recovery has achieved by centrifugation for 30 minutes at 4000 rev/min. Finally, the products (Boc protected PSar) were dried under vacuum at room temperature overnight. The synthesised polymer was Boc protected $PSar_{136}$ (Boc-$PSar_{136}$). Boc-$PSar_{58}$, Boc-$PSar_{78}$ and Boc-$PSar_{137}$ were also produced using the same procedure and the quantity of reactants were sarcosine NCA (0.341 g, 2.96 mmol), sarcosine NCA (0.457 g, 3.98 mmol) and sarcosine NCA (0.804 g, 6.99 mmol), respectively. Boc-$PSar_{136}$: 0.427 g, 85.3 wt. % (white powdery solid). ^{1}H NMR (400 MHz, DMSO-d_6, δ, ppm): 4.48 – 3.79 (m, 272H, $(OCC\underline{H}_2NCH_3)_{136}$), 3.70 – 3.56 (m, 4H, $C\underline{H}_2C\underline{H}_2$), 2.96 - 2.70 (m, 408H, $(OCCH_2NC\underline{H}_3)_{136}$), 2.27 – 2.25 (s, 1H, $(OCCH_2NCH_3)_{136}\underline{H}$) 1.40 – 1.36 (s, 9H, $(\underline{H}_3C)_3OCO$). FTIR: ν_{max}/cm^{-1} (solid): 3448 cm^{-1} (secondary amine N-H stretch), 2936 cm^{-1} (alkane C-H stretch), 1641 cm^{-1} (secondary amide C=O stretch), 1396 cm^{-1} (alkane C-H stretch), 1227 (ester C-O stretch) and 1098 cm^{-1} (amine C-N stretch).

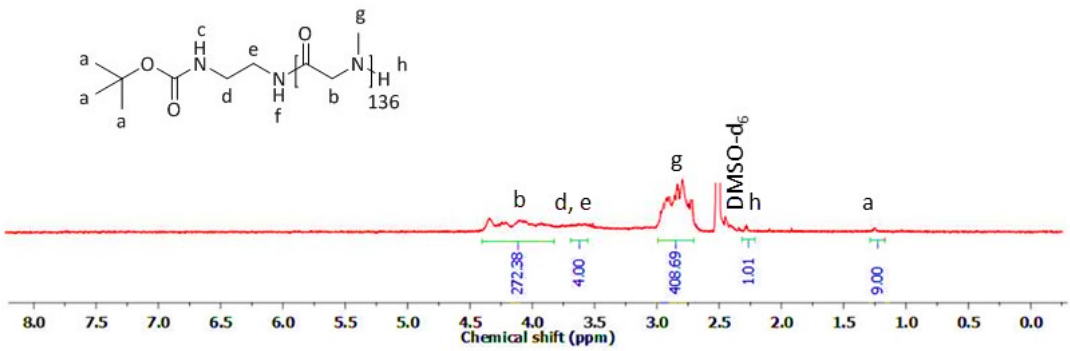

Figure 3. 2. The 400 MHz ^{1}H-NMR spectrum of Boc-PSar$_{136}$ in DMSO at 25 °C.

Boc-PSar$_{58}$: 0.190 g, 87.1 wt. % (white powdery solid). ^{1}H NMR (400 MHz, DMSO-d$_6$, δ, ppm): 4.24 – 4.17 (m, 116H, (OCC$\underline{H}_2$NCH$_3$)$_{58}$), 3.75 – 3.59 (m, 4H, C$\underline{H}_2$C$\underline{H}_2$), 3.17 - 2.86 (m, 174H, (OCCH$_2$NC$\underline{H}_3$)$_{58}$), 1.40 – 1.36 (s, 9H, ($\underline{H}_3$C)$_3$OCO). FTIR: ν_{max}/cm^{-1} (solid): 3463 cm^{-1} (secondary amine N-H stretch), 2936 cm^{-1} (alkane C-H stretch), 1648 cm^{-1} (secondary amide C=O stretch), 1396 cm^{-1} (alkane C-H stretch), 1227 (ester C-O stretch) and 1098 cm^{-1} (amine C-N stretch).

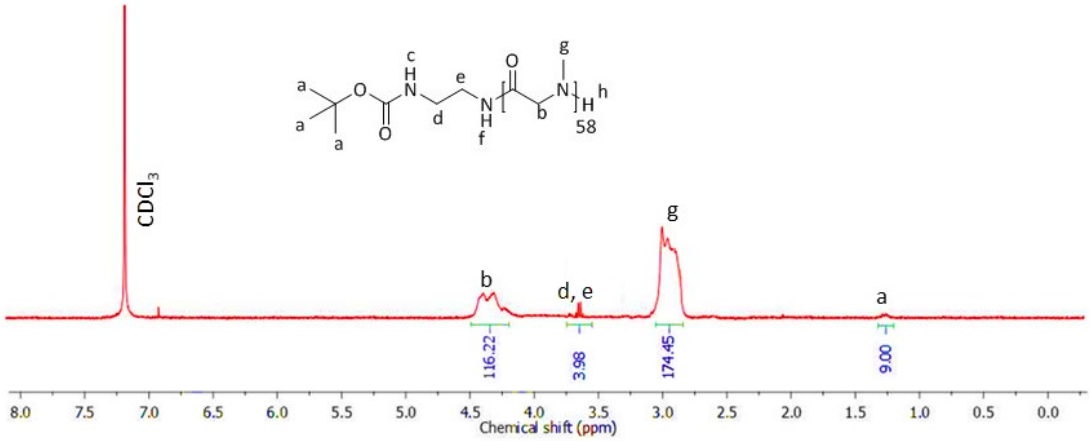

Figure 3. 3. The 400 MHz ^{1}H-NMR spectrum of Boc-PSar$_{58}$ in CDCl$_3$ at 25 °C.

Boc-PSar$_{78}$: 0.236 g, 81.2 wt. % (white powdery solid). ^{1}H-NMR (400 MHz, DMSO-d$_6$, δ, ppm): 4.48 – 3.79 (m, 156H, (OCC$\underline{H}_2$NCH$_3$)$_{78}$), 3.43 – 3.40 (s, 4H, C$\underline{H}_2$C$\underline{H}_2$), 3.18 - 2.86 (m, 234H, (OCCH$_2$NC$\underline{H}_3$)$_{78}$), 1.40 – 1.36 (s, 9H, ($\underline{H}_3$C)$_3$OCO). FTIR: ν_{max}/cm^{-1} (solid): 3461 cm^{-1} (secondary amine N-H stretch), 2939 cm^{-1} (alkane C-H stretch), 1634 cm^{-1} (secondary amide C=O stretch), 1396 cm^{-1} (alkane C-H stretch), 1233 (ester C-O stretch) and 1098 cm^{-1} (amine C-N stretch).

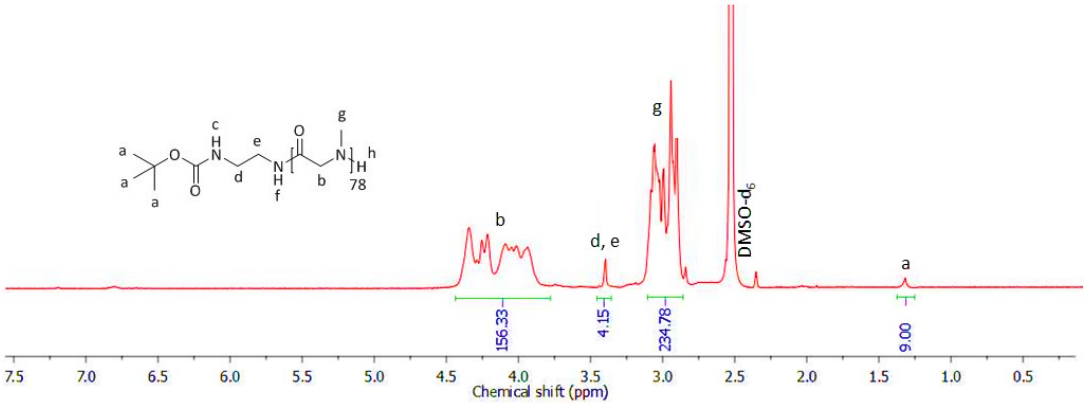

Figure 3. 4. The 400 MHz ^{1}H-NMR spectrum of Boc-PSar$_{78}$ in DMSO at 25 °C.

Boc-PSar$_{137}$: 0.421 g, 83.4 wt. % (white powdery solid). ^{1}H-NMR (400 MHz, DMSO-d$_6$, δ, ppm): 4.48 – 3.79 (m, 274H, (OCC<u>H</u>$_2$NCH$_3$)$_{137}$), 2.86-2.57 (m, 411H, (OCCH$_2$NC<u>H</u>$_3$)$_{137}$), 1.42 – 1.34 (s, 9H, (<u>H</u>$_3$C)$_3$OCO). FTIR: ν_{max}/cm^{-1} (solid): 3463 cm^{-1} (secondary amine N-H stretch), 2939 cm^{-1} (alkane C-H stretch), 1634 cm^{-1} (secondary amide C=O stretch), 1396 cm^{-1} (alkane C-H stretch), 1227 (ester C-O stretch) and 1098 cm^{-1} (amine C-N stretch).

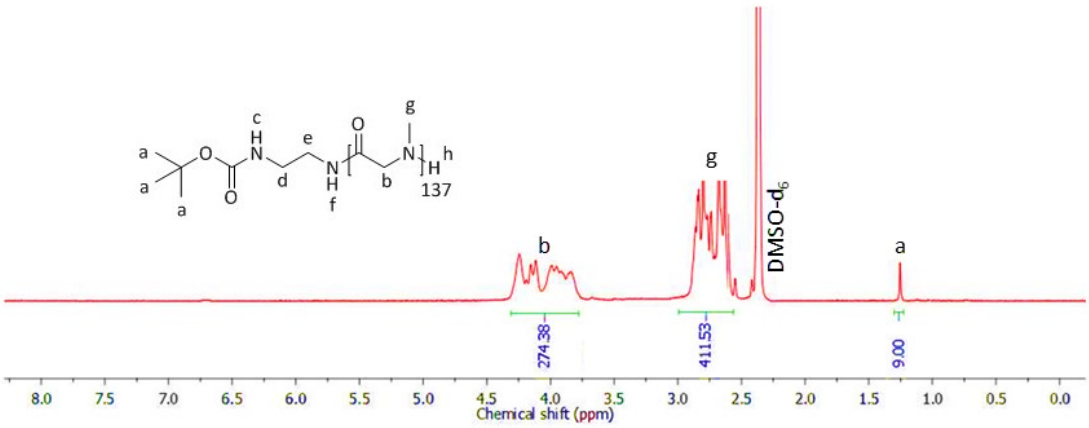

Figure 3. 5. The 400 MHz ^{1}H-NMR spectrum of Boc-PSar$_{137}$ in DMSO at 25 °C.

3.2.3 Boc cleavage from PSar-conjugated *N*-Boc-ethylenediamine

PSar-conjugated *N*-Boc-ethylenediamine (0.40 g, 0.041 mmol) was dissolved in TFA (6.0 mL), and the reaction was stirred overnight at room temperature. The solution was then added dropwise to cold diethyl ether (60.0 mL), to isolate the product, which was recovered by centrifugation at 4000 rev/min for 30 minutes. Finally, the products were dried in a vacuum oven overnight. The produced polymer was Boc cleaved PSar$_{136}$. PSar$_{58}$, PSar$_{78}$ and PSar$_{137}$ were also produced using the same procedure and the quantity of the reactants were Boc-PSar$_{58}$ (0.190 g, 0.044 mmol), Boc-PSar$_{78}$ (0.230 g, 0.040 mmol) and

Boc-PSar$_{137}$ (0.40 g, 0.040 mmol). PSar$_{136}$: 0.313 g, 79.0 wt. % (brown viscous solution). ^{1}H-NMR (400 MHz, DMSO-d$_6$, δ, ppm): 4.47 – 3.96 (m, 272H, (OCC$\underline{H}_2$NCH$_3$)$_{136}$H), 3.68 – 3.60 (m, 4H, H$_2$NC$\underline{H}_2$C$\underline{H}_2$NH), 3.23 - 2.70 (m, 408H, (OCCH$_2$NC$\underline{H}_3$)$_{136}$H). FTIR: ν_{max}/cm^{-1} (solid): 3439 cm^{-1} (secondary and primary amine N-H stretch), 2943 cm^{-1} (alkane C-H stretch), 1737 cm^{-1} and 1634 cm^{-1} (secondary amide C=O stretch), 1396 cm^{-1} (alkane C-H stretch) and 1128 cm^{-1} (amine C-N stretch).

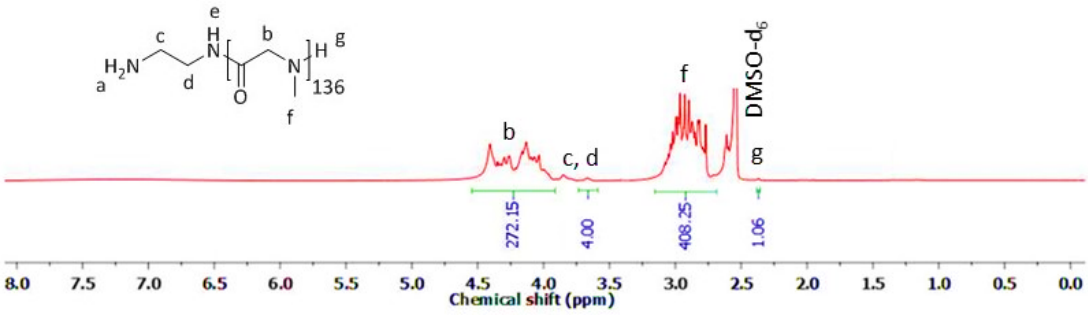

Figure 3. 6. The 400 MHz ^{1}H-NMR spectrum of deprotected PSar$_{136}$ in DMSO at 25 °C.

PSar$_{58}$: 0.153 g, 82.7 wt. % (brown viscous solution). ^{1}H-NMR (400 MHz, DMSO-d$_6$, δ, ppm): 4.45 – 3.79 (m, 116H, (OCC$\underline{H}_2$NCH$_3$)$_{58}$H), 3.70 – 3.46 (m, 4H, H$_2$NC$\underline{H}_2$C$\underline{H}_2$NH), 3.23 - 2.80 (m, 174H, (OCCH$_2$NC$\underline{H}_3$)$_{58}$H). FTIR: ν_{max}/cm^{-1} (solid): 3457 cm^{-1} (secondary and primary amine N-H stretch), 2933 cm^{-1} (alkane C-H stretch), 1641 cm^{-1} (secondary amide C=O stretch), 1396 cm^{-1} (alkane C-H stretch) and 1149 cm^{-1} (amine C-N stretch).

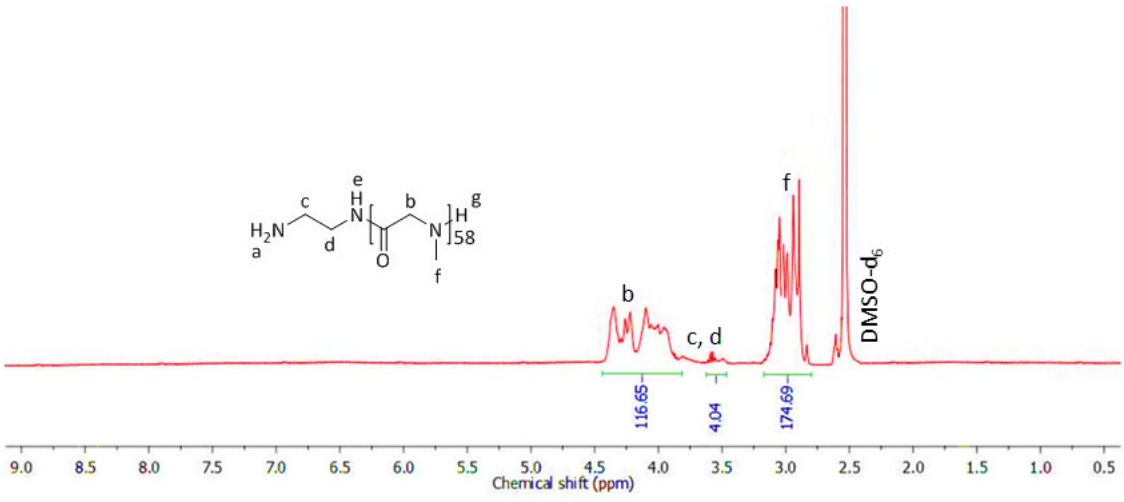

Figure 3. 7. The 400 MHz ^{1}H-NMR spectrum of deprotected PSar$_{58}$ in DMSO-d$_6$ at 25 °C.

PSar$_{78}$: 0.184 g, 81.4 wt. % (brown viscous solution). ^{1}H-NMR of PSar$_{78}$ (400 MHz, DMSO-d$_6$, δ, ppm): 4.66 – 3.68 (m, 156H, (OCC$\underline{H}_2$NCH$_3$)$_{78}$H), 3.70 – 3.55 (m, 4H, H$_2$NC$\underline{H}_2$C$\underline{H}_2$NH), 3.23 - 2.73 (m, 234H, (OCCH$_2$NC$\underline{H}_3$)$_{78}$H). FTIR: ν_{max}/cm^{-1} (solid): 3444 cm^{-1} (secondary and

primary amine N-H stretch), 2939 cm^{-1} (alkane C-H stretch), 1781 cm^{-1} and 1627 cm^{-1} (secondary amide C=O stretch), 1396 cm^{-1} (alkane C-H stretch) and 1151 cm^{-1} (amine C-N stretch).

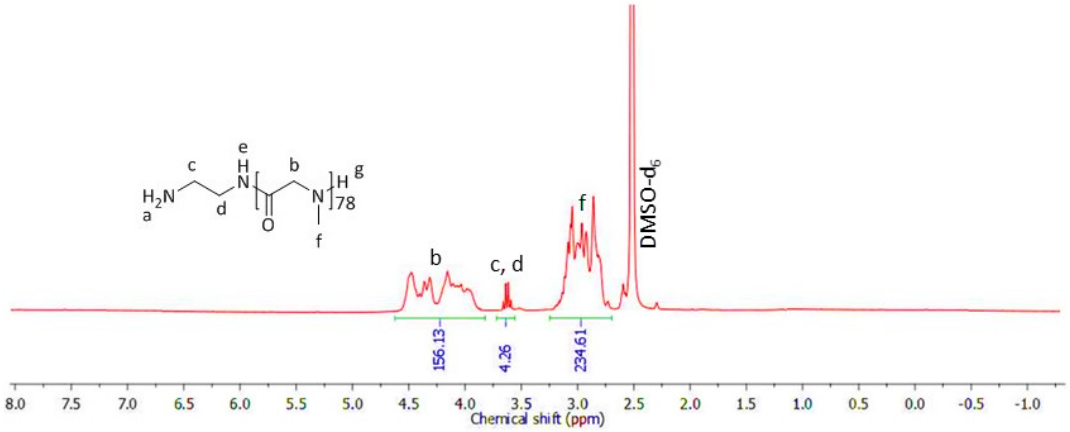

Figure 3. 8. The 400 MHz ^{1}H-NMR spectrum of deprotected $PSar_{78}$ in DMSO at 25 °C.

$PSar_{137}$: 0.335 g, 84.6 wt. % (brown viscous solution). ^{1}H-NMR of $PSar_{137}$ (400 MHz, DMSO-d_6, δ, ppm): 4.52 – 3.97 (m, 274H, $(OCC\underline{H}_2NCH_3)_{137}H$), 3.70 – 3.68 (m, 4H, $H_2NC\underline{H}_2C\underline{H}_2NH$), 3.23 - 2.73 (m, 411H, $(OCCH_2NC\underline{H}_3)_{137}H$). FTIR: ν_{max}/cm^{-1} (solid): 3453 cm^{-1} (secondary and primary amine N-H stretch), 2939 cm^{-1} (alkane C-H stretch), 1777 cm^{-1} and 1634 cm^{-1} (secondary amide C=O stretch), 1396 cm^{-1} (alkane C-H stretch) and 1143 cm^{-1} (amine C-N stretch).

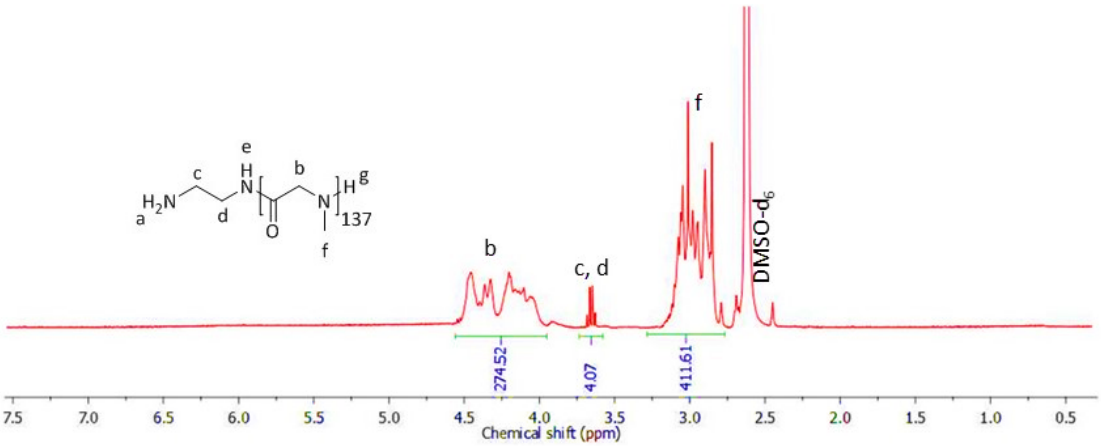

Figure 3. 9. The 400 MHz ^{1}H-NMR spectrum of deprotected $PSar_{137}$ in DMSO at 25 °C.

3.2.4 SCPDB conjugation to amine-bearing polysarcosine

Under a nitrogen atmosphere, SCPDB (0.035 g, 0.093 mmol) and the deprotected PSar (0.30 g, 0.031 mmol) were independently dissolved in anhydrous DCM (1.0 mL and 12.0

mL, respectively). The solution containing PSar was then added dropwise to the SCPDB solution, and the mixture stirred overnight. Consequently, the solution was added dropwise to cold diethyl ether (60.0 mL), resulting in the formation of a pink solid, which was isolated by centrifugation for 30 minutes at 4000 rev/min and then dried in a vacuum oven overnight. The product was washed with DCM before a second recrystallisation was performed, prior to product isolation and drying overnight under vacuum. The produced polymer was $PSar_{136}$-macro-RAFT agent. $PSar_{58}$-macro-RAFT agent, $PSar_{78}$-macro-RAFT agent and $PSar_{137}$-macro-RAFT agent were also synthesised using the same procedure and the quantity of the reactants were SCPDB (0.041 g, 0.108 mmol), $PSar_{58}$ (0.15 g, 0.036 mmol); SCPDB (0.041 g, 0.108 mmol), $PSar_{78}$ (0.18 g, 0.032 mmol); and SCPDB (0.038 g, 0.102 mmol), $PSar_{137}$ (0.33 g, 0.034 mmol), respectively. $PSar_{136}$-macro-RAFT agent: 0.189 g, 61.2 wt. % (pink solid). ^{1}H-NMR (400 MHz, DMSO-d_6, δ, ppm): 7.42 – 7.40 (d, 2H, Ar<u>H</u>), 7.25 – 7.20 (t, 1H, Ar<u>H</u>), 7.09 – 7.00 (t, 2H, Ar<u>H</u>), 4.60 – 4.12 (m, 272H, (OCC<u>H</u>$_2$NCH$_3$)$_{136}$H), 3.75 – 3.73 (m, 4H, HNC<u>H</u>$_2$C<u>H</u>$_2$NH), 3.20 - 2.73 (m, 408H, (OCCH$_2$NC<u>H</u>$_3$)$_{136}$H). FTIR: ν_{max}/cm^{-1} (solid): 3439 cm^{-1} (secondary amine N-H stretch), 2943 cm^{-1} (alkane C-H stretch), 2172 cm^{-1} (nitrile C≡N stretch), 1733 cm^{-1} and 1634 cm^{-1} (secondary amide C=O stretch), 1396 cm^{-1} (alkane C-H stretch) and 1193 cm^{-1} (amine C-N stretch).

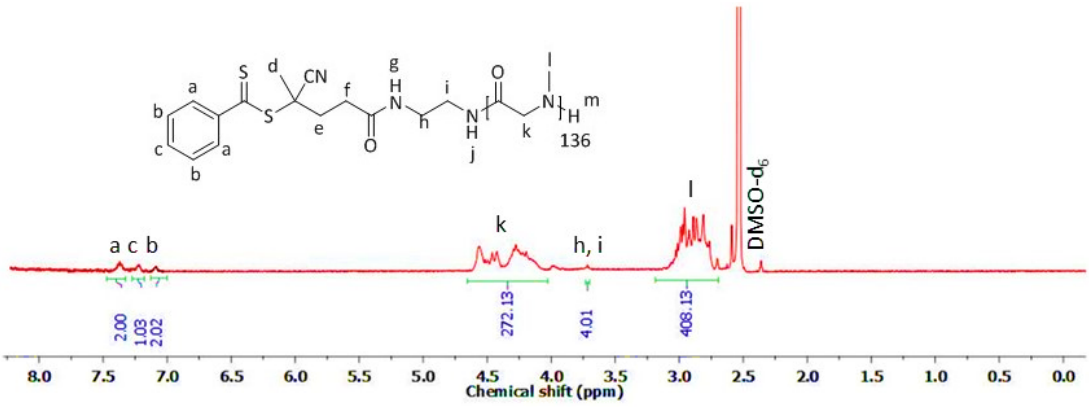

Figure 3. 10. The 400 MHz ^{1}H-NMR spectrum of dialysed $PSar_{136}$-macro-RAFT agent in DMSO at 25 °C.

$PSar_{58}$-macro-RAFT agent: 0.079 g, 49.4 wt. % (pink solid). ^{1}H-NMR of $PSar_{58}$-macro-RAFT agent (400 MHz, DMSO-d_6, δ, ppm): 7.42 – 7.40 (d, 2H, Ar<u>H</u>), 7.25 – 7.20 (t, 1H, Ar<u>H</u>), 7.09 – 7.00 (t, 2H, Ar<u>H</u>), 4.23 – 3.56 (m, 116H, (OCC<u>H</u>$_2$NCH$_3$)$_{58}$H), 3.27 – 2.78 (m, 174H,

$(OCCH_2NC\underline{H}_3)_{58}H$). FTIR: ν_{max}/cm^{-1} (solid): 3469 cm^{-1} (secondary amine N-H stretch), 2946 cm^{-1} (alkane C-H stretch), 2112 cm^{-1} (nitrile C≡N stretch), 1739 cm^{-1} and 1634 cm^{-1} (secondary amide C=O stretch), 1396 cm^{-1} (alkane C-H stretch) and 1195 cm^{-1} (amine C-N stretch).

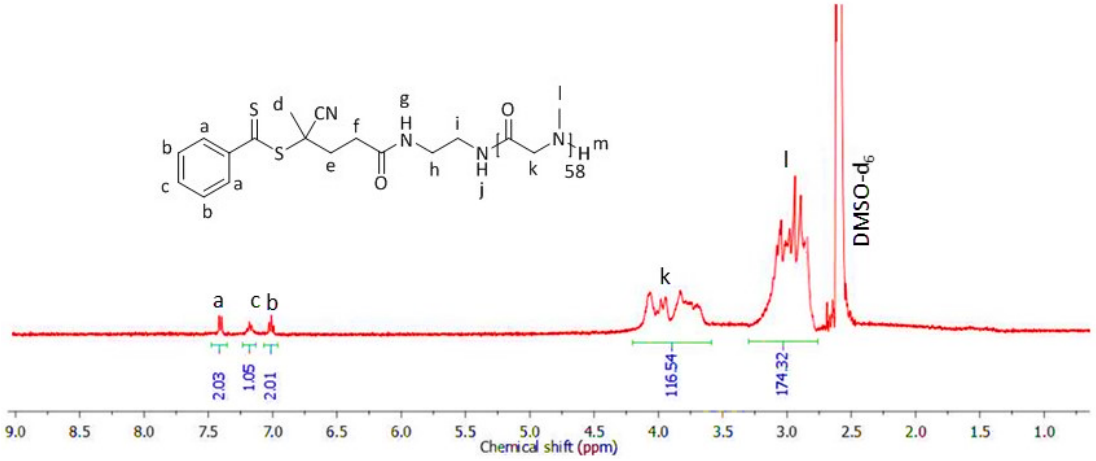

Figure 3. 11. The 400 MHz ^{1}H-NMR spectrum of $PSar_{58}$-macro-RAFT agent in DMSO-d_6 at 25 °C.

$PSar_{78}$-macro-RAFT agent: 0.115 g, 60.9 wt. % (pink solid). ^{1}H-NMR of $PSar_{78}$-macro-RAFT agent (400 MHz, DMSO-d_6, δ, ppm): 7.42 – 7.40 (d, 2H, Ar$\underline{H}$), 7.25 – 7.20 (t, 1H, Ar$\underline{H}$), 7.09 – 6.92 (t, 2H, Ar$\underline{H}$), 4.46 – 3.90 (m, 156H, $(OCC\underline{H}_2NCH_3)_{78}H$), 3.60 – 3.48 (m, 6H, $\underline{H}NC\underline{H}_2C\underline{H}_2N\underline{H}$), 3.05 - 2.78 (m, 234H, $(OCCH_2NC\underline{H}_3)_{78}H$). FTIR: ν_{max}/cm^{-1} (solid): 3463 cm^{-1} (secondary amine N-H stretch), 2939 cm^{-1} (alkane C-H stretch), 2100 cm^{-1} (nitrile C≡N stretch), 1735 cm^{-1} and 1627 cm^{-1} (secondary amide C=O stretch), 1396 cm^{-1} (alkane C-H stretch) and 1189 cm^{-1} (amine C-N stretch).

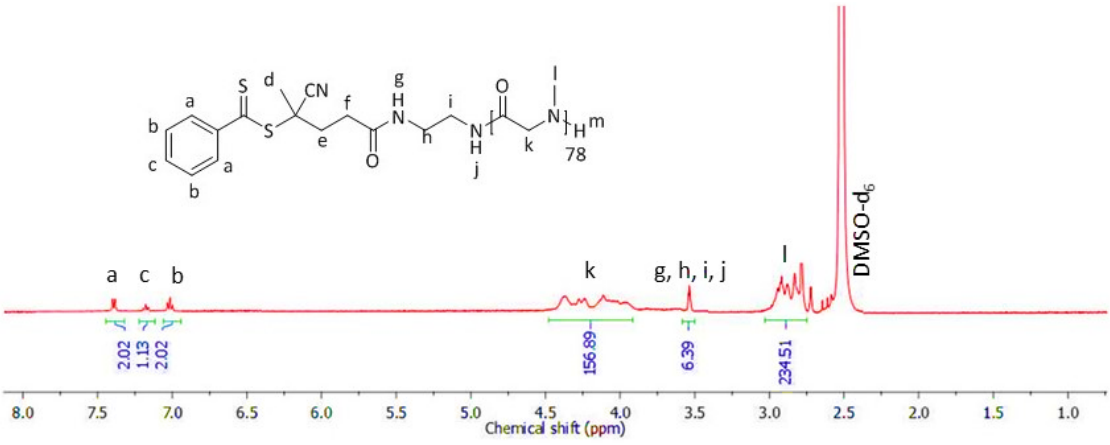

Figure 3. 12. The 400 MHz ^{1}H-NMR spectrum of $PSar_{78}$-macro-RAFT agent in DMSO at 25 °C.

$PSar_{137}$-macro-RAFT agent: 0.213 g, 62.8 wt. % (pink solid). ^{1}H-NMR of $PSar_{137}$-macro-RAFT agent (400 MHz, DMSO-d_6, δ, ppm): 7.42 – 7.40 (d, 2H, ArH), 7.25 – 7.20 (t, 1H, ArH), 7.09 – 7.00 (t, 2H, ArH), 4.46 – 3.85 (m, 274H, $(OCCH_2NCH_3)_{137}H$), 3.05 – 2.64 (m, 411H, $(OCCH_2NCH_3)_{137}H$). FTIR: ν_{max}/cm^{-1} (solid): 3463 cm^{-1} (secondary amine N-H stretch), 2939 cm^{-1} (alkane C-H stretch), 2149 cm^{-1} (nitrile C≡N stretch), 1732 cm^{-1} and 1634 cm^{-1} (secondary amide C=O stretch), 1396 cm^{-1} (alkane C-H stretch) and 1195 cm^{-1} (amine C-N stretch).

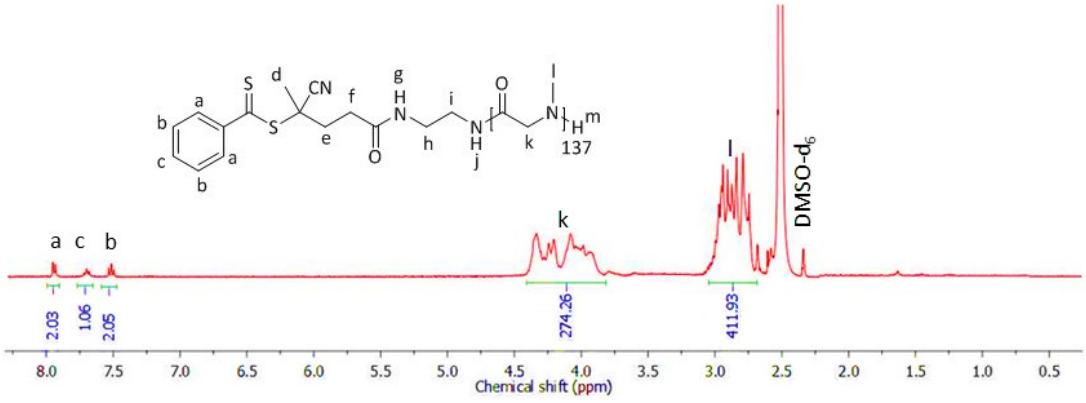

Figure 3. 13. The 400 MHz ^{1}H-NMR spectrum of $PSar_{137}$-macro-RAFT agent in DMSO at 25 °C.

3.2.5 HPMA polymerisation from the PSar-macro-RAFT agent

Absolute ethanol and deionised water underwent nitrogenation overnight. The PSar-macro-RAFT agent (0.095 g, 0.010 mmol) was dissolved in the absolute ethanol (2.0 mL) and followed by 30 minutes of ultrasonication. APPH (0.006 g, 0.030 mmol) was dissolved in deionised water (10.0 mL). Next, the HPMA monomer (0.076 g, 0.530 mmol) was added to the macro-RAFT agent solution, before the AAPH solution, in addition to deionised water (3.0 mL), were added. The mixture was stirred and stirred and degassed with nitrogen for 30 minutes before the mixture was heated in an oil bath for 4 hours at 55 °C. Every hour the reaction mixture (1.5 mL) was removed from the polymerisation, and DLS analysis was performed. Finally, the product was dialysed for six days, freeze dried for two days and stored in a desiccator. The synthesised polymer was $PSar_{136}$-*b*-$PHPMA_{53}$. $PSar_{58}$-*b*-$PHPMA_{82}$, $PSar_{78}$-*b*-$PHPMA_{130}$, $PSar_{137}$-*b*-$PHPMA_{273}$ and $PSar_{136}$-*b*-$PHPMA_{14}$ were also produced using the same procedure and the quantity of the reactants were $PSar_{58}$-macro-RAFT agent (0.07 g, 0.016 mmol), HPMA (0.189 g, 1.32 mmol), AAPH (0.010 g, 0.048 mmol); $PSar_{78}$-macro-RAFT agent (0.115 g, 0.020 mmol),

HPMA (0.372 g, 2.60 mmol), AAPH (0.012 g, 0.063 mmol); $PSar_{137}$-macro-RAFT agent (0.213 g, 0.021 mmol), HPMA (0.819 g, 5.73 mmol), AAPH (0.012 g, 0.060 mmol); $PSar_{136}$-macro-RAFT agent (0.095 g, 0.010 mmol), HPMA (0.020 g, 0.140 mmol), AAPH (0.006 g, 0.030 mmol), respectively. $PSar_{136}$- *b*-$PHPMA_{53}$: 0.109 g, 65.0 wt. % (pale pink solid). ^{1}H-NMR (400 MHz, DMSO-d_6, δ, ppm): 7.46 – 7.35 (d, 2H, Ar<u>H</u>), 7.33 – 7.20 (t, 1H, Ar<u>H</u>), 7.19 – 6.86 (t, 2H, Ar<u>H</u>), 4.74 – 4.17 (m, 272H, $(OCC\underline{H}_2NCH_3)_{136}H$), 4.00 – 3.76 (m, 53H, $(H_3CCCOOCH_2C\underline{H}OHCH_3CH_2)_{53}$), 3.41 – 3.24 (m, 106H, $(H_3CCCOOC\underline{H}_2CHOHCH_3CH_2)_{53}$), 3.22 – 2.70 (m, 408H, $(H_3CCCOOC\underline{H}_2CHOHCH_3CH_2)_{53}CCH_3CNCH_2CH_2CONHCH_2CH_2NH(COCH_2NC\underline{H}_3)_{136}H$), 2.23 – 1.80 (s, 106H, $(H_3CCCOOCH_2CHOHCH_3C\underline{H}_2)_{53}$), 1.75 – 0.76 (m, 318H, $(\underline{H}_3CCCOOCH_2CHOHC\underline{H}_3CH_2)_{53}$). FTIR: ν_{max}/cm^{-1} (solid): 3473 cm^{-1} (alcohol and secondary amine), 2937 cm^{-1} (alkane C-H stretch), 2046 cm^{-1} (nitrile C≡N stretch), 1721 cm^{-1} and 1646 cm^{-1} (secondary amide C=O stretch), 1396 cm^{-1} (alkane C-H stretch) and 1098 cm^{-1} (amine C-N stretch).

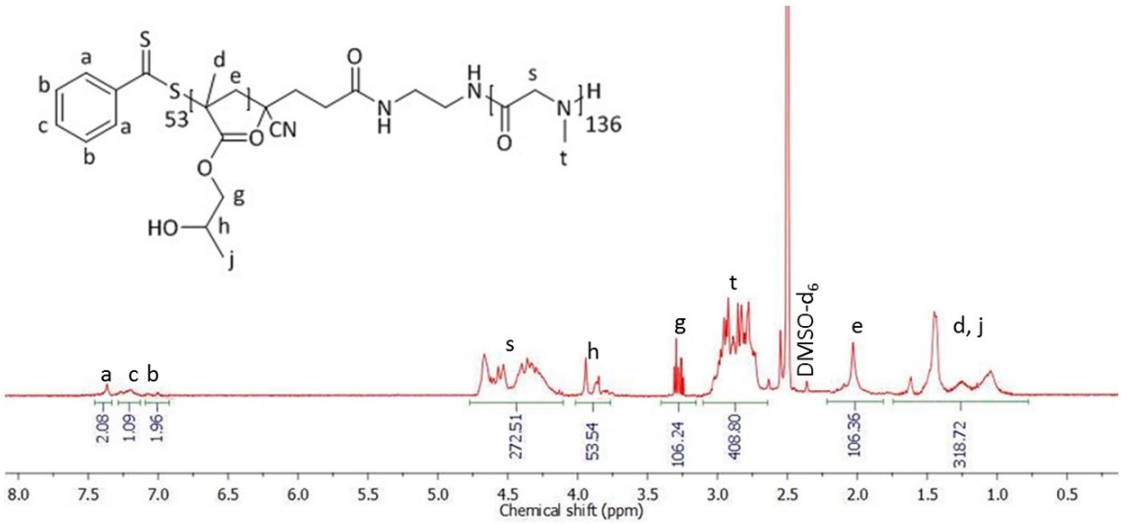

Figure 3. 14. The 400 MHz ^{1}H-NMR spectrum of dialysed $PSar_{136}$-*b*-$PHPMA_{53}$ in DMSO at 25 °C.

$PSar_{58}$-*b*-$PHPMA_{82}$: 0.163 g, 63.6 wt. % (orange/ pink solid). ^{1}H-NMR (400 MHz, DMSO-d_6, δ, ppm): 7.45 – 7.40 (d, 2H, Ar<u>H</u>), 7.25 – 7.20 (t, 1H, Ar<u>H</u>) 7.15 – 6.98 (t, 2H, Ar<u>H</u>), 4.48 – 3.72 (m, 198H, $(H_3CCCOOCH_2C\underline{H}OHCH_3CH_2)_{82}CCH_3CNCH_2CH_2CONHCH_2CH_2NH(COC\underline{H}_2NCH_3)_{58}H$), 3.34 – 3.08 (s, 164H, $(H_3CCCOOC\underline{H}_2CHOHCH_3CH_2)_{82}$), 3.06 – 2.59 (m, 174H, $(OCCH_2NC\underline{H}_3)_{58}H$), 2.23 – 1.84 (s, 164H, $(H_3CCCOOCH_2CHOHCH_3C\underline{H}_2)_{82}$), 1.25 – 0.45 (m, 492H, $(\underline{H}_3CCCOOCH_2CHOHC\underline{H}_3CH_2)_{82}$). FTIR: ν_{max}/cm^{-1} (solid): 3486 cm^{-1} (alcohol and secondary

amine), 2959 cm^{-1} (alkane C-H stretch), 2210 cm^{-1} (nitrile C≡N stretch), 1725 cm^{-1} (secondary amide C=O stretch), 1396 cm^{-1} (alkane C-H stretch) and 1156 cm^{-1} (amine C-N stretch).

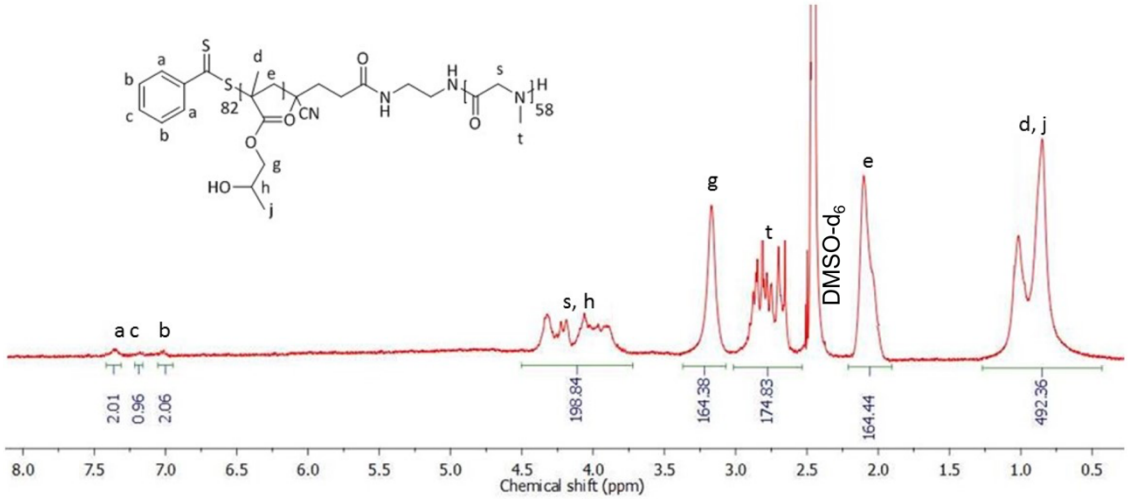

Figure 3. 15. The 400 MHz ^{1}H-NMR spectrum of dialysed $PSar_{58}$-*b*-$PHPMA_{82}$ in DMSO-d_6 at 25 °C.

$PSar_{78}$-*b*-$PHPMA_{130}$: 0.317 g, 65.8 wt. % (light pink solid). ^{1}H-NMR (400 MHz, DMSO-d_6, δ, ppm): 7.49 – 7.40 (d, 2H, ArH), 7.25 – 7.20 (t, 1H, ArH), 7.15 – 6.98 (t, 2H, ArH), 5.20 – 4.92 (m, 10H, $CH_2CH_2CONHCH_2CH_2NH$), 4.36 – 3.80 (m, 156H, $(OCCH_2NCH_3)_{78}H$), 3.40 – 3.08 (m, 260H, $(H_3CCCOOCH_2CHOHCH_3CH_2)_{130}$), 2.80 – 2.57 (m, 234H, $(OCCH_2NCH_3)_{78}H$), 2.41 – 1.80 (m, 260H, $(H_3CCCOOCH_2CHOHCH_3CH_2)_{130}$), 1.64 – 0.77 (m, 780H, $(H_3CCCOOCH_2CHOHCH_3CH_2)_{130}$). FTIR: ν_{max}/cm^{-1} (solid): 3536 cm^{-1} (alcohol and secondary amine), 2946 cm^{-1} (alkane C-H stretch), 2069 cm^{-1} (nitrile C≡N stretch), 1731 cm^{-1} (secondary amide C=O stretch), 1396 cm^{-1} (alkane C-H stretch) and 1189 cm^{-1} (amine C-N stretch).

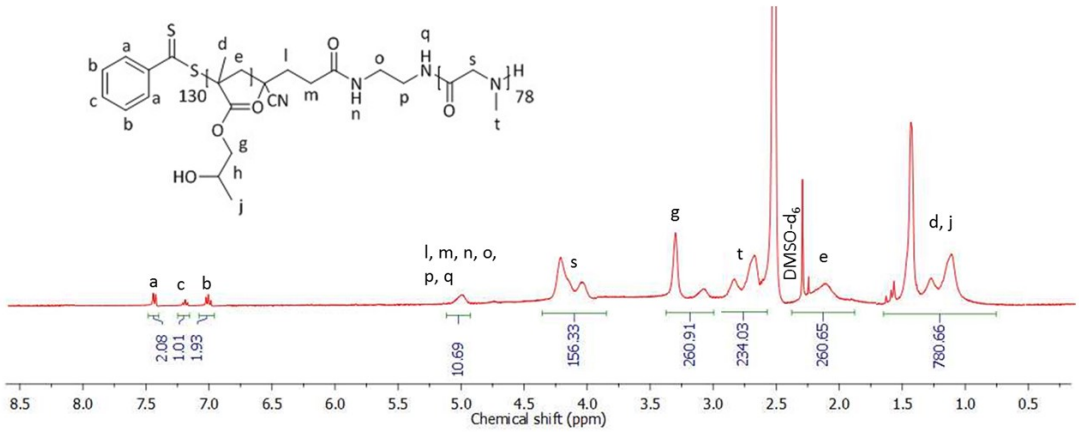

Figure 3. 16. The 400 MHz ^{1}H-NMR spectrum of dialysed $PSar_{78}$-*b*-$PHPMA_{130}$ in DMSO at 25 °C.

$PSar_{137}$-*b*-$PHPMA_{273}$: 0.719 g, 68.7 wt. % (orange/ pink crystalline solid). ^{1}H-NMR (400 MHz, DMSO-d_6, δ, ppm): 7.41 – 7.39 (m, 2H, Ar<u>H</u>),), 7.30 – 7.24 (t, 1H, Ar<u>H</u>), 7.20 – 7.10 (t, 2H, Ar<u>H</u>), 5.08 – 4.83 (s, 10H, $C\underline{H}_2C\underline{H}_2CON\underline{H}C\underline{H}_2C\underline{H}_2N\underline{H}$), 4.78 – 4.17 (m, 274H, $(OCC\underline{H}_2NCH_3)_{137}H$), 3.97 – 3.53 (m, 273H, $(H_3CCCOOCH_2C\underline{H}OHCH_3CH_2)_{273}$), 3.46 – 2.64 (m, 954H, $(H_3CCCOOC\underline{H}_2CHOHCH_3CH_2)_{273}CCH_3CNCH_2CH_2CONHCH_2CH_2NH(COCH_2NC\underline{H}_3)_{137}H$), 2.36 – 1.58 (m, 546H, $(H_3CCCOOCH_2CHOHCH_3C\underline{H}_2)_{273}$), 1.51 – 0.25 (m, 1638H, $(\underline{H}_3CCCOOCH_2CHOHC\underline{H}_3CH_2)_{273}$). FTIR: ν_{max}/cm^{-1} (solid): 3543 cm^{-1} (alcohol and secondary amine), 2972 cm^{-1} (alkane C-H stretch), 2164 cm^{-1} (nitrile C≡N stretch), 1718 cm^{-1} (secondary amide C=O stretch), 1396 cm^{-1} (alkane C-H stretch) and 1146 cm^{-1} (amine C-N stretch).

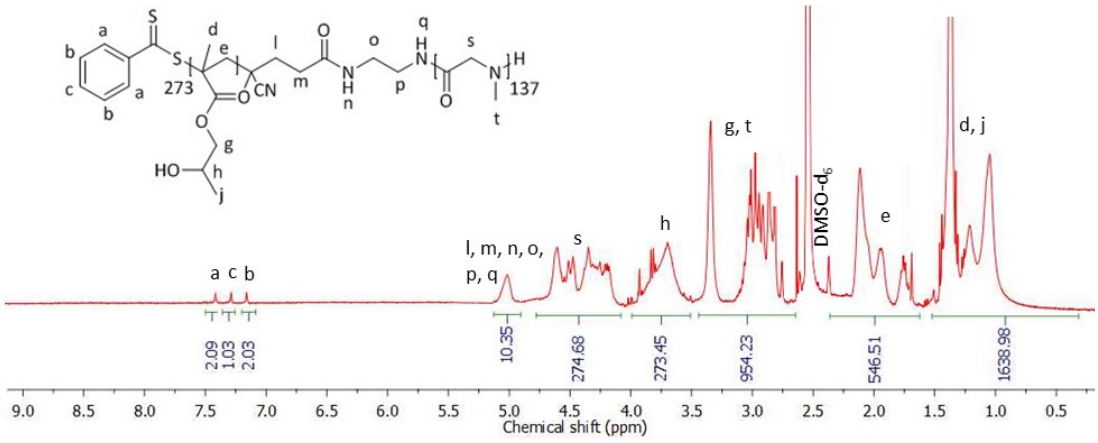

Figure 3. 17. The 400 MHz ^{1}H-NMR spectrum of dialysed $PSar_{137}$-*b*-$PHPMA_{273}$ in DMSO at 25 °C.

$PSar_{136}$- *b*-$PHPMA_{14}$: 0.071 g, 62.2 wt. % (pale pink solid). ^{1}H-NMR (400 MHz, DMSO-d_6, δ, ppm): 7.45 – 7.40 (d, 2H, Ar<u>H</u>), 7.25 – 7.20 (t, 1H, Ar<u>H</u>), 7.15 – 6.98 (t, 2H, Ar<u>H</u>), 4.73 – 4.10 (m, 272H, $(OCC\underline{H}_2NCH_3)_{136}H$), 4.00 – 3.81 (m, 14H, $(H_3CCCOOCH_2C\underline{H}OHCH_3CH_2)_{14}$), 3.82 – 3.22 (m, 28H, $(H_3CCCOOC\underline{H}_2CHOHCH_3CH_2)_{14}$), 3.21 – 2.74 (m, 408H, $(H_3CCCOOC\underline{H}_2CHOHCH_3CH_2)_{14}CCH_3CNCH_2CH_2CONHCH_2CH_2NH(COCH_2NC\underline{H}_3)_{136}H$), 2.19 – 2.00 (s, 28H, $(H_3CCCOOCH_2CHOHCH_3C\underline{H}_2)_{14}$), 1.41 – 1.05 (m, 84H, $(\underline{H}_3CCCONHCH_2CHOHC\underline{H}_3CH_2)_{14}$). FTIR: ν_{max}/cm^{-1} (solid): 3479 cm^{-1} (alcohol and secondary amine), 2931 cm^{-1} (alkane C-H stretch), 2034 cm^{-1} (nitrile C≡N stretch), 1721 cm^{-1} and 1646 cm^{-1} (secondary amide C=O stretch), 1396 cm^{-1} (alkane C-H stretch) and 1098 cm^{-1} (amine C-N stretch).

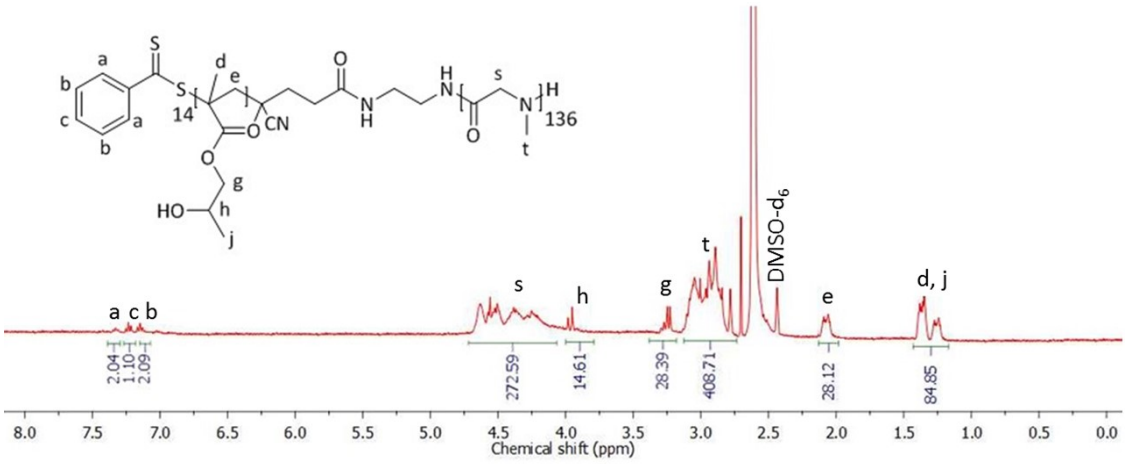

Figure 3. 18. The 400 MHz ^{1}H-NMR spectrum of dialysed $PSar_{136}$-*b*-$PHPMA_{14}$ in DMSO at 25 °C.

$PSar_{136}$- *b*-$PHPMA_5$: 0.028 g, (pale pink solid). ^{1}H-NMR (400 MHz, DMSO-d_6, δ, ppm): 7.68 – 7.32 (d, 2H, Ar<u>H</u>), 7.31 – 7.20 (t, 1H, Ar<u>H</u>), 7.19 – 6.79 (t, 2H, Ar<u>H</u>), 4.72 – 4.13 (m, 272H, $(OCC\underline{H}_2NCH_3)_{136}H$), 4.11 – 3.78 (m, 5H, $(H_3CCCOOCH_2C\underline{H}OHCH_3CH_2)_5$), 3.30 – 2.77 (m, 418H, $(H_3CCCOOC\underline{H}_2CHOHCH_3CH_2)_5CCH_3CNCH_2CH_2CONHCH_2CH_2NH(COCH_2NC\underline{H}_3)_{136}H$), 2.23 – 2.02 (s, 10H, $(H_3CCCOOCH_2CHOHCH_3C\underline{H}_2)_5$), 1.41 – 1.05 (m, 30H, $(\underline{H}_3CCCONHCH_2CHOHC\underline{H}_3CH_2)_5$). FTIR: ν_{max}/cm^{-1} (solid): 3475 cm^{-1} (alcohol and secondary amine), 2932 cm^{-1} (alkane C-H stretch), 2203 cm^{-1} (nitrile C≡N stretch), 1641 cm^{-1} (secondary amide C=O stretch), 1396 cm^{-1} (alkane C-H stretch) and 1098 cm^{-1} (amine C-N stretch).

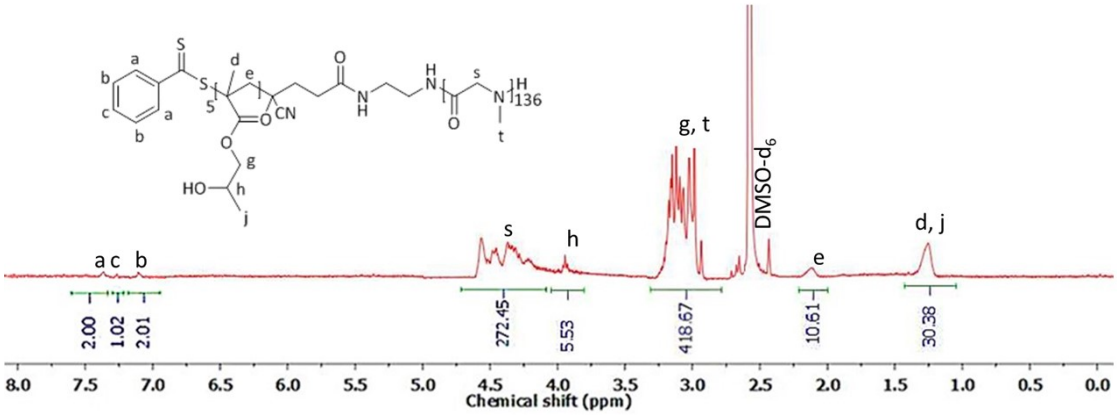

Figure 3. 19. The 400 MHz ^{1}H-NMR spectrum of dialysed $PSar_{136}$-*b*-$PHPMA_5$ in DMSO at 25 °C.

$PSar_{136}$- *b*-$PHPMA_{21}$: 0.031 g, (pale pink solid). ^{1}H-NMR (400 MHz, DMSO-d_6, δ, ppm): 7.45 – 7.40 (d, 2H, Ar<u>H</u>), 7.25 – 7.20 (t, 1H, Ar<u>H</u>), 7.15 – 6.98 (t, 2H, Ar<u>H</u>), 4.73 – 4.10 (m, 272H, $(OCC\underline{H}_2NCH_3)_{136}H$), 4.00 – 3.77 (m, 21H, $(H_3CCCOOCH_2C\underline{H}OHCH_3CH_2)_{21}$), 3.36 – 2.79 (m, 450H,

($H_3CCCOOC\underline{H}_2CHOHCH_3CH_2)_{21}CCH_3CNCH_2CH_2CONHCH_2CH_2NH(COCH_2NC\underline{H}_3)_{136}H$), 2.20 – 1.85 (s, 42H, ($H_3CCCOOCH_2CHOHCH_3C\underline{H}_2)_{21}$), 1.49 – 1.14 (m, 126H, ($\underline{H}_3CCCONHCH_2CHOHC\underline{H}_3CH_2)_{21}$). FTIR: ν_{max}/cm^{-1} (solid): 3489 cm^{-1} (alcohol and secondary amine), 2932 cm^{-1} (alkane C-H stretch), 2010 cm^{-1} (nitrile C≡N stretch), 1721 cm^{-1} and 1646 cm^{-1} (secondary amide C=O stretch), 1396 cm^{-1} (alkane C-H stretch) and 1098 cm^{-1} (amine C-N stretch).

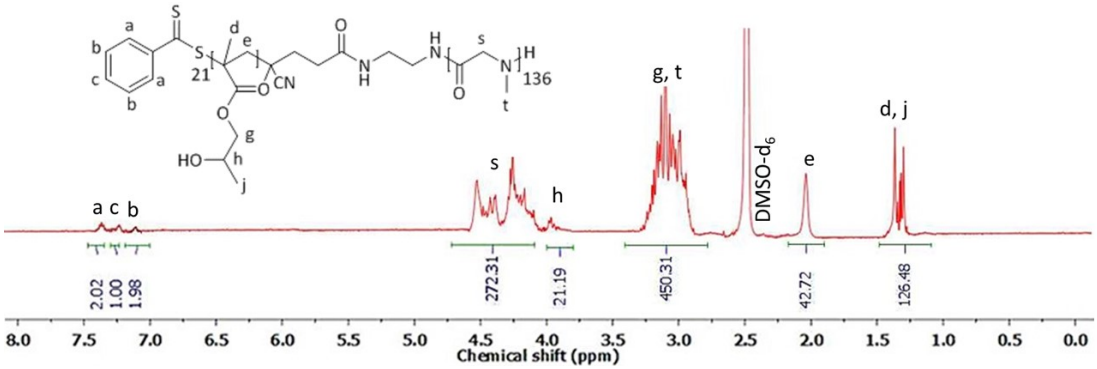

Figure 3. 20. The 400 MHz ^{1}H-NMR spectrum of dialysed $PSar_{136}$-*b*-$PHPMA_{21}$ in DMSO at 25 °C.

3.2.6 Cytotoxicity assays

All cell lines were originally purchased from the European collection of authenticated cell cultures (ECACC) and tested negative for mycoplasma. All cell lines were short tandem repeat (STR) profiled to confirm their identity. Cell lines were grown in dulbecco's modified eagle medium (DMEM) (Invitrogen) supplemented with 10 % fetal bovine serum (FCS) (Sigma). 5000 cells (MCF-7) or 10,000 cells (MDA-MB-231 and MDA-MB-453) were plated per well in a 96 well plate. After 24 hours serial dilutions of nanoparticle containing Dox or equivalent polymer was added to the wells in quadruplicate. The 96 well plates were either placed at 37 °C or at 41 °C (sealed in a zip lock bag and placed in a water bath) for 51 minutes. A thermometer was used to verify that 11 minutes was required for 100 µL volume of media to reach 41 °C. 40 minutes was allowed for the release of Dox from the polymer. Following this, all plates were placed in a humidified incubator at 37 °C, 5 % CO_2 for a further 72 hours. 3-(4,5-Dimethylthiazol-2-yl)-2,5-diphenyl tetrazolium bromide (MTT) was then added to each well (at a final concentration of 0.5 mg mL^{-1}) and the cells incubated for 3 hours before the removal of the media. The formazan crystals were dissolved in 150 µL of DMSO and the absorbance

was read on a plate-reader at 620 nm. The experiment was repeated 3 times in total and the results were fitted with a four-parameter log inhibition curve using GraphPad Prism version 5 to generate a half maximal inhibitory concentration (IC_{50}).

3.3 Results and discussion

Sarcosine NCA was synthesised initially, polymerisation of sarcosine NCA from *N*-Boc-ethylenediamine was then done followed by Boc cleavage in TFA. Then the amine-bearing PSar was conjugated to a RAFT agent. HPMA monomer was introduced and polymerised from the PSar-macro-RAFT agent. As the degree of polymerisation of the second chain (PHPMA) increased, the diblock copolymer ($PSar_x$-*b*-$PHPMA_y$) cannot molecularly dissolve in solvent, resulting in nanoparticle formation (PISA). Various chain lengths of PSar (58, 78, 136 and 137) and PHPMA (5, 14, 21, 53, 82, 130 and 273) were synthesised in order to produce nanoparticles of varied dimensions. Due to thermoresponsive property of PHPMA, Dox can be released from $PSar_x$-*b*-$PHPMA_y$ nanoparticles at 41 °C.

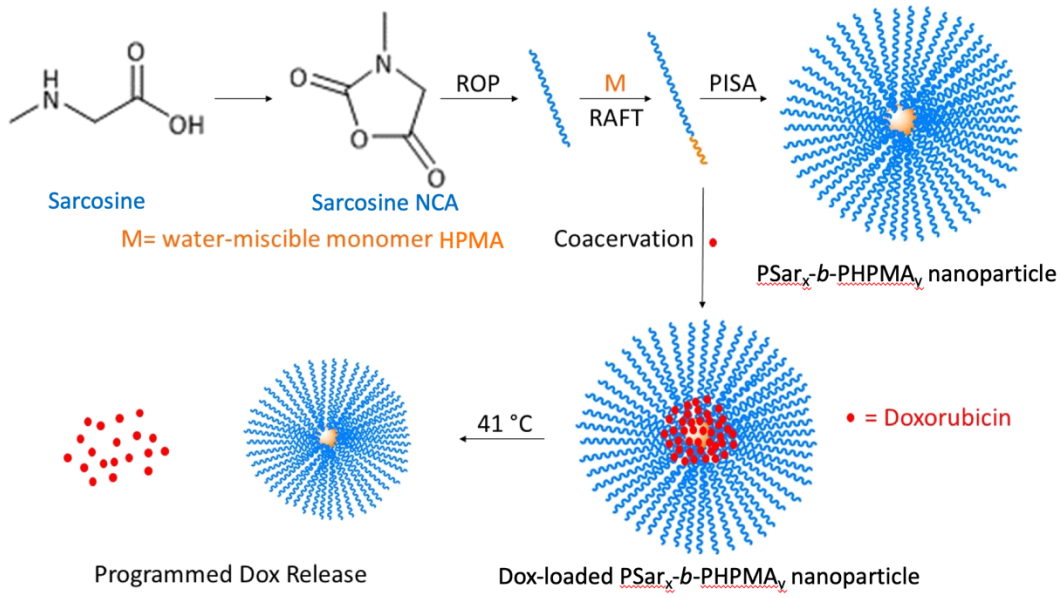

Scheme 3. 1. Reaction outline of the creation of thermoresponsive $PSar_x$-*b*-$PHPMA_y$ nanoparticles that facilitate Dox release at 41 °C in PBS buffer solution.

Sarcosine NCA was synthesised from sarcosine, triphosgene, α-pinene in anhydrous THF (Scheme 3.2 a). *N*-Boc-ethylenediamine was selected as a dual initiator for NCA ROP, and

upon Boc group cleavage, RAFT polymerisation. The primary amine presented by the initiator enables the ROP of sarcosine NCA, yielding Boc group protected PSar (Scheme 3.2 b). Boc cleavage was achieved using TFA (Scheme 3.2 c), yielding a range of homopolymers that contained PSar with chain lengths of 58, 78, 136 and 137 repeat units. The primary amine group liberated was used for RAFT agent SCPDB conjugation (Scheme 3.2 d), before HPMA polymerisation was conducted in an ethanol/water mixture to yield a range of block copolymers (Scheme 3.2 e).

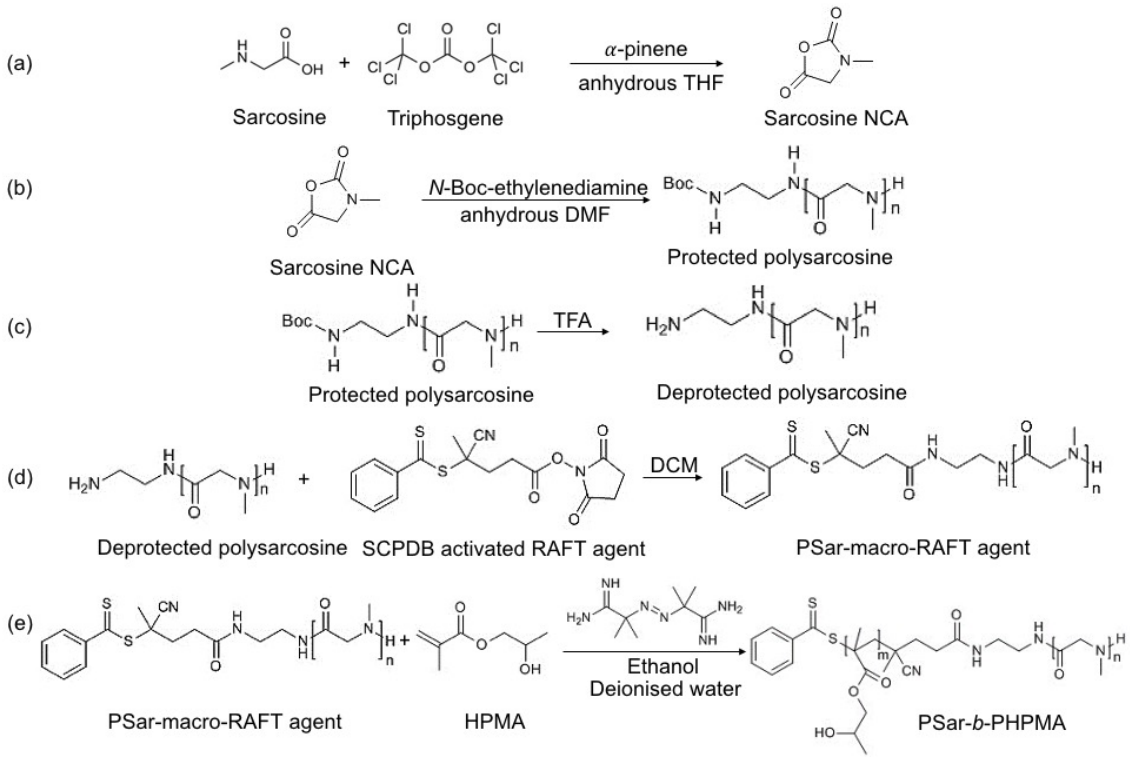

Scheme 3. 2. The synthetic route to PSar-*b*-PHPMA. (a) The synthesis of sarcosine NCA. (b) The synthesis of Boc protected PSar. (c) Boc group cleavage to provide primary amine functionality to PSar. (d) RAFT agent conjugation to PSar. (e) RAFT polymerisation of HPMA from PSar.

Synthesis of sarcosine NCA

^{1}H NMR revealed that the integrations of a and b environments matched to the number of hydrogen atoms, which were 3 and 2, respectively (Figure 3.1). In the FTIR analysis, tertiary amine N-H (3227 cm^{-1}), alkyl C-H (2948 cm^{-1}) and anhydride (1846 cm^{-1} and 1757 cm^{-1}) were shown in the FTIR spectrum of sarcosine NCA (Figure 3.21). Therefore, sarcosine NCA was synthesised successfully.

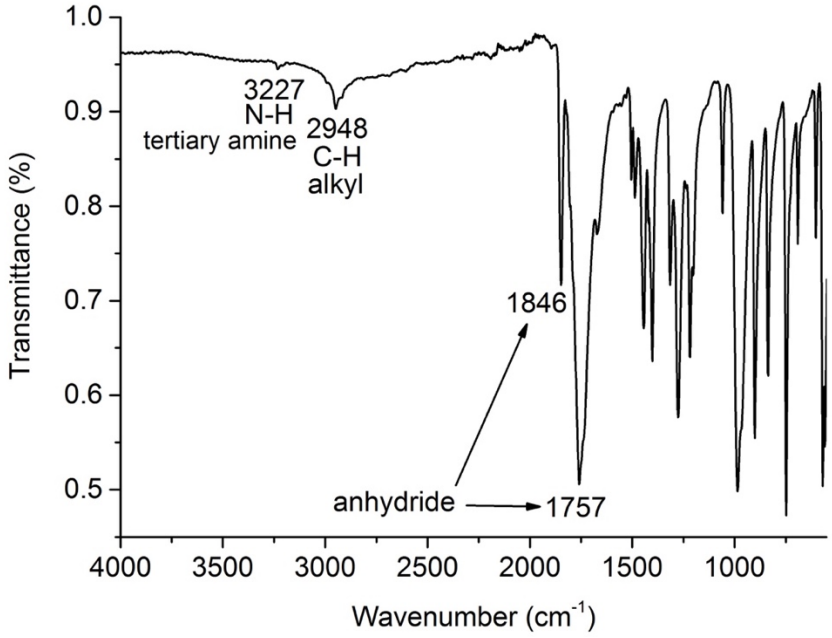

Figure 3. 21. FTIR spectrum of sarcosine NCA.

Synthesis of Boc protected PSar, PSar-marco-RAFT agent and PSar-*b*-PHPMA

PSar was then created from sarcosine NCA, using *N*-Boc-ethylenediamine as the initiator. The chain lengths of PSar can be calculated by ^{1}H NMR by comparing the integral of the peak that was representative of the proton environment a in the Boc protecting group with either proton environment present in the sarcosine repeat unit. The number of sarcosine repeat units were 58 (Figure 3.3), 78 (Figure 3.4), 137 (Figure 3.5) and 136 (Figure 3.2). Boc cleavage was done to provide a primary amine group to the PSar formed. This group may be then exploited for RAFT agent conjugation. Boc deprotection was successful as no peaks were present in the product ^{1}H NMR at around 1.38 ppm. Moreover, TFA did not hydrolyse PSar since the integrals of the environments b and f still proved that the chain length of PSar remained 58 (Figure 3.7), 78 (Figure 3.8), 137 (Figure 3.9) and 136 (Figure 3.6). Therefore, the Boc protecting group was removed completely. In the ^{1}H NMR spectra of deprotected $PSar_{58}$ (Figure 3.7), deprotected $PSar_{78}$ (Figure 3.8), deprotected $PSar_{137}$ (Figure 3.9) and deprotected $PSar_{136}$ (Figure 3.6), the integrations of environments b and f also matched the number of hydrogen atoms, 116 and 174; 156 and 234; 274 and 411; 272 and 408, respectively. RAFT agent conjugation to the polymer was verified by ^{1}H NMR, which revealed three peaks in the spectrum between 7.50 ppm to 7.00 ppm in a 2:1:2 ratio representative of the RAFT agent aromatic group, which

signifies successful conjugation to the deprotected PSar (Figures 3.10-3.13). Moreover, environments k and l can be seen in the ^{1}H NMR spectra and the integrals were the same as the number of hydrogen atoms of the desired $PSar_{58}$-macro-RAFT agent (Figure 3.11), $PSar_{78}$-macro-RAFT agent (Figure 3.12), $PSar_{137}$-macro-RAFT agent (Figure 3.13) and $PSar_{136}$-macro-RAFT agent (Figure 3.10) signifying the complete capping of the formerly deprotected polymer with the RAFT agent. HPMA was then polymerised from the RAFT agent-conjugated $PSar_{58}$. The chain lengths of HPMA can be calculated from the integrations of g, e, d and j environments which were 164, 164 and 492, respectively (Figure 3.15). The integrations of proton environments a, c and b were in a 2:1:2 ratio and there were 174 hydrogen atoms presented in the t environment. The peaks from the proton environments s and h merged together and the integration was 198. From this data, it can be concluded that 82 HPMA repeat units were conjugated, on average, per $PSar_{58}$-macro-raft agent macromolecule. The ^{1}H NMR spectra of $PSar_{78}$-*b*-$PHPMA_{130}$ (Figure 3.16), $PSar_{137}$-*b*-$PHPMA_{273}$ (Figure 3.17), $PSar_{136}$-*b*-$PHPMA_{5}$ (Figure 3.19), $PSar_{136}$-*b*-$PHPMA_{21}$ (Figure 3.20), $PSar_{136}$-*b*-$PHPMA_{14}$ (Figure 3.18) and $PSar_{136}$-*b*-$PHPMA_{53}$ (Figure 3.14) were also analysed, using integrals of the proton environments to measure the chain lengths of PSar and PHPMA of each diblock copolymer.

Progress towards the desired block copolymers was monitored by FTIR (Figure 3.22 and Figures A3.1-A3.4). FTIR spectra of Boc protected $PSar_{58}$, deprotected $PSar_{58}$, $PSar_{58}$-marco-RAFT agent, $PSar_{58}$-*b*-$PHPMA_{82}$, Boc protected $PSar_{78}$, deprotected $PSar_{78}$, $PSar_{78}$-marco-RAFT agent, $PSar_{78}$-*b*-$PHPMA_{130}$, Boc protected $PSar_{137}$, deprotected $PSar_{137}$, $PSar_{137}$-marco-RAFT agent, $PSar_{137}$-*b*-$PHPMA_{273}$, Boc protected $PSar_{136}$, deprotected $PSar_{136}$, $PSar_{136}$-marco-RAFT agent, $PSar_{136}$-*b*-$PHPMA_{5}$, $PSar_{136}$-*b*-$PHPMA_{21}$, $PSar_{136}$-*b*-$PHPMA_{14}$ and $PSar_{136}$-*b*-$PHPMA_{53}$ were shown in Figure 3.22 and Figures A3.1-A3.4. The secondary amide peak (1734 cm^{-1} and 1641 cm^{-1}) corresponding to PSar presented throughout the synthesis (Figure 3.22 and Figures A3.1-A3.4), but the ester peak attributed to the presence of the Boc protecting group (1227 cm^{-1}) disappeared as expected upon Boc group cleavage (Figure 3.22 red and Figures A3.1-A3.3 red). The grafting of the RAFT agent to PSar resulted in the emergence of peaks representative of aromatic groups in the 900 cm^{-1} to 500 cm^{-1} region (Figure 3.22 blue and Figures A3.1-A3.3 blue). The peak corresponding to the nitrile functional group was visible, however,

this peak was very weak since there was designed to be only a single nitrile group per polymer chain (Figure 3.22 blue and pink, Figures A3.1-A3.3 blue and pink, and Figure A3.4). The FTIR spectrum of the final product, revealed the presence of the alcohol functional group (3486 cm $^{-1}$, merged with secondary amine) (Figure 3.22 pink, Figures A3.1-A3.3 pink and Figure A3.4).

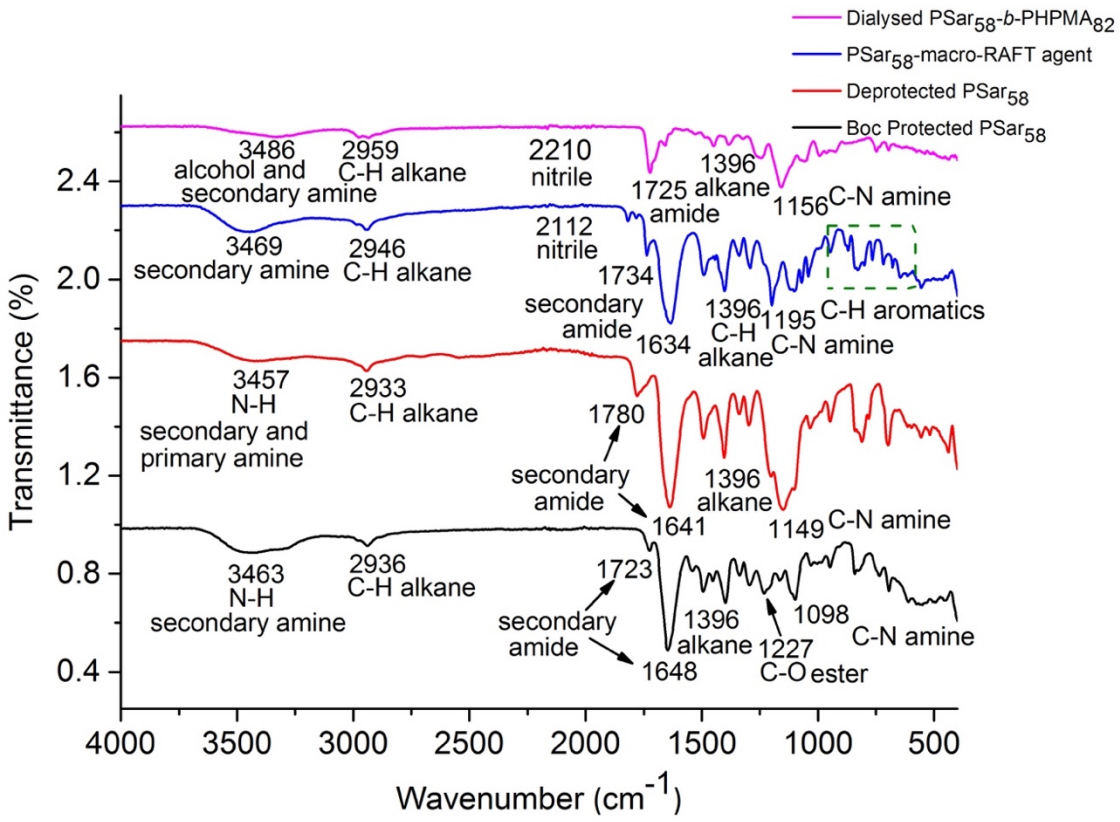

Figure 3. 22. FTIR spectra of Boc-PSar$_{58}$, deprotected PSar$_{58}$, PSar$_{58}$-macro-RAFT agent and dialysed PSar$_{58}$-*b*-PHPMA$_{82}$.

During each polymerisation, nanoparticle formation was tracked by DLS using intensity size analysis. For intensity size distribution, size analysis is determined by the intensity of light scattered by the nanoparticles. The volume and number size distribution can be determined from the intensity distribution using Mie theory, size analysis can be calculated from the intensity analysis of inputting the correct refractive index and absorption for the polymer nanoparticle. Refractive index and absorption of PSar-*b*-PHPMA cannot be found in literature. Therefore, the refractive index and absorption of PSar were used which were 1.503 and 0.100, respectively [41]. The volume and number size analysis need accurate refractive index and absorption of the sample but intensity

size analysis depends on light scattering of the sample. Therefore, intensity size analysis of the sample is more reliable. Initially, two block copolymers ($PSar_{58}$-*b*-$PHPMA_{82}$ and $PSar_{137}$-*b*-$PHPMA_{273}$, where the number of repeat units represent complete monomer conversion to the final polymer after four hours polymerisation) were synthesised and examined (Table 3.1, DLS data presented in Figures 3.23-3.24).

Table 3. 1. Nanoparticle size and PDI values for nanoparticles formed *in situ*.

Duration	$PSar_{58}$-*b*-$PHPMA_{82}$ (nm)	PDI	$PSar_{137}$-*b*-$PHPMA_{273}$ (nm)	PDI
1 h	393 ± 14	0.409	129 ± 23	0.326
2 h	544 ± 17	0.626	226 ± 18	0.345
3 h	554± 11	0.174	365± 27	0.306
4 h	488± 21	0.481	325 ± 30	0.331

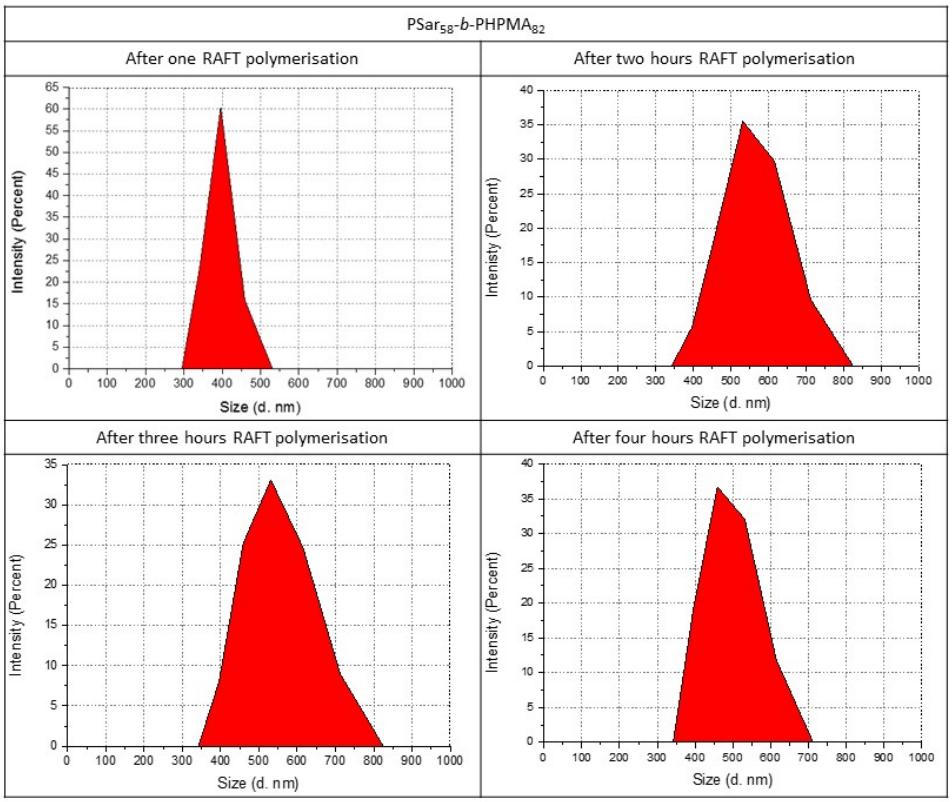

Figure 3. 23. DLS distribution of $PSar_{58}$-*b*-$PHPMA_{82}$ during four hours of polymerisation.

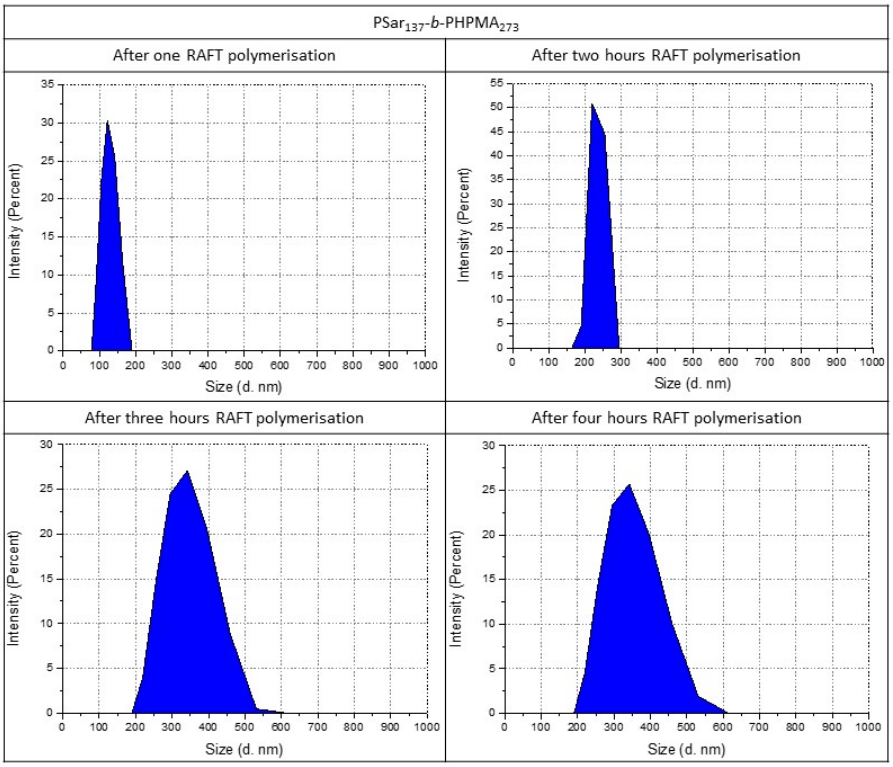

Figure 3. 24. DLS distribution of $PSar_{137}$-*b*-$PHPMA_{273}$ during four hours of polymerisation.

Nanoparticle size increased with time following a non-linear relationship, suggesting nanoparticle growth was mostly complete after approximately three hours. In addition, the particles became excessively large, with the exception of $PSar_{137}$-*b*-$PHPMA_{273}$ when polymerised for up to two hours. Consequently, it was decided that SCPDB conjugated to PSar (137 repeat units) is a suitable macroinitiator for HPMA polymerisation, but the extent of HPMA polymerisation must be limited to yield desirable particles of less than 200 nm hydrodynamic diameter. The correlogram of $PSar_{137}$-*b*-$PHPMA_{273}$ after one hour polymerisation is shown in Figure 3.25. The particle size of $PSar_{137}$-*b*-$PHPMA_{273}$ after one hour polymerisation was (129±23) nm, therefore, the small (light) the nanoparticles, the fast they were, so the correlogram decayed quick (steep gradient).

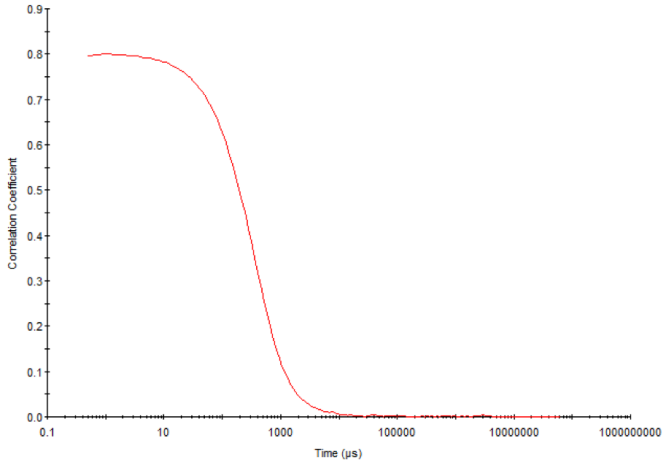

Figure 3. 25. Correlogram of $PSar_{137}$-*b*-$PHPMA_{273}$ after one hour polymerisation.

A third block copolymer, $PSar_{78}$-*b*-$PHPMA_{130}$ after four hours polymerisation, was also produced and exhibited *in situ* particle formation during HPMA polymerisation (Table 3.2, DLS data presented in Figure 3.26). However, this polymer was not progressed due to relatively large hydrodynamic diameters/PDI values obtained for the particles formed. PDI equals 0.3 (specific to the polymer nanoparticles in this thesis) is the limit before the intensity size distribution (peak) splits into two. This was found by a previous PhD student (Dr. Mthulisi Khuphe). The PDI limit depends on the specific sample analysed.

Table 3. 2. Nanoparticle size and PDI values for nanoparticles formed during the polymerisation that yield $PSar_{78}$-*b*-$PHPMA_{130}$.

Duration	$PSar_{78}$-*b*-$PHPMA_{130}$ (nm)	PDI
1 h	191 ± 26	0.431
2 h	233 ± 31	0.456
3 h	257 ± 13	0.510
4 h	297 ± 24	0.313

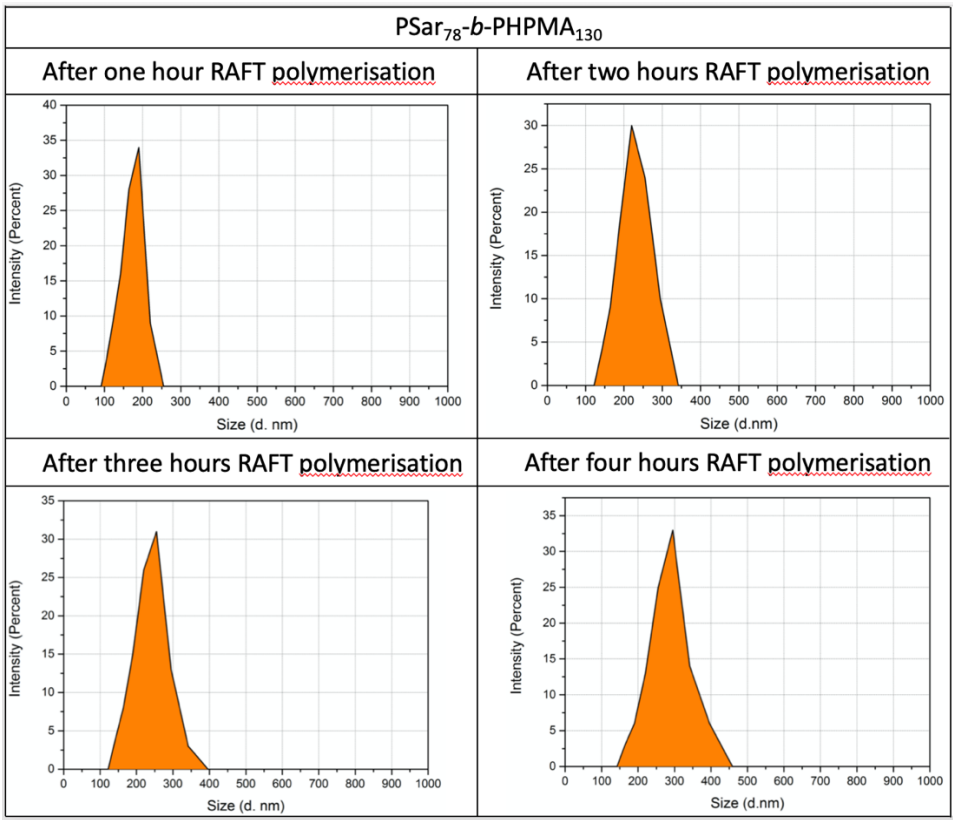

Figure 3. 26. DLS distribution of $PSar_{78}$-*b*-$PHPMA_{130}$ during four hours of polymerisation.

Studies were undertaken whereby two target polymers, $PSar_{136}$-*b*-$PHPMA_{53}$ and $PSar_{136}$-*b*-$PHPMA_{14}$, were produced over a 4-hour period, with polymer being isolated from the reaction vessel every hour. Polymer self-assembly by coacervation was undertaken and the nanoparticles formed analysed by DLS. Whilst $PSar_{136}$ was unable to self-assemble to form nanoparticles in aqueous solution, SCPDB conjugation to $PSar_{136}$ resulted in the formation of nanoparticles with a mean diameter of 114 nm and a PDI value of 0.454. Subsequent HPMA polymerisation from the macroinitiator resulted in the creation of nanoparticles of increased diameter (Table 3.3, DLS data presented in Figures A3.5-A3.6). Nanoparticle stability, in terms of both size and dispersity, was provided in Table 3.4 (DLS data presented in Figure A3.7). The dimensions of many of the nanoparticle samples formed rendered many suitable candidates for use as potential drug delivery vehicles. Nanoparticles isolated from $PSar_{136}$-*b*-$PHPMA_{14}$ and $PSar_{136}$-*b*-$PHPMA_{53}$ polymerisations after two hours were deemed the most appropriate to be advanced to Dox release studies. After two hours, the average particle size of $PSar_{136}$-*b*-$PHPMA_{14}$ and $PSar_{136}$-*b*-$PHPMA_{53}$ were (151 ± 22) nm and 178 ± 25) nm, respectively, which can potentially be used as drug delivery vehicles in human body [42]. The structures of these polymers were

found to be $PSar_{136}$-*b*-$PHPMA_5$ and $PSar_{136}$-*b*-$PHPMA_{21}$, respectively, as determined by ^1H NMR spectroscopy (Figures 3.19-3.20). The molecular weights and dispersity values of the polymers were found to be 11600 g mol^{-1} and 1.26, respectively, for $PSar_{136}$-*b*-$PHPMA_5$ (Figure A3.8), and 14000 g mol^{-1} and 1.07, respectively, for $PSar_{136}$-*b*-$PHPMA_{21}$ (Figure A3.9), as determined by GPC.

Table 3. 3. Nanoparticle size and PDI values for nanoparticles formed from $PSar_{136}$-*b*-$PHPMA_{14}$ and $PSar_{136}$-*b*-$PHPMA_{53}$ following polymer coacervation.

Duration	$PSar_{136}$-*b*-$PHPMA_{14}$ (nm)	PDI	$PSar_{136}$-*b*-$PHPMA_{53}$ (nm)	PDI
1 h	144 ± 35	0.176	149 ± 41	0.129
2 h	151 ± 22	0.559	178 ± 25	0.147
3 h	247 ± 31	0.336	195 ± 32	0.058
4 h	315 ± 38	0.121	272 ± 15	0.007

Table 3. 4. A comparison of stability of the nanoparticles formed upon polymer precipitation at hourly intervals during the synthesis of $PSar_{136}$-*b*-$PHPMA_{14}$ and $PSar_{136}$-*b*-$PHPMA_{53}$.

$PSar_{136}$-*b*-$PHPMA_{14}$	After 24 hours (nm)	PDI	After 14 days (nm)	PDI	After 21 days (nm)	PDI
1 h	187 ± 18	0.289	160 ± 15	0.304	178 ± 18	0.197
2 h	207 ± 21	0.152	135 ± 13	0.288	156 ± 23	0.215
3 h	234 ± 26	0.212	171 ± 20	0.204	195 ± 30	0.158
4 h	284 ± 15	0.081	271 ± 27	0.076	293 ± 27	0.191
$PSar_{136}$-*b*-$PHPMA_{53}$	After 24 hours (nm)	PDI	After 14 days (nm)	PDI	After 21 days (nm)	PDI
1 h	154 ± 33	0.166	151 ± 25	0.168	159 ± 24	0.175
2 h	197 ± 13	0.258	140 ± 23	0.184	148 ± 31	0.282
3 h	148 ± 15	0.206	169 ± 28	0.205	163 ± 33	0.220
4 h	288 ± 12	0.080	276 ± 21	0.082	288 ± 26	0.089

The particle size of $PSar_{136}$-*b*-$PHPMA_5$ nanoparticles at room temperature and at 50 °C for 24 hours, and Dox-loaded $PSar_{136}$-*b*-$PHPMA_5$ nanoparticles at 50 °C for 24 hours were measured by DLS (Figure 3.27). The particle size decreased from (166±14)nm to (136±16)nm as temperature increased from room temperature to 50 °C which may be

due thermoresponsive property of the PHPMA block. For Dox-loaded $PSar_{136}$-*b*-$PHPMA_5$ nanoparticles, a second small peak (34±9)nm appeared on the DLS spectrum that may be assigned to the released Dox aggregates or degradation of the nanoparticles. Dox has vinyl groups and aromatic rings which may produce π- π stacking interactions and cause aggregation.

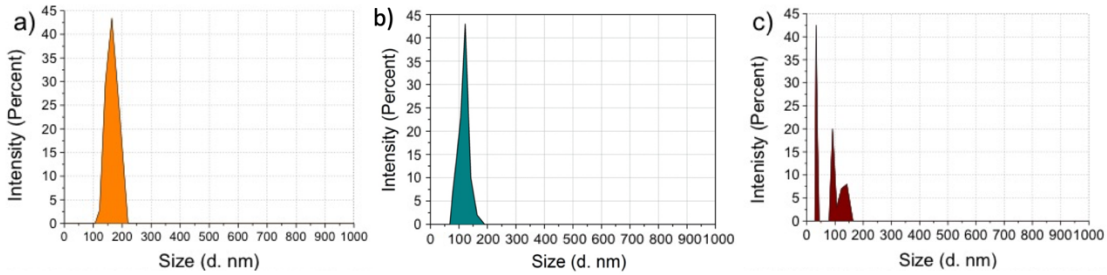

Figure 3. 27. Particle size determination of a) $PSar_{136}$-*b*-$PHPMA_5$ at room temperature, b) $PSar_{136}$-*b*-$PHPMA_5$ at 50 °C for 24 hours, c) Dox-loaded $PSar_{136}$-*b*-$PHPMA_5$ at 50 °C for 24 hours in deionised water, by DLS.

SEM analysis was conducted with Dr. David Green. SEM study revealed the formation of discrete nanoparticles from with and without Dox-loaded $PSar_{136}$-*b*-$PHPMA_5$, and $PSar_{136}$-*b*-$PHPMA_{21}$ copolymers (Figures 3.28 a,b -3.29 b). The change in the morphology of the nanoparticles that contained Dox could clearly be evidenced by SEM analysis, after heating the nanoparticles to 50 °C for 24 hours (Figure 3.28 b). Less spherical, more elongated, particles were observed by SEM analysis, further confirming that a thermally-induced nanoparticle morphological transition had occurred. There were three peaks on the particle size distribution of $PSar_{136}$-*b*-$PHPMA_5$ nanoparticles, the full width at half maximum (FWHM) were (37±9)nm, (37±4)nm and (25±9)nm, respectively, and the R^2 values was 0.92 (figure 3.28 c). The particle size (Figure 3.28 c) measured from statistical analysis of SEM image were (220±4)nm, (300±2)nm and (425±8)nm which was larger than that was analysed by DLS (166±14)nm. The SEM samples were prepared by air-drying method, some nanoparticles may be overlaid which may cause large particles on SEM images. There were two peaks on the particle size distribution of Dox-loaded $PSar_{136}$-*b*-$PHPMA_5$ nanoparticles heated at 50 °C for 24 hours, the FWHM values were (17±2)nm and (262±171)nm, and the R^2 value was 0.97 (Figure 2.28 d). The particle size (Figure 3.28 d) measured from statistical analysis of SEM image were (37±1)nm and (144±9)nm. The small particles (37±1)nm may be assigned to released Dox aggregates

or degradation of the nanoparticles.

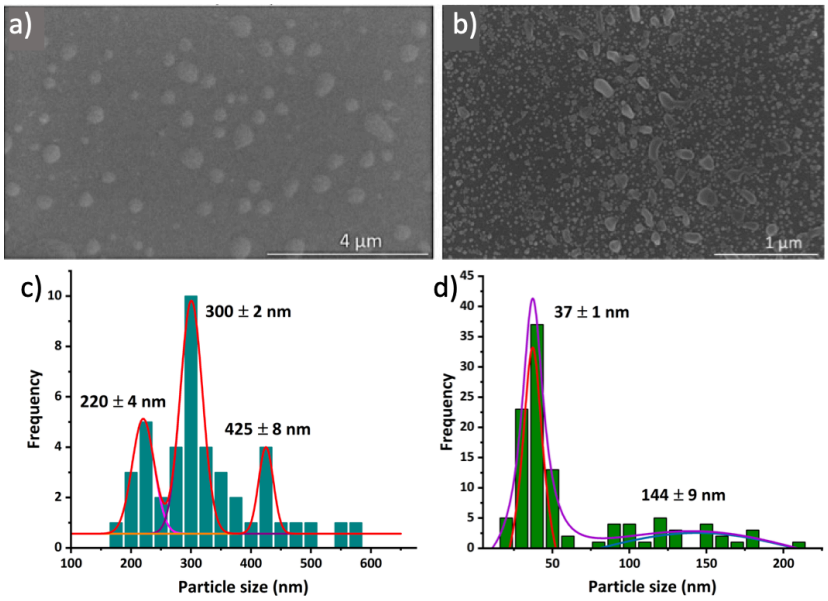

Figure 3. 28. a) SEM micrograph of $PSar_{136}$-b-$PHPMA_5$ nanoparticles at room temperature. Scale bar represents 4 µm. b) SEM image corresponding to Dox-loaded nanoparticles formed from $PSar_{136}$-b-$PHPMA_5$ that had been subjected to heating to 50 °C for 24 hours. Scale bar represents 1 µm. c) Statistical analysis of $PSar_{136}$-b-$PHPMA_5$ anoparticles determined by SEM image. d) Statistical analysis of Dox-loaded $PSar_{136}$-b-$PHPMA_5$ nanoparticles at 50 °C for 24 hours determined by SEM image.

The particle size of $PSar_{136}$-*b*-$PHPMA_{21}$ nanoparticles at room temperature measured by DLS was (239±21)nm (Figure 3.29 a) which was larger than the $PSar_{136}$-*b*-$PHPMA_5$ (166±14)nm. This may be caused by the chain length of PHPMA, the longer the PHPMA chains, the greater the particle size. Particle size determined by SEM microscopy (Figure 3.29 b) showed larger (336nm) and smaller (113nm) nanoparticles compared to the size measured by DLS (239±21)nm. The particle size distribution from the SEM image (Figure 3.29 b) cannot be fitted to acceptable quality, the R^2 value was 0.55 (smaller than 0.85). The greater particle size may be caused by overlaid nanoparticles during air-drying (sample preparation). The $PSar_{136}$-*b*-$PHPMA_{21}$ nanoparticles measured by DLS was in aqueous state, forming hydrogen bonding interactions between the polymer chains (hydroxyl group) and aqueous solution. The SEM samples were prepared by air-drying method, the hydrogen bonding interactions disappeared, which may lead to particle size decrease in SEM analysis.

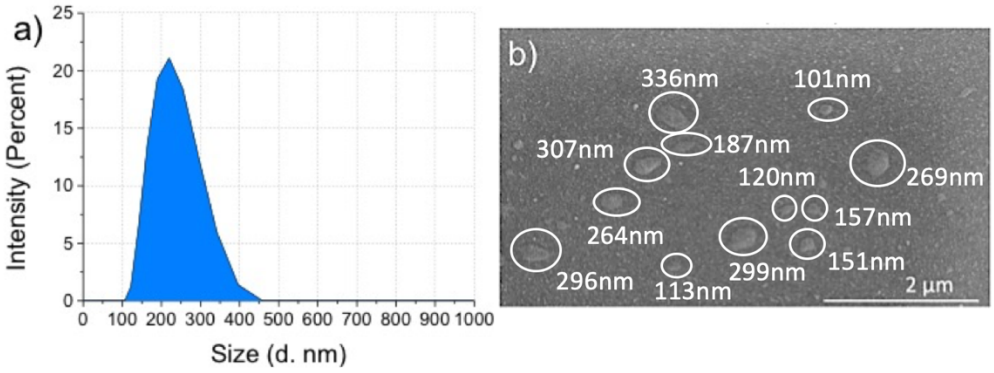

Figure 3. 29. a) Particle size determination and b) SEM image of $PSar_{136}$-*b*-$PHPMA_{21}$ nanoparticles at room temperature.

Energy dispersive X-ray analysis revealed the presence of sulfur only where particles were found, confirming the retention of the RAFT agent (contained sulfur element) and successful polymerisation (Figure 3.30). Carbon can found in both nanoparticles and background. Nanoparticles contained carbon. Sulfur wafer was used as the background which also contained carbon.

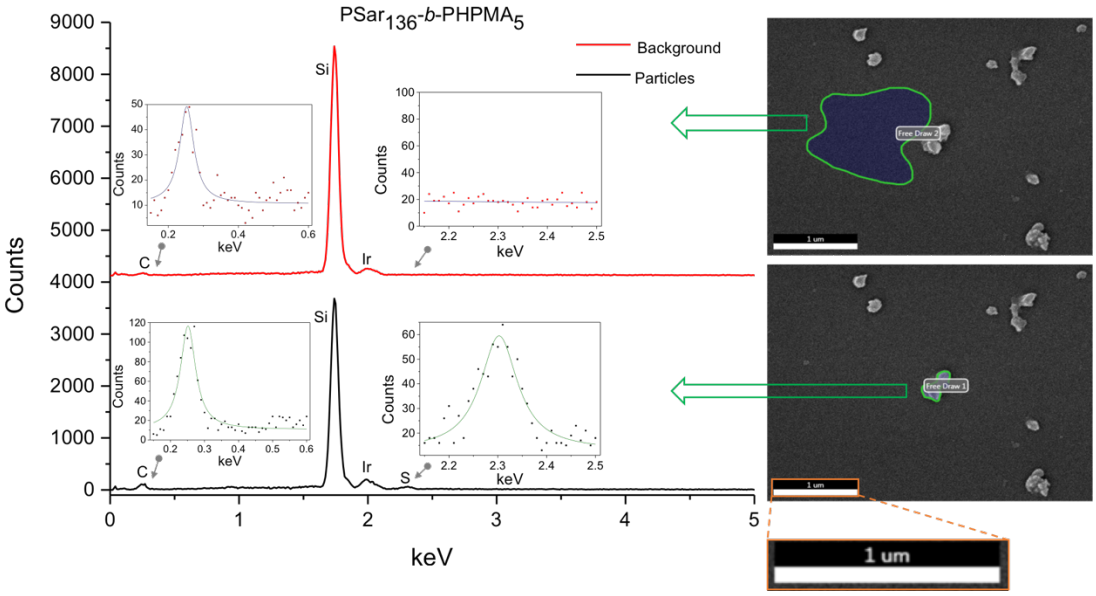

Figure 3. 30. Energy dispersive X-ray analysis of $PSar_{136}$-*b*-$PHPMA_5$ nanoparticles. Scale bar represents 1 µm.

Although the particles disclosed in this chapter may readily be applied as materials that enable the controlled release of a range of molecular cargoes, the loading, and release, of an anticancer drug (Dox) into/from the particles was selected for further evaluation.

The particles were deemed suitable candidates as drug delivery vehicles owing to their limited non-degradable polymer content, which was restricted to five repeat units on average per polymer chain in the case of $PSar_{136}$-*b*-$PHPMA_5$. Dox loading into polymer nanoparticles was achieved by 'dropping in' a solution of polymer dissolved in DMF to vigorously stirred PBS solution that contained Dox [43]. Approximately 97% of Dox was loaded in all conditions. 0.294 mg of Dox was loaded within 2 mg of $PSar_{136}$-*b*-$PHPMA_5$ particles in pH 7.4 solution, 0.291 mg of Dox was loaded within 2 mg of $PSar_{136}$-*b*-$PHPMA_5$ particles in pH 5 solution. 0.292 mg of Dox was loaded within 2 mg of $PSar_{136}$-*b*-$PHPMA_{21}$ particles in pH 7.4 solution and 0.289 mg Dox was loaded within 2 mg of $PSar_{136}$-*b*-$PHPMA_{21}$ particles in pH 5 solution. $PSar_{136}$-*b*-$PHPMA_5$ yielded Dox-loaded particles of 161 nm (PDI = 0.240) and $PSar_{136}$-*b*-$PHPMA_{21}$ yielded Dox-loaded particles of 159 nm (PDI = 0.264). The $PSar_{136}$-*b*-$PHPMA_5$ particles were found to be stable in PBS buffer at both 25 °C and 37 °C for at least 21 days (Tables 3.5-3.6, DLS data presented in Figure A3.10). However, in this instance the main peak did not change, but there was an appearance of a second smaller species. After 21 days, the species that possessed a hydrodynamic diameter of 31 nm was measured. The overall PDI of the sample was therefore relatively large (0.437), and indicated that Dox release may occur to a limited extent when $PSar_{136}$-*b*-$PHPMA_5$ particles were stored at 37 °C for extended periods or due to the nanoparticle degradation, further study of the species can be conducted, for instance x-ray photoelectron spectroscopy (XPS).

Table 3. 5. Hydrodynamic diameters of Dox-loaded $PSar_{136}$-*b*-$PHPMA_5$ nanoparticles maintained at 25 °C.

Time	Size (nm)	PDI
After 24 hours	161 ± 7	0.240
After 7 days	159 ± 5	0.264
After 14 days	167 ± 12	0.167
After 21 days	156 ± 8	0.189

Table 3. 6. Hydrodynamic diameters of Dox-loaded $PSar_{136}$-*b*-$PHPMA_5$ nanoparticles maintained at 37 °C.

Time	Size (nm)	PDI
After 24 hours	130 ± 5	0.389
After 7 days	128 ± 7 27 ± 2	0.316
After 14 days	125 ± 5 32 ± 4	0.338
After 21 days	129 ± 7 31 ± 2	0.437

Dox release from $PSar_{136}$-*b*-$PHPMA_5$ particles independently maintained in PBS solution (pH 7.4) and acetate buffer (pH 5) at 37 °C (same buffer solutions were used in both dialysis bags and beakers), under steady agitation, revealed that at 37 °C, both polymers released Dox slowly, with 20% of Dox released from $PSar_{136}$-*b*-$PHPMA_5$ at pH 5 and 4 % of loaded Dox released from the same polymer after 18 days incubation at pH 7.4 (Figure 3.31 a). 10 % (pH 5) and 2 % (pH 7.4) of loaded Dox was released from $PSar_{136}$-*b*-$PHPMA_{21}$ after 18 days incubation (Figure 3.31 b). Greater Dox release occurred from nanoparticles stored in pH 5 solution compared to those stored in pH 7.4 solution, which may be explained by the primary amine of Dox being protonated when in pH 5 solution, enhancing the water solubility of the drug and aiding its release into acidic solution.

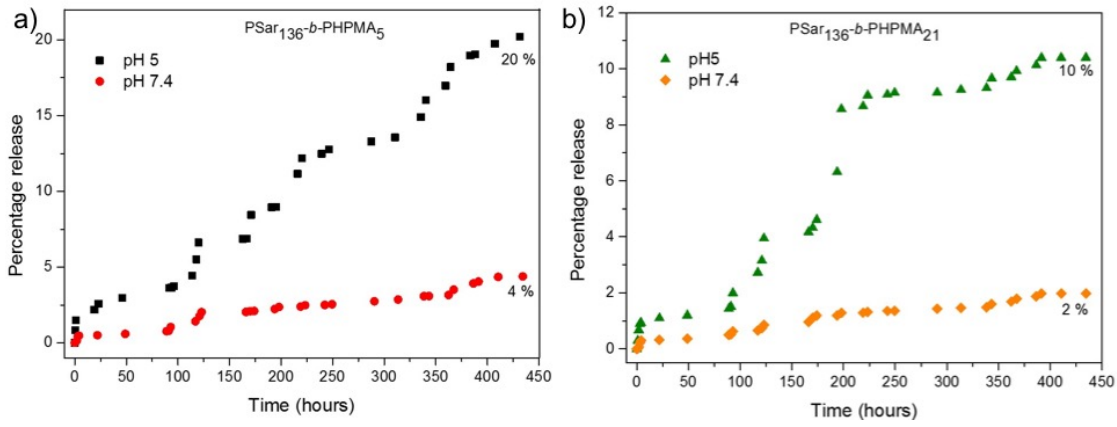

Figure 3. 31. Doxorubicin release from a) $PSar_{136}$-*b*-$PHPMA_5$ and b) $PSar_{136}$-*b*-$PHPMA_{21}$ at pH 5 and pH 7.4 at 37 °C.

Subsequent heating of both sets of nanoparticles to 50 °C was done to assess their thermoresponse. Enhanced Dox release (91% in pH 5 solution, 83% in pH 7.4 solution)

of Dox from $PSar_{136}$-*b*-$PHPMA_5$ particles occurred following reassessment after a further 7 days of heating at the elevated temperature. $PSar_{136}$-*b*-$PHPMA_{21}$ particles also demonstrated enhanced Dox release upon heating at 50 °C, but in this case 30% (pH 5) and 16% (pH 7.4) of payload was released from the nanoparticles following reassessment after 7 days of heating. The slower rate of Dox release from $PSar_{136}$-*b*-$PHPMA_{21}$ may be assigned to the increased length of the thermoresponsive PHPMA section within the composition. Altering the PHPMA block length to manipulate drug release extent/rate was a feature that may be further exploited. The critical temperature at which Dox release from $PSar_{136}$-*b*-$PHPMA_5$ nanoparticles was triggered was then determined. Initially, DLS studies revealed that the size of unloaded nanoparticles did not change significantly upon increasing the solution temperature from 25 °C ((166 ± 14) nm) to 37 °C ((164 ± 19) nm) (Figure 3.32, DLS data presented in Table A3.1). Upon increasing the temperature to 50 °C, the particle size decreased to (132 ± 16) nm. All PDI values for the unloaded nanoparticles were less than 0.3, signifying that the nanoparticles were stable at room temperature, 37 °C and 50 °C. $PSar_{136}$-*b*-$PHPMA_5$ nanoparticles loaded with Dox had a hydrodynamic diameter of (161 ± 22) nm in aqueous solution at 25 °C. It decreased to (130 ± 28) nm as the temperature was increased to 37 °C. Upon further solution temperature increase to 50 °C, the particle size decreased further to (91 ± 25) nm. This dramatic decrease in nanoparticle diameter, and the consequent expulsion of Dox from the nanoparticles, was proposed to be the reason for extensive Dox release at 50 °C. The PDI values of the Dox-loaded nanoparticles at 37 °C (0.389) and 50 °C (0.468) were above 0.3; such instability was likely to be due to the release of Dox. PDI equals 0.3 (specific to this kind of polymer nanoparticle) is the limit before the intensity size distribution splits into two. Therefore, PDI value below 0.3 was considered that the nanoparticles were stable in the media.

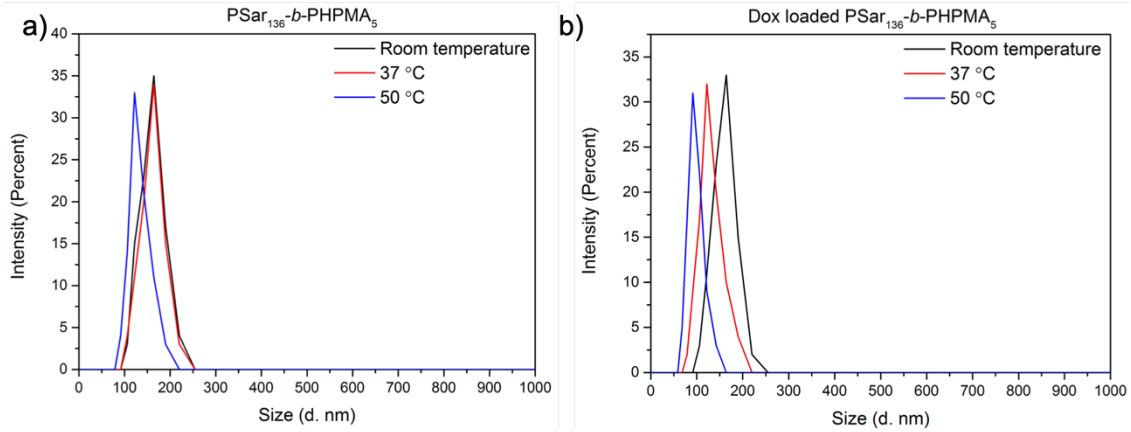

Figure 3. 32. DLS analysis of a) unloaded $PSar_{136}$-*b*-$PHPMA_5$ and b) Dox-loaded $PSar_{136}$-*b*-$PHPMA_5$ nanoparticles at room temperature, 37 °C and 50 °C in deionised water.

The release of Dox from $PSar_{136}$-*b*-$PHPMA_5$ nanoparticles was then monitored in response to incremental PBS solution temperature increases whereby the solution temperature was raised by 1 °C step size, and the solution was maintained at the increased temperature for 24 hours, and the amount of Dox released at the each increased temperature was measured (Figure 3.33 a). Dox release occurred slowly and increased steadily to 16 % as the solution temperature was increased from 25 °C to 39°C over 360 hours. At passing this temperature, the percentage of Dox released increased markedly to 78 % at 41 °C, signifying that the critical temperature for Dox burst release, which may be caused by glass transition temperature of the hydrated block copolymer which may between 39 °C and 41 °C. A more detailed study in which the loaded nanoparticles were monitored at 40 °C for 24 hours confirmed that 62 % Dox release was achieved by heating the nanoparticles to 40 °C for 24 hours (Figure 3.33 b). This offered validation that the reported nanoparticles are pharmacologically relevant; payload release can be actuated by nanoparticle heating to a temperature that was not detrimental to cell survival. The temperature threshold for detrimental cell survival is 42 °C [44].

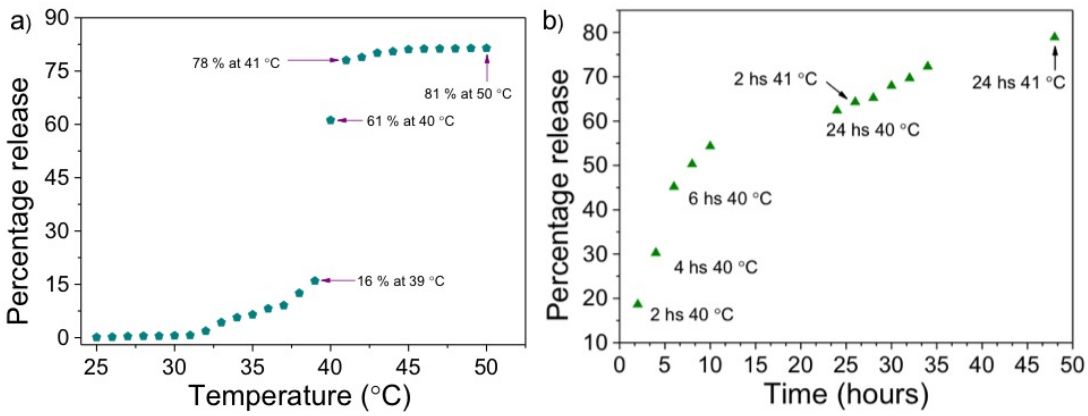

Figure 3. 33. a) The temperature-dependent release of Dox from $PSar_{136}$-*b*-$PHPMA_5$ nanoparticles upon incremental solution temperature increase. b) Detailed study of Dox release from $PSar_{136}$-*b*-$PHPMA_5$ nanoparticles maintained in solution of 40 °C (24 hours) and then 41 °C (24 hours).

Dr. Nicola Ingram (from St James Hospital) conducted cytotoxicity analysis for Dox-loaded and unloaded $PSar_{136}$-*b*-$PHPMA_5$ nanoparticles. The cytotoxicity of the nanoparticles formed from $PSar_{136}$-*b*-$PHPMA_5$ were assessed on MCF-7 breast cancer cells, triple-negative breast cancer cells (MDA-MB-231), and Her2-enriched (ER and PR negative) breast cancer cells (MDA-MB-453), to assess the capability of the materials to potentially treat chemo-refractory disease. Free Dox was used as a positive control (Tables 3.7). In all instances, the polymer nanoparticles were found to cause negligible cell death at both 37 °C and at 41°C, validating the non-cytotoxicity of the polymers produced (Figure 3.34). Dox-loaded nanoparticles were then assessed against the three same cell lines; in each instance pronounced cell death occurred that became progressively greater with enhanced polymer concentration. It may be hypothesised that the nanoparticles were of sufficiently small dimensions to undergo endocytosis both at the lower and elevated temperature, and that Dox leakage from the nanoparticles was sufficiently significant to cause cell death following nanoparticle uptake. The IC_{50} values of Dox-loaded nanoparticles at 41 °C of all cell lines [(0.07±0.44)μg mL^{-1}, (0.23±0.36)μg mL^{-1} and (0.18±1.25)μg mL^{-1}] were lower compared to that at 37 °C [(0.10±0.35)μg mL^{-1}, (0.32±0.34)μg mL^{-1}, and (0.17±0.59)μg mL^{-1}]. Lower concentration of Dox-loaded nanoparticles at 41 °C can kill 50 % of cancer cells than that of at 37 °C. For MCF-7 cancer cell line, the IC_{50} value of Dox-loaded nanoparticles at 37 °C, (0.10±0.35)μg mL^{-1} was higher than that of free Dox, (0.002±7.01)μg mL^{-1}. $PSar_{136}$-*b*-$PHPMA_5$ nanoparticles

reduced Dox toxicity to MCF-7 cancer cell line. For MDA-MB-453 and MDA-MB231 cancer cell lines, the IC_{50} values were not significant different of Dox-loaded nanoparticles at 41 °C, 37 °C and free Dox at 37 °C for each cancer cell line.

Table 3. 7. The IC_{50} values of Dox loaded $PSar_{136}$-*b*-$PHPMA_5$ nanoparticles and free Dox obtained for the cell lines tested.

	IC_{50} Value ($\mu g\ mL^{-1}$)		
	41 °C	37 °C	Free Dox at 37 °C
MCF-7	0.07 ± 0.44	0.10 ± 0.35	0.002 ± 7.01
MDA-MB-231	0.23 ± 0.36	0.32 ± 0.34	0.49 ± 0.39
MDA-MB-453	0.18 ± 1.25	0.17 ± 0.59	0.16 ± 0.39

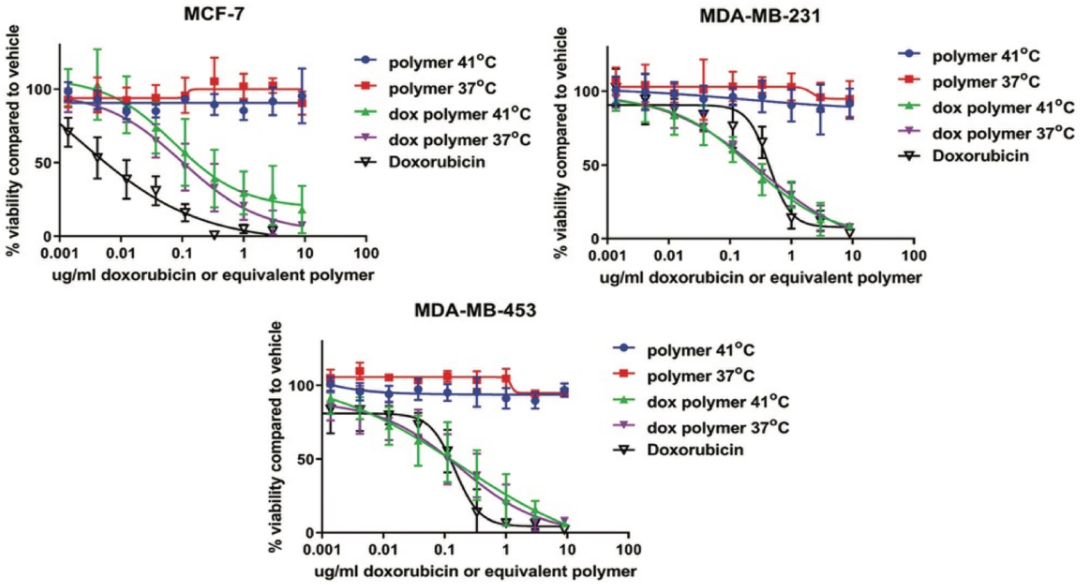

Figure 3. 34. Cytotoxicity of $PSar_{136}$-*b*-$PHPMA_5$ either empty (polymer only) or loaded with doxorubicin (dox polymer) on three breast cancer cell lines. Serial dilutions of polymer or dox polymer were incubated with MCF-7, MDA-MB-231 (triple negative) or MDA-MB-453 (double negative) cell lines for 72 hours either with or without incubation of the cells at 41 °C for 40 minutes within the first hour of incubation. Graphs of the mean and standard deviation from 3 independent experiments were fitted with a four-parameter log inhibitor curve.

3.4 Conclusions

Combining NCA ROP and RAFT polymerisation was a viable route to the creation of

amphiphilic block copolymers that were thermoresponsive. The synthesis of a PSar-*b*-PHPMA in a water/ethanol mixture leaded to the *in situ* formation of particles, as assessed by DLS. Using DLS in this manner enables the elucidation of the ideal composition of PSar-*b*-PHPMA for the creation of suitably sized, stable, nanoparticles for controlled release applications. Modifying PSar with a very limited amount of PHPMA had a profound effect on the thermoresponsive nanoparticle formation in aqueous solution. $PSar_{136}$-*b*-$PHPMA_5$ self-assembly in the presence of Dox yielded drug-loaded nanoparticles, and Dox release from the nanoparticles could be actuated by an increase in environmental temperature to 41 °C. Such nanoparticles were non-cytotoxic against the three breast cancer cell lines tested, in contrast to Dox-loaded nanoparticles which instigated pronounced cell death in each case. Consequently, the nanoparticles disclosed had potential application for the thermally-triggered release of guest molecules to external solution, and the encapsulation, distribution, and release of Dox to breast cancer cells as a mode of therapeutic delivery.

3.5 References

1. Saravanakumar, G., Park, H., Kim, J., Park, D., Pramanick, S., Kim, D.H. and Kim, W.J. Miktoarm Amphiphilic Block Copolymer with Singlet Oxygen-Labile Stereospecific beta-Aminoacrylate Junction: Synthesis, Self-Assembly, and Photodynamically Triggered Drug Release. Biomacromolecules. 2018, 19(6), pp.2202-2213.
2. Ihsanullah, K.M., Kumar, B.N., Zhao, Y.Y., Muhammad, H., Liu, Y., Wang, L., Liu, H. and Jiang, W. Stepwise-activatable hypoxia triggered nanocarrier-based photodynamic therapy for effective synergistic bioreductive chemotherapy. *Biomaterials.* 2020, **245**, 119982.
3. Chountoulesi, M., Perinelli, D.R., Pippa, N., Chrysostomou, V., Forys, A., Otulakowski, L., Bonacucina, G., Trzebicka, B., Pispas, S. and Demetzos, C. Physicochemical, morphological and thermal evaluation of lyotropic lipidic liquid crystalline nanoparticles: The effect of stimuli-responsive polymeric stabilizer. *Colloids and Surfaces a-Physicochemical and Engineering Aspects.* 2020, **595**, 124678.
4. Razavi, B., Abdollahi, A., Roghani-Mamaqani, H. and Salami-Kalajahi, M. Light-, temperature-, and pH-responsive micellar assemblies of spiropyran-initiated amphiphilic block copolymers: Kinetics of photochromism, responsiveness, and smart drug delivery. *Materials Science & Engineering C-Materials for Biological Applications.* 2020, **109**, 110542.
5. Mohamed, H.A., Khuphe, M., Boardman, S.J., Shepherd, S., Phillips, R.M., Thornton, P.D. and Willans, C.E. Polymer encapsulation of anticancer silver-N-heterocyclic carbene complexes. Rsc Advances. 2018, 8(19), pp.10474-10477.
6. Meng, L.J., Zhang, X.K., Lu, Q.H., Fei, Z.F. and Dyson, P.J. Single walled carbon nanotubes as drug delivery vehicles: Targeting doxorubicin to tumors. Biomaterials. 2012, 33(6), pp.1689-1698.

7. Davis, M.E., Chen, Z. and Shin, D.M. Nanoparticle therapeutics: an emerging treatment modality for cancer. Nature Reviews Drug Discovery. 2008, 7(9), pp.771-782.
8. Paasonen, L., Romberg, B., Storm, G., Yliperttula, M., Urtti, A. and Hennink, W.E. Temperature-sensitive poly(N-(2-hydroxypropyl)methacrylamide mono/dilactate)-coated liposomes for triggered contents release. Bioconjugate Chemistry. 2007, 18(6), pp.2131-2136.
9. Wang, X., Li, C., Fan, N., Li, J., He, Z.G. and Sun, J. Multimodal nanoporous silica nanoparticles functionalized with aminopropyl groups for improving loading and controlled release of doxorubicin hydrochloride. Materials Science & Engineering C-Materials for Biological Applications. 2017, 78, pp.370-375.
10. Kalafatovic, D., Nobis, M., Son, J.Y., Anderson, K.I. and Ulijn, R.V. MMP-9 triggered self-assembly of doxorubicin nanofiber depots halts tumor growth. Biomaterials. 2016, 98, pp.192-202.
11. Li, Y., Sun, J., Chen, Q.P., Chen, Z.P. and Zhu, L. Fast Drug Release of Liposome-Gold Conjugation Under Light Irradiation and the Comparison with Liposome-Gold Hybrid. Nanoscience and Nanotechnology Letters. 2017, 9(6), pp.982-987.
12. Rafiee, E., Nobakht, N. and Behbood, L. Influence of pH, temperature, and alternating magnetic field on drug release from Keggin-type heteropoly acid encapsulated in iron-carboxylate nanoscale metal-organic framework. Research on Chemical Intermediates. 2017, 43(2), pp.951-969.
13. Chung, S.H., Mehta, R., Tromberg, B.J. and Yodh, A.G. NON-INVASIVE MEASUREMENT OF DEEP TISSUE TEMPERATURE CHANGES CAUSED BY APOPTOSIS DURING BREAST CANCER NEOADJUVANT CHEMOTHERAPY: A CASE STUDY. Journal of Innovative Optical Health Sciences. 2011, 4(4), pp.361-372.
14. Chan, B.A., Xuan, S.T., Li, A., Simpson, J.M., Sternhagen, G.L., Yu, T.Y., Darvish, O.A., Jiang, N.S. and Zhang, D.H. Polypeptoid polymers: Synthesis, characterization, and properties. *Biopolymers.* 2018, **109**(1), 23070.
15. Hu, Y.L., Hou, Y.Q., Wang, H. and Lu, H. Polysarcosine as an Alternative to PEG for Therapeutic Protein Conjugation. Bioconjugate Chemistry. 2018, 29(7), pp.2232-2238.
16. Weber, B., Birke, A., Fischer, K., Schmidt, M. and Barz, M. Solution Properties of Polysarcosine: From Absolute and Relative Molar Mass Determinations to Complement Activation. *Macromolecules.* 2018, **51**(7), pp.2653-2661.
17. Chapman, R.G., Ostuni, E., Liang, M.N., Meluleni, G., Kim, E., Yan, L., Pier, G., Warren, H.S. and Whitesides, G.M. Polymeric thin films that resist the adsorption of proteins and the adhesion of bacteria. *Langmuir.* 2001, **17**(4), pp.1225-1233.
18. Huesmann, D., Sevenich, A., Weber, B. and Barz, M. A head-to-head comparison of poly(sarcosine) and poly(ethylene glycol) in peptidic, amphiphilic block copolymers. *Polymer.* 2015, **67**, pp.240-248.
19. Lau, K.H.A., Ren, C.L., Sileika, T.S., Park, S.H., Szleifer, I. and Messersmith, P.B. Surface-Grafted Polysarcosine as a Peptoid Antifouling Polymer Brush. *Langmuir.* 2012, **28**(46), pp.16099-16107.
20. Fetsch, C., Grossmann, A., Holz, L., Nawroth, J.F. and Luxenhofer, R. Polypeptoids from N-Substituted Glycine N-Carboxyanhydrides: Hydrophilic, Hydrophobic, and Amphiphilic Polymers with Poisson Distribution. *Macromolecules.* 2011, **44**(17), pp.6746-6758.
21. Gangloff, N., Hoferth, M., Stepanenko, V., Sochor, B., Schummer, B., Nickel, J., Walles, H., Hanke, R., Wurthner, F., Zuckermann, R.N. and Luxenhofer, R. Linking two worlds in polymer chemistry: The influence of block uniformity and dispersity in amphiphilic block copolypeptoids on their self-assembly. *Biopolymers.* 2019, **110**(4), 23259.

22. Fetsch, C., Flecks, S., Gieseler, D., Marschelke, C., Ulbricht, J., van Pee, K.H. and Luxenhofer, R. Self-Assembly of Amphiphilic Block Copolypeptoids with C-2-C-5 Side Chains in Aqueous Solution. *Macromolecular Chemistry and Physics.* 2015, **216**(5), pp.547-560.

23. Cui, S.D., Pan, X.F., Gebru, H., Wang, X., Liu, J.Q., Liu, J.J., Li, Z.J. and Guo, K. Amphiphilic star-shaped poly(sarcosine)-block-poly(epsilon-caprolactone) diblock copolymers: one-pot synthesis, characterization, and solution properties. *Journal of Materials Chemistry B.* 2017, **5**(4), pp.679-690.

24. Deng, Y.W., Zou, T., Tao, X.F., Semetey, V., Trepout, S., Marco, S., Ling, J. and Li, M.H. Poly(epsilon-caprolactone)-block-polysarcosine by Ring-Opening Polymerization of Sarcosine N-Thiocarboxyanhydride: Synthesis and Thermoresponsive Self-Assembly. *Biomacromolecules.* 2015, **16**(10), pp.3265-3274.

25. Doriti, A., Brosnan, S.M., Weidner, S.M. and Schlaad, H. Synthesis of polysarcosine from air and moisture stable N-phenoxycarbonyl-N-methylglycine assisted by tertiary amine base. *Polymer Chemistry.* 2016, **7**(18), pp.3067-3070.

26. Tao, X.F., Deng, C. and Ling, J. PEG-Amine-Initiated Polymerization of Sarcosine N-Thiocarboxyanhydrides Toward Novel Double-Hydrophilic PEG-b-Polysarcosine Diblock Copolymers. *Macromolecular Rapid Communications.* 2014, **35**(9), pp.875-881.

27. Du, J.W., Tian, C., Liu, Y.J., Ling, J. and Wang, Y.X. Azo-capped polysarcosine-b-polylysine as polypeptide gene vector: A new strategy to improve stability and easy optimization via host-guest interaction. *Colloids and Surfaces B-Biointerfaces.* 2015, **130**, pp.31-39.

28. Birke, A., Ling, J. and Barz, M. Polysarcosine-containing copolymers: Synthesis, characterization, self-assembly, and applications. *Progress in Polymer Science.* 2018, **81**, pp.163-208.

29. Kim, C.J., Ueda, M., Imai, T., Sugiyama, J. and Kimura, S. Tuning the Viscoelasticity of Peptide Vesicles by Adjusting Hydrophobic Helical Blocks Comprising Amphiphilic Polypeptides. *Langmuir.* 2017, **33**(22), pp.5423-5429.

30. Birke, A., Huesmann, D., Kelsch, A., Weilbacher, M., Xie, J., Bros, M., Bopp, T., Becker, C., Landfester, K. and Barz, M. Polypeptoid-block-polypeptide Copolymers: Synthesis, Characterization, and Application of Amphiphilic Block Copolypept(o)ides in Drug Formulations and Miniemulsion Techniques. *Biomacromolecules.* 2014, **15**(2), pp.548-557.

31. Holm, R., Weber, B., Heller, P., Klinker, K., Westmeier, D., Docter, D., Stauber, R.H. and Barz, M. Synthesis and Characterization of Stimuli-Responsive Star-Like Polypept(o) ides: Introducing Biodegradable PeptoStars. *Macromolecular Bioscience.* 2017, **17**(6), 1600514.

32. Viricel, W., Fournet, G., Beaumel, S., Perrial, E., Papot, S., Dumontet, C. and Joseph, B. Monodisperse polysarcosine-based highly-loaded antibody-drug conjugates. *Chemical Science.* 2019, **10**(14), pp.4048-4053.

33. Khuphe, M., Kazlauciunas, A., Huscroft, M. and Thornton, P.D. The formation of biodegradable micelles from a therapeutic initiator for enzyme-mediated drug delivery. *Chemical Communications.* 2015, **51**(8), pp.1520-1523.

34. Khuphe, M., Mahon, C.S. and Thornton, P.D. Glucose-bearing biodegradable poly(amino acid) and poly(amino acid)-poly(ester) conjugates for controlled payload release. *Biomaterials Science.* 2016, **4**(12), pp.1792-1801.

35. Gao, C.Q., Zhou, H., Qu, Y.Q., Wang, W., Khan, H. and Zhang, W.Q. In Situ Synthesis of Block Copolymer Nanoassemblies via Polymerization-Induced Self-Assembly in Poly(ethylene glycol). *Macromolecules.* 2016, **49**(10), pp.3789-3798.

36. Hu, X.Y., Wang, Y.M., Xu, M., Zhang, L.L., Zhang, J.F. and Dong, W. Development of photocrosslinked salecan composite hydrogel embedding titanium carbide nanoparticles as cell scaffold. *International Journal of Biological Macromolecules.* 2019, **123**, pp.549-557.

37. Bertal, K., Shepherd, J., Douglas, C.W.I., Madsen, J., Morse, A., Edmondson, S., Armes, S.P., Lewis, A. and MacNeil, S. Antimicrobial activity of novel biocompatible wound dressings based on triblock copolymer hydrogels. *Journal of Materials Science.* 2009, **44**(23), pp.6233-6246.

38. Warren, N.J. and Armes, S.P. Polymerization-Induced Self-Assembly of Block Copolymer Nano-objects via RAFT Aqueous Dispersion Polymerization. *Journal of the American Chemical Society.* 2014, **136**(29), pp.10174-10185.

39. Varlas, S., Georgiou, P.G., Bilalis, P., Jones, J.R., Hadjichristidis, N. and O'Reilly, R.K. Poly(sarcosine)-Based Nano-Objects with Multi-Protease Resistance by Aqueous Photoinitiated Polymerization-Induced Self-Assembly (Photo-PISA). *Biomacromolecules.* 2018, **19**(11), pp.4453-4462.

40. Klinker, K., Holm, R., Heller, P. and Barz, M. Evaluating chemical ligation techniques for the synthesis of block copolypeptides, polypeptoids and block copolypept(o)ides: a comparative study. *Polymer Chemistry.* 2015, **6**(25), pp.4612-4623.

41. Warren, N.J., Mykhaylyk, O.O., Mahmood, D., Ryan, A.J. and Armes, S.P. RAFT Aqueous Dispersion Polymerization Yields Poly(ethylene glycol)-Based Diblock Copolymer Nano-Objects with Predictable Single Phase Morphologies. *Journal of the American Chemical Society.* 2014, **136**(3), pp.1023-1033.

42. Talelli, M., Rijcken, C.J.F., Lammers, T., Seevinck, P.R., Storm, G., van Nostrum, C.F. and Hennink, W.E. Superparamagnetic Iron Oxide Nanoparticles Encapsulated in Biodegradable Thermosensitive Polymeric Micelles: Toward a Targeted Nanomedicine Suitable for Image-Guided Drug Delivery. *Langmuir.* 2009, **25**(4), pp.2060-2067.

43. Khuphe, M. and Thornton, P.D. Poly(hydroxy acid) Nanoparticles for the Encapsulation and Controlled Release of Doxorubicin. *Macromolecular Chemistry and Physics.* 2018, **219**(23), 1800352.

44. Beachy, S.H. and Repasky, E.A. Toward establishment of temperature thresholds for immunological impact of heat exposure in humans. *International Journal of Hyperthermia.* 2011, **27**(4), pp.344-352.

Chapter 4. Meticulous Doxorubicin Release from pH-Responsive Nanoparticles Entrapped within an Injectable Thermoresponsive Depot

Preamble

This chapter is based on work published as:

Yu H.; Ingram N.; Rowley JV.; Green DC.; Thornton P.D. *Chemistry – A European Journal,* 2020.

Abstract

The dual stimuli-controlled release of doxorubicin from gel-embedded nanoparticles is reported. Non-cytotoxic polymer nanoparticles are formed from poly(ethylene glycol)-b-poly(benzyl glutamate) that, uniquely, contain a central ester link. This connection renders the nanoparticles pH-responsive, enabling extensive doxorubicin release in acidic solutions (pH 6.5), but not in solutions of physiological pH (pH 7.4). Doxorubicin-loaded nanoparticles were found to be stable for at least 31 days and lethal against the three breast cancer cell lines tested. Furthermore, doxorubicin-loaded nanoparticles could be incorporated within a thermoresponsive poly(2-hydroxypropyl methacrylate) gel depot, which forms immediately upon injection of poly(2-hydroxypropyl methacrylate) in dimethyl sulfoxide solution into aqueous solution. The combination of the poly(2-hydroxypropyl methacrylate) gel and poly(ethylene glycol)-b-poly(benzyl glutamate) nanoparticles yields an injectable doxorubicin delivery system that facilities near-complete drug release when maintained at elevated temperatures (37 °C) in acidic solution (pH 6.5). In contrast, negligible payload release occurs when the material is stored at room temperature in non-acidic solution (pH 7.4). The system has great potential as a vehicle for the prolonged, site-specific, release of chemotherapeutics.

4.1 Introduction

The design of effective methods to deliver anti-cancer drugs in a controlled manner is a key goal of medicinal chemistry [1]. Materials which assist drug encapsulation and distribution must prolong the circulation lifetime of drug molecules, and reduce the toxicity of free chemotherapeutic molecules on healthy cells [2-5]. The development of innovative systems that can encapsulate appreciable drug concentrations, before releasing the drug at a targeted, or localised, site is essential for precise cancer treatment in the absence of side-effects.

Polymeric nanoparticles are promising materials for drug delivery vehicles owing to their capability to encapsulate and distribute poorly water-soluble therapeutic molecules *in vivo* [6-9]. Polymers can also be designed to have sensitivity to a variety of stimuli, triggering payload release from polymeric nanoparticles [10-25]. Altered environmental pH is particularly relevant as an actuator for chemotherapeutic release as cancerous tissue (pH 5-pH 6.8) is more acidic than both healthy tissue and the blood (pH 7.4) [26-30]. However, many nanoparticles proposed as potential drug delivery vehicles lack biodegradability *in vivo*, and long-term stability whilst stored prior to administration, rendering their practical application unworkable. Consequently, there is an urgent demand for polymer nanoparticles that preserve drug molecules within their structure for prolonged periods prior to administration, before releasing the therapeutic payload at a controlled rate at a target site upon injection (*in vivo*).

Poly(amino acids) (PAAs) are excellent candidates to be deployed as drug delivery vehicles owing to their capability to readily self-assemble into discrete, stable, structures in solution [31-36]. In addition, PAAs are bio-derived, present a wide-range of functional groups, and offer biodegradability and biocompatibility [37-39]. ROP of α-amino acid NCA monomers produces PAAs in an efficient and controlled manner, enabling the generation of block copolymers that can form materials for controlled release applications [40-43]. However, there are currently no examples of PAA-based nanoparticles that undergo polymer backbone cleavage and drug release in response to acidic media, such as that presented by tumour tissue, owing to the stability of constituent amide bonds against acid-mediated hydrolysis.

The localised release of chemotherapeutic molecules from polymeric nanoparticles to the tumour site is essential to minimise cytotoxic effects on healthy tissue, and the resultant highly-detrimental physiological side-effects. Polymer-based injectable gels which slowly release the therapeutic to the surrounding, target, tissue, offer an effective method to administer cytotoxic therapeutics *in vivo* [44-46]. Recently, the creation of a poly(*N*-isopropylacrylamine)-based microgel enriched with the anti-HIV drug Lopinavir has been reported. Solid drug nanoparticles suspended within the *in situ*-forming implant enabled sustained drug release over four months [47]. This acts as an excellent template for the creation nanoparticle-containing depot that forms upon injection into aqueous media, essential for nanoparticle immobilisation at the target site.

In this chapter, PBLG-*b*-PEG block copolymer is reported that, crucially, contains an acid-sensitive ester bond between the polymeric blocks. Dox-loaded PBLG-*b*-PEG nanoparticles maintained a stable dispersion with negligible Dox release in aqueous solution of pH 7.4. Conversely, extensive Dox release was observed when the nanoparticles were maintained in acidic solution (pH 6.5). In order to realise an injectable drug delivery system, Dox-loaded nanoparticles were entrapped within a thermoresponsive PHPMA gel depot which prolongs nanoparticle residence time and controls their release at a target site. The combination of PAA-based pH-responsive nanoparticles, and a thermoresponsive gel depot, offers a highly sensitive injectable delivery system for the meticulously controlled delivery of chemotherapeutic molecules.

4.2 Experimental

4.2.1 Synthesis of PBLG-*b*-PEG

The experiment was conducted as reported by Gradišar *et al.* under a nitrogen atmosphere [48]. Dry chloroform was degassed with nitrogen for one hour. BLG NCA (0.041 g, 0.156 mmol), poly(ethylene glycol)methyl ether (Meo-PEG) (Mn 5000) (0.157 g, 0.031 mmol) and methansulfonic acid (MSA) (6.0 µL, 0.092 mmol) were dissolved in dry chloroform (5.0 mL). The reaction was stirred in an oil bath at 40 °C for 24 hours. Then the reaction mixture was cooled to room temperature and put in an ice bath. *N*-Ethyldiisopropylamine (DIPEA) (13.0 µL, 0.076 mmol) was added into the reaction

mixture. The reaction was stirred at room temperature without nitrogen atmosphere for 24 hours. Then the reaction mixture was added dropwise into cold diethyl ether (60.0 mL). Next, the solution was centrifuged for 30 minutes at 4000 rev/min and dried in a vacuum oven at 45 °C overnight. The product was dialysed against deionised water for 3 days, freeze-dried for 2 days to yield a white solid. The synthesised polymer was $PBLG_2$-*b*-PEG_{113}. $PBLG_{26}$-*b*-PEG_{113} and $PBLG_{35}$-*b*-PEG_{113} were also produced using the same procedure, the quantities of the reactants were BLG NCA (0.408 g, 1.55 mmol), Meo-PEG (0.155 g, 0.031 mmol), MSA (6.0 μL; 0.093 mmol), DIPEA (14.0 μL, 0.078 mmol); BLG NCA (0.552 g, 2.10 mmol), Meo-PEG (0.152 g, 0.030 mmol), MSA (6.0 μL, 0.090 mmol), DIPEA (13.0 μL, 0.075 mmol), respectively. $PBLG_2$-*b*-PEG_{113}: 0.140 g, 83.0 wt. % (white solid). APC (THF, PMMA standards): M_w= 5300 g mol^{-1}. Dispersity= 1.18. ^{1}H-NMR (500 MHz, DMSO-d_6, δ, ppm): 7.48 – 7.38 (m, 10H, (ArH)$_2$), 5.20 – 5.16 (m, 4H, (ArHCH_2CO)$_2$), 4.18 – 3.61 (s, 452H, H_3C(OCH_2CH_2)$_{113}$), 2.20 – 1.73 (m, 8H, (OCCHCH_2CH_2NH)$_2$H), 1.38 – 1.30 (m, 4H, H$_3$C(OCH$_2$CH$_2$)$_{113}$O(OCCHNH)$_2$H). FTIR: ν_{max}/cm^{-1} (solid): 2881 cm^{-1} (alkane C-H stretch), 1743 cm^{-1} (ester C=O stretch) and 1096 cm^{-1} (ether C-O stretch).

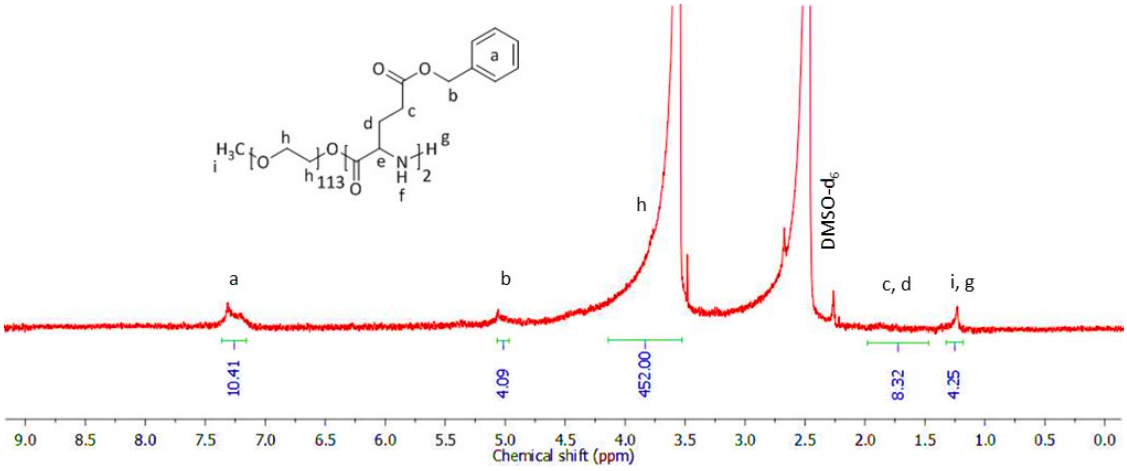

Figure 4. 1. The 500 MHz ^{1}H-NMR spectrum of dialysed $PBLG_2$-*b*-PEG_{113} in DMSO-d_6 at 25 °C.

$PBLG_{26}$-*b*-PEG_{113}: 0.285 g, 85.9 wt. % (white solid). APC (THF, PMMA standards): M_w= 9100 g mol^{-1}. Dispersity= 1.13. ^{1}H-NMR (500 MHz, DMSO-d_6, δ, ppm): 8.40 – 7.82 (m, 26H, (COCHNH)$_{26}$H, 7.48 – 7.20 (m, 130H, (ArH)$_{26}$), 5.20 – 4.86 (m, 52H, (ArHCH_2CO)$_{26}$), 4.41 – 3.70 (m, 26H, (COCHNH)$_{26}$H), 3.68 – 3.46 (s, 452H, H_3C(OCH_2CH_2)$_{113}$), 2.42 – 1.25 (m, 104H, (OCCHCH_2CH_2NH)$_{26}$H), 1.30 – 1.20 (m, 4H, H$_3$C(OCH$_2$CH$_2$)$_{113}$O(OCCHNH)$_{26}$H). FTIR: ν_{max}/cm^{-1} (solid): 3291 cm^{-1} (primary amine N-H stretch), 2881 cm^{-1} (alkane C-H stretch), 1731 cm^{-1} and 1650 cm^{-1} (ester C=O stretch) and 1096 cm^{-1} (ether C-O stretch).

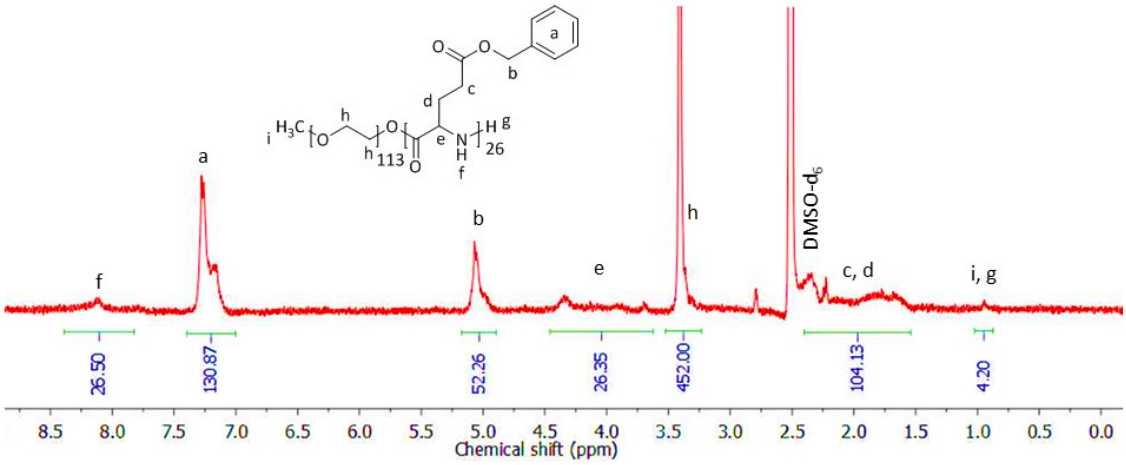

Figure 4. 2. The 500 MHz ^{1}H-NMR spectrum of dialysed $PBLG_{26}$-*b*-PEG_{113} in DMSO-d_6 at 25 °C.

$PBLG_{35}$-*b*-PEG_{113}: 0.342 g, 90.0 wt. % (white solid). APC (THF, PMMA standards): M_w= 12000 g mol^{-1}. Dispersity= 1.16. ^{1}H-NMR (500 MHz, DMSO-d_6, δ, ppm): 8.68 – 7.80 (m, 35H, $(COCHN\underline{H})_{35}H$, 7.45 – 7.21 (m, 175H, $(Ar\underline{H})_{35}$), 5.23 – 4.85 (m, 70H, $(ArHC\underline{H}_2CO)_{35}$), 4.46 – 3.81 (m, 35H, $H_3C(OCC\underline{H}NH)_{35}$), 3.58 – 3.46 (s, 452H, $H_3C(OC\underline{H}_2C\underline{H}_2)_{113}$), 2.42 – 1.22 (m, 140H, $(OCCHC\underline{H}_2C\underline{H}_2NH)_{35}H$), 1.30 – 1.20 (m, 4H, $\underline{H}_3C(OCH_2CH_2)_{113}O(OCCHNH)_{35}\underline{H}$). FTIR: ν_{max}/cm^{-1} (solid): 3292 cm^{-1} (primary amine N-H stretch), 2882 cm^{-1} (alkane C-H stretch), 1742 cm^{-1} and 1650 cm^{-1} (ester C=O stretch) and 1096 cm^{-1} (ether C-O stretch).

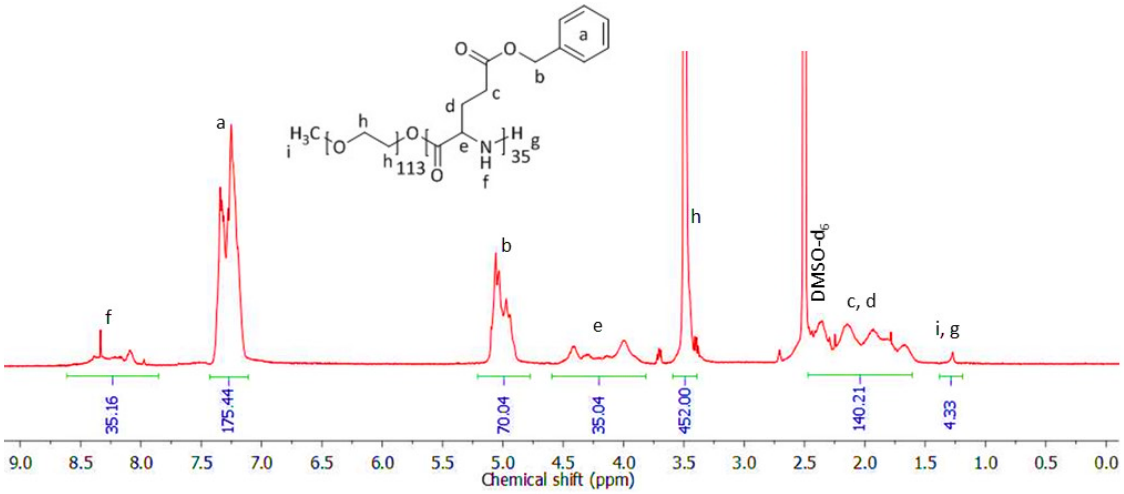

Figure 4. 3. The 500 MHz ^{1}H-NMR spectrum of dialysed $PBLG_{35}$-*b*-PEG_{113} in DMSO-d_6 at 25 °C.

4.2.2 Synthesis of PHPMA

The reaction was performed in a sealed environment. 4-Cyano-4-((phenylcarbonothioyl)thio) pentanoic acid (0.030 g, 0.107 mmol) was dissolved in

acetone (2.0 mL) and deionised water (1.0 mL). AAPH (0.215 g, 0.793 mmol) was added in the reaction mixture followed by deionised water (1.0 mL)). When everything dissolved, HPMA (3.09 g, 21.4 mmol) was added into the reaction followed by deionised water (1.0 mL). The reaction was stirred at 60 °C overnight and a cream colour gel was formed. Different chain lengths of PHPMA were prepared which were 80 and 200. The synthesised polymer was $PHPMA_{200}$. $PHPMA_{80}$ was also produced using the same procedure and quantity of the reactants were 4-cyano-4-((phenylcarbonothioyl)thio) pentanoic acid (0.032 g, 0.115 mmol), AAPH (0.218 g, 0.805 mmol), and HPMA (1.33 g, 9.2 mmol). 0.103 g of $PHPMA_{80}$ and $PHPMA_{200}$ gels were freeze dried, percentages of polymer in each gel were 36.4 % and 65.3 %, respectively. $PHPMA_{200}$: 2.76 g, 88.7 wt. % (pale yellow transparent gel). APC (THF, PMMA standards): M_w= 28500 g mol^{-1}. Dispersity= 1.24. ^{1}H-NMR (500 MHz, DMSO-d_6, δ, ppm): 8.12 – 7.82 (s, 1H, COOH), 7.81 – 7.77 (d, 2H, ArH), 7.76 – 7.73 (t, 1H, ArH), 7.72 – 7.62 (d, 2H, ArH), 5.12 – 4.56 (m, 200H, $(OCH_2CHOHCH_3)_{200}$), 4.18 – 3.43 (m, 400H, $(OCH_2CHOHCH_3)_{200}$), 3.42 – 3.22 (m, 200H, $(OCH_2CHOHCH_3)_{200}$), 2.30 – 1.37 (m, 407H, $(CH_3CCH_2)_{200}CCH_3CNCH_2CH_2$), 1.33 – 0.47 (m, 1200H, $(CH_3CCOOCH_2CHOHCH_3)_{200}$). FTIR: ν_{max}/cm^{-1} (solid): 3360 cm^{-1} (alcohol O-H stretch), 2979 cm^{-1} (carboxylic acid O-H stretch), 1718 cm^{-1} (ester C=O stretch), 1452 cm^{-1} (alkane C-H stretch), 1244 cm^{-1} (C=S stretch), 1143 cm^{-1} (ester C-O stretch) and 990 cm^{-1} (C-S stretch).

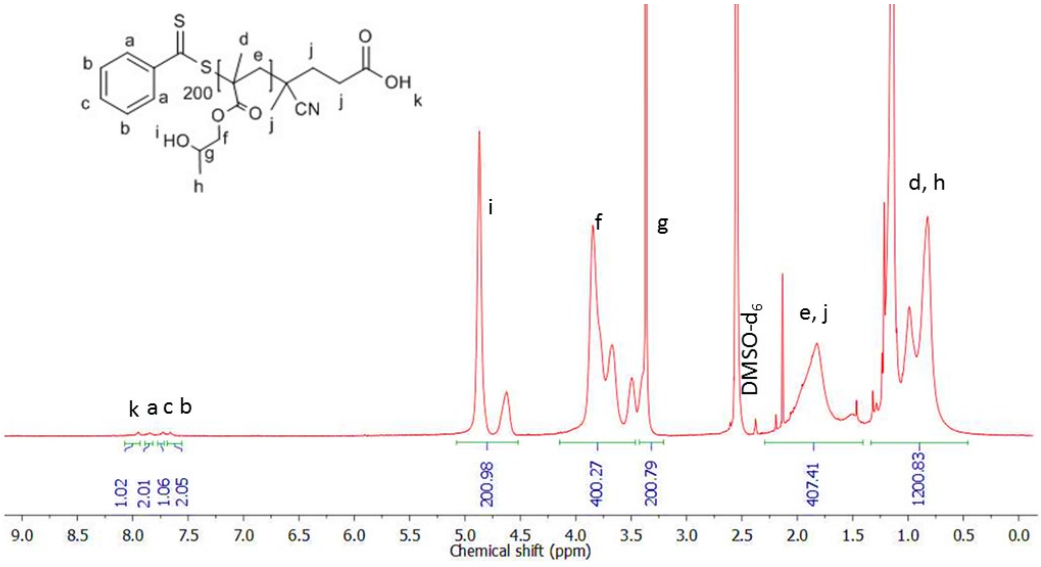

Figure 4. 4. The 500 MHz ^{1}H-NMR spectrum of $PHPMA_{200}$ in DMSO-d_6 at 25 °C.

$PHPMA_{80}$: 1.17 g, 86.3 wt. % (pale yellow transparent gel). APC (THF, PMMA standards):

M_w= 11700 g mol^{-1}. Dispersity= 1.15. ^{1}H-NMR (500 MHz, DMSO-d_6, δ, ppm): 8.21 – 8.18 (s, 1H, COOH), 7.84 – 7.79 (d, 2H, ArH), 7.78 – 7.68 (t, 1H, ArH), 7.67 – 7.43 (d, 2H, ArH), 5.02 – 4.49 (m, 80H, $(OCH_2CHOHCH_3)_{80}$), 3.80 – 3.62 (m, 160H, $(OCH_2CHOHCH_3)_{80}$), 3.61 – 3.29 (m, 80H, $(OCH_2CHOHCH_3)_{80}$), 2.20 – 1.63 (m, 160H, $(CH_3CCH_2)_{80}CCH_3CNCH_2CH_2$), 1.53 – 1.29 (m, 7H, $CH_3CNCH_2CH_2$), 1.28 – 0.68 (m, 480H, $(CH_3CCOOCH_2CHOHCH_3)_{80}$). FTIR: ν_{max}/cm^{-1} (solid): 3351 cm^{-1} (alcohol O-H stretch), 2924 cm^{-1} (carboxylic acid O-H stretch), 1714 cm^{-1} (ester C=O stretch), 1452 cm^{-1} (alkane C-H stretch), 1244 cm^{-1} (C=S stretch), 1146 cm^{-1} (ester C-O stretch) and 994 cm^{-1} (C-S stretch).

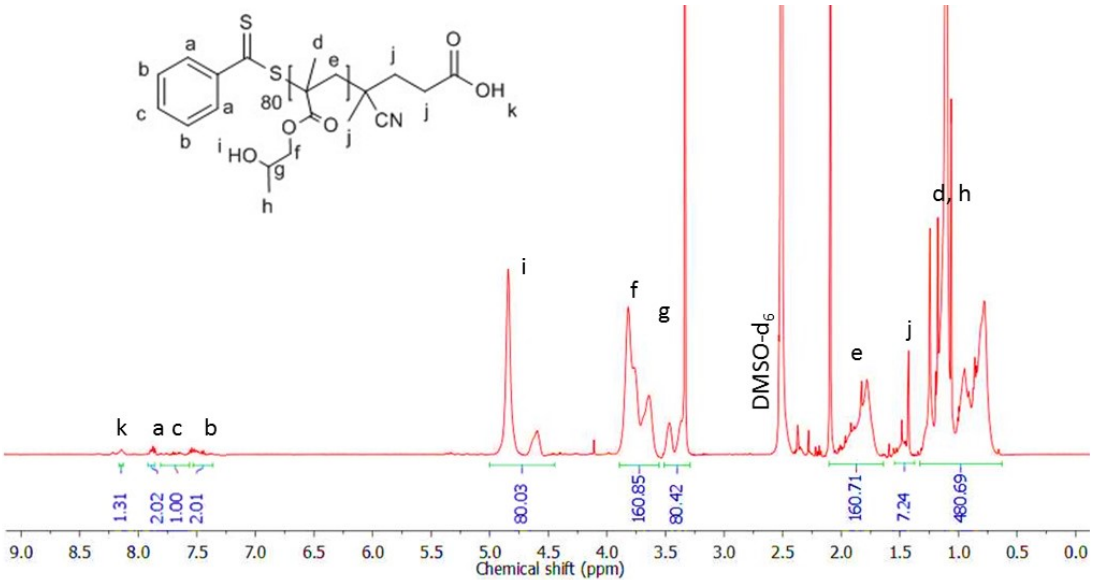

Figure 4. 5. The 500 MHz ^{1}H-NMR spectrum of $PHPMA_{80}$ in DMSO-d_6 at 25 °C.

4.2.3 Cytotoxicity assays

MCF-7, MDA-MB-231 cells were obtained from ECACC and MDA-MB- 453, MCF10A and HB2 from American type culture collection (ATCC). All were cultured in DMEM (Invitrogen) supplemented with 10 % (v/v) FCS at 37 °C in 5 % CO_2 apart from MCF10A which were cultured in DMEM/F12 supplemented with 5 % (v/v) horse serum, 20 ng mL^{-1} epidermal growth factor, 0.5 ug mL^{-1} hydrocortisone, 10 ug mL^{-1} insulin and 100 ng mL^{-1} cholera toxin. The vehicle control is tissue culture media containing 0.1% (v/v) DMSO. The cells were certified mycoplasma-free and were STR profiled for verification. $5x10^3$ MCF-7 cells, $1x10^4$ MDA-MB-231 cells, $2x10^4$ MDA-MB-453, 5 x 10^3 MCF10A and 4 x 10^3 HB2 cells were plated per well in 96-well plates. 24 hours later, Dox-loaded polymers were added to the cells in quadruplicate at each concentration. Equivalent

concentrations of polymer alone were also added to cells alongside free Dox. Cells were incubated with the polymers and drug for 72 hours before the medium was replaced with 0.5 mg mL^{-1} MTT-containing medium. After incubation for 3 hours at 37 °C, the medium was removed and DMSO was added. The absorbance at 620 nm of each well was read on a plate-reader (BertholdTech Mithras). Each entire experiment was carried out in quadruplicate. To obtain an IC_{50} value, the results were fitted with a three-parameter log(inhibitor) vs. response curve or a log(inhibitor) vs normalised response variable slope curve using GraphPad Prism software version 8.0.0.

4.3 Results and discussion

4.3.1 PBLG-*b*-PEG synthesis

The hydroxyl group of MeO-PEG was used to initiate the BLG NCA ROP to afford an ester-containing polymer, using MSA as the acid catalyst (Scheme 4.1). The amine group is protonated, restricting propagation, before DIPEA was added to trigger amine deprotonation and polymerisation. PBLG chain lengths of 2, 26 and 35, in PBLG-*b*-PEG_{113}, were synthesised in order to produce nanoparticles of varied dimensions. Dox-loaded $PBLG_{26}$-*b*-PEG_{113} nanoparticles and $PHPMA_{200}$ were dissolved in DMSO, a Dox-loaded gel depot was formed by injecting the prepared DMSO solution in pH 6.5 acetate buffer solution, significant amount of Dox released at 37 °C in the pH 6.5 environment (Scheme 4.1).

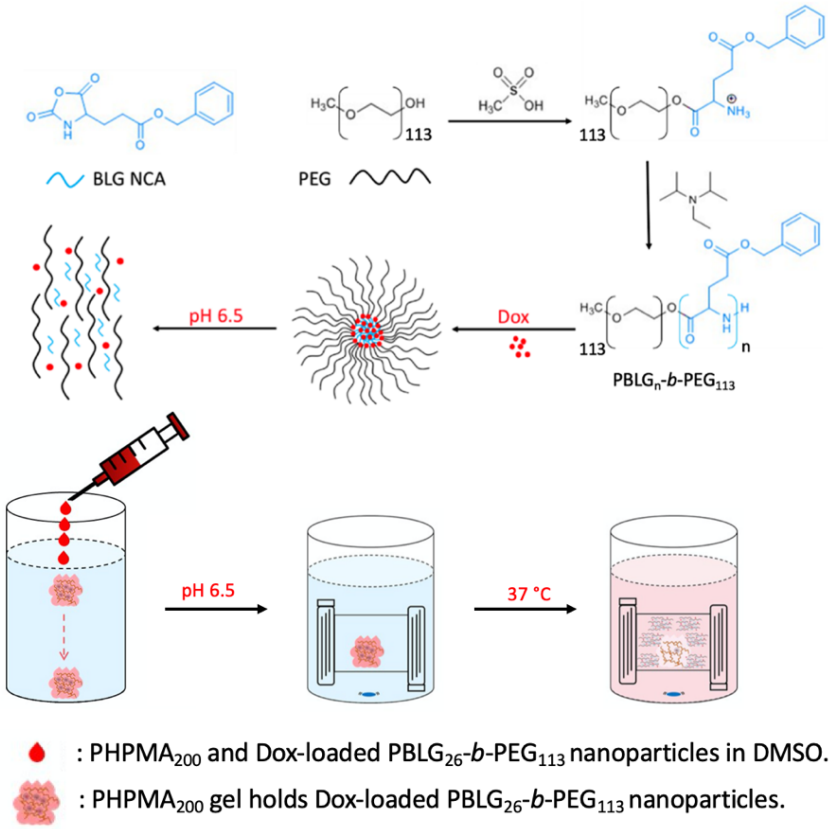

Scheme 4. 1. Reaction outline for the creation of PBLG$_n$-*b*-PEG$_{113}$ nanoparticles that contain ester linkages to facilitate Dox release when stored in acidic solution. An injectable Dox-loaded nanoparticle gel depot was synthesised by dissolving PHPMA$_{200}$ gel and Dox-loaded PBLG$_{26}$-*b*-PEG$_{113}$ nanoparticles in DMSO then injected in pH 6.5 acetate buffer solution.

The chemical structures and molecular weight of PBLG-*b*-PEG macromolecules were confirmed by ^{1}H NMR spectroscopy and APC (Figures 4.1-4.3 and Table 4.1). The extent of PBLG grafting from PEG was determined by normalising the proton environment that corresponds to the four protons of PEG (h in Figures 4.1-4.3) and comparing the integration value to peaks that correspond to PBLG (a, b, c, d, e, f, i and g in Figures 4.1-4.3). This data confirmed the successful preparation of the target block copolymers PBLG$_2$-*b*-PEG$_{113}$, PBLG$_{26}$-*b*-PEG$_{113}$ and PBLG$_{35}$-*b*-PEG$_{113}$. The molecular weight of PBLG$_2$-*b*-PEG$_{113}$, PBLG$_{26}$-*b*-PEG$_{113}$ and PBLG$_{35}$-*b*-PEG$_{113}$ determined by APC (Table 4.1), the theoretical and actual molecular weight are comparable. FTIR analysis was used to confirm the presence of expected ester (C=O stretching 1742 cm^{-1}, 1731 cm^{-1}, 1650 cm^{-1} and 1743 cm^{-1}), ether (C-O stretching 1096 cm^{-1}), and aromatic groups (C=C bending 745cm^{-1} and 698 cm $^{-1}$) (Figure 4.6).

Table 4. 1. Advanced Polymer Chromatography for polymers created for use as nanoparticles.

Copolymers	Theoretical M_w (g. mol^{-1})	Actual M_w (g. mol^{-1})	PDI
$PBLG_2$-*b*-PEG_{113}	5442	5300	1.18
$PBLG_{26}$-*b*-PEG_{113}	10698	9100	1.13
$PBLG_{35}$-*b*-PEG_{113}	12669	12000	1.16

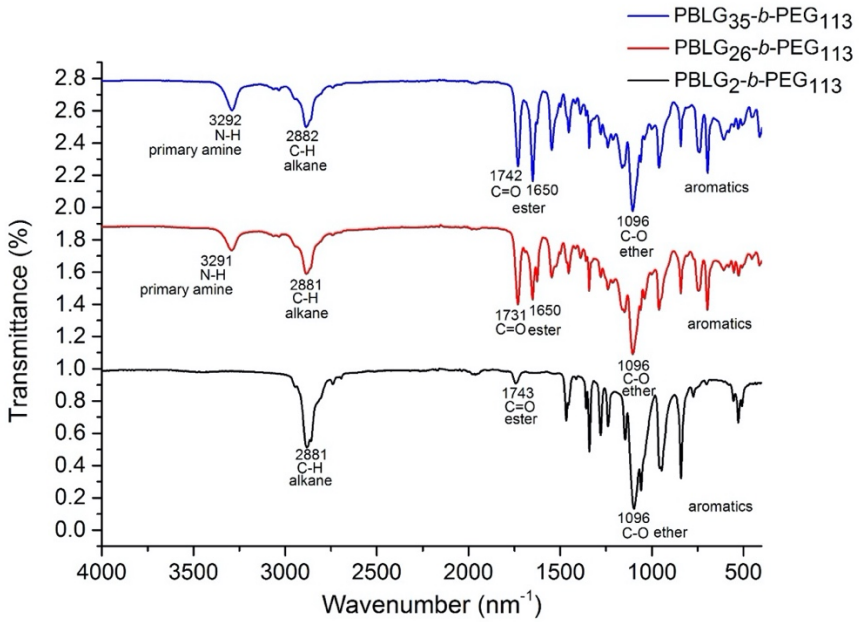

Figure 4. 6. FTIR spectra of dialysed $PBLG_{35}$-*b*-PEG_{113}, dialysed $PBLG_{26}$-*b*-PEG_{113} and dialysed $PBLG_2$-*b*-PEG_{113}.

RAFT polymerisation featuring 4-cyano-4-((phenylcarbonothioyl)thio)pentanoic acid (RAFT agent), AAPH (initiator) and HPMA was performed in an acetone/water mixture, yielding PHPMA with 80 and 200 repeat units. In the ^{1}H NMR spectra of $PHPMA_{200}$ (Figure 4.4) and $PHPMA_{80}$ (Figure 4.5), the integral of the aromatic proton environments a, c and b were normalised to 2, 1, and 2. Then the chain lengths of PHPMA were measured using the integral of the proton environments d, e, f, g and h, indicating the synthesised polymers were $PHPMA_{200}$ and $PHPMA_{80}$. FTIR spectra revealed that alcohol (O-H stretching 3360 cm^{-1} and 3351 cm^{-1}), ester (C=O stretching 1718 cm^{-1}, 1714 cm^{-1}, 1143 cm^{-1} and 1146 cm^{-1}), C=S (stretching 1244 cm^{-1}) and C-S (stretching 990 cm^{-1} and 994 cm^{-1}) groups were in $PHPMA_{200}$ and $PHPMA_{80}$ (Figure 4.7). The molecular weight of $PHPMA_{200}$ and $PHPMA_{80}$ determined by APC (Table 4.2), the theoretical and actual molecular weights are comparable. Therefore, polymer analysis via ^{1}H NMR

spectroscopy, FTIR spectroscopy and APC (Figures 4.4-4.5, 4.7 and Table 4.2) confirmed successful $PHPMA_{200}$ and $PHPMA_{80}$ synthesis.

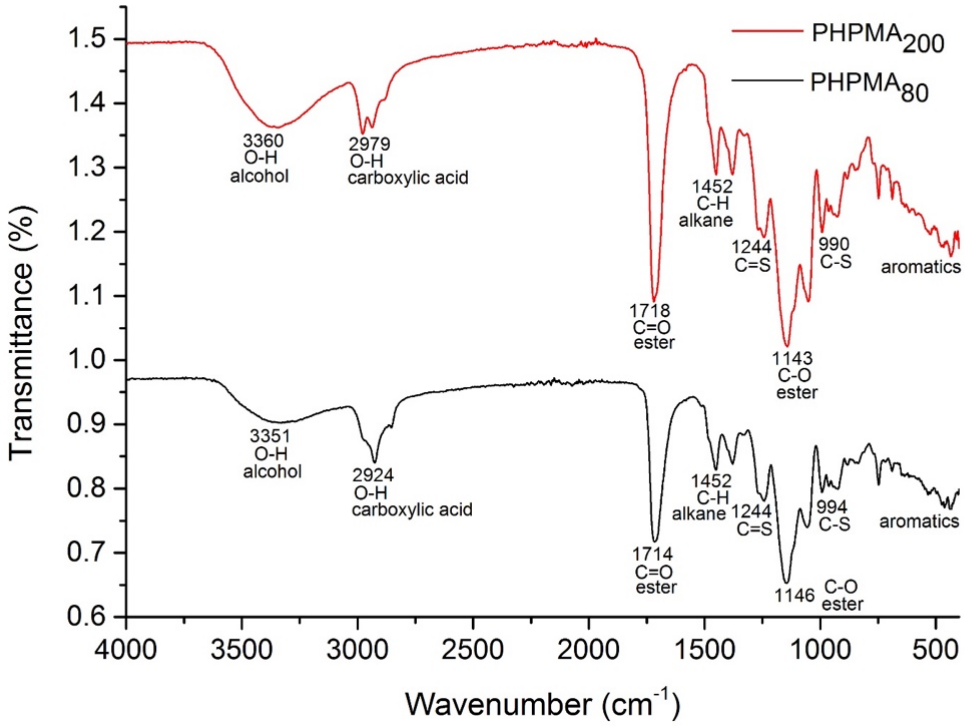

Figure 4. 7. FTIR spectra of $PHPMA_{200}$ and $PHPMA_{80}$.

Table 4. 2. Advanced Polymer Chromatography for the polymers created for use as the depot.

Polymers	Theoretical M_w (g. mol^{-1})	Actual M_w (g. mol^{-1})	PDI
$PHPMA_{80}$	11799	11700	1.15
$PHPMA_{200}$	29079	28500	1.24

4.3.2 Nanoparticle Formation

Nanoparticles were produced from the three polymer types by coacervation [49]. Each polymer was dissolved in DMF then added dropwise into deionised water with stirring, making a concentration of 0.1 mg mL^{-1}. Intensity size distribution was used for particle size measurements. Refractive index and absorption of PBLG-*b*-PEG_{113} cannot be found in the literature. Therefore, refractive index and absorption of PEG_{113} were used which were 1.402 and 0.100 [50], respectively. The volume and number size analysis need accurate refractive index and absorption of the sample but intensity size analysis depends on light scattering of the sample. Therefore, intensity size analysis of the sample

is more reliable. DLS analysis revealed increased nanoparticle size with an increased proportion of hydrophobic PBLG within the block copolymer (Table 4.3, DLS data presented in Figure A4.1). The correlogram of $PBLG_{26}$-*b*-PEG_{113} was shown in Figure 4.8. The particle size of $PBLG_{26}$-*b*-PEG_{113} was (158±2) nm, the small (light) the nanoparticles, the fast they were, so the correlogram decayed quick and had a steep gradient. PDI values of $PBLG_2$-*b*-PEG_{113} and $PBLG_{26}$-*b*-PEG_{113} were less than, or close to 0.3, indicating the particle stability. PDI equals 0.3 (specific to this kind of polymer nanoparticles) is the limit before the intensity size distribution splits into two. Therefore, PDI value below 0.3 was considered that the nanoparticles were stable in the media. $PBLG_{35}$-*b*-PEG_{113} nanoparticles were considered unstable, after 21 days of storage due to the recorded PDI value (0.437). Therefore, $PBLG_2$-*b*-PEG_{113} and $PBLG_{26}$-*b*-PEG_{113} nanoparticles were chosen for drug release studies due to their appropriate size and PDI values after 21 days storage in aqueous solution.

Table 4. 3. DLS data of $PBLG_2$-*b*-PEG_{113}, $PBLG_{26}$-*b*-PEG_{113} and $PBLG_{35}$-*b*-PEG_{113} nanoparticles after 21 days. The hydrophobic content refers to the number of PBLG repeat units as a percentage of the total polymer repeat units.

Copolymers	Hydrophobic chain length (%)	Size (nm)	PDI
$PBLG_2$-*b*-PEG_{113}	1.7	85 ±9	0.284
$PBLG_{26}$-*b*-PEG_{113}	18.7	158 ±2	0.327
$PBLG_{35}$-*b*-PEG_{113}	23.6	311 ±3	0.437

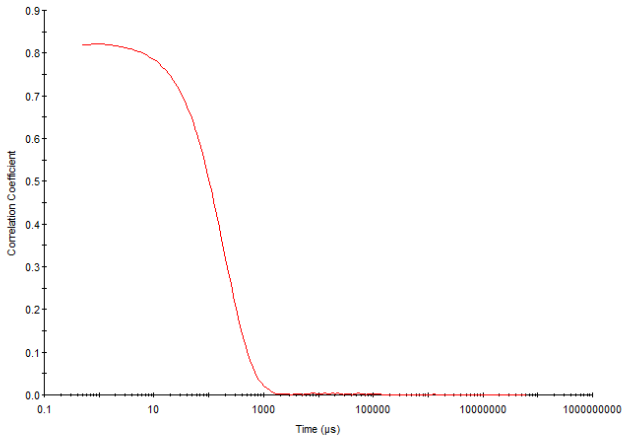

Figure 4. 8. Correlogram of $PBLG_{26}$-*b*-PEG_{113} nanoparticles in deionised water at room temperature.

Dr. David Green conducted SEM analysis for $PBLG_2$-*b*-PEG_{113} and $PBLG_{26}$-*b*-PEG_{113} nanoparticles. SEM analysis confirmed the presence of spherical nanoparticles (Figure 4.9). Particle size distributions of the SEM images (Figure 4.9 a, b), the R^2 values were 0.30 and 0.33, respectively (less than 0.85) so cannot be fitted to acceptable quality. Particle size analysed by SEM of $PBLG_2$-*b*-PEG_{113} and $PBLG_{26}$-*b*-PEG_{113} nanoparticles were smaller compared to that measured by DLS which were (85±9)nm and (158±2)nm, respectively. In DLS analysis, the nanoparticles were in aqueous state, forming hydrogen bonding interactions between the polymer chains (amine groups) and aqueous solution. Air-drying method was used for preparing SEM samples so the nanoparticles lost the hydrogen bonding interactions which may lead to particle size decrease. The dimensions of Dox-loaded $PBLG_2$-*b*-PEG_{113} and $PBLG_{26}$-*b*-PEG_{113} nanoparticles were then measured by DLS (Table 4.4). In both cases the mean nanoparticle diameter was less than 200 nm. The PDI values corresponding to $PBLG_2$-*b*-PEG_{113} exceeded 0.3, but the PDI values corresponding to $PBLG_{26}$-*b*-PEG_{113} nanoparticles remained less than 0.3, even after 21 days storage in solution.

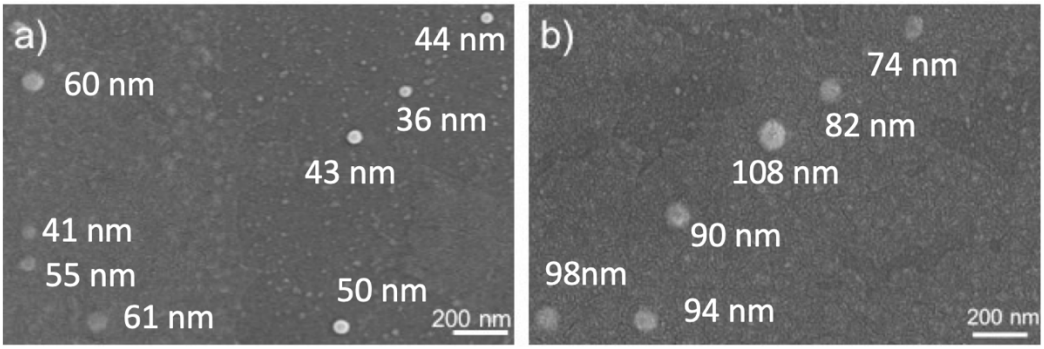

Figure 4. 9. SEM images of a) $PBLG_2$-*b*-PEG_{113} and b) $PBLG_{26}$-*b*-PEG_{113}; scale bars represent 200 nm.

Table 4. 4. DLS data revealing the size and stability of Dox-loaded $PBLG_2$-*b*-PEG_{113} and $PBLG_{26}$-*b*-PEG_{113} nanoparticles in water.

Copolymers	24h		7 days		14 days		21 days	
	Size (nm)	PDI	Size (nm)	PDI	Size (nm)	PDI	Size (nm)	PDI
$PBLG_2$-*b*-PEG_{113}	94 ± 5	0.478	93 ± 4	0.681	91 ± 7	0.533	86 ± 8	0.618
$PBLG_{26}$-*b*-PEG_{113}	160 ± 11	0.234	162 ± 16	0.225	160 ±18	0.231	161 ± 19	0.233

4.3.3. Dox Release Studies

Dox release studies from $PBLG_2$-*b*-PEG_{113} and $PBLG_{26}$-*b*-PEG_{113} nanoparticles were performed in both pH 7.4 (PBS) and pH 6.5 (TRIS acetate) buffer solutions. Extremely limited loading efficiencies of 5% (loading per total polymer mass) were recorded for Dox encapsulation within $PBLG_2$-*b*-PEG_{113} nanoparticles in both pH 6.5 and pH 7.4 aqueous solution. In contrast, Dox loading efficiencies of 44% were recorded for $PBLG_{26}$-*b*-PEG_{113} nanoparticles in solutions of pH 6.5 and pH 7.4. Such enhanced drug loading may be ascribed to the more sizeable hydrophobic compartment that $PBLG_{26}$-*b*-PEG_{113} nanoparticles present. Initially, Dox release was monitored from both nanoparticle sets at 37 °C. After 576 h, Dox release to pH 6.5 solution (39%, $PBLG_2$-*b*-PEG_{113}; 24%, $PBLG_{26}$-*b*-PEG_{113}) exceeded release to pH 7.4 solution (10%, $PBLG_2$-*b*-PEG_{113}; 1%, $PBLG_{26}$-*b*-PEG_{113}) (Figure 4.10). The rate of release into pH 6.5 buffer solution decreased over time, possibly due to Dox having to travel a greater distance increasingly from the nanoparticle core as time progressed, although release was very gradual; after 48 h Dox release from $PBLG_2$-*b*-PEG_{113} nanoparticles was 10% and release from $PBLG_{26}$-*b*-PEG_{113} nanoparticles was 12%. The environmental temperature was increased after 576 h to 41 °C as cancer tumour tissue is slightly higher in temperature compared to healthy tissue in the human body [51-53], but Dox release was not significantly enhanced. The excessive release of Dox from $PBLG_2$-*b*-PEG_{113} nanoparticles in pH 7.4 solution, coupled with limited Dox loading, rendered the nanoparticles imperfect as potential drug delivery vehicles. However, only 1 % of loaded Dox was released from $PBLG_{26}$-*b*-PEG_{113} nanoparticles in pH 7.4 buffer solution after 744 hours; such negligible unwanted release makes this class of nanoparticle an excellent drug delivery vehicle candidate. In a pH 6.5 environment, 24 % of Dox was released progressively from $PBLG_{26}$-*b*-PEG_{113} nanoparticles after 744 hours, offering a system that permits prolonged drug release, minimising the number of repeat administrations that the patient has to suffer.

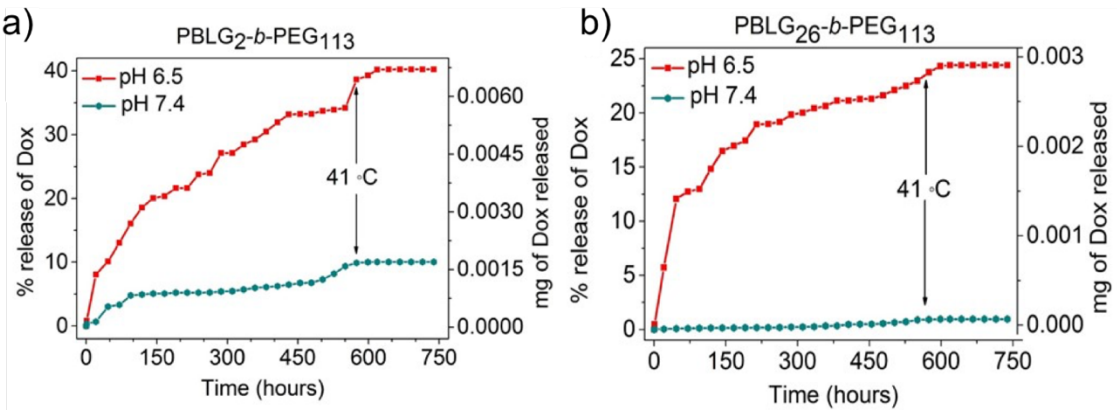

Figure 4. 10. a) Doxorubicin release from $PBLG_2$-*b*-PEG_{113} nanoparticles in pH 6.5 and pH 7.4 environments. b) Doxorubicin release from $PBLG_{26}$-*b*-PEG_{113} nanoparticles in pH 6.5 and pH 7.4 environments.

4.3.4. Cytotoxicity Analysis

Dr. Nicola Ingram (from St James Hospital) did cytotoxicity analysis for Dox-loaded $PBLG_{26}$-*b*-PEG_{113} nanoparticles and vacant $PBLG_{26}$-*b*-PEG_{113} nanoparticles. $PBLG_{26}$-*b*-PEG_{113} nanoparticles that contained, or lacked, Dox were assessed against MCF-7 breast cancer cells, triple-negative breast cancer cells (MDA-MB-231), and Her2-enriched (ER and PR negative) breast cancer cells (MDA-MB-453) in order to assess their ability to treat chemo-refractory disease. Free Dox was used as a positive control (Table 4.5). Negligible cell death was found for empty polymer nanoparticles at 37 °C for all types of breast cancer cells proving $PBLG_{26}$-*b*-PEG_{113} nanoparticles to be non-toxic (Figure 4.11). Dox-loaded nanoparticles were assessed against the same three cancer cell lines, and significant cell death occurred with enhanced polymer concentration. Such nanoparticles were not as lethal as unloaded/free Dox added to the cell types at the same concentration, signifying the effective Dox encapsulation within, and continuous Dox release from, the nanoparticles. The difference in IC_{50} values between the polymer nanoparticles, Dox-loaded nanoparticles, and free Dox are significantly different for each cell line. The IC_{50} values of Dox-loaded $PBLG_{26}$-*b*-PEG_{113} nanoparticles [(15±0.39)μg mL^{-1}, (65±0.58)μg mL^{-1}, (4.7±0.34)μg mL^{-1} and (10±0.66)μg mL^{-1}] were larger than the IC_{50} values of free Dox of each cell lines [(0.6±0.33)μg mL^{-1}, (2.0±0.31)μg mL^{-1}, (4.8±0.33)μg mL^{-1}, (0.2±0.30)μg mL^{-1} and (0.4±0.51)μg mL^{-1}]. Higher concentration of the Dox-loaded nanoparticles was needed compared to that of free Dox in order to kill 50 % of cells. The

Dox-loaded nanoparticles need to break ester linkage then release Dox. With enhanced Dox-loaded nanoparticle concentration, the amount of Dox release increased, resulting in cancer cell death. Therefore, the IC_{50} values of Dox-loaded nanoparticles were higher than free Dox. The Dox-loaded nanoparticles may have a smoother effect to patients compared to free Dox and human body may not get severe side-effects due to anti-cancer therapy. For R^2 values, the closer to 1, the better the curve fitted the data. However, when comparing with the IC_{50} values, the best fit for the majority of cells and particles must be chosen.

Table 4. 5. The IC_{50} values obtained for the cell lines tested.

	IC_{50} ($\mu g\ mL^{-1}$)	
	Dox loaded (R^2)	Free dox (R^2)
MCF-7	15 ± 0.39(0.8381)	0.6 ± 0.33(0.8900)
MDA-MB-231	65 ± 0.58(0.8814)	2.0 ± 0.31(0.9294)
MDA-MB-453	ambiguous	4.8 ± 0.33(0.9069)
HB2	4.7 ± 0.34(0.8759)	0.2 ± 0.30(0.9545)
MCF10A	10 ± 0.66(0.7111)	0.4 ± 0.51(0.8199)

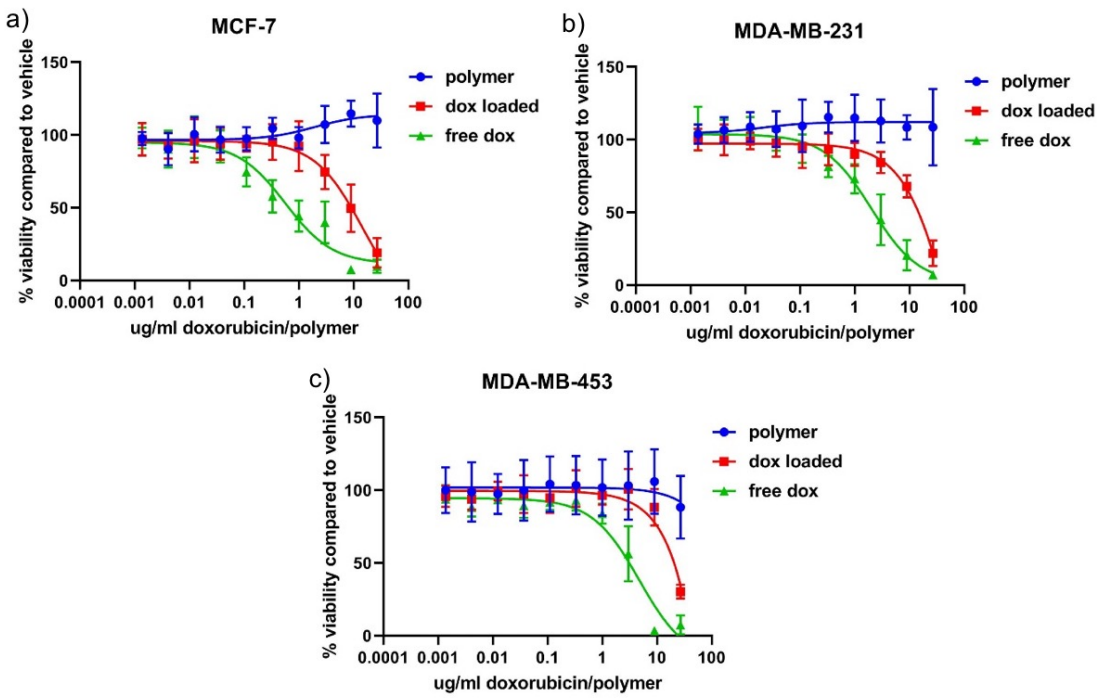

Figure 4. 11. Cytotoxicity of $PBLG_{26}$-*b*-PEG_{113} either empty (polymer only) or loaded with doxorubicin (dox loaded) on three breast cancer cell lines. Serial dilutions of polymer or dox polymer were incubated with a) MCF-7, b) MDA-MB-231 (triple negative) and c) MDA-MB-453 (double negative) cell lines.

The nanoparticles were assessed against non-cancer cell lines to determine if their therapeutic action was specific against cancer cells. HB2 and MCF10A normal breast cell lines were sensitive to Dox delivered *via* nanoparticle encapsulation and as free drug (Figure 4.12). Surprisingly, the polymer nanoparticles demonstrated some cytotoxic effect versus HB2 cells at concentrations of 10 µg mL^{-1} and greater, although further studies are required to determine if such extensive nanoparticle accumulation, and cell death, is likely to occur *in vivo.* HB2 and MCF10 were two normal cell lines which had lower IC_{50} values of both Dox-loaded nanoparticles and free Dox compared to that of the three cancer cell lines, showing less drug resistance than the breast cancer cell lines. Although the IC_{50} values were greater when nanoparticles were employed to encapsulate dox ((4.7±0.34)µg mL^{-1} (nanoparticle) *vs*. (0.2±0.30)µg mL^{-1} (free dox) for HB2 cells, (10±0.66)µg mL^{-1} (nanoparticle) *vs.* (0.4±0.51)µg mL^{-1} (free dox) for MCF10A cells), the action of the nanoparticles against non-cancerous cells suggest they are predominantly suited for site specific injection at the tumour site.

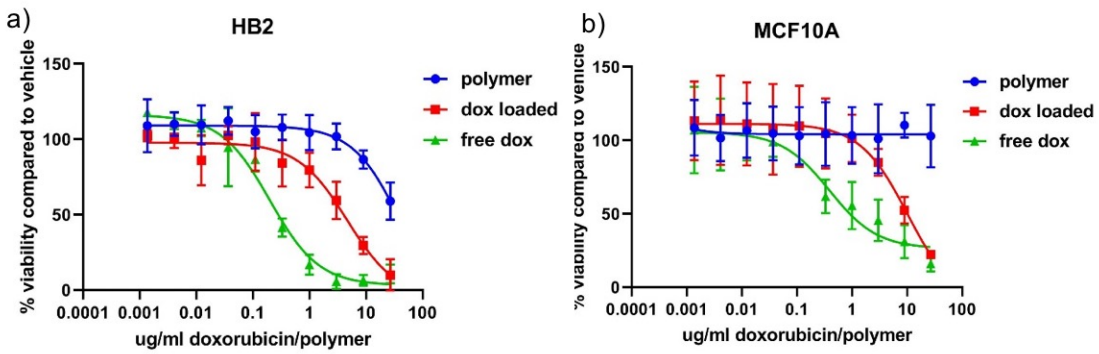

Figure 4. 12. Cytotoxicity of $PBLG_{26}$-*b*-PEG_{113} particles either empty (polymer only) or loaded with doxorubicin (dox loaded) against two normal breast cell lines. Serial dilutions of polymer particles or dox loaded polymer particles were incubated with a) HB2 and b) MCF10A cell lines.

4.3.5. $PHPMA_{200}$ Injectable Depot Creation

In order to realise localised Dox release, a polymeric material capable of undergoing a solution to gel transition in aqueous solution was developed. PHPMA was identified as a suitable biocompatible polymer that could act as an injectable vehicle capable of forming a matrix in aqueous solution. Once formed, the matrix holds the nanoparticles specifically at the tumour site, limiting their access to healthy cells. In order to treat cancer, Dox stops unlimited proliferation of cancer cells. At the same time, naturally fast growth and divide human cells, for instance hair follicle stem cells (responsible for human hair growth), are also affected by Dox, resulting in temporary hair loss as a side-effect [54-55]. Therefore, localised Dox delivery to tumours (without destroying healthy cells) is vital. The transformation of PHPMA from solution to gel phase was achieved by dissolving the polymer in DMSO, before injecting the solution into aqueous solution to form a scaffold maintained by polymer chain interactions (Figure 4.13).

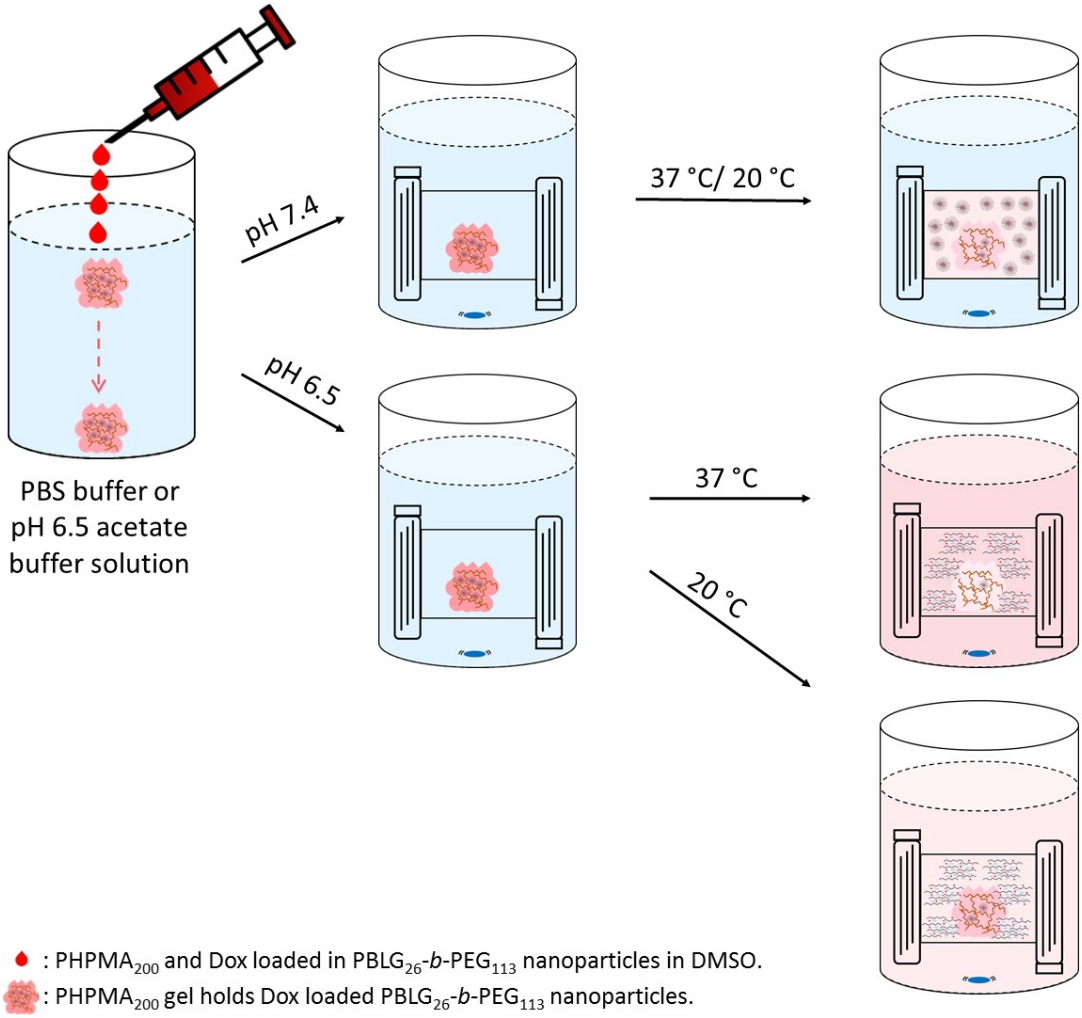

Figure 4. 13. Dox release from $PBLG_{26}$-*b*-PEG_{113} nanoparticles encapsulated in $PHPMA_{200}$ gel in pH 7.4 PBS and pH 6.5 acetate buffer solutions, at 37 °C and at 20 °C.

$PHPMA_{80}$ was unable to form stable gels, and therefore could not entrap Dox-loaded $PBLG_{26}$-*b*-PEG_{113} nanoparticles, in either pH 6.5 or 7.4 buffered solutions. However, $PHPMA_{200}$ was able to form a depot that contains a vacant core and smooth surface in both aqueous solutions, and so was progressed to be used as the injectable depot (Figure 4.14). There were holes formed inside the lyophilised $PHPMA_{200}$ depot which may be due to ice crystal growth during lyophilisation.

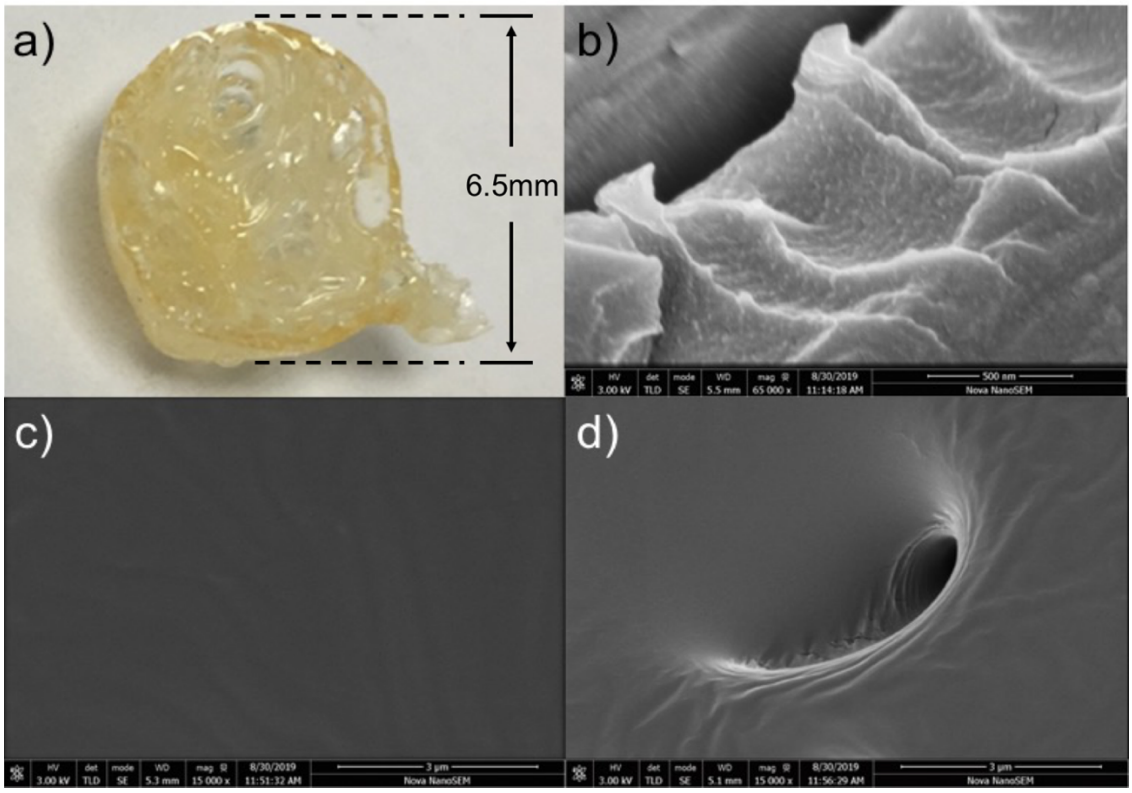

Figure 4. 14. a) Lyophilised $PHPMA_{200}$ gels were subject to SEM analysis. b) The hollow core contained a rough surface; scale bar represents 500 nm. c) The surface was smooth and largely pristine; scale bar represents 3 μm. d) although some pores were detected; scale bar represents 3 μm.

The suitability of $PHPMA_{200}$ as an injectable depot capable of storing Dox-loaded nanoparticles was then determined. Free Dox or Dox-loaded $PBLG_{26}$-*b*-PEG_{113} nanoparticles were added to a $PHPMA_{200}$ solution in DMSO. A depot containing either free Dox or Dox-loaded nanoparticles was then formed by injecting each solution into PBS buffer (Figure 4.15). $PHPMA_{200}$ depot did not sequester free dox, resulting in considerable release of dox into the PBS buffer supernatant (pH 7.4) within 72 hours. Conversely, $PHPMA_{200}$ depot that contained Dox-loaded $PBLG_{26}$-*b*-PEG_{113} nanoparticles withheld the chemotherapeutic payload in PBS buffer (pH 7.4), highlighting the significance of the pH-responsive nanoparticles within the formulation.

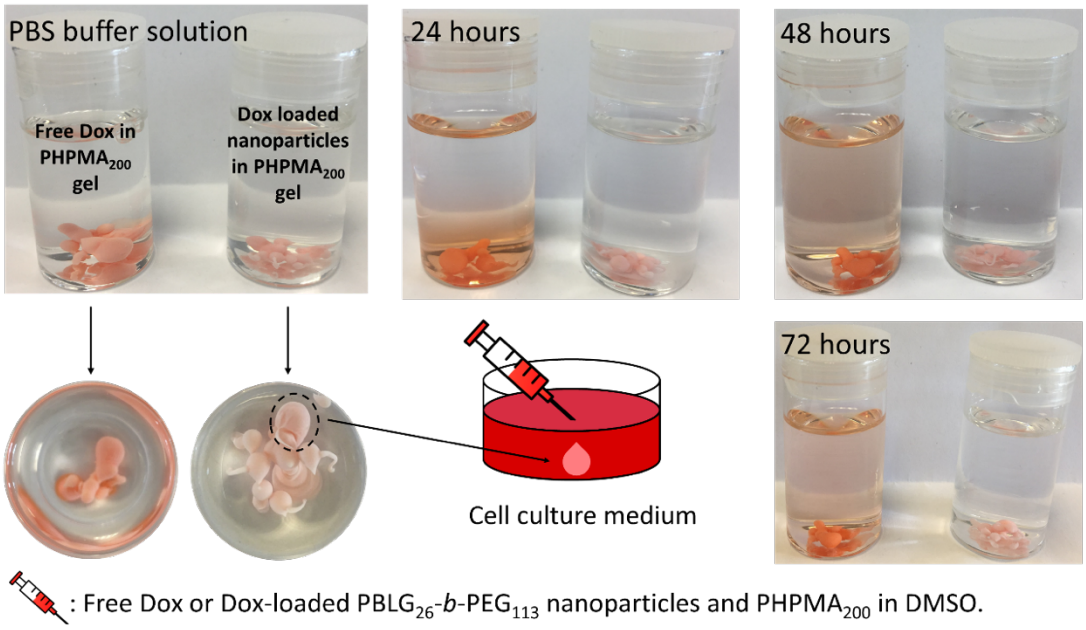

Figure 4. 15. Comparison of free Dox and Dox-loaded $PBLG_{26}$-*b*-PEG_{113} nanoparticles in $PHPMA_{200}$ in PBS buffer solution.

Both gels contain an equal mass of Dox; Free Dox loading = 0.063 mg of free Dox, and 0.46 mL of Dox containing $PBLG_{26}$-*b*-PEG_{113} nanoparticles in DMSO, with 44% loading efficiency, contain 0.063 mg of Dox. $PHPMA_{200}$ gel depot was utilised as an injective media which was designed to encapsulate the Dox-loaded nanoparticles or free Dox. Free Dox released from $PHPMA_{200}$ gel depot after 24 hours which might be due to Dox being a small molecule. Dox did not release from the Dox-loaded nanoparticles after 72 hours because the pH-responsive property of $PBLG_{26}$-*b*-PEG_{113}, the ester linkage cannot break in PBS buffer (pH 7.4) and release Dox.

Dr. Nicola Ingram did cytotoxicity analysis for $PHPMA_{200}$ gel depot, $PBLG_{26}$-*b*-PEG_{113} nanoparticles in $PHPMA_{200}$ gel depot, Dox-loaded $PBLG_{26}$-*b*-PEG_{113} nanoparticles in $PHPMA_{200}$ gel depot and free Dox in $PHPMA_{200}$ gel depot. The cytotoxicity of the $PHPMA_{200}$ depot and $PHPMA_{200}$ depot formed in the presence of Dox-loaded $PBLG_{26}$-*b*-PEG_{113} nanoparticles were determined by injecting PHPMA and Dox-loaded nanoparticles in DMSO, respectively, directly into cell culture medium that contained either MDA-MB-231 triple-negative breast cancer cells or HFFF2 fibroblast cells (Figure 4.16). This was conducted to determine the feasibility of applying the injectable material *in vivo* against normal and cancerous cells. The cell viability of MDA-MB-231 cells remained above 88 % after 48 hours in all instances; cell viability against the PHPMA depot with Dox-loaded $PBLG_{26}$-*b*-PEG_{113} nanoparticles incorporated was (88±2)% after

48 hours. At least 75 % of HFFF2 fibroblast cells remained viable after 48 h in all instances; cell viability against the PHPMA gel with Dox-loaded $PBLG_{26}$-*b*-PEG_{113} nanoparticles included was (86±11)% after 48 hours. A Two-way ANOVA test was conducted to determine statistical difference between samples/cell lines (Table 4.6). The results demonstrate the appropriateness of the system as an injectable material, particularly for the injection, localisation and potential long-term release of a chemotherapeutic at a tumour tissue site. All the P values were less than 0.05 which means treatments 1 and 2 were significantly different and so did not have any relationship.

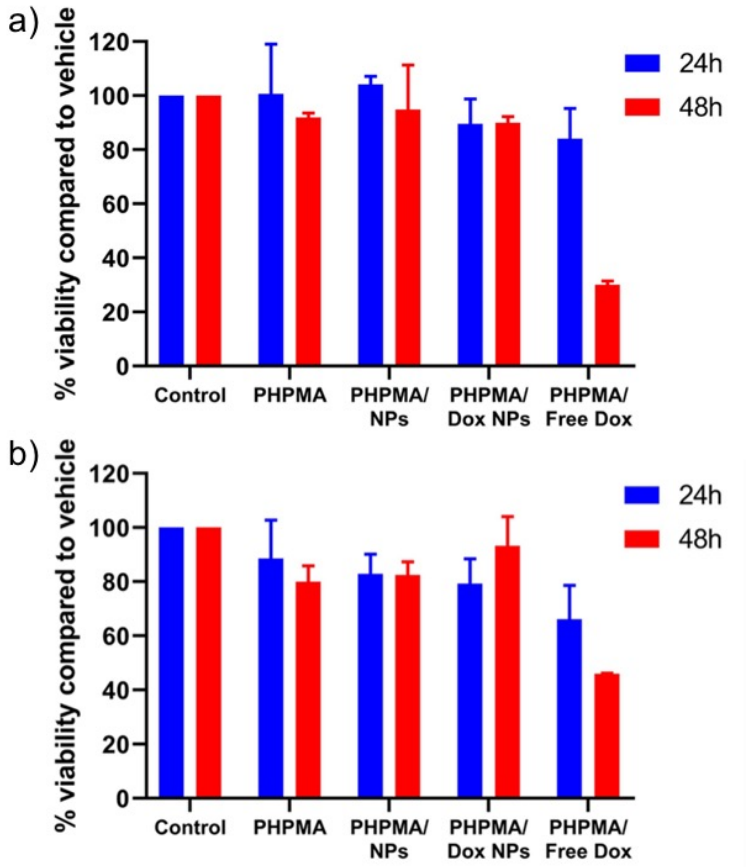

Figure 4. 16. Cell viability studies for the *in situ* formation of $PHPMA_{200}$ gel, $PHPMA_{200}$ with blank $PBLG_{26}$-*b*-PEG_{113} nanoparticles incorporated, and $PHPMA_{200}$ with Dox-loaded $PBLG_{26}$-*b*-PEG_{113} nanoparticles incorporated against a) MDA-MB-231 triple-negative breast cancer cells and b) HFFF2 fibroblast cells.

Table 4. 6. Two-way ANOVA test with Tukey's multiple comparison. All other comparisons were not statistically significantly different.

Cell line	Time Point (h)	Treatment 1	Treatment 2	P value
MDA-MB-231	48	Control	PHPMA/free Dox	<0.0001
MDA-MB-231	48	PHPMA	PHPMA/free Dox	0.0004
MDA-MB-231	48	PHPMA/NPs	PHPMA/free Dox	0.0003
MDA-MB-231	48	PHPMA/Dox NPs	PHPMA/free Dox	0.0005
HFFF2	24	Control	PHPMA/free Dox	0.0137
HFFF2	48	Control	PHPMA/free Dox	0.0005
HFFF2	48	PHPMA	PHPMA/free Dox	0.0132
HFFF2	48	PHPMA/NPs	PHPMA/free Dox	0.0084
HFFF2	48	PHPMA/Dox NPs	PHPMA/free Dox	0.013

4.3.6. Dox Release from Nanoparticles Embedded within an Injectable $PHPMA_{200}$ Depot

A detailed release study revealed the control over Dox release that the system presents. An insignificant amount of Dox was initially released from $PBLG_{26}$-*b*-PEG_{113} nanoparticles in $PHPMA_{200}$ gel that was maintained in both pH 6.5 acetate buffer solution and PBS buffer solution, either at room temperature or at 37 °C (Figure 4.17). 4 % Dox release was recorded for the first 192 h when the nanoparticle-loaded gel was maintained in pH 6.5 solution at 37 °C. At this point, enhanced Dox release into the pH 6.5 environment commenced in studies conducted at both room temperature and at 37 °C. After 384 h, 84 % of Dox was released from gel stored in pH 6.5 solution at 37 °C. This compares to 41 % release from gel stored at pH 6.5 at room temperature. Whilst at this time point the depot was intact, it may be surmised that sufficient $PHPMA_{200}$ disassembly had occurred to enable increased interaction between pH 6.5 buffer solution and nanoparticles that have increased mobility, enabling nanoparticle fragmentation and consequent Dox release. When the nanoparticle-loaded gel was maintained in solution of pH 7.4, insignificant Dox release occurred after 500 h, whether the material was heated to 37 °C or not. It can be concluded that Dox release from the reported injectable system is highly sensitive to environmental pH, the extent of release can be modified by

changes in external environmental temperature, and that long-term storage (> 500 h) of Dox within nanoparticle encased gels can be realised. The system offers both rapid Dox release (freely-loaded Dox in the $PHPMA_{200}$ depot), and prolonged Dox release from acid-sensitive nanoparticles that are embedded within the injectable $PHPMA_{200}$ depot.

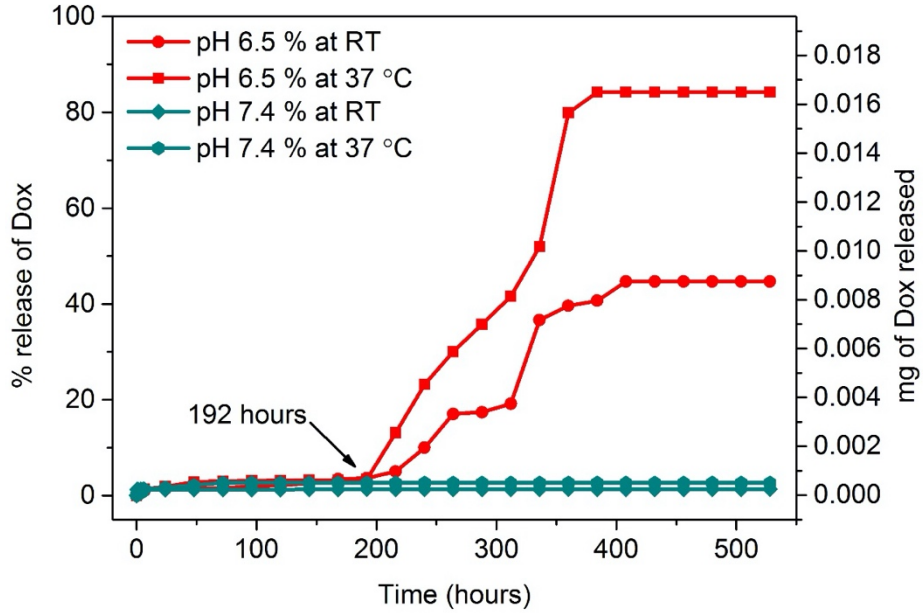

Figure 4. 17. Dox release from $PBLG_{26}$-*b*-PEG_{113} nanoparticles embedded within $PHPMA_{200}$ depot formed in pH 6.5 acetate buffer solution and pH 7.4 PBS buffer solution, at room temperature and at 37 °C.

4.4 Conclusions

pH-Responsive PBLG-*b*-PEG polymer nanoparticles were synthesised via hydroxyl-initiated NCA ROP. The nanoparticles were well separated and stable in pH 7.4 aqueous environment after 21 days, as revealed by DLS analysis. In a pH 6.5 aqueous environment, a considerable amount of Dox (24 %) was released from $PBLG_{26}$-*b*-PEG_{113} nanoparticles after 31 days due to the intended hydrolysis of the ester links that are an essential feature of nanoparticle design. Crucially, a negligible amount of Dox was released from the nanoparticles when they were maintained in aqueous solution of pH 7.4 after 31 days (1 %), suggesting that the formulation may be stored in solution for prolonged periods prior to clinical deployment, an important, but often overlooked, feature of any potential viable drug delivery system. $PBLG_{26}$-*b*-PEG_{113} nanoparticles were non-toxic against a variety of breast cancer cell lines, but Dox-loaded $PBLG_{26}$-*b*-PEG_{113} nanoparticles were toxic against the same breast cancer cells. In order to provide a vehicle that enables nanoparticle injection and perpetuation at a cancerous site, a

$PHPMA_{200}$ depot was developed that formed upon injection into aqueous solution. A limited amount of Dox was released from Dox-loaded $PBLG_{26}$-*b*-PEG_{113} nanoparticles that were withheld within $PHPMA_{200}$ depot that was maintained within PBS buffer solution, both at room temperature and 37 °C. Dox release was enhanced from the same material when stored in pH 6.5 acetate buffer solution at both room temperature (45%) and 37 °C (84%) after 16 days. The combination of pH-responsive $PBLG_{26}$-*b*-PEG_{113} nanoparticles and a thermoresponsive $PHPMA_{200}$ gel depot yields a highly-sensitive injectable delivery system that may be deployed for the localised, highly-controlled and prolonged release of Dox at cancer tumour sites.

4.5 References

1. Chao, Y.H., Liang, Y.H., Fang, G.H., He, H.B., Yao, Q., Xu, H., Chen, Y.R. and Tang, X. Biodegradable Polymersomes as Nanocarriers for Doxorubicin Hydrochloride: Enhanced Cytotoxicity in MCF-7/ADR Cells and Prolonged Blood Circulation. *Pharmaceutical Research.* 2017, **34**(3), pp.610-618.
2. Cui, W., Li, J.B. and Decher, G. Self-Assembled Smart Nanocarriers for Targeted Drug Delivery. *Advanced Materials.* 2016, **28**(6), pp.1302-1311.
3. Blanco, E., Shen, H. and Ferrari, M. Principles of nanoparticle design for overcoming biological barriers to drug delivery. *Nature Biotechnology.* 2015, **33**(9), pp.941-951.
4. Pawar, V.K., Singh, Y., Sharma, K., Shrivastav, A., Sharma, A., Singh, A., Meher, J.G., Singh, P., Raval, K., Bora, H.K., Datta, D., Lal, J. and Chourasia, M.K. Doxorubicin Hydrochloride Loaded Zymosan-Polyethylenimine Biopolymeric Nanoparticles for Dual 'Chemoimmunotherapeutic' Intervention in Breast Cancer. *Pharmaceutical Research.* 2017, **34**(9), pp.1857-1871.
5. Pan, D.Y., Zheng, X.L., Zhang, Q.F., Li, Z.Q., Duan, Z.Y., Zheng, W., Gong, M., Zhu, H.Y., Zhang, H., Gong, Q.Y., Gu, Z.W. and Luo, K. Dendronized-Polymer Disturbing Cells' Stress Protection by Targeting Metabolism Leads to Tumor Vulnerability. *Advanced Materials.* 2020, **32**(14), 1907490.
6. Xu, X.D., Saw, P.E., Tao, W., Li, Y.J., Ji, X.Y., Bhasin, S., Liu, Y.L., Ayyash, D., Rasmussen, J., Huo, M., Shi, J.J. and Farokhzad, O.C. ROS-Responsive Polyprodrug Nanoparticles for Triggered Drug Delivery and Effective Cancer Therapy. *Advanced Materials.* 2017, **29**(33), 1700141.
7. Li, W.C., Liu, S.Q., Yao, H., Liao, G.X., Si, Z.W., Gong, X.J., Ren, L. and Wang, L.G. Microparticle templating as a route to nanoscale polymer vesicles with controlled size distribution for anticancer drug delivery. *Journal of Colloid and Interface Science.* 2017, **508**, pp.145-153.
8. Fenton, O.S., Olafson, K.N., Pillai, P.S., Mitchell, M.J. and Langer, R. Advances in Biomaterials for Drug Delivery. *Advanced Materials.* 2018, **30**(29), 1705328.
9. Zheng, X.L., Pan, D.Y., Chen, M., Dai, X.H., Cai, H., Zhang, H., Gong, Q.Y., Gu, Z.W. and Luo, K. Tunable Hydrophile-Lipophile Balance for Manipulating Structural Stability and Tumor Retention of Amphiphilic Nanoparticles. *Advanced Materials.* 2019, **31**(35), 1901586.
10. Yu, H.Y., Ingram, N., Rowley, J.V., Parkinson, S., Green, D.C., Warren, N.J. and Thornton, P.D. Thermoresponsive polysarcosine-based nanoparticles (vol 7, pg 4217, 2019). *Journal of Materials Chemistry B.* 2019, **7**(48), pp.7795-7795.

11. Paasonen, L., Romberg, B., Storm, G., Yliperttula, M., Urtti, A. and Hennink, W.E. Temperature-sensitive poly(N-(2-hydroxypropyl)methacrylamide mono/dilactate)-coated liposomes for triggered contents release. *Bioconjugate Chemistry.* 2007, **18**(6), pp.2131-2136.
12. Zhou, W.Q., Wang, L., Li, F., Zhang, W.N., Huang, W., Huo, F.W. and Xu, H.P. Selenium-Containing Polymer@Metal-Organic Frameworks Nanocomposites as an Efficient Multiresponsive Drug Delivery System. *Advanced Functional Materials.* 2017, **27**(6), 1605465.
13. Wang, X., Li, C., Fan, N., Li, J., He, Z.G. and Sun, J. Multimodal nanoporous silica nanoparticles functionalized with aminopropyl groups for improving loading and controlled release of doxorubicin hydrochloride. *Materials Science & Engineering C-Materials for Biological Applications.* 2017, **78**, pp.370-375.
14. Richardson, J.J., Choy, M.Y., Guo, J.L., Liang, K., Alt, K., Ping, Y., Cui, J.W., Law, L.S., Hagemeyer, C.E. and Caruso, F. Polymer Capsules for Plaque-Targeted In Vivo Delivery (vol 28, pg 7703, 2016). *Advanced Materials.* 2016, **28**(36), pp.7820-7820.
15. Guo, X., Wang, L., Duval, K., Fan, J., Zhou, S.B. and Chen, Z. Dimeric Drug Polymeric Micelles with Acid-Active Tumor Targeting and FRET-Traceable Drug Release. *Advanced Materials.* 2018, **30**(3), 1705436.
16. Sun, C.Y., Liu, Y., Du, J.Z., Cao, Z.T., Xu, C.F. and Wang, J. Facile Generation of Tumor-pH-Labile Linkage-Bridged Block Copolymers for Chemotherapeutic Delivery. *Angewandte Chemie-International Edition.* 2016, **55**(3), pp.1010-1014.
17. Chen, K., Liao, S.S., Guo, S.W., Zhang, H., Cai, H., Gong, Q.Y., Gu, Z.W. and Luo, K. Enzyme/pH-sensitive dendritic polymer-DOX conjugate for cancer treatment. *Science China-Materials.* 2018, **61**(11), pp.1462-1474.
18. Kalafatovic, D., Nobis, M., Son, J.Y., Anderson, K.I. and Ulijn, R.V. MMP-9 triggered self-assembly of doxorubicin nanofiber depots halts tumor growth. *Biomaterials.* 2016, **98**, pp.192-202.
19. Thornton, P.D., Mart, R.J. and Ulijn, R.V. Enzyme-responsive polymer hydrogel particles for controlled release. *Advanced Materials.* 2007, **19**(9), pp.1252-1256.
20. Li, Y.M., Liu, G.H., Wang, X.R., Hu, J.M. and Liu, S.Y. Enzyme-Responsive Polymeric Vesicles for Bacterial-Strain-Selective Delivery of Antimicrobial Agents. *Angewandte Chemie-International Edition.* 2016, **55**(5), pp.1760-1764.
21. Li, Y., Sun, J., Chen, Q.P., Chen, Z.P. and Zhu, L. Fast Drug Release of Liposome-Gold Conjugation Under Light Irradiation and the Comparison with Liposome-Gold Hybrid. *Nanoscience and Nanotechnology Letters.* 2017, **9**(6), pp.982-987.
22. Wei, J.R., Sun, J., Yang, X., Ji, S.F., Wei, Y.H. and Li, Z.B. Self-crosslinking assemblies with tunable nanostructures from photoresponsive polypeptoid-based block copolymers. *Polymer Chemistry.* 2020, **11**(2), pp.337-343.
23. Zhou, D.F., Guo, J.S., Kim, G.B., Li, J.Z., Chen, X.S., Yang, J. and Huang, Y.B. Simultaneously Photo-Cleavable and Activatable Prodrug-Backboned Block Copolymer Micelles for Precise Anticancer Drug Delivery. *Advanced Healthcare Materials.* 2016, **5**(19), pp.2493-2499.
24. Peters, C., Hoop, M., Pane, S., Nelson, B.J. and Hierold, C. Degradable Magnetic Composites for Minimally Invasive Interventions: Device Fabrication, Targeted Drug Delivery, and Cytotoxicity Tests. *Advanced Materials.* 2016, **28**(3), pp.533-538.
25. Rafiee, E., Nobakht, N. and Behbood, L. Influence of pH, temperature, and alternating magnetic field on drug release from Keggin-type heteropoly acid encapsulated in iron-carboxylate nanoscale metal-organic framework. *Research on Chemical Intermediates.* 2017, **43**(2), pp.951-969.
26. Zhou, M.L., Tang, M.L., Zhang, H., Luo, K. and Huang, Y. HPMA Polymeric Nanocarriers for Anticancer Drugs with Tumor Microenvironment-Responsive Extracellular

Biodegradation and Intracellular Drug Release. *Journal of Biomedical Nanotechnology.* 2019, **15**(8), pp.1688-1700.
27. Ray, P., Confeld, M., Borowicz, P., Wang, T., Mallik, S. and Quadir, M. PEG-b-poly (carbonate)-derived nanocarrier platform with pH-responsive properties for pancreatic cancer combination therapy. *Colloids and Surfaces B-Biointerfaces.* 2019, **174**, pp.126-135.
28. Pola, C.C., Moraes, A.R.F., Medeiros, E.A.A., Teofilo, R.F., Soares, N.F.F. and Gomes, C.L. Development and optimization of pH-responsive PLGA-chitosan nanoparticles for triggered release of antimicrobials. *Food Chemistry.* 2019, **295**, pp.671-679.
29. Chen, X.J., Niu, T.Y., Gao, Y.Z., Liang, X., Li, S.N., Zhang, L.Y., Li, L., Wang, T.T., Su, Z.M. and Wang, C.G. Tunable synthesis of pH-responsive biodegradable ZnO nanospheres assembled from ultrasmall particles for cancer chemotherapy. *Chemical Engineering Journal.* 2019, **371**, pp.443-451.
30. Gao, G., Jiang, Y.W., Sun, W., Guo, Y.X., Jia, H.R., Yu, X.W., Pan, G.Y. and Wu, F.G. Molecular Targeting-Mediated Mild-Temperature Photothermal Therapy with a Smart Albumin-Based Nanodrug. *Small.* 2019, **15**(33), 1900501.
31. Shen, W., He, P., Xiao, C.S. and Chen, X.S. From Antimicrobial Peptides to Antimicrobial Poly(alpha-amino acid)s. *Advanced Healthcare Materials.* 2018, **7**(20), 1800354.
32. Khuphe, M., Kazlauciunas, A., Huscroft, M. and Thornton, P.D. The formation of biodegradable micelles from a therapeutic initiator for enzyme-mediated drug delivery. *Chemical Communications.* 2015, **51**(8), pp.1520-1523.
33. Grazon, C., Salas-Ambrosio, P., Ibarboure, E., Buol, A., Garanger, E., Grinstaff, M.W., Lecommandoux, S. and Bonduelle, C. Aqueous Ring-Opening Polymerization Induced Self-Assembly (ROPISA) of N-carboxyanhydrides. *Angewandte Chemie-International Edition.* 2020, **59**(2), pp.622-626.
34. Jiang, J.H., Zhang, X.Y., Fan, Z. and Du, J.Z. Ring-Opening Polymerization of N-Carboxyanhydride-Induced Self-Assembly for Fabricating Biodegradable Polymer Vesicles. *Acs Macro Letters.* 2019, **8**(10), pp.1216-1221.
35. Song, Z.Y., Tan, Z.Z. and Cheng, J.J. Recent Advances and Future Perspectives of Synthetic Polypeptides from N-Carboxyanhydrides. *Macromolecules.* 2019, **52**(22), pp.8521-8539.
36. McAvan, B.S., Khuphe, M. and Thornton, P.D. Polymer hydrogels for glutathione-mediated protein release. *European Polymer Journal.* 2017, **87**, pp.468-477.
37. Zhou, X.F. and Li, Z.B. Advances and Biomedical Applications of Polypeptide Hydrogels Derived from alpha-Amino Acid N-Carboxyanhydride (NCA) Polymerizations. *Advanced Healthcare Materials.* 2018, **7**(15), 1800020.
38. De Jong, W.H. and Borm, P.J.A. Drug delivery and nanoparticles: Applications and hazards. *International Journal of Nanomedicine.* 2008, **3**(2), pp.133-149.
39. Borase, T. and Heise, A. Hybrid Nanomaterials by Surface Grafting of Synthetic Polypeptides Using N-Carboxyanhydride (NCA) Polymerization. *Advanced Materials.* 2016, **28**(27), pp.5725-5731.
40. Khuphe, M., Mahon, C.S. and Thornton, P.D. Glucose-bearing biodegradable poly(amino acid) and poly(amino acid)-poly(ester) conjugates for controlled payload release. *Biomaterials Science.* 2016, **4**(12), pp.1792-1801.
41. Price, D.J., Khuphe, M., Davies, R.P.W., McLaughlan, J.R., Ingram, N. and Thornton, P.D. Poly(amino acid)-polyester graft copolymer nanoparticles for the acid-mediated release of doxorubicin. *Chemical Communications.* 2017, **53**(62), pp.8687-8690.
42. Fan, J.W., Li, R.C., Wang, H., He, X., Nguyen, T.P., Letteri, R.A., Zou, J. and Wooley, K.L. Multi-responsive polypeptide hydrogels derived from N-carboxyanhydride

terpolymerizations for delivery of nonsteroidal anti-inflammatory drugs. *Organic & Biomolecular Chemistry.* 2017, **15**(24), pp.5145-5154.
43. Khuphe, M., Ingram, N. and Thornton, P.D. Exploiting poly(alpha-hydroxy acids) for the acid-mediated release of doxorubicin and reversible inside-out nanoparticle self-assembly. *Nanoscale.* 2018, **10**(29), pp.14201-14206.
44. Famili, A., Kahook, M.Y. and Park, D. A Combined Micelle and Poly(Serinol Hexamethylene Urea)-Co-Poly(N-Isopropylacrylamide) Reverse Thermal Gel as an Injectable Ocular Drug Delivery System. *Macromolecular Bioscience.* 2014, **14**(12), pp.1719-1729.
45. Yan, J.X., Miao, Y.T., Tan, H.P., Zhou, T.L., Ling, Z.H., Chen, Y., Xing, X.D. and Hu, X.H. Injectable alginate/hydroxyapatite gel scaffold combined with gelatin microspheres for drug delivery and bone tissue engineering. *Materials Science & Engineering C-Materials for Biological Applications.* 2016, **63**, pp.274-284.
46. Jin, K.M. and Kim, Y.H. Injectable, thermo-reversible and complex coacervate combination gels for protein drug delivery. *Journal of Controlled Release.* 2008, **127**(3), pp.249-256.
47. Town, A.R., Giardiello, M., Gurjar, R., Siccardi, M., Briggs, M.E., Akhtar, R. and McDonald, T.O. Dual-stimuli responsive injectable microgel/solid drug nanoparticle nanocomposites for release of poorly soluble drugs. *Nanoscale.* 2017, **9**(19), pp.6302-6314.
48. Gradisar, S., Zagar, E. and Pahovnik, D. Ring-Opening Polymerization of N-Carboxyanhydrides Initiated by a Hydroxyl Group. *Acs Macro Letters.* 2017, **6**(6), pp.637-640.
49. Khuphe, M. and Thornton, P.D. Poly(hydroxy acid) Nanoparticles for the Encapsulation and Controlled Release of Doxorubicin. *Macromolecular Chemistry and Physics.* 2018, **219**(23), 1800352.
50. Warren, N.J., Mykhaylyk, O.O., Mahmood, D., Ryan, A.J. and Armes, S.P. RAFT Aqueous Dispersion Polymerization Yields Poly(ethylene glycol)-Based Diblock Copolymer Nano-Objects with Predictable Single Phase Morphologies. *Journal of the American Chemical Society.* 2014, **136**(3), pp.1023-1033.
51. Zhang, X.J., Niu, S.W., Williams, G.R., Wu, J.R., Chen, X., Zheng, H. and Zhu, L.M. Dual-responsive nanoparticles based on chitosan for enhanced breast cancer therapy. *Carbohydrate Polymers.* 2019, 221, pp.84-93.
52. Ferjaoui, Z., Al Dine, E.J., Kulmukhamedova, A., Bezdetnaya, L., Chan, C.S., Schneider, R., Mutelet, F., Mertz, D., Begin-Colin, S., Quiles, F., Gaffet, E. and Alem, H. Doxorubicin-Loaded Thermoresponsive Superparamagnetic Nanocarriers for Controlled Drug Delivery and Magnetic Hyperthermia Applications. *Acs Applied Materials & Interfaces.* 2019, **11**(34), pp.30610-30620.
53. Atanackovic, D., Pollok, K., Faltz, C., Boeters, I., Jung, R., Nierhaus, A., Braumann, K.M., Hossfeld, D.K. and Hegewisch-Becker, S. Patients with solid tumors treated with high-temperature whole body hyperthermia show a redistribution of naive/memory T-cell subtypes. *American Journal of Physiology-Regulatory Integrative and Comparative Physiology.* 2006, **290**(3), pp.585-594.
54. Patel, A.G. and Kaufmann, S.H. CANCER How does doxorubicin work? *Elife.* 2012, **1**, p.3.
55. Dong, D.K., Chen, S.J., Feng, C., Xiong, H.Z. and Xu, X.W. NB-UVB Induces Melanocytic Differentiation of Human Hair Follicle Neural Crest Stem Cells. *Annals of Dermatology.* 2020, 32(4), pp.289-297.

Chapter 5. Fucose-Modified Thermoresponsive Nanoparticles for Controlled Doxorubicin Release from an Injectable Depot

Preamble

This chapter is based on work published as:

Yu H.; Rowley J.; Green DC.; Thornton P.D. *Materials Advances,* 2020.

Abstract

The modification of poly(2-hydroxypropyl methacrylate) with a single fucose group per polymer chain enabled macromolecular self-assembly, and the formation of thermoresponsive nanoparticles. In addition, poly(2-hydroxypropyl methacrylate)$_{200}$ formed a self-healing material that may act as an injectable vehicle and depot for poly(2-hydroxypropyl methacrylate) nanoparticle delivery and localisation at a particular site. In combination, the injectable depot permits the controlled release of doxorubicin from the fucose–presenting nanoparticles that it contains following injection. Such thermoresponsive materials are highly promising candidates for the treatment of diseases that may be remedied by exploiting targeted fucose-cell binding, such as pancreatic cancer.

5.1 Introduction

Effective cancer treatment in the absence of extremely intrusive side-effects remains a key challenge in contemporary medicine [1]. Providing a remedy that destroys the cancer cells, whilst leaving healthy cells relatively unaffected must be realised for this challenge to be overcome [2]. Encapsulating a toxic anti-cancer drug within a shielding polymer carrier protects the drug from interacting with cells, thus preventing the damage of non-cancerous cells and the aggressive side-effects that are associated with this occurring during chemotherapy [3-5]. Extensive drug loading into polymeric nanoparticles, and a

mechanism for the programmed release of the drug from the nanoparticles, are essential features of effective treatments [6-10]. Additionally, next-generation drug delivery vehicles must present cell-binding groups that enable extensive therapeutic interaction with target cells only [11-13].

Fucose plays a key role in mammalian development, immunity and cancer metastasis [14]. Increased expression of fucosyltransferases is associated with pancreatic cancer, whereby enzymes accelerate malignant transformation through the fucosylation of sialylated precursors, and pancreatic cancer cells display enhanced fucose uptake. Pancreatic cancer is an extremely aggressive cancer with a dismal survival rate; it is estimated that the 5-year survival rate is 5% owing to its aggressiveness, and a lack of effective therapies [15]. Currently, patients that undergo treatment with the chemotherapy drug Gemcitabine (Gemzar®) have a median survival time reported to be only 5.7 months [16]. A plausible, explanation for this abysmal inefficiency is the extremely inefficient delivery of anticancer drugs to the tumor site. There is enormous demand for the creation of fucose-presenting nanoparticles to be deployed as increasingly advanced drug delivery systems for the treatment of pancreatic cancer.

PHPMA is non-toxic and biocompatible [17-18]. PHPMA-containing block copolymers can be readily formed by RAFT aqueous dispersion polymerisation [19]. Such polymers have been reported to self-assemble into a plethora of arrangements dependent on their macromolecular configuration, and the environment in which they are maintained. For instance, poly(glycidyl methacrylate)-*b*-PHPMA may be manipulated to form an array of morphologies including spheres, worms and vesicles dependent on the composition of the block copolymer, and the temperature of the aqueous solution in which the polymer is dispersed [20]. PHPMA, and PHPMA-based materials have been applied to the thermally-triggered release of drug molecules [21-25], and controlled release applications [26-30].

Implantable polymer-based materials with injectable and self-healing properties for drug and cell delivery have attracted significant recent attention [31-37]. Such materials may facilitate the immobilisation of drug-loaded nanoparticles at the target site, ensuring extensive drug release at diseased areas, and minimal drug release to healthy tissue. This

enhances the efficacy of the treatment, reducing the side-affects that are caused by drug interaction with non-target, healthy cells. An implantable depot that enables the controlled and prolonged release of fucose-presenting nanoparticles for long-term pancreatic cancer treatment is a noteworthy long-term goal.

The research in this chapter reports the simple modification of PHPMA polymer chains with a single fucose unit enables the polymer to self-assemble, forming nanoparticles in aqueous solution. Such nanoparticles are stable at room temperature, but undergo a morphological change upon heating to physiological temperature, which may be exploited to actuate therapeutic payload release. Unmodified PHPMA can form an injectable depot that undergoes a sol-gel transition at a temperature slightly above physiological temperature. Consequently, the depot, which is self-healing and can withhold guest molecules itself, may act as an injectable host for the controlled release of Dox from fucose-capped PHPMA nanoparticles.

5.2 Experimental

5.2.1 Fucose conjugation of ethylenediamine

L(-)-Fucose (0.100 g, 0.609 mmol) was dissolved in deionised water (10.0 mL). Then sodium meta-periodate (0.391 g, 1.83 mmol) was added into the fucose solution and stirred overnight in the dark to activate aldehyde group. Ethylenediamine (41.0 µL, 0.614 mmol) was added into the mixture and stirred overnight. Sodium cyanoborohydride (0.038 g, 0.605 mmol) was added into the mixture and stirred for 3 hours followed by freeze drying for 48 hours. Fucose-amine: 0.123 g, 96.8 wt. % (white solid). ^{1}H-NMR (500 MHz, D_2O, δ, ppm): 8.36 – 8.30 (s, 1H, $H_3CCHOHCHOHCHOHCHOHCO\underline{H}$), 5.22 – 5.18 (t, 1H, $H_3CCHOHCHOHC\underline{H}OHCHOHCOH$), 4.51 – 4.48 (d, 1H, $H_3CCHOHCHOHCHOHC\underline{H}OHCOH$), 4.27 – 4.20 (s, 1H, $H_3CCHOHCHOHCHOHCHO\underline{H}COH$), 3.60 – 3.53 (t, 1H, $H_3CCHOHC\underline{H}OHCHOHCHOHCOH$), 3.45 - 3.39 (m, 1H, $H_3CC\underline{H}OHCHOHCHOHCHOHCOH$), 1.19 – 1.01 (m, 5H, $\underline{H}_3CCHOHCHO\underline{H}CHO\underline{H}CHOHCOH$). ^{13}C-NMR (125 MHz, D_2O, δ, ppm): 90.2 ($H_3CCHOHC\underline{H}$), 73.1 ($H_3CCHOHCHOHC\underline{H}OH$), 70.7 ($H_3CCHOHCHOHCHOHC\underline{H}OH$), 65.9 ($H_3CC\underline{H}OH$), 49.1 ($NHC\underline{H}_2$), 44.5 ($C\underline{H}_2NH$), 42.6

($C\underline{H_2}NH_2$) and 15.4 ($\underline{H_3}CCHOH$). FTIR: ν_{max}/cm^{-1} (solid): 3474 cm^{-1} (O-H and N-H stretch), 1636 cm^{-1} (N-H bend) and 1119 cm^{-1} (alcohol O-H stretch).

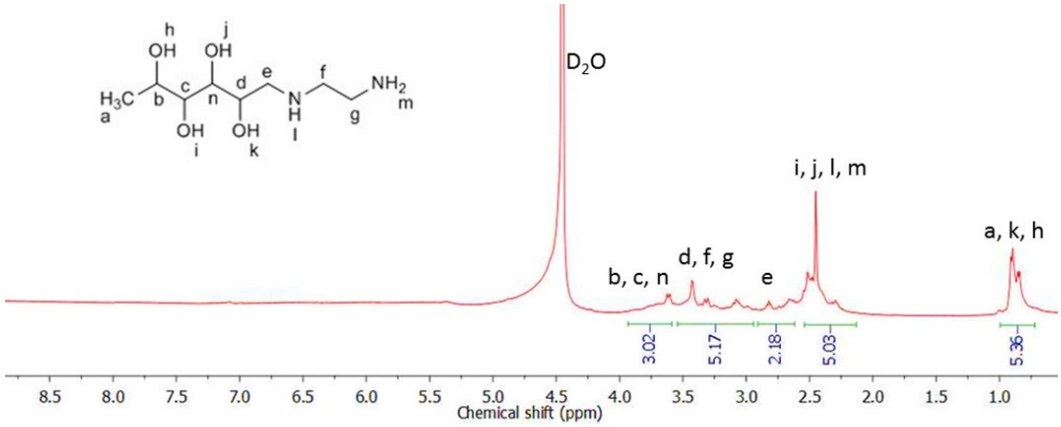

Figure 5. 1. The 500 MHz ^{1}H-NMR spectrum of fucose-amine in D_2O at 25 °C.

5.2.2 SCPDB conjugation of amine-bearing fucose

Fucose-amine (0.118 g, 0.567 mmol) and SCPDB RAFT agent (0.214 g, 0.568 mmol) were dissolved in deionised water (5.0 mL) and acetone (20.0 mL), respectively. SCPDB RAFT agent solution was added dropwise into the fucose-amine solution with stirring followed by acetic acid (3.0 mL) added in. The mixture was stirred at 60 °C overnight. Then the solution was rotary evaporated at 60 °C and freeze dried. The fucose-RAFT agent was washed with DCM, centrifugation for 30 minutes at 4500 rev/min and dried in a vacuum oven at room temperature overnight. Fucose-RAFT agent: 0.191 g, 71.9 wt. % (orange solid). ^{1}H-NMR (500 MHz, DMSO-d_6, δ, ppm): 8.23 – 7.87 (d, 2H, Ar$\underline{H}$), 7.76 – 7.62 (t, 1H, Ar$\underline{H}$), 7.57 – 7.45 (d, 2H, Ar$\underline{H}$), 4.76 – 4.73 (t, 1H, CON$\underline{H}C\underline{H_2}$), 2.73 – 2.56 (m, 5H, NHC$\underline{H_2}$C$\underline{H_2}$N$\underline{H}$), 2.42 – 2.27 (m, 4H, CCNC$\underline{H_2}$C$\underline{H_2}$CO), 2.23 – 2.14 (m, 6H, NHC$\underline{H_2}$C$\underline{H}$OHC$\underline{H}$OHC$\underline{H}$OHC$\underline{H}$OHCH_3), 1.98 – 1.87 (m, 7H, C$\underline{H_3}$CCNCH_2CH_2CONHCH_2CH_2NHCH_2CHO$\underline{H}$CHO$\underline{H}$CHO$\underline{H}$CHO$\underline{H}$CH$_3$), 1.49 – 1.46 (s, 3H, CHOHC$\underline{H_3}$). FTIR: ν_{max}/cm^{-1} (solid): 3503 cm^{-1} (secondary amine N-H stretch), 2941 cm^{-1} (alkane C-H stretch), 1702 cm^{-1} (secondary amide C=O stretch), 1372 cm^{-1}(alkane C-H stretch), 1229 cm^{-1} (C=S stretch), 1048 cm^{-1} (secondary alcohol O-H stretch) and 998 cm^{-1} (C-S bend).

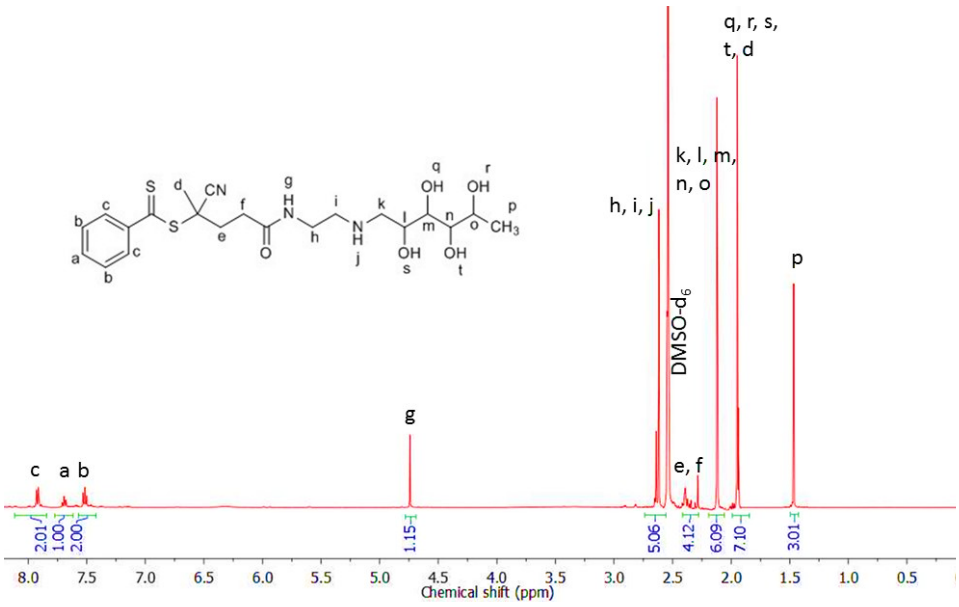

Figure 5. 2. The 500 MHz ^{1}H-NMR spectrum of fucose-RAFT agent in DMSO-d_6 at 25 °C.

5.2.3. HPMA Polymerisation from the fucose-RAFT agent

Fucose-RAFT agent (0.052 g, 0.111 mmol) was dissolved in acetone (3.0 mL) and deionised water (2.0 mL). Then AAPH (0.091 g, 0.336 mmol) was dissolved into the mixture. HPMA (1.61 g, 11.2 mmol) was added dropwise into the reaction and stirred at 55 °C for 24 hours. The product was rotary evaporated at 50 °C for 20 minutes and freeze dried. Finally fucose-PHPMA was washed with deionised water, centrifugation for 30 minutes at 4500 rev/min and freeze dried for 48 hours. The synthesised polymer was fucose-PHPMA$_{100}$. Fucose-PHPMA$_{20}$, fucose-PHPMA$_{40}$, fucose-PHPMA$_{60}$ and fucose-PHPMA$_{80}$ were also synthesised using the same procedure and quantity of reactants were HPMA (0.320 g, 2.22 mmol), HPMA (0.640 g, 4.44 mmol), HPMA (0.860 g, 6.66 mmol), HPMA (1.28 g, 8.88 mmol), respectively. Fucose-PHPMA$_{100}$: 1.57 g, 94.9 wt. % (white solid). APC (PMMA standards): M_w= 16000 g mol^{-1}. Dispersity= 1.82. ^{1}H-NMR (500 MHz, DMSO-d_6, δ, ppm): 7.96 – 7.88 (d, 2H, ArH), 7.86 – 7.76 (t, 1H, ArH), 7.74 – 7.50 (d, 2H, ArH), 4.98 – 4.48 (m, 100H, (HOCH$_2$CHOHCH$_3$)$_{100}$), 4.13– 3.72 (m, 200H, (HOCH$_2$CHOHCH$_3$)$_{100}$), 3.70 – 3.39 (m, 100H, (HOCH$_2$CHOHCH$_3$)$_{100}$), 2.70 – 2.68 (m, 4H, CCNCH$_2$CH$_2$CONH), 2.25 – 1.68 (m, 200H, (CH$_3$CCH$_2$)$_{100}$), 1.48 – 1.45 (m, 12H, NHCH$_2$CH$_2$NHCH$_2$CHOHCHOHCHOHCHOHCH$_3$), 1.25 – 1.23 (m, 7H, CHOHCHOHCHOHCHOHCH$_3$), 1.20 – 0.50 (m, 600H, (CH$_3$CCH$_2$COOHCH$_2$CHOHCH$_3$)$_{100}$). FTIR: ν_{max}/cm^{-1} (solid): 3447 cm^{-1} (N-H and O-H stretch), 2979 cm^{-1} (alkane C-H stretch),

1713 cm^{-1} (C=O stretch), 1449 cm^{-1}(alkane C-H stretch), 1245 cm^{-1} (C=S stretch), 1146 cm^{-1} and 1053 cm^{-1} (C-O stretch) and 992 cm^{-1} (C-S bend).

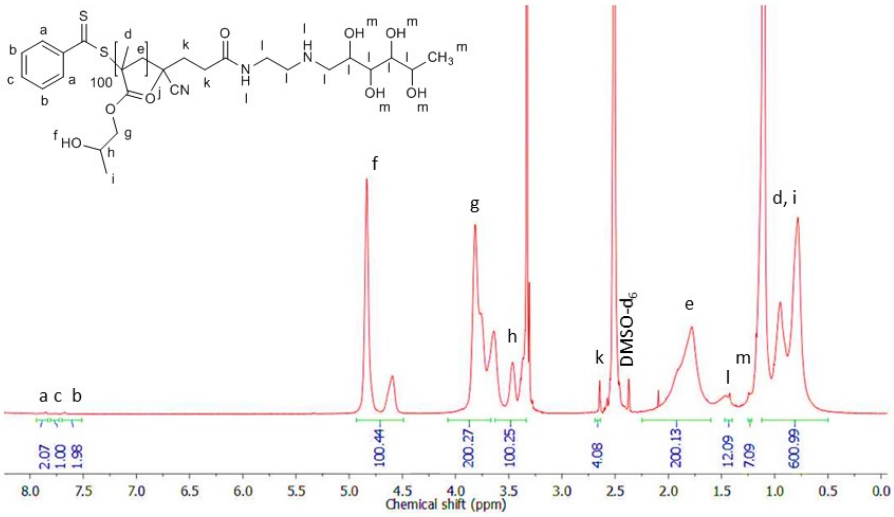

Figure 5. 3. The 500 MHz ^{1}H-NMR spectrum of fucose-PHPMA$_{100}$ in DMSO-d_6 at 25 °C.

Fucose-PHPMA$_{20}$: 0.301 g, 80.9 wt. % (white solid). APC (PMMA standards): M_w= 3700 g mol^{-1}. Dispersity= 1.38. ^{1}H-NMR (500 MHz, DMSO-d_6, δ, ppm): 8.23 – 7.95 (d, 2H, ArH), 7.90 – 7.80 (t, 1H, ArH), 7.73 – 7.63 (d, 2H, ArH), 5.12 – 4.51 (m, 22H, (HOCH$_2$CHOHCH$_3$)$_{20}$), 4.12 – 3.70 (m, 40H, (HOCH$_2$CHOHCH$_3$)$_{20}$), 3.69 – 3.38 (m, 20H, (HOCH$_2$CHOHCH$_3$)$_{20}$), 2.72 – 2.54 (m, 4H, CCNCH$_2$CH$_2$CONH), 2.23 – 1.70 (m, 40H, (CH$_3$CCH$_2$)$_{20}$), 1.69 – 1.25 (m, 12H, NHCH$_2$CH$_2$NHCH$_2$CHOHCHOHCHOHCHOHCH$_3$), 1.23 – 1.20 (m, 7H, CHOHCHOHCHOHCHOHCH$_3$), 1.17 – 0.46 (m, 120H, (CH$_3$CCH$_2$COOHCH$_2$CHOHCH$_3$)$_{20}$). FTIR: ν_{max}/cm^{-1} (solid): 3458 cm^{-1} (N-H and O-H stretch), 2958 cm^{-1} (alkane C-H stretch), 1718 cm^{-1} (C=O stretch), 1449 cm^{-1}(alkane C-H stretch), 1245 cm^{-1} (C=S stretch), 1146 cm^{-1} and 1058 cm^{-1} (C-O stretch) and 992 cm^{-1} (C-S bend).

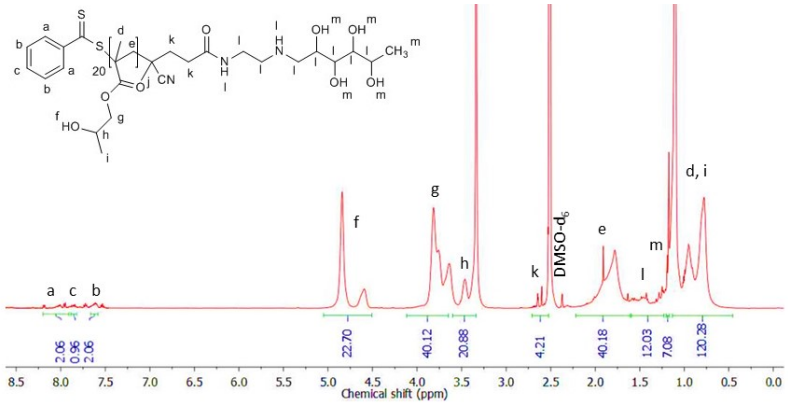

Figure 5. 4. The 500 MHz ^{1}H-NMR spectrum of fucose-PHPMA$_{20}$ in DMSO-d_6 at 25 °C.

Fucose-PHPMA$_{40}$: 0.587 g, 84.9 wt. % (white solid). APC (PMMA standards): M_w= 7600 g mol^{-1}. Dispersity= 1.48.^{1}H-NMR (500 MHz, DMSO-d$_6$, δ, ppm): 8.20 – 7.75 (d, 2H, ArH), 7.70 – 7.67 (t, 1H, ArH), 7.55 – 7.48 (d, 2H, ArH), 4.99 – 4.51 (m, 40H, (HOCH$_2$CHOHCH$_3$)$_{40}$), 4.13 – 3.72 (m, 80H, (HOCH$_2$CHOHCH$_3$)$_{40}$), 3.69 – 3.35 (m, 40H, (HOCH$_2$CHOHCH$_3$)$_{40}$), 2.70 – 2.56 (m, 4H, CCNCH$_2$CH$_2$CONH), 2.25 – 1.72 (m, 80H, (CH$_3$CCH$_2$)$_{40}$), 1.60 – 1.42 (m, 12H, NHCH$_2$CH$_2$NHCH$_2$CHOHCHOHCHOHCHOHCH$_3$), 1.32 – 1.24 (m, 7H, CHOHCHOHCHOHCHOHCH$_3$), 1.20 – 0.65 (m, 240H, (CH$_3$CCH$_2$COOHCH$_2$CHOHCH$_3$)$_{40}$). FTIR: ν_{max}/cm^{-1} (solid): 3447 cm^{-1} (N-H and O-H stretch), 2958 cm^{-1} (alkane C-H stretch), 1713 cm^{-1} (C=O stretch), 1449 cm^{-1}(alkane C-H stretch), 1251 cm^{-1} (C=S stretch), 1146 cm^{-1} and 1058 cm^{-1} (C-O stretch) and 992 cm^{-1} (C-S bend).

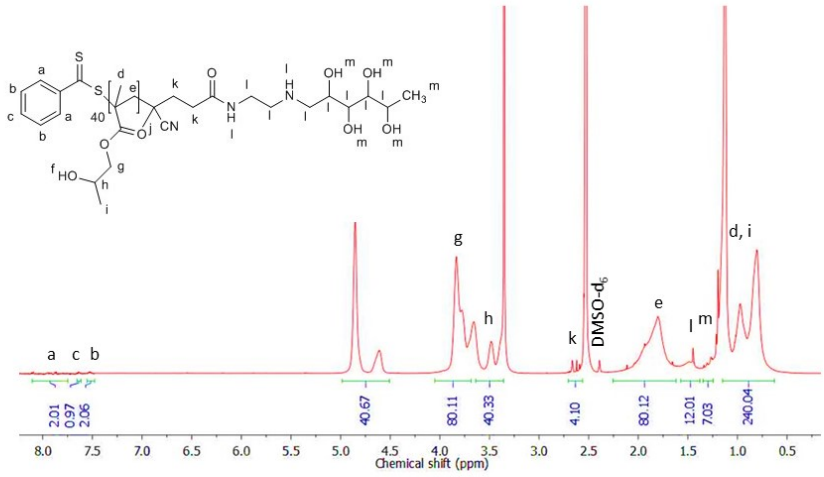

Figure 5. 5. The 500 MHz ^{1}H-NMR spectrum of fucose-PHPMA$_{40}$ in DMSO-d$_6$ at 25 °C.

Fucose-PHPMA$_{60}$: 0.880 g, 87.0 wt. % (white solid). APC (PMMA standards): M_w= 11400 g mol^{-1}. Dispersity= 1.69. ^{1}H-NMR of fucose-PHPMA$_{60}$ (500 MHz, DMSO-d$_6$, δ, ppm): 8.14 – 7.93 (d, 2H, ArH), 7.86 – 7.75 (t, 1H, ArH), 7.73 – 7.69 (d, 2H, ArH), 4.91 – 4.60 (m, 60H, (HOCH$_2$CHOHCH$_3$)$_{60}$), 4.20 – 3.72 (m, 120H, (HOCH$_2$CHOHCH$_3$)$_{60}$), 3.69 – 3.35 (m, 61H, (HOCH$_2$CHOHCH$_3$)$_{60}$), 2.75 – 2.57 (m, 4H, CCNCH$_2$CH$_2$CONH), 2.23 – 1.68 (m, 120H, (CH$_3$CCH$_2$)$_{60}$), 1.52 – 1.43 (m, 12H, NHCH$_2$CH$_2$NHCH$_2$CHOHCHOHCHOHCHOHCH$_3$), 1.31 – 1.24 (m, 7H, CHOHCHOHCHOHCHOHCH$_3$), 1.23 – 0.44 (m, 361H, (CH$_3$CCH$_2$COOHCH$_2$CHOHCH$_3$)$_{60}$). FTIR: ν_{max}/cm^{-1} (solid): 3458 cm^{-1} (N-H and O-H stretch), 2985 cm^{-1} (alkane C-H stretch), 1708 cm^{-1} (C=O stretch), 1449 cm^{-1}(alkane C-H stretch), 1245 cm^{-1} (C=S stretch), 1146 cm^{-1} and 1058 cm^{-1} (C-O stretch) and 992 cm^{-1} (C-S bend).

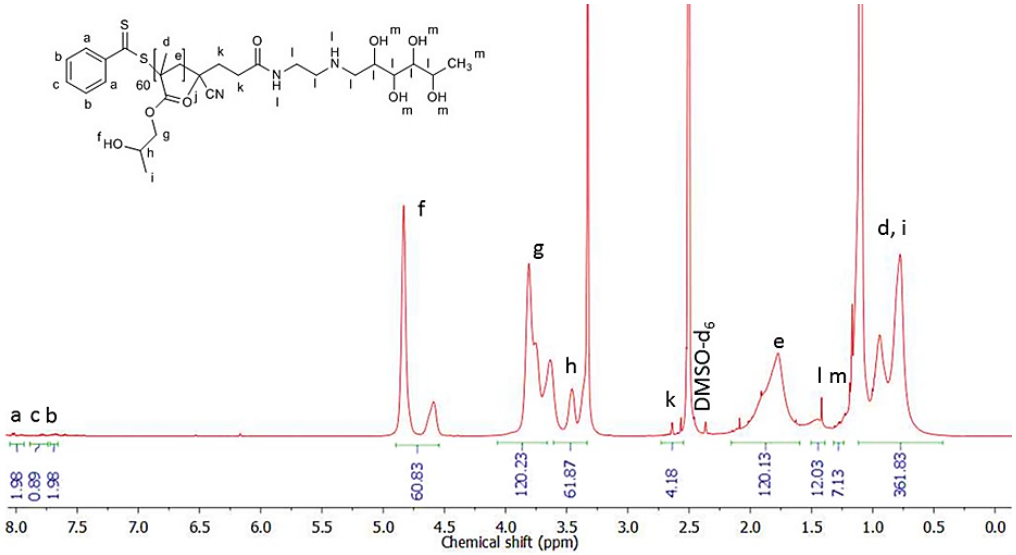

Figure 5. 6. The 500 MHz ^{1}H-NMR spectrum of fucose-PHPMA$_{60}$ in DMSO-d$_6$ at 25 °C.

Fucose-PHPMA$_{80}$: 1.21 g, 91.3 wt. % (white solid). APC (PMMA standards): M_w= 15500 g mol^{-1}. Dispersity= 1.55. ^{1}H-NMR of fucose-PHPMA$_{80}$ (500 MHz, DMSO-d$_6$, δ, ppm): 8.16 – 8.16 (d, 2H, ArH), 7.90 – 7.92 (t, 1H, ArH), 7.77 – 7.65 (d, 2H, ArH), 5.01 – 4.66 (m, 80H, (HOCH$_2$CHOHCH$_3$)$_{80}$), 4.22– 3.74 (m, 160H, (HOCH$_2$CHOHCH$_3$)$_{80}$), 3.71 – 3.41 (m, 80H, (HOCH$_2$CHOHCH$_3$)$_{80}$), 2.77 – 2.73 (m, 4H, CCNCH$_2$CH$_2$CONH), 2.25 – 1.73 (m, 160H, (CH$_3$CCH$_2$)$_{80}$), 1.55 – 1.49 (m, 12H, NHCH$_2$CH$_2$NHCH$_2$CHOHCHOHCHOHCHOHCH$_3$), 1.43 – 1.39 (m, 7H, CHOHCHOHCHOHCHOHCH$_3$), 1.24 – 0.52 (m, 480H, (CH$_3$CCH$_2$COOHCH$_2$CHOHCH$_3$)$_{80}$). FTIR: ν_{max}/cm^{-1} (solid): 3436 cm^{-1} (N-H and O-H stretch), 2979 cm^{-1} (alkane C-H stretch), 1718 cm^{-1} (C=O stretch), 1449 cm^{-1}(alkane C-H stretch), 1245 cm^{-1} (C=S stretch), 1146 cm^{-1} and 1048 cm^{-1} (C-O stretch) and 992 cm^{-1} (C-S bend).

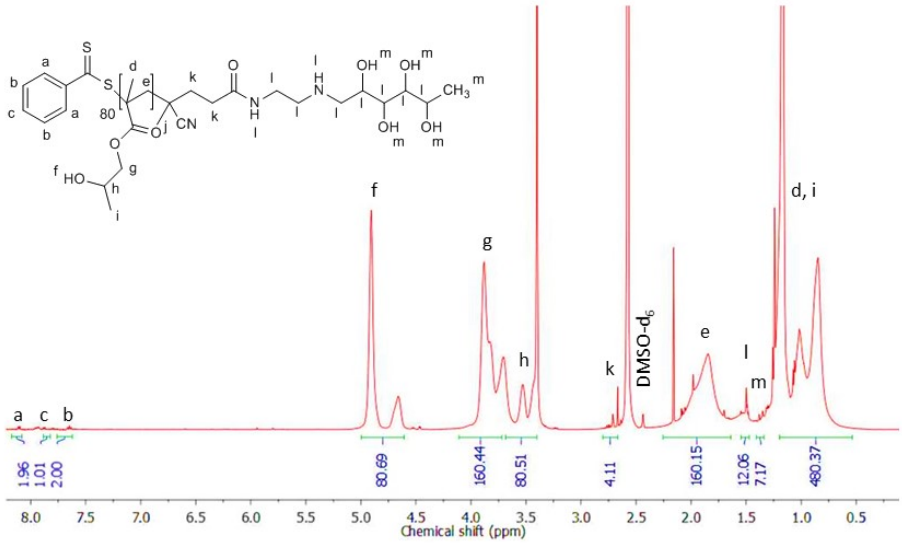

Figure 5. 7. The 500 MHz ^{1}H-NMR spectrum of fucose-PHPMA$_{80}$ in DMSO-d$_6$ at 25 °C.

5.2.4. PHPMA Synthesis: HPMA polymerisation from 4-cyano-4-(phenylcarbonothioyl)thiopentanoic acid

4-Cyano-4-((phenylcarbonothioyl)thiopentanoic acid RAFT agent (0.020 g, 0.072 mmol) was dissolved in acetone (3.0 mL) and deionised water (2.0 mL), respectively. Then AAPH (0.059 g, 0.218 mmol) was dissolved into the mixture. HPMA (1.04 g, 7,2 mmol) was added dropwise into the reaction and stirred at 55 °C for 24 hours. The product was rotary evaporated at 50 °C for 20 minutes and freeze dried for 48 hours. Finally, PHPMA was washed with deionised water, centrifugation for 30 minutes at 4500 rev/min and freeze dried for 48 hours. The synthesised polymer was $PHPMA_{100}$. $PHPMA_{20}$, $PHPMA_{40}$, $PHPMA_{60}$ and $PHPMA_{80}$ were also synthesised using the same procedure and quantity of reactants were HPMA (0.208 g, 1.44 mmol), HPMA (2.88 mmol), HPMA (0.415 g, 4.32 mmol) and HPMA (0.830 g, 5.76 mmol), respectively. $PHPMA_{100}$: 0.741 g, 71.0 wt. % (yellow solid). APC (PMMA standards): M_w= 14400 g mol^{-1}. Dispersity= 1.33. ^{1}H-NMR of $PHPMA_{100}$ (500 MHz, DMSO-d_6, δ, ppm): 8.17 – 8.14 (s, 1H, COO<u>H</u>), 8.01 – 7.92 (d, 2H, Ar<u>H</u>), 7.80 – 7.74 (t, 1H, Ar<u>H</u>), 7.67 – 7.50 (d, 2H, Ar<u>H</u>), 4.97 – 4.47 (m, 100H, (<u>H</u>OCH$_2$CHOHCH$_3$)$_{100}$), 4.25– 3.32 (m, 200H, (HOC<u>H$_2$</u>CHOHCH$_3$)$_{100}$), 3.31 – 3.23 (m, 100H, (HOCH$_2$C<u>H</u>OHCH$_3$)$_{100}$), 2.28 – 1.67 (m, 207H, (CH$_3$CC<u>H$_2$</u>)$_{100}$C<u>H$_3$</u>CCNC<u>H$_2$</u>C<u>H$_2$</u>), 1.51 – 0.45 (m, 600H, (C<u>H$_3$</u>CCH$_2$COOHCH$_2$CHOHC<u>H$_3$</u>)$_{100}$). FTIR: ν_{max}/cm^{-1} (solid): 3377 cm^{-1} (alcohol O-H stretch), 2975 cm^{-1} (carboxylic acid O-H stretch), 1717 cm^{-1} (ester C=O stretch), 1453 cm^{-1}(alkane C-H stretch), 1241 cm^{-1} (C=S stretch), 1149 cm^{-1} (alcohol C-O stretch) and 993 cm^{-1} (C-S bend).

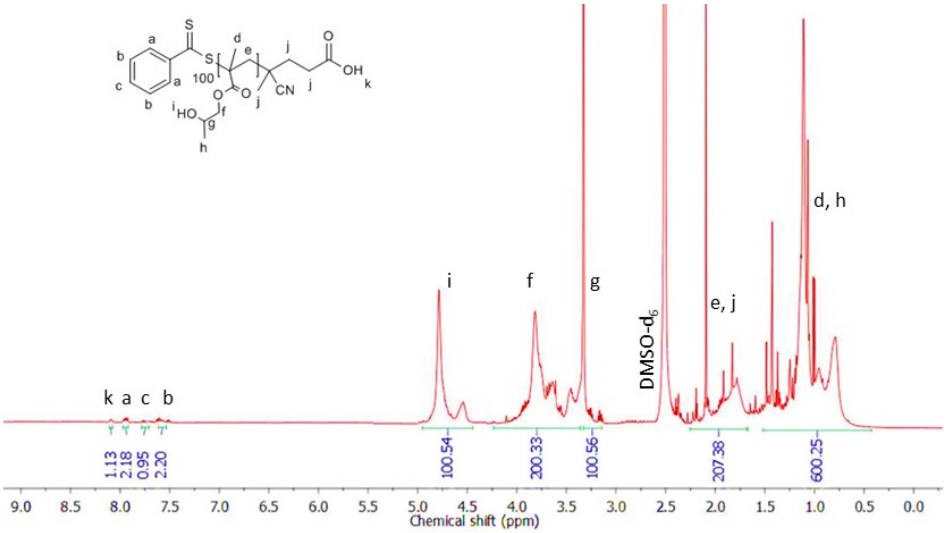

Figure 5. 8. The 500 MHz ^{1}H-NMR spectrum of $PHPMA_{100}$ in DMSO-d_6 at 25 °C.

$PHPMA_{20}$: 0.162 g, 72.3 wt. % (yellow solid). APC (PMMA standards): M_w= 3100 g mol^{-1}. Dispersity= 1.22. ^{1}H-NMR of $PHPMA_{20}$ (500 MHz, DMSO-d_6, δ, ppm): 8.20 – 8.06 (s, 1H, COOH), 8.05 – 7.85 (d, 2H, ArH), 7.83 – 7.74 (t, 1H, ArH), 7.72 – 7.65 (d, 2H, ArH), 5.12 – 4.60 (m, 20H, $(HOCH_2CHOHCH_3)_{20}$), 4.35– 3.57 (m, 40H, $(HOCH_2CHOHCH_3)_{20}$), 3.53 – 3.27 (m, 20H, $(HOCH_2CHOHCH_3)_{20}$), 2.23 – 1.62 (m, 40H, $(CH_3CCH_2)_{20}$), 1.60 – 1.45 (m, 7H, $CH_3CCNCH_2CH_2$), 1.32 – 0.68 (m, 120H, $(CH_3CCH_2COOHCH_2CHOHCH_3)_{20}$). FTIR: ν_{max}/cm^{-1} (solid): 3371 cm^{-1} (alcohol O-H stretch), 2975 cm^{-1} (carboxylic acid O-H stretch), 1717 cm^{-1} (ester C=O stretch), 1447 cm^{-1}(alkane C-H stretch), 1241 cm^{-1} (C=S stretch), 1149 cm^{-1} (alcohol C-O stretch) and 993 cm^{-1} (C-S bend).

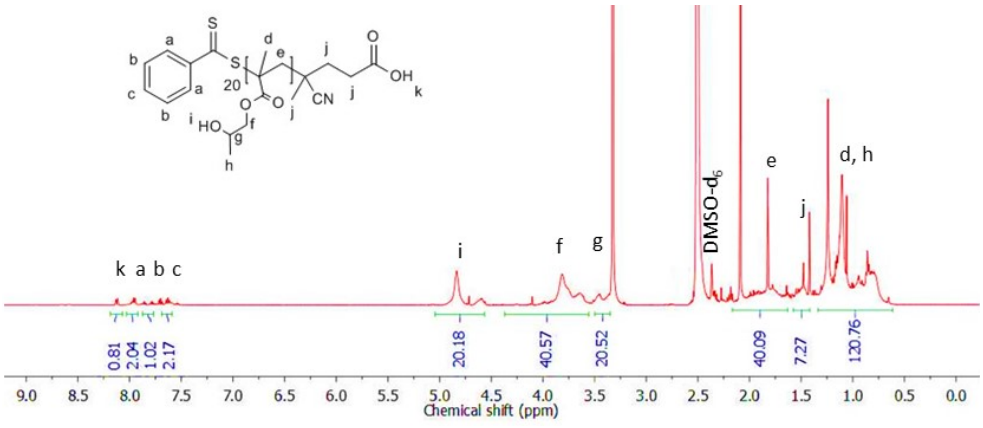

Figure 5. 9. The 500 MHz ^{1}H-NMR spectrum of $PHPMA_{20}$ in DMSO-d_6 at 25 °C.

$PHPMA_{40}$: 0.257 g, 59.9 wt. % (yellow solid). APC (PMMA standards): M_w= 6000 g mol^{-1}. Dispersity= 1.37. ^{1}H-NMR of $PHPMA_{40}$ (500 MHz, DMSO-d_6, δ, ppm): 8.30 – 8.18 (s, 1H, COOH), 8.10 – 8.05 (d, 2H, ArH), 7.87 – 7.82 (t, 1H, ArH), 7.75 – 7.70 (d, 2H, ArH), 5.15 –

4.49 (m, 40H, (HOCH$_2$CHOHCH$_3$)$_{40}$), 4.20– 3.59 (m, 80H, (HOCH$_2$CHOHCH$_3$)$_{40}$), 3.54 – 3.28 (m, 40H, (HOCH$_2$CHOHCH$_3$)$_{40}$), 2.18 – 1.75 (m, 80H, (CH$_3$CCH$_2$)$_{40}$), 1.70 – 1.47 (m, 7H, CH$_3$CCNCH$_2$CH$_2$), 1.25 – 0.72 (m, 240H, (CH$_3$CCH$_2$COOHCH$_2$CHOHCH$_3$)$_{40}$). FTIR: ν_{max}/cm^{-1} (solid): 3365 cm^{-1} (alcohol O-H stretch), 2975 cm^{-1} (carboxylic acid O-H stretch), 1717 cm^{-1} (ester C=O stretch), 1453 cm^{-1}(alkane C-H stretch), 1241 cm^{-1} (C=S stretch), 1149 cm^{-1} (alcohol C-O stretch) and 993 cm^{-1} (C-S bend).

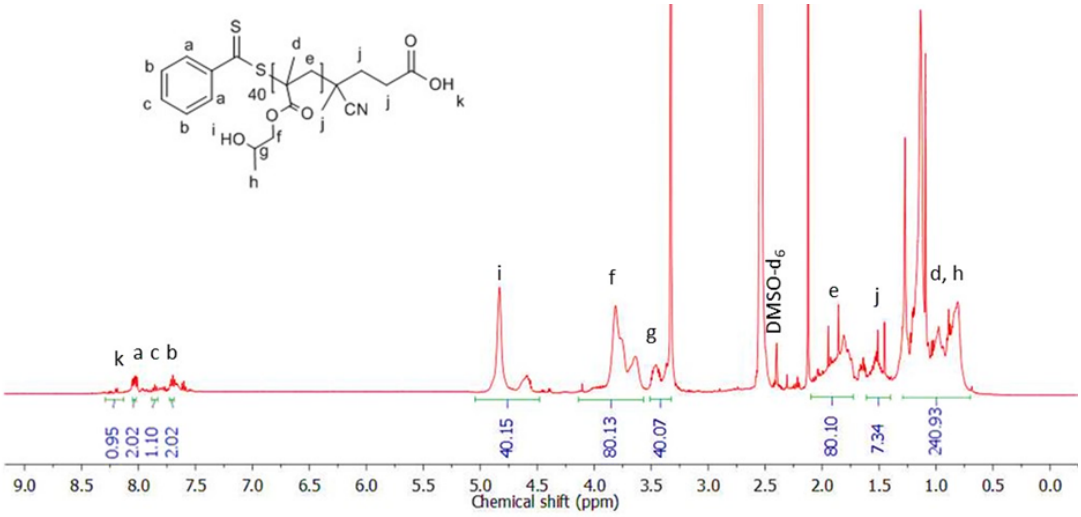

Figure 5. 10. The 500 MHz ^{1}H-NMR spectrum of PHPMA$_{40}$ in DMSO-d$_6$ at 25 °C.

PHPMA$_{60}$: 0.394 g, 62.1 wt. % (yellow solid). APC (PMMA standards): M_w= 8800 g mol^{-1}. Dispersity= 1.12. ^{1}H-NMR of PHPMA$_{60}$ (500 MHz, DMSO-d$_6$, δ, ppm): 8.25 – 8.09 (s, 1H, COOH), 8.05 – 7.99 (d, 2H, ArH), 7.83 – 7.75 (t, 1H, ArH), 7.72 – 7.66 (d, 2H, ArH), 5.10 – 4.53 (m, 60H, (HOCH$_2$CHOHCH$_3$)$_{60}$), 4.41– 3.51 (m, 120H, (HOCH$_2$CHOHCH$_3$)$_{60}$), 3.50 – 3.26 (m, 60H, (HOCH$_2$CHOHCH$_3$)$_{60}$), 2.30 – 1.70 (m, 127H, (CH$_3$CCH$_2$)$_{60}$ CH$_3$CCNCH$_2$CH$_2$), 1.63 – 0.30 (m, 360H, (CH$_3$CCH$_2$COOHCH$_2$CHOHCH$_3$)$_{60}$). FTIR: ν_{max}/cm^{-1} (solid): 3360 cm^{-1} (alcohol O-H stretch), 2975 cm^{-1} (carboxylic acid O-H stretch), 1717 cm^{-1} (ester C=O stretch), 1453 cm^{-1}(alkane C-H stretch), 1241 cm^{-1} (C=S stretch), 1149 cm^{-1} (alcohol C-O stretch) and 993 cm^{-1} (C-S bend).

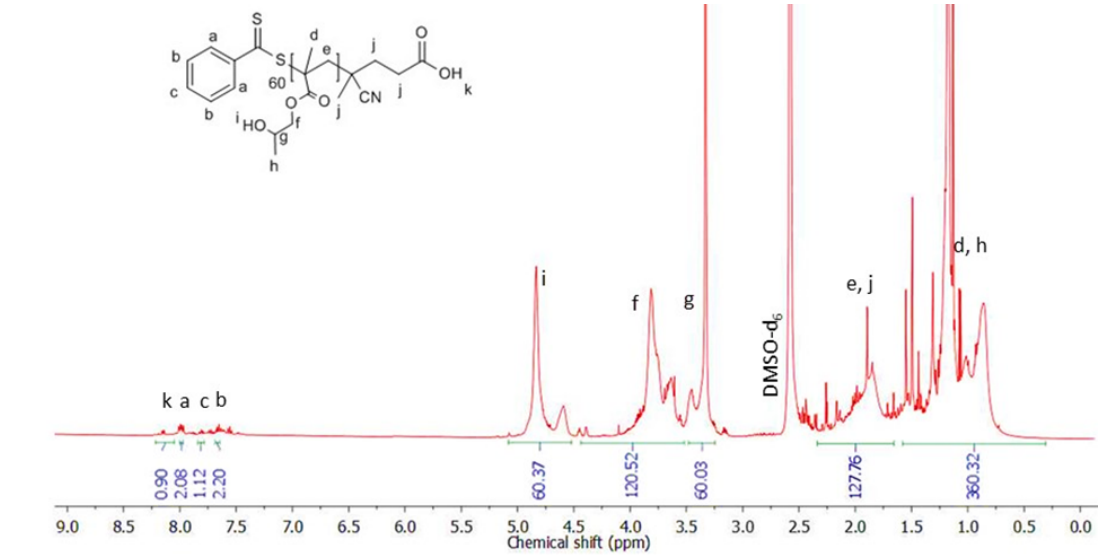

Figure 5. 11. The 500 MHz ^{1}H-NMR spectrum of $PHPMA_{60}$ in DMSO-d_6 at 25 °C.

$PHPMA_{80}$: 0.575 g, 68.6 wt. % (yellow solid). APC (PMMA standards): M_w= 11700 g mol^{-1}. Dispersity= 1.15. ^{1}H-NMR of $PHPMA_{80}$ (500 MHz, DMSO-d_6, δ, ppm): 8.20 – 8.16 (s, 1H, COOH), 7.92 – 7.86 (d, 2H, ArH), 7.85 – 7.54 (t, 1H, ArH), 7.52 – 7.45 (d, 2H, ArH), 5.02 – 4.46 (m, 80H, $(HOCH_2CHOHCH_3)_{80}$), 3.80– 3.58 (m, 160H, $(HOCH_2CHOHCH_3)_{80}$), 3.48 – 3.29 (m, 80H, $(HOCH_2CHOHCH_3)_{80}$), 2.15 – 1.66 (m, 160H, $(CH_3CCH_2)_{80}$), 1.58 – 1.31 (m, 7H, $CH_3CCNCH_2CH_2$), 1.28 – 0.67 (m, 480H, $(CH_3CCH_2COOHCH_2CHOHCH_3)_{80}$). FTIR: ν_{max}/cm^{-1} (solid): 3371 cm^{-1} (alcohol O-H stretch), 2975 cm^{-1} (carboxylic acid O-H stretch), 1717 cm^{-1} (ester C=O stretch), 1453 cm^{-1}(alkane C-H stretch), 1241 cm^{-1} (C=S stretch), 1149 cm^{-1} (alcohol C-O stretch) and 993 cm^{-1} (C-S bend).

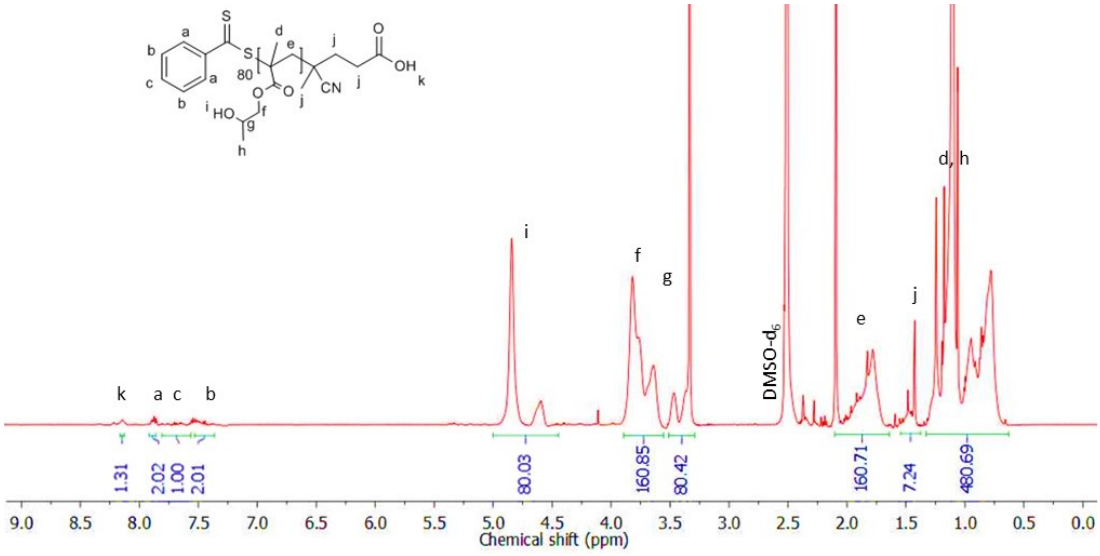

Figure 5. 12. The 500 MHz ^{1}H-NMR spectrum of $PHPMA_{80}$ in DMSO-d_6 at 25 °C.

5.2.5. PHPMA gel synthesis: HPMA polymerisation from 4-cyano-4-(phenylcarbonothioyl)thiopentanoic acid

The synthetic procedure was the same as that described in chapter 4.2.2. Briefly, 4-cyano-4-((phenylcarbonothioyl)thiopentanoic acid RAFT agent (0.030 g, 0.107 mmol) was dissolved in acetone (2.0 mL) and deionised water (1.0 mL). Then AAPH (0.215 g, 0.793 mmol) was added into the mixture followed by deionised water (1.0 mL). When everything dissolved, HPMA (3.09 g, 21.4 mmol) was added dropwise into the reaction followed by deionised water (1.0 mL) and stirred at 60 °C overnight. The polymer synthesised was $PHPMA_{200}$. $PHPMA_{80}$ was also synthesised using the same procedure and quantity of HPMA was (1.23 g, 5.760 mmol). ^{1}H NMR, FTIR, APC analysis were the same as that described in chapter 4.2.2.

5.3. Results and discussion

The overall route to fucose-capped PHPMA nanoparticles that were able to withhold, and gradually release, Dox is presented in Scheme 5.1, and detailed reaction schemes are provided in Schemes 5.2 and 5.3. Dox-loaded fucose-$PHPMA_{100}$ nanoparticles and $PHPMA_{200}$ gel depot were dissolved in DMSO. A Dox loaded gel depot can be formed by injecting the prepared DMSO solution in PBS buffer solution, significant amount of Dox released in pH 7.4 environment at 37 °C (Scheme 5.1).

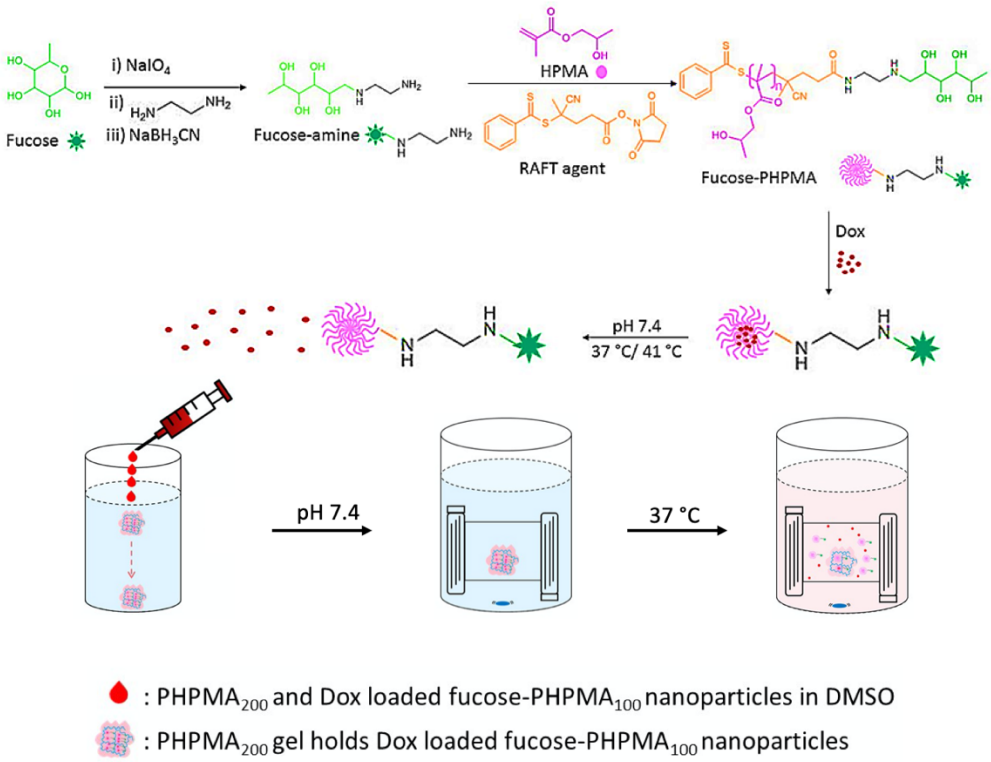

Scheme 5. 1. Reaction outline for the creation of fucose-PHPMA nanoparticles that are capable of encapsulating and releasing Dox, at physiological temperature. A Dox loaded gel depot can be prepared by dissolving Dox-loaded fucose-PHPMA$_{100}$ nanoparticles and PHPMA$_{200}$ in DMSO and injecting in PBS buffer solution, Dox can be released in pH 7.4 environment at 37 °C.

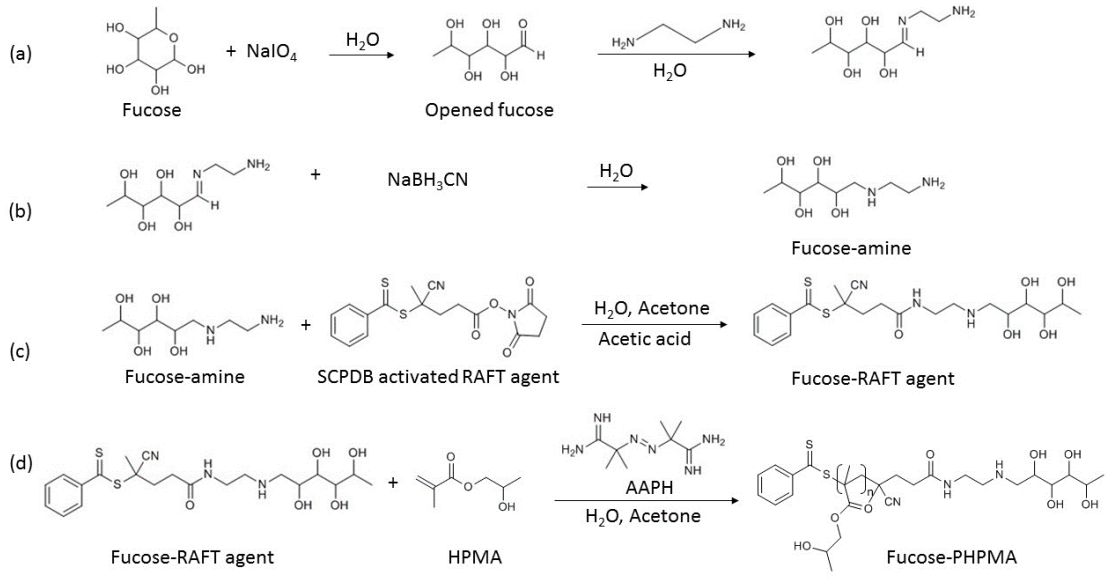

Scheme 5. 2. The synthesis steps to fucose-PHPMA. a) The fucose conjugation to ethylenediamine. b) Reduction of the imine to fucose-amine. c) SCPDB RAFT agent conjugation to fucose-amine. d) HPMA polymerisation from the fucose-RAFT agent.

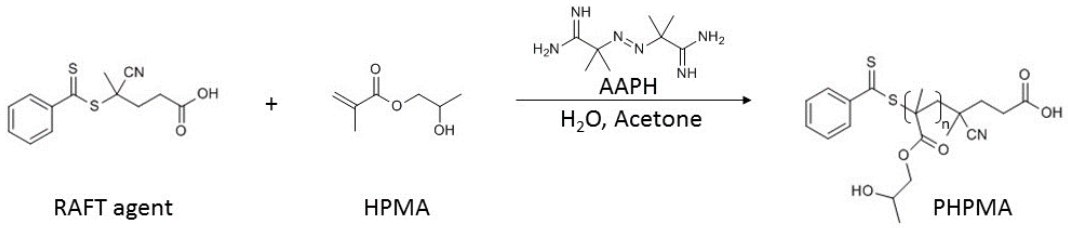

Scheme 5. 3. The synthesis of PHPMA.

Fucose was successfully oxidised by sodium meta-periodate as indicated by the proton from the aldehyde group showed in Figure 5.13. Chemical shift of i and f were decreased due to addition of electron density from oxygen atoms which might be overlapped with proton environment j. An amine group was conjugated to the opened fucose by reacting to ethylenediamine to form an imine linkage followed by reduction with sodium cyanoborohydride. There were no aldehyde functional groups in the ^{1}H NMR shown in Figure 5.1 so the amine conjugation and reduction progressed well and produced fucose-amine. Since the ^{1}H NMR spectra of opened fucose and fucose-amine were very similar, ^{13}C NMR was employed for fucose-amine analysis in order to confirm fucose-amine was synthesised. The peaks between 40-55 ppm correspond to the amine part of fucose-amine, but the chemical environment h was higher than other environments which needs further analysis (Figure 5.14). There were no peaks from 55-40 ppm in Figure 5.15 (reactant fucose) so the peaks in that region (Figure 5.14) were from the amine group in synthesised fucose-amine. The peaks in the aromatic region (Figure 5.2) showed that the RAFT agent was conjugated to fucose-amine after washing with DCM.

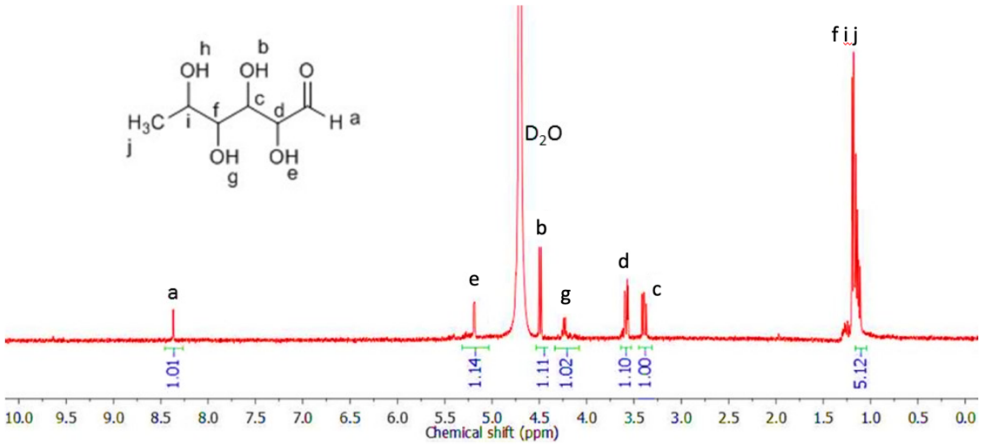

Figure 5. 13. The 500 MHz ^{1}H-NMR spectrum of opened fucose in D_2O at 25 °C.

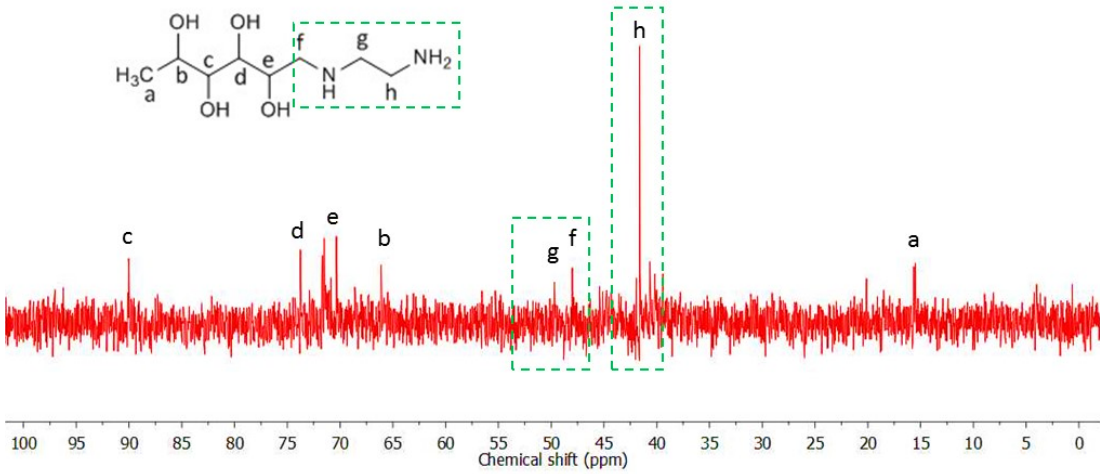

Figure 5. 14. The 125 MHz ^{13}C-NMR spectrum of fucose-amine in D_2O at 25 °C.

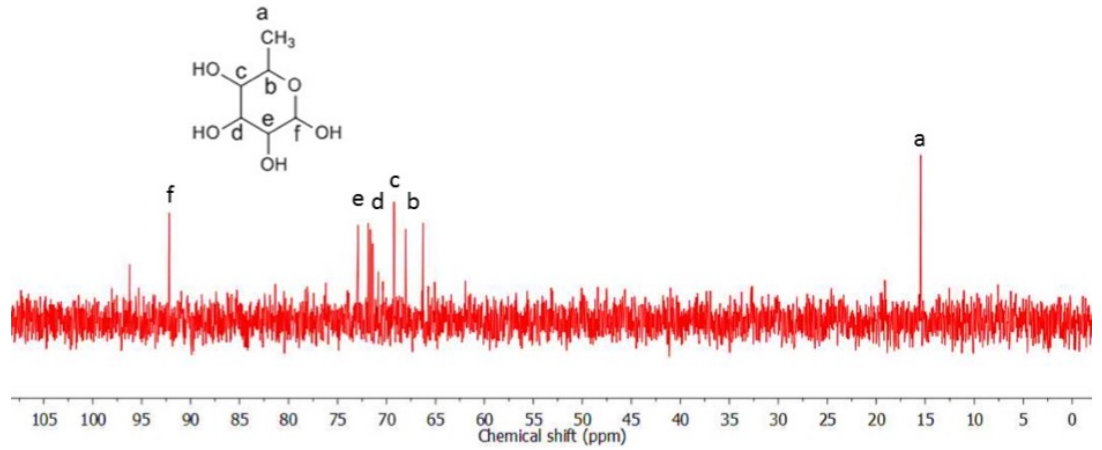

Figure 5. 15. The 125 MHz ^{13}C-NMR spectrum of fucose in D_2O at 25 °C.

Different chain lengths (20, 40, 60, 80 and 100) of fucose-PHPMA were synthesised (Figures 5.3 -5.7). The integration values corresponding to the proton environments f, g, h, e, d and i progressively increased in Figures 5.3 -5.7 suggesting longer chain lengths of PHPMA were produced. In order to compare the differences between fucose-PHPMA and PHPMA with same chain lengths (via DLS analysis), PHPMA with 20, 40, 60, 80, and 100 repeat units were produced successfully via RAFT polymerisation (Scheme 5.3). Aromatic functional groups between 8.10 ppm and 7.40 ppm and carboxylic acid groups between 8.30 ppm and 8.10 ppm indicating PHPMA was synthesised by RAFT polymerisation (Figures 5.8-5.12). The molecular weight of fucose-PHPMA and PHPMA with 20, 40, 60, 80, 100 and 200 repeat units determined by APC (Table 5.1), the theoretical and actual molecular weights are comparable.

Table 5. 1. APC data for Fucose-PHPMA and PHPMA polymers.

Polymer	Theoretical M_w ($g.mol^{-1}$)	Actual M_w ($g.mol^{-1}$)	PDI
Fucose-$PHPMA_{20}$	3348	3700	1.38
Fucose-$PHPMA_{40}$	6228	7600	1.48
Fucose-$PHPMA_{60}$	9108	11400	1.69
Fucose-$PHPMA_{80}$	11988	15500	1.55
Fucose-$PHPMA_{100}$	14868	16000	1.82
$PHPMA_{20}$	3159	3100	1.22
$PHPMA_{40}$	6039	6000	1.37
$PHPMA_{60}$	8919	8800	1.12
$PHPMA_{80}$	11799	11700	1.15
$PHPMA_{100}$	14679	14400	1.33
$PHPMA_{200}$	29079	28500	1.24

The products from each step (Schemes 5.2 and 5.3) were analysed via FTIR spectroscopy. The aldehyde (C=O stretching 1631 cm^{-1}) functional group in opened fucose (Figure 5.16 black) confirmed fucose was completely oxidised by sodium meta-periodate. Amine groups (N-H stretching 3474 cm^{-1}) showed in the fucose-amine FTIR spectrum (Figure 5.16 red) suggested that the aldehyde functional group of opened fucose was reduced by sodium cyanoborohydride. There was excess nitrile (C≡N stretching 2335 cm^{-1}) in the FTIR spectrum of fucose-amine (Figure 5.16 purple square) which was washed by water in the final synthesis step (Scheme 5.2 (d)). C=S (stretching 1229 cm^{-1}), C-S (bending 998 cm^{-1}) and aromatic groups can be found in both of fucose-RAFT agent and fucose-PHPMA FTIR spectra (Figure 5.16 blue and pink, Figure 5.17). Therefore, activated SCPDB agent conjugated to fucose-amine cannot be washed away by DCM and water, showing covalent conjugation. A strong and broad peak corresponding to the C-O alcohol group (1053 cm^{-1}) appeared on the fucose-PHPMA FTIR spectra (Figure 5.16 pink and Figure 5.17) confirming HPMA monomers propagated extensively from the fucose-RAFT agent. Alcohol (O-H stretching 3371 cm^{-1}), carboxylic acid (COOH stretching 2975 cm^{-1}), ester (C=O stretching 1717 cm^{-1}) and C=S groups (stretching 1241 cm^{-1}) were in the FTIR

spectra (Figure 5.18) confirming PHPMA with 20, 40, 60, 80 and 100 repeat units were synthesised.

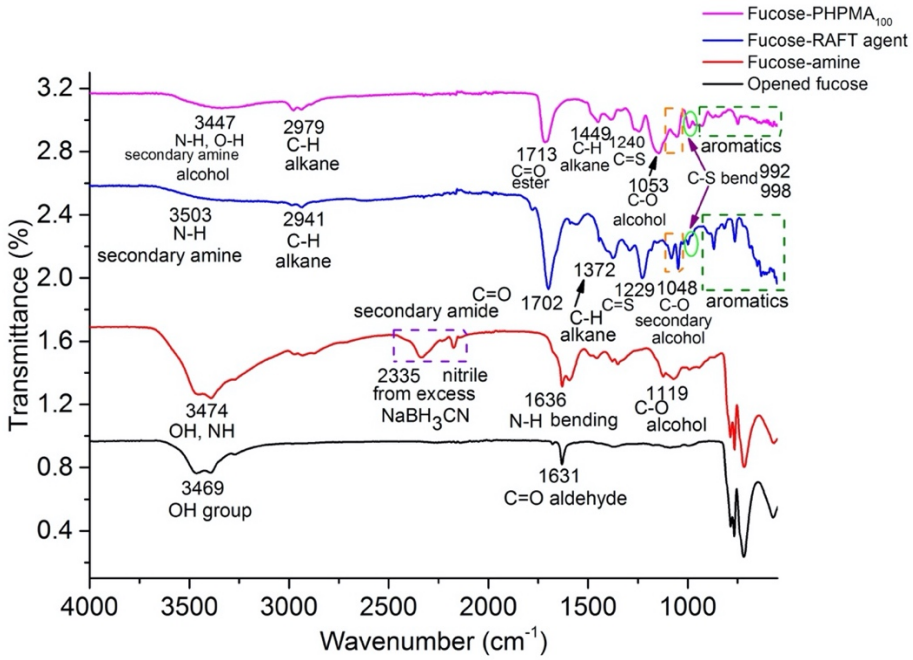

Figure 5. 16. FTIR spectra of opened fucose, fucose-amine, fucose-RAFT agent and fucose-PHPMA$_{100}$.

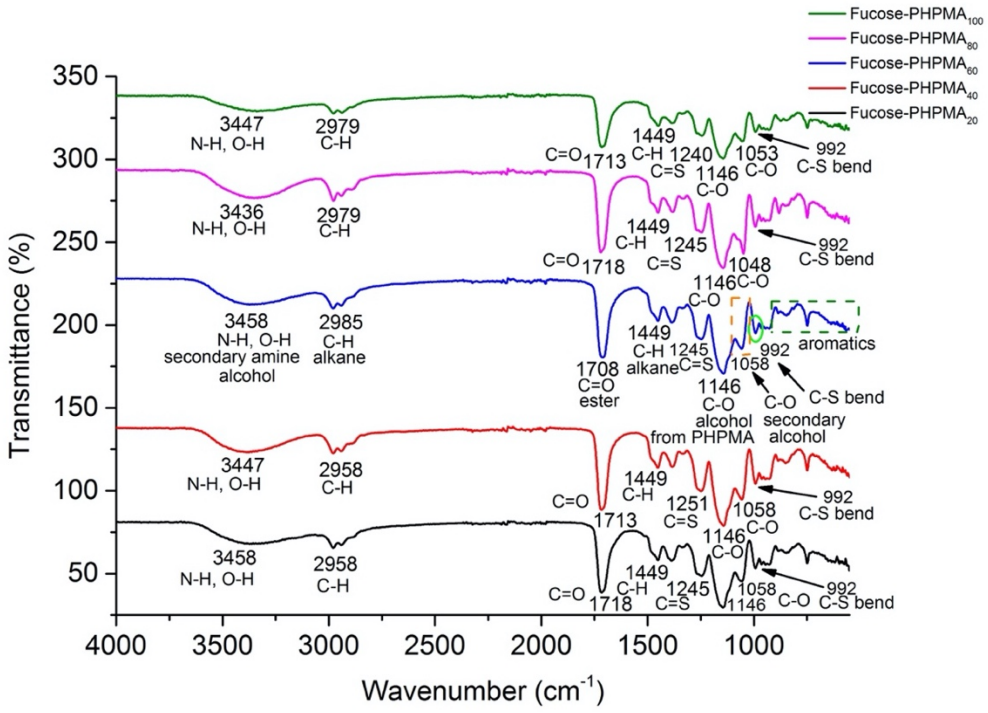

Figure 5. 17. FTIR spectra of fucose-PHPMA with 20, 40, 60, 80 and 100 chain lengths.

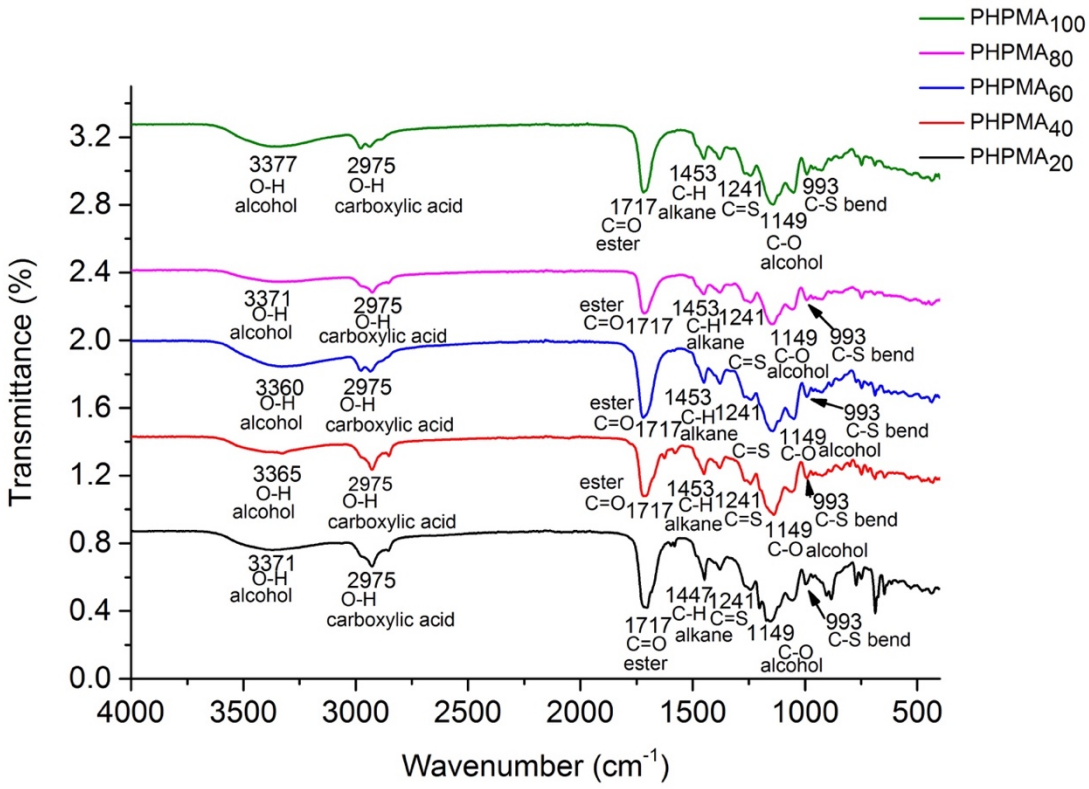

Figure 5. 18. FTIR spectra of PHPMA with 20, 40, 60, 80 and 100 chain lengths.

In order to discover if particles of appropriate dimensions for drug loading and release can be created, fucose-PHPMA with different PHPMA chain lengths (20, 40, 60, 80, and 100) were synthesised. Particle samples were prepared by coacervation. Each polymer was dissolved in DMF then added dropwise into deionised water under stirring to make a final concentration of polymer 0.1 mg mL^{-1}. Intensity size distribution was used to analyse nanoparticle size. Refractive index and absorption of fucose-PHPMA cannot be found in the literature. Therefore, refractive index and absorption of PHPMA were used which were 1.548 and 0.100, respectively [38]. The volume and number size analysis need accurate refractive index and absorption of the sample but intensity size analysis depends on light scattering of the sample. Therefore, intensity size analysis of the sample is more reliable. The correlogram of fucose-$PHPMA_{100}$ showed in Figure 5.19. The correlogram decayed quick and had a steep gradient means that the particle size of the particles was small ((217±3)nm).

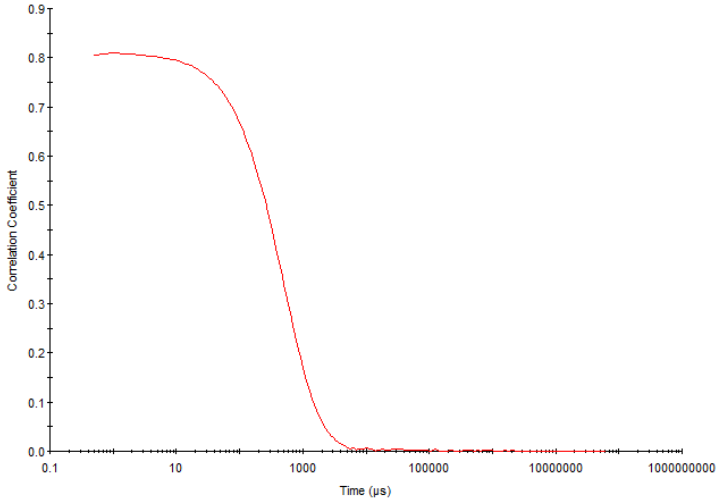

Figure 5. 19. Correlogram of fucose-PHPMA$_{100}$ nanoparticle at room temperature.

The particle size became larger as the PHPMA chain lengths of the polymers increased (Table 5.2, DLS data presented in Figure A5.1). At room temperature, the particle size of Dox-loaded and blank polymer nanoparticles were very similar, fucose-PHPMA$_{20}$ and Dox-loaded fucose-PHPMA$_{20}$ were (93±5)nm and (91±2)nm, respectively; fucose-PHPMA$_{40}$ and Dox-loaded fucose-PHPMA$_{40}$ were (106±6)nm and (108±4)nm, respectively; fucose-PHPMA$_{60}$ and Dox-loaded fucose-PHPMA$_{60}$ were (121±1)nm and (122±1)nm, respectively; fucose-PHPMA$_{80}$ and Dox-loaded fucose-PHPMA$_{80}$ were (163±6)nm and (165±2)nm, respectively; and fucose-PHPMA$_{100}$ and Dox-loaded fucose-PHPMA$_{100}$ were (217±3)nm and (219±2)nm, respectively (Table 5.2). All of the PDI values were lower than 0.3 (Table 5.2), the polymer nanoparticles with and without Dox loaded were very stable in water. PHPMA (without fucose) nanoparticles with different chain lengths (20, 40, 60, 80 and 100) may aggregated in water with large particle sizes which were (441±56)nm, (801±100)nm, (722±92)nm, (1992±265)nm and (488±284)nm, respectively at room temperature. All of the PDI values were above 0.6 (Table 5.3, DLS analysis presented in Figure A5.2), emphasising the importance of fucose acting as a hydrophilic section in nanoparticle creation. Dox loading does not influence the particle size and stability of fucose-PHPMA nanoparticles. Since fucose-PHPMA$_{100}$ nanoparticles without and with Dox loaded have the lowest PDI values (0.151 and 0.181, respectively) compared to others, it was considered as the most promising candidate for Dox release analysis.

Table 5. 2. Nanoparticle size and PDI values obtained for nanoparticles formed from fucose-PHPMA, maintained at room temperature. The nanoparticles were measured both when vacant, and loaded with Dox.

Polymer	Size (nm)	PDI
Fucose-PHPMA$_{20}$	93 ±5	0.170
Fucose-PHPMA$_{40}$	106 ±6	0.205
Fucose-PHPMA$_{60}$	121 ±1	0.169
Fucose-PHPMA$_{80}$	163 ±6	0.165
Fucose-PHPMA$_{100}$	217 ±3	0.151
Fucose-PHPMA$_{20}$ (Dox)$^{\pm}$	91 ±2	0.209
Fucose-PHPMA$_{40}$ (Dox)$^{\pm}$	108 ±4	0.218
Fucose-PHPMA$_{60}$ (Dox)$^{\pm}$	122 ±1	0.186
Fucose-PHPMA$_{80}$ (Dox)$^{\pm}$	165 ±2	0.217
Fucose-PHPMA$_{100}$ (Dox)$^{\pm}$	219 ±2	0.181

± Denotes Dox-loaded nanoparticles. 0.033mg, 0.093mg, 0.158mg, 0.221mg and 0.245mg of Dox were loaded in 3.0 mg of each fucose-PHPMA$_{20}$, fucose-PHPMA$_{40}$, fucose-PHPMA$_{60}$, fucose-PHPMA$_{80}$, and fucose-PHPMA$_{100}$ nanoparticles, respectively.

Table 5. 3. Nanoparticle size and PDI values for nanoparticles formed from PHPMA$_{20}$, PHPMA$_{40}$, PHPMA$_{60}$, PHPMA$_{80}$ and PHPMA$_{100}$ at room temperature.

Polymer	Size (nm)	PDI
PHPMA$_{20}$	85 ±11 441 ±56	0.683
PHPMA$_{40}$	801 ±100	0.837
PHPMA$_{60}$	722 ±92	0.786
PHPMA$_{80}$	1992 ±265	0.644
PHPMA$_{100}$	488 ±284	0.653

Dr. David Green conducted SEM analysis for Dox loaded and without Dox-loaded fucose-PHPMA$_{100}$ nanoparticles at room temperature and at 37 °C. SEM analysis was conducted to image fucose-PHPMA$_{100}$ and Dox-loaded fucose-PHPMA$_{100}$ nanoparticles in deionised water at room temperature (Figure 5.20 b and e). Statistical analysis of particle size of fucose-PHPMA$_{100}$ and Dox-loaded fucose-PHPMA$_{100}$ nanoparticles were determined

from the SEM images (Figure 5.20 c and f). FWHM value of particle size distribution of fuose-PHPMA$_{100}$ nanoparticles (Figure 5.20 c) was (23±5)nm, and the R^2 value was 0.87. For particle size distribution of Dox-loaded fuose-PHPMA$_{100}$ nanoparticles (Figure 5.20 f), FWHM value was (158±74)nm, R^2 value was 0.88. DLS analysis was performed again in order to confirm the samples were stable after a re-suspension in water (Figure 5.20 a and d). Fucose-PHPMA$_{100}$ without and with Dox-loaded were shown as spherical nanoparticles in SEM images which proved that the nanoparticles were synthesised (Figure 5.20 b and e). The particle size from the statistical analysis of fucose-PHPMA$_{100}$ nanoparticles and Dox-loaded fucose-PHPMA$_{100}$ nanoparticles were (101±3)nm and (166±14)nm, respectively, which were smaller than the size measured by DLS (217±3)nm and (219±2)nm, respectively. In DLS analysis, the nanoparticles were in hydrated state, and have hydrogen bonding interactions between hydroxyl groups and aqueous solution. However, SEM samples were prepared by extracting 2 μL of the sample by a micropipette, placing on a silicon wafer and air-dried at room temperature in a fumehood so the hydrogen bonding interactions disappeared. Therefore, the particle size may be decreased due to this effect. There were particles with size above 200 nm and 300 nm shown in the SEM images (Figure 5.20 b and e) presented in histograms (Figure 5.20 c and f). During air-drying process, some nanoparticles may be overlaid so large particles may be shown on SEM images. This may be optimised by diluting the sample and find a best concentration.

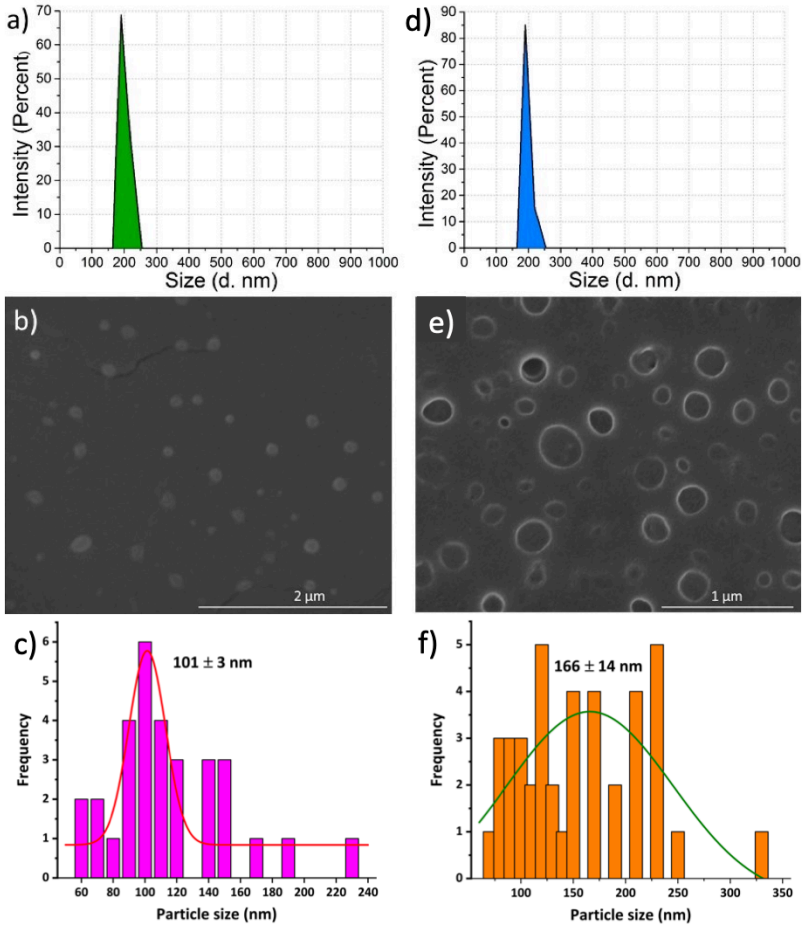

Figure 5. 20. a) Particle size determination of fucose-PHPMA$_{100}$ via DLS, b) SEM micrograph of fucose-PHPMA$_{100}$ nanoparticles at room temperature, Scale bar represents 2 µm, c) Statistical analysis of fucose-PHPMA$_{100}$ nanoparticles as determined by SEM image, d) Particle size determination and e) SEM images corresponding to Dox-loaded nanoparticles formed from fucose-PHPMA$_{100}$ at room temperature. Scale bar represents 1 µm, f) Statistical analysis of Dox-loaded fucose-PHPMA$_{100}$ nanoparticles as determined by SEM image.

The aim for the synthesised nanoparticles was their utilisation as anti-cancer drug carriers and so particle size and appearance must be analysed at 37 °C (human body temperature). The particle size recorded of all the Dox loaded and unloaded fucose-PHPMA nanoparticles decreased significantly at 37 °C (Table 5.4, DLS data presented in Figure A5.3). For Dox-loaded fucose-PHPMA nanoparticles with 20, 40, 60, 80 and 100 PHPMA chain lengths, the particle size decreased from (91±2)nm to (11±2)nm, (108±4)nm to (16±1)nm, (122±1)nm to (19±1)nm, (165±2)nm to (22±2)nm, and (219±2)nm to (32±1)nm, respectively. For pure fucose-PHPMA nanoparticles (without Dox loaded) with 20, 40, 60, 80 and 100 PHPMA chain lengths, the particle size decreased

from (93±5)nm to (12±1)nm, (106±6)nm to (16±3)nm, (121±1)nm to (19±1)nm, (163±6)nm to (22±1)nm, (217±3)nm to (32±3)nm, respectively. PDI values of all the Dox loaded and unloaded nanoparticles at 37 °C (Table 5.4) were slightly higher than that at room temperature (Table 5.2) since faster movement of the nanoparticles at higher temperature (37 °C) might disturb the very stable environment [39]. All of the PDI values were lower than 0.3 so the particles without and with Dox loaded remained stable (Table 5.4). At 37 °C, the particle size of each sample without and with Dox loaded were very similar to each other which proved that Dox loading into fucose-PHPMA nanoparticles does not affect the particle size (Figure 5.21). Particle size measured by statistical analysis of the SEM images of fucose-PHPMA$_{100}$ nanoparticles with and without Dox loaded were (36±2)nm and (37±1)nm, respectively (Figure 5.21 f and c) which matched the particle size determined by DLS, (32±1)nm and (32±3)nm, respectively (Table 5.4). FWHM values and R^2 values of the particle size distributions of fucose-PHPMA$_{100}$ nanoparticles and Dox-loaded fucose-PHPMA$_{100}$ nanoparticles (Figure 5.21 c and f) were (12±4)nm and 0.87, (20±6)nm and 0.88, respectively. The particle size of all the nanoparticles with and without Dox loaded decreased significantly from room temperature to 37 °C which proved thermoresponsive property of fucose-PHPMA nanoparticles.

Table 5. 4. Nanoparticle size and PDI values obtained for nanoparticles formed from fucose-PHPMA, maintained in aqueous solution at 37 °C. The nanoparticles were measured both when vacant, and loaded with Dox.

Polymer	Size (nm)	PDI
Fucose-PHPMA$_{20}$	12 ±1	0.203
Fucose-PHPMA$_{40}$	16 ±3	0.215
Fucose-PHPMA$_{60}$	19 ±1	0.217
Fucose-PHPMA$_{80}$	22 ±1	0.218
Fucose-PHPMA$_{100}$	32 ±3	0.232
Fucose-PHPMA$_{20}$ (Dox)$^{\pm}$	11 ±2	0.238
Fucose-PHPMA$_{40}$ (Dox)$^{\pm}$	16 ±1	0.251
Fucose-PHPMA$_{60}$ (Dox)$^{\pm}$	19 ±1	0.256
Fucose-PHPMA$_{80}$ (Dox)$^{\pm}$	22 ±2	0.233
Fucose-PHPMA$_{100}$ (Dox)$^{\pm}$	32 ±1	0.201

± Denotes Dox-loaded nanoparticles.

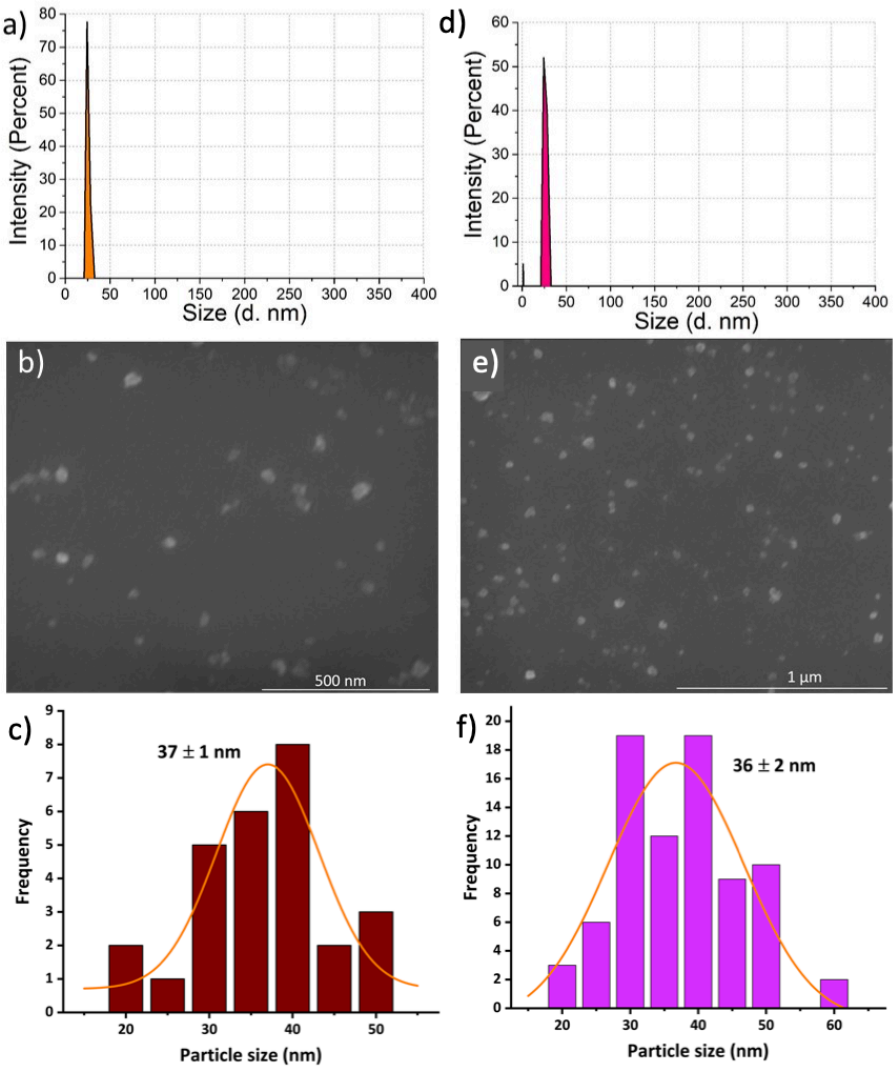

Figure 5. 21. The condition was at 37 °C for 24 hours and applied to all the samples. a) Particle size determination of fucose-PHPMA$_{100}$, b) SEM image of fucose-PHPMA$_{100}$ nanoparticles, c) Statistical analysis of fucose-PHPMA$_{100}$ nanoparticles as determined by SEM image, d) Particle size determination of Dox-loaded fucose-PHPMA$_{100}$ nanoparticles, e) SEM image of Dox-loaded fucose-PHPMA$_{100}$ nanoparticles, f) Statistical analysis of Dox-loaded fucose-PHPMA$_{100}$ nanoparticles as determined by SEM image.

All fucose-PHPMA (3.0 mg) with 20, 40, 60, 80 and 100 chain lengths were loaded with 0.3 mg of Dox, the longer the PHPMA chain length, more of Dox can be loaded. The longer the PHPMA chain length, the greater amount of Dox can be loaded. 0.033 mg (11%), 0.093 mg (31%), 0.158 mg (53%), 0.221 mg (74%) and 0.245 mg (82%) of Dox was then loaded into fucose-PHPMA$_{20}$, fucose-PHPMA$_{40}$, fucose-PHPMA$_{60}$, fucose-PHPMA$_{80}$ and fucose-PHPMA$_{100}$ nanoparticles in PBS buffer solution, respectively. The extent of Dox release from each configuration of fucose-PHPMA nanoparticles was assessed at room

temperature and at 37 °C (Figure 5.22). Negligible release of Dox after 168 hours (≈ 2 % for all nanoparticle samples) from the series of particles demonstrated that Dox can largely be held within all nanoparticles at room temperature (Figure 5.22 a). Particles created from fucose-PHPMA$_{20}$ revealed the most rapid release of Dox at 37 °C, with complete release occurring after 29 hours (Figure 5.22 b). Restricted Dox release corresponded with greater HPMA content within the nanoparticles, enabling the release rate to be tuned by altering the polymer composition. The extent of Dox release was determined to be 100 %, 66 %, 46 % and 31 % for fucose-PHPMA$_{40}$, fucose-PHPMA$_{60}$, fucose-PHPMA$_{80}$ and fucose-PHPMA$_{100}$ nanoparticles respectively after 168 hours (Figure 5.22 b).

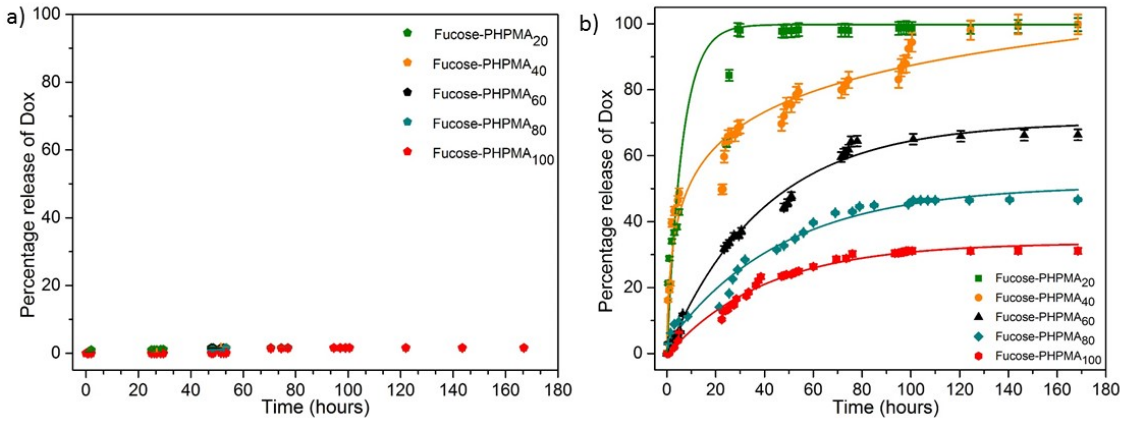

Figure 5. 22. Dox release from fucose-PHPMA$_{20}$, fucose-PHPMA$_{40}$, fucose-PHPMA$_{60}$, fucose-PHPMA$_{80}$ and fucose-PHPMA$_{100}$ nanoparticles (a) at room temperature in PBS buffer solution (the data points overlapped with each other) and (b) at 37 °C in PBS buffer solution.

Since fucose-PHPMA$_{100}$ nanoparticles (with and without Dox) possessed the lowest PDI values, this polymer was taken forward for further analysis. The initial release studies revealed that 13 % of Dox was released from the fucose-PHPMA$_{100}$ particles after 24 hours at 37 °C, the lowest release of all nanoparticle samples (Figure 5.22 b). Detailed release studies were then conducted in order to investigate the specific temperature that lead to the complete Dox release. To begin with, the Dox release study ran over a temperature range from 22 °C to 50 °C and the solution temperature was increased by 1 °C every 15 minutes (Figure 5.23 a). Extensive Dox release occurred between 39 °C (19 %) and 46 °C (47 %) (Figure 5.23 a). The temperature range of greatest Dox release can be narrowed to between 35 °C and 46 °C, and so this temperature range was studied

more thoroughly by increasing the solution temperature by 1 °C every 40 minutes. Extensive Dox release (19 %, 0.04 mg) occurred between 41 °C and 42 °C (Figure 5.23 b), demonstrating the potential of the reported materials to release more extensively to cancer tumour tissue upon heating. Further Dox release studies were carried out to determine the time required for complete Dox release to occur at 41 °C. 22 % (0.05 mg) of Dox was released in the first hour (Figure 5.23 c), with continuous release culminating in 51 % (0.13 mg), 74 % (0.18 mg) and 90 % (0.22 mg) Dox release after 24 hours, 48 hours and 72 hours, respectively (Figure 5.23 d). Dox release from the fucose-PHPMA$_{100}$ nanoparticles reached 100 % (0.25 mg) after 96 hours.

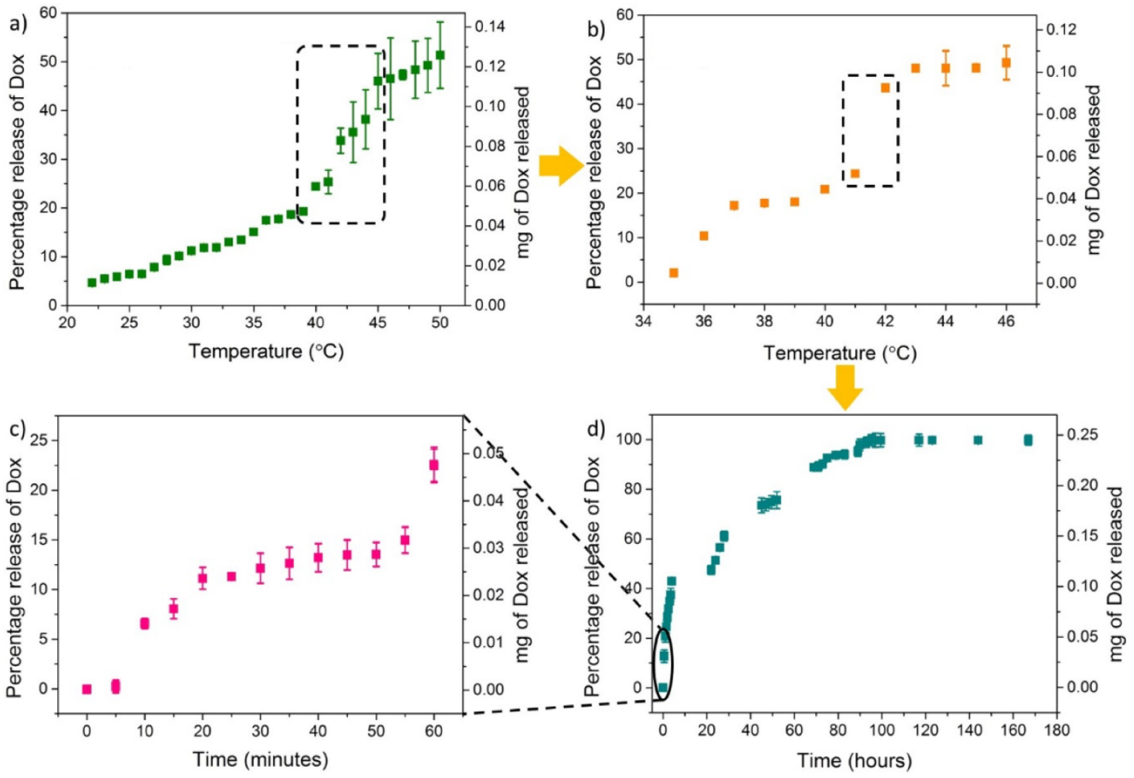

Figure 5. 23. a) Dox release from fucose-PHPMA$_{100}$ nanoparticles into solution increasing in temperature from 22 °C to 50 °C at a rate of 1 °C every 15 minutes. b) Dox release from fucose-PHPMA$_{100}$ nanoparticles into solution increasing in temperature from 35 °C to 46 °C at a rate of 1 °C every 40 minutes c) Dox release from fucose-PHPMA$_{100}$ nanoparticles, monitored every five minutes at 41 °C. d) Dox release from nanoparticles at 41 °C over 7 days.

Next, a thermoresponsive PHPMA depot was employed (discussed in chapter 4) that may act as an injectable delivery vehicle, and host, for Dox-loaded fucose-PHPMA$_{100}$ nanoparticles that enables localised drug release (Figure 5.24). PHPMA$_{80}$ and PHPMA$_{200}$ depots were synthesised by RAFT polymerisation (Scheme 5.3) and conducted ^{1}H NMR,

FTIR and APC analysis which were discussed in chapter 4. PHPMA depot formation occurred upon polymer/DMSO solution being added to PBS buffer solution.

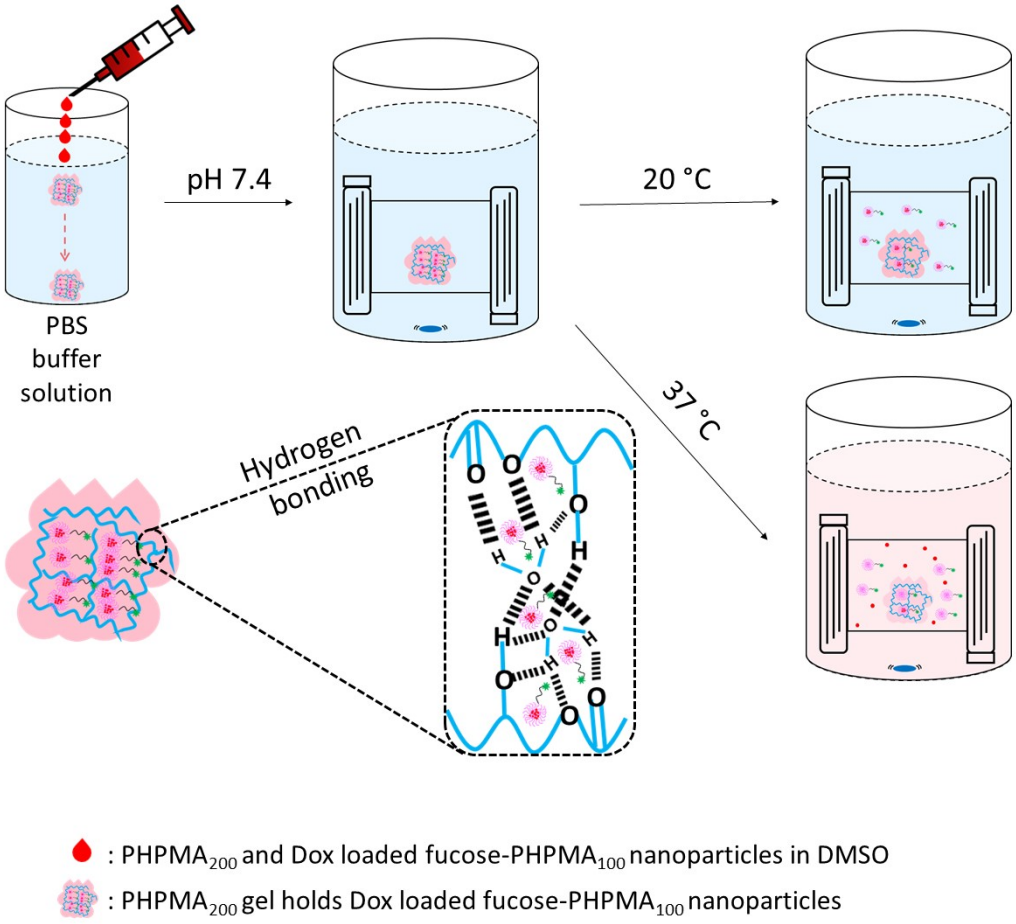

Figure 5. 24. Dox release from fucose-$PHPMA_{100}$ nanoparticles encapsulated in $PHPMA_{200}$ gel in PBS buffer solution at 20 °C and at 37 °C; inside structure of Dox-loaded fucose-$PHPMA_{100}$ nanoparticles encapsulated in $PHPMA_{200}$ gel in PBS buffer solution.

The glass transition temperature of the PHPMA depots was greater with increased polymer chain length (Figure 5.25), and the water content of the two depots were 87.1 % ($PHPMA_{80}$) and 82.5 % ($PHPMA_{200}$), by mass (Table 5.5). The loss modulus (G") of $PHPMA_{200}$ depot formed in PBS buffer solution was constant across the 0.1-100 frequency range so the material was stable. The storage modulus (G') was lower than the loss modulus (G"), indicating that the material was inelastic (Figure 5.26). $PHPMA_{80}$ and $PHPMA_{200}$ depots were then created in the presence of Dox-loaded fucose-$PHPMA_{100}$ nanoparticles (Figure 5.27). $PHPMA_{80}$ cannot form a gel depot in PBS buffer at room temperature which might due to the shorter PHPMA chain length and less hydrogen bonding interactions with PBS buffer solution.

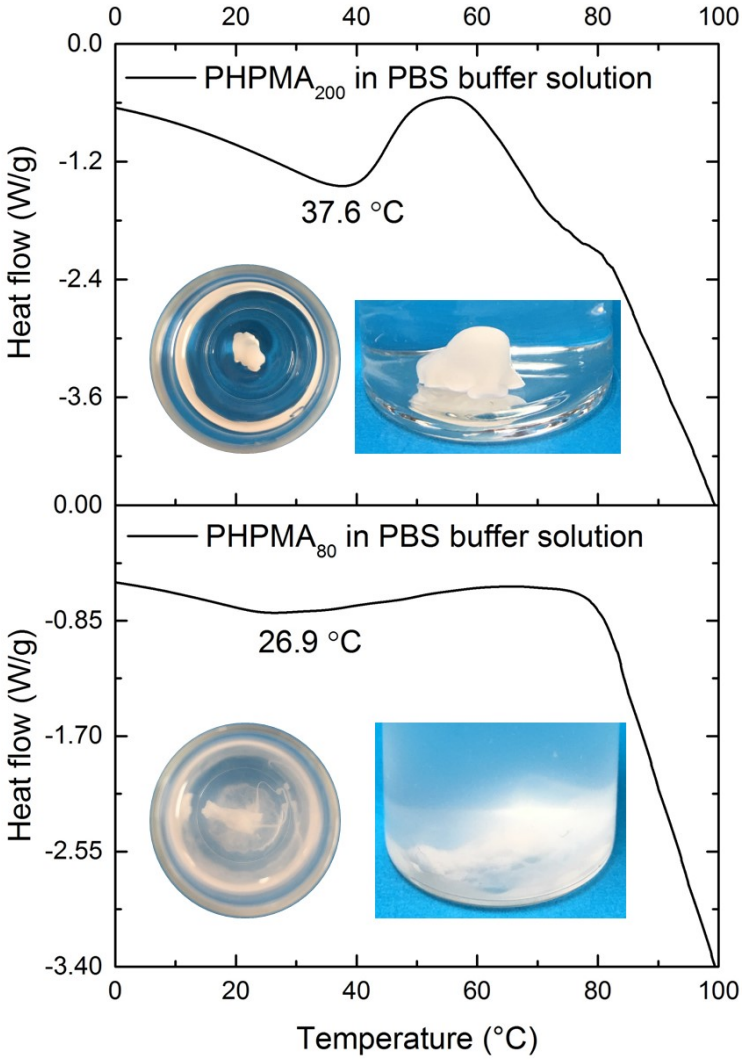

Figure 5. 25. DSC analysis of $PHPMA_{200}$ and $PHPMA_{80}$ depots formed in PBS buffer solution.

Table 5. 5. Water and polymer content of each depot formed, as determined gravimetrically.

Polymer	Percentage of polymer in Depot	Percentage of water in Depot
$PHPMA_{80}$	36.4	63.6
$PHPMA_{80}$ formed in water	12.9	87.1
$PHPMA_{200}$	65.3	34.7
$PHPMA_{200}$ formed in water	17.5	82.5

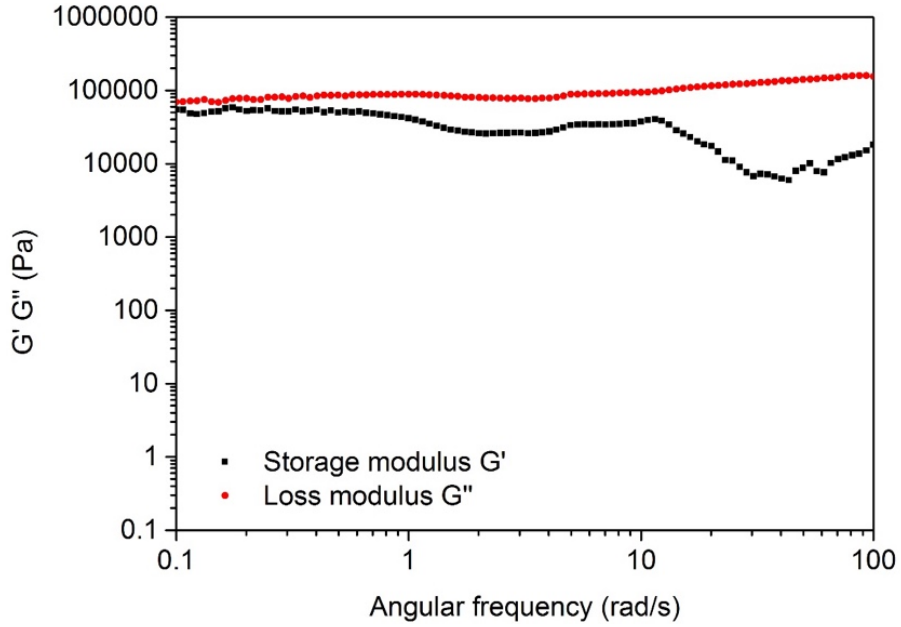

Figure 5. 26. Rheology of $PHPMA_{200}$ depot formed in PBS buffer solution.

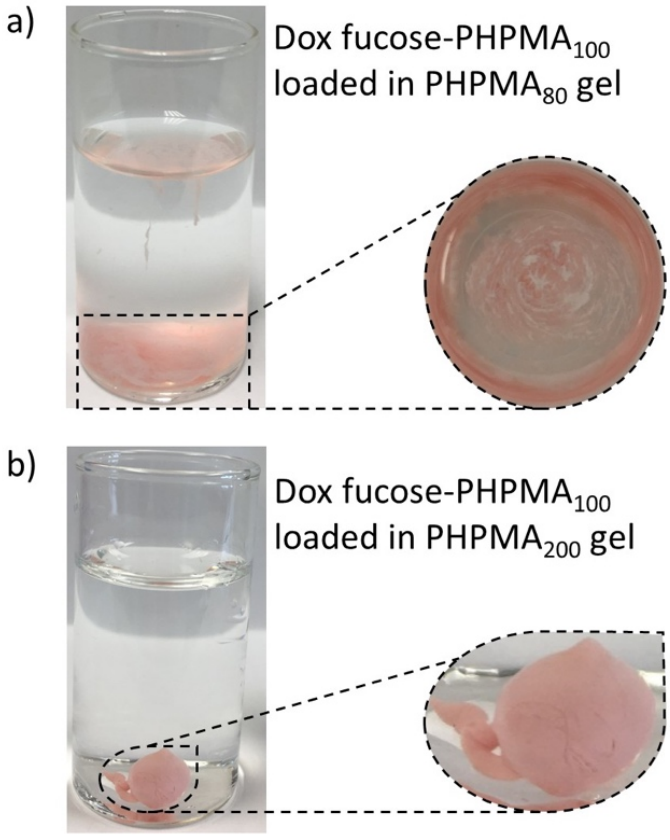

Figure 5. 27. a) Dox-loaded fucose-$PHPMA_{100}$ nanoparticles within $PHPMA_{80}$ gel that is formed by dissolving the contents in DMSO and injecting the solution in PBS buffer solution; b) Dox-loaded fucose-$PHPMA_{100}$ nanoparticles within $PHPMA_{200}$ gel that is formed by dissolving the contents in DMSO and injecting the solution in PBS buffer solution.

Due to the enhanced thermal and mechanical stability of the $PHPMA_{200}$ depot, Dox release from nanoparticles embedded within this material was studied at room temperature and at 37 °C (Figure 5.28). Dox release increased up to 168 hours to solution maintained at 37 °C, before 44 % (0.011 mg) Dox release was recorded after 288 hours. Only a negligible amount of Dox release (2.3 %, 0.0006 mg) occurred at room temperature after 288 hours. The polymer nanoparticles are unable to penetrate through the $PHPMA_{200}$ depot, ensuring that following their injection they remain at the injection site.

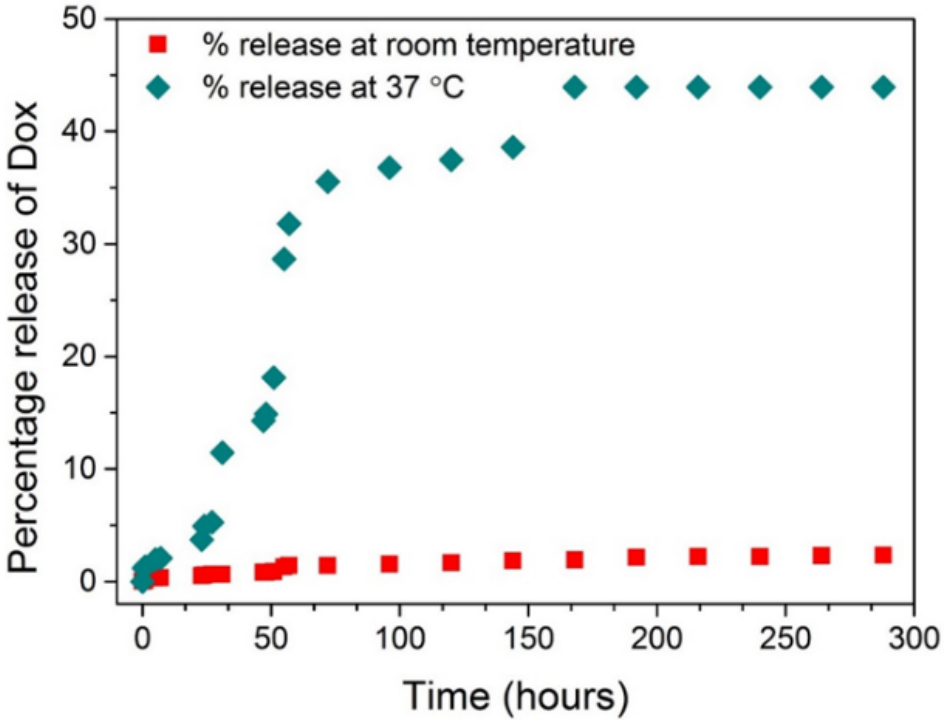

Figure 5. 28. The percentage of Dox release from fucose-$PHPMA_{100}$ nanoparticles loaded in $PHPMA_{200}$ depot that is maintained in PBS buffer solution at room temperature, and at 37 °C.

Further studies revealed that the $PHPMA_{200}$ depot possesses self-healing properties. Two batches of the $PHPMA_{200}$ material were produced; one consisting of aqueous rhodamine b solution incorporated and the other consisting of water only, for illustrative purposes. The $PHPMA_{200}$ material can be stretched to 24.0 cm unevenly, which corresponds to 1200% elongation (Figure 5.29 a). Rhodamine b-containing material was placed in contact with unloaded $PHPMA_{200}$ material, in the presence and absence of PBS buffer solution at 25 °C and at 37 °C (Figure 5.29 c, g, k and o). Over 1 hour, the two independent materials connected to reveal the self-healing properties of the $PHPMA_{200}$ depot,

indicating its potential suitability to be maintained for extended periods, and self-heal if damaged (Figure 5.29 e, i, m and q).

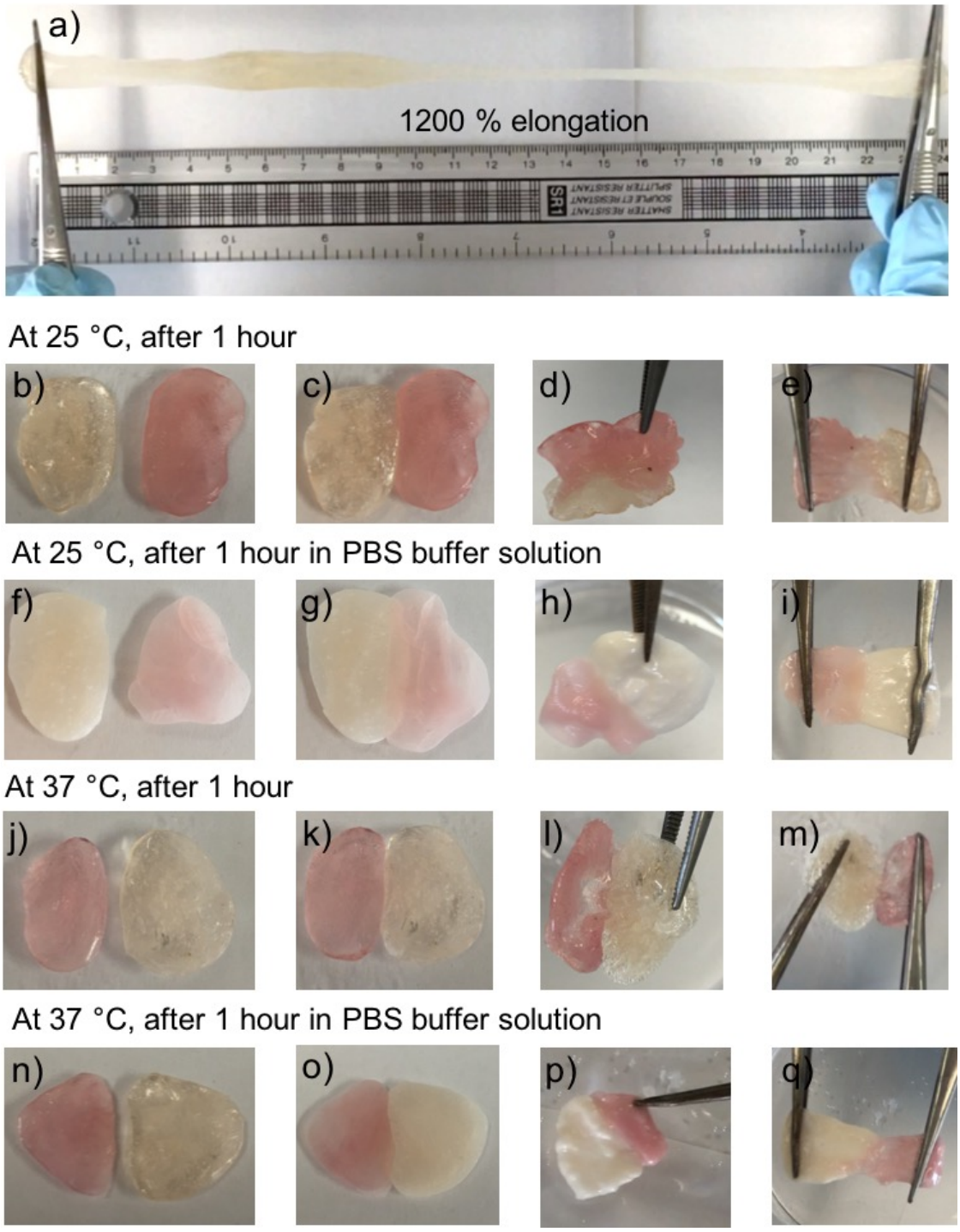

Figure 5. 29. 0.002 mg mL^{-1} of rhodamine b was used to partially colour $PHPMA_{200}$. a) Stretching $PHPMA_{200}$; b-e) Demonstration of $PHPMA_{200}$ self-healing at 25 °C for one hour; f-i) Demonstration of $PHPMA_{200}$ self-healing at 25 °C for one hour in PBS buffer solution; j-m) Demonstration of $PHPMA_{200}$ self-healing at 37 °C for one hour; n-q) Demonstration of $PHPMA_{200}$ self-healing at 37 °C for one hour in PBS buffer solution.

The $PHPMA_{200}$ depot could also withhold rhodamine b in the absence of nanoparticles and be manipulated to form distinct and stable forms in PBS buffer solution. Rhodamine b-containing material could be formed upon injection onto a glass sheet as a viscous liquid (Figure 5.30 a). Upon the addition of PBS buffer solution, a depot formed on the glass sheet that maintained both the loaded rhodamine b, and the defined structure. These materials were able to be rearranged and float on the buffer solution (Figure 5.30 c). The material dimensions and rhodamine b payload were both retained in PBS buffer solution, before the shapes were retrieved from solution and placed on a different glass sheet (Figure 5.30 d). The letters could be removed intact from solution, and placed on a new glass sheet.

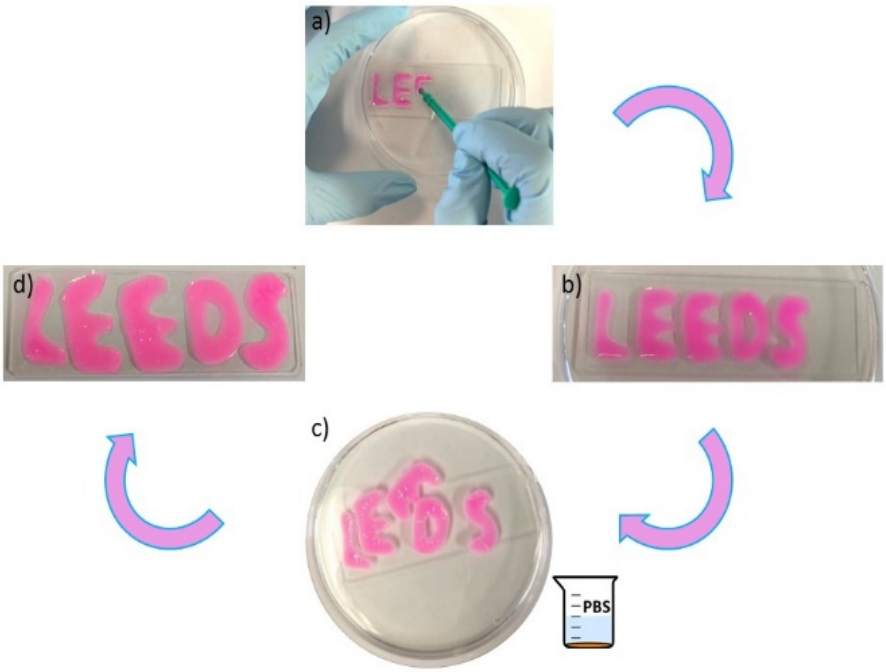

Figure 5. 30. a) Writing "LEEDS" on a glass sheet covered with PBS solution using $PHPMA_{200}$ DMSO solution containing 0.004 mg mL^{-1} rhodamine b; b) Writing complete; c) Upon the addition of further PBS buffer solution to the plate, the characters floated on the PBS buffer solution surface; d) the letters could be removed and placed on another glass sheet.

5.4. Conclusions

Thermally-responsive fucose-modified PHPMA nanoparticles were synthesised by RAFT polymerisation. A single fucose group per polymer chain was sufficient to instigate polymer self-assembly to form nanoparticles in aqueous solution. Spherical fucose-

PHPMA nanoparticles that contained or lacked Dox were very stable at room temperature and at 37 °C, as determined by DLS and SEM analysis. Dox loading into the nanoparticles was achieved by coacervation; negligible Dox release from the nanoparticles occurred at room temperature, whilst extensive release occurring upon the solution temperature increasing to 41 °C. An injectable $PHPMA_{200}$ depot was synthesised by RAFT polymerisation as a delivery vehicle for fucose-$PHPMA_{100}$ nanoparticles. This material possessed self-healing properties in PBS buffer solution, offering great promise to enable nanoparticle localisation at a target site for the prolonged release of anticancer therapeutics.

5.5. References

1. Jacob, J., Haponiuk, J.T., Thomas, S. and Gopi, S. Biopolymer based nanomaterials in drug delivery systems: A review. *Materials Today Chemistry.* 2018, **9**, pp.43-55.
2. Qiao, X.R., Wang, X.F., Shang, Y., Li, Y. and Chen, S.Z. Azithromycin enhances anticancer activity of TRAIL by inhibiting autophagy and up-regulating the protein levels of DR4/5 in colon cancer cells in vitro and in vivo. *Cancer Communications.* 2018, **38**, 13.
3. Canfarotta, F., Lezina, L., Guerreiro, A., Czulak, J., Petukhov, A., Daks, A., Smolinska-Kempisty, K., Poma, A., Piletsky, S. and Barlev, N.A. Specific Drug Delivery to Cancer Cells with Double-Imprinted Nanoparticles against Epidermal Growth Factor Receptor. *Nano Letters.* 2018, **18**(8), pp.4641-4646.
4. Novoselova, M.V., Loh, H.M., Trushina, D.B., Ketkar, A., Abakumova, T.O., Zatsepin, T.S., Kakran, M., Brzozowska, A.M., Lau, H.H., Gorin, D.A., Antipina, M.N. and Brichkina, A.I. Biodegradable Polymeric Multilayer Capsules for Therapy of Lung Cancer. *Acs Applied Materials & Interfaces.* 2020, **12**(5), pp.5610-5623.
5. Miyazaki, M., Yuba, E., Hayashi, H., Harada, A. and Kono, K. Hyaluronic Acid-Based pH-Sensitive Polymer-Modified Liposomes for Cell-Specific Intracellular Drug Delivery Systems. *Bioconjugate Chemistry.* 2018, **29**(1), pp.44-55.
6. Bordat, A., Boissenot, T., Nicolas, J. and Tsapis, N. Thermoresponsive polymer nanocarriers for biomedical applications. *Advanced Drug Delivery Reviews.* 2019, **138**, pp.167-192.
7. Qu, Y., Chu, B.Y., Wei, X.W., Lei, M.Y., Hu, D.R., Zha, R.Y., Zhong, L., Wang, M.Y., Wang, F.F. and Qian, Z.Y. Redox/pH dual-stimuli responsive camptothecin prodrug nanogels for "on-demand" drug delivery. *Journal of Controlled Release.* 2019, **296**, pp.93-106.
8. Price, D.J., Khuphe, M., Davies, R.P.W., McLaughlan, J.R., Ingram, N. and Thornton, P.D. Poly(amino acid)-polyester graft copolymer nanoparticles for the acid-mediated release of doxorubicin. *Chemical Communications.* 2017, **53**(62), pp.8687-8690.
9. Khuphe, M., Ingram, N. and Thornton, P.D. Exploiting poly(alpha-hydroxy acids) for the acid-mediated release of doxorubicin and reversible inside-out nanoparticle self-assembly. *Nanoscale.* 2018, **10**(29), pp.14201-14206.
10. Shi, J.J., Votruba, A.R., Farokhzad, O.C. and Langer, R. Nanotechnology in Drug Delivery and Tissue Engineering: From Discovery to Applications. *Nano Letters.* 2010, **10**(9), pp.3223-3230.

11. Araste, F., Abnous, K., Hashemi, M., Taghdisi, S.M., Ramezani, M. and Alibolandi, M. Peptide-based targeted therapeutics: Focus on cancer treatment. *Journal of Controlled Release.* 2018, **292**, pp.141-162.
12. Cao, W.Q., Zhou, J., Mann, A., Wang, Y. and Zhu, L. Folate-Functionalized Unimolecular Micelles Based on a Degradable Amphiphilic Dendrimer-Like Star Polymer for Cancer Cell-Targeted Drug Delivery. *Biomacromolecules.* 2011, **12**(7), pp.2697-2707.
13. Khuphe, M., Mahon, C.S. and Thornton, P.D. Glucose-bearing biodegradable poly(amino acid) and poly(amino acid)-poly(ester) conjugates for controlled payload release. *Biomaterials Science.* 2016, **4**(12), pp.1792-1801.
14. Schneider, M., Al-Shareffi, E. and Haltiwanger, R.S. Biological functions of fucose in mammals. *Glycobiology.* 2017, **27**(7), pp.601-618.
15. Lepage, C., Capacaccia, R., Hackl, M., Lemmens, V., Molina, E., Pierannunzio, D., Sant, M., Trama, A., Faivre, J. and Grp, E.W. Survival in patients with primary liver cancer, gallbladder and extrahepatic biliary tract cancer and pancreatic cancer in Europe 1999-2007: Results of EUROCARE-5. *European Journal of Cancer.* 2015, **51**(15), pp.2169-2178.
16. Boeck, S., Haas, M., Kruger, S. and Heinemann, V. Long-term Progression-free Survival in A Metastatic Pancreatic Cancer Patient Treated with First-line Nab-paclitaxel and Gemcitabine. *In Vivo.* 2014, **28**(6), pp.1189-1192.
17. Penfold, N.J.W., Whatley, J.R. and Armes, S.P. Thermoreversible Block Copolymer Worm Gels Using Binary Mixtures of PEG Stabilizer Blocks. *Macromolecules.* 2019, **52**(4), pp.1653-1662.
18. Madsen, J., Armes, S.P., Bertal, K., MacNeil, S. and Lewis, A.L. Preparation and Aqueous Solution Properties of Thermoresponsive Biocompatible AB Diblock Copolymers. *Biomacromolecules.* 2009, **10**(7), pp.1875-1887.
19. Sugihara, S., Armes, S.P., Blanazs, A. and Lewis, A.L. Non-spherical morphologies from cross-linked biomimetic diblock copolymers using RAFT aqueous dispersion polymerization. *Soft Matter.* 2011, **7**(22), pp.10787-10793.
20. Warren, N.J., Derry, M.J., Mykhaylyk, O.O., Lovett, J.R., Ratcliffe, L.P.D., Ladmiral, V., Blanazs, A., Fielding, L.A. and Armes, S.P. Critical Dependence of Molecular Weight on Thermoresponsive Behavior of Diblock Copolymer Worm Gels in Aqueous Solution. *Macromolecules.* 2018, **51**(21), pp.8357-8371.
21. Orakdogen, N. and Sanay, B. Tunable elasticity and thermodynamic parameters of hydroxypropyl methacrylate-based gels with varying extents of monomer concentration: Statistical mechanics treatments of physical observations. *Journal of Applied Polymer Science.* 2018, **135**(8), 45889.
22. Yin, J., Chen, Y., Zhang, Z.H. and Han, X. Stimuli-Responsive Block Copolymer-Based Assemblies for Cargo Delivery and Theranostic Applications. *Polymers.* 2016, **8**(7), p.29.
23. Sentoukas, T. and Pispas, S. Poly(Dimethylaminoethyl Methacrylate)-b-Poly(Hydroxypropyl Methacrylate) Copolymers: Synthesis and pH/Thermo-Responsive Behavior in Aqueous Solutions. *Journal of Polymer Science Part a-Polymer Chemistry.* 2018, **56**(17), pp.1962-1977.
24. Thi, T.T.H., Pilkington, E.H., Nguyen, D.H., Lee, J.S., Park, K.D. and Truong, N.P. The Importance of Poly(ethylene glycol) Alternatives for Overcoming PEG Immunogenicity in Drug Delivery and Bioconjugation. *Polymers.* 2020, **12**(2), 298.
25. Mura, S., Nicolas, J. and Couvreur, P. Stimuli-responsive nanocarriers for drug delivery. *Nature Materials.* 2013, **12**(11), pp.991-1003.

26. Yu, H.Y., Ingram, N., Rowley, J.V., Parkinson, S., Green, D.C., Warren, N.J. and Thornton, P.D. Thermoresponsive polysarcosine-based nanoparticles (vol 7, pg 4217, 2019). *Journal of Materials Chemistry B.* 2019, **7**(48), pp.7795-7795.
27. Oh, K.T., Yin, H.Q., Lee, E.S. and Bae, Y.H. Polymeric nanovehicles for anticancer drugs with triggering release mechanisms. *Journal of Materials Chemistry.* 2007, **17**(38), pp.3987-4001.
28. Mable, C.J., Derry, M.J., Thompson, K.L., Fielding, L.A., Mykhaylyk, O.O. and Armes, S.P. Time-Resolved SAXS Studies of the Kinetics of Thermally Triggered Release of Encapsulated Silica Nanoparticles from Block Copolymer Vesicles. *Macromolecules.* 2017, **50**(11), pp.4465-4473.
29. Zhao, J., Lee, V.E., Liu, R. and Priestley, R.D. Responsive Polymers as Smart Nanomaterials Enable Diverse Applications. In: Prausnitz, J.M. ed. *Annual Review of Chemical and Biomolecular Engineering, Vol 10*. Palo Alto: Annual Reviews, 2019, pp.361-382.
30. Ribeiro, L.N.M., Alcantara, A.C.S., da Silva, G.H.R., Franz-Montan, M., Nista, S.V.G., Castro, S.R., Couto, V.M., Guilherme, V.A. and de Paula, E. Advances in Hybrid Polymer-Based Materials for Sustained Drug Release. *International Journal of Polymer Science.* 2017, 2017.
31. Wang, W.D., Xiang, L., Gong, L., Hu, W.H., Huang, W.J., Chen, Y.J., Asha, A.B., Srinivas, S., Chen, L.Y., Narain, R. and Zeng, H.B. Injectable, Self-Healing Hydrogel with Tunable Optical, Mechanical, and Antimicrobial Properties. *Chemistry of Materials.* 2019, **31**(7), pp.2366-2376.
32. Chen, M.H., Wang, L.L., Chung, J.J., Kim, Y.H., Atluri, P. and Burdick, J.A. Methods To Assess Shear-Thinning Hydrogels for Application As Injectable Biomaterials. *Acs Biomaterials Science & Engineering.* 2017, **3**(12), pp.3146-3160.
33. Town, A.R., Giardiello, M., Gurjar, R., Siccardi, M., Briggs, M.E., Akhtar, R. and McDonald, T.O. Dual-stimuli responsive injectable microgel/solid drug nanoparticle nanocomposites for release of poorly soluble drugs. *Nanoscale.* 2017, **9**(19), pp.6302-6314.
34. Pramanik, N.B., Nando, G.B. and Singha, N.K. Self-healing polymeric gel via RAFT polymerization and Diels-Alder click chemistry. *Polymer.* 2015, **69**, pp.349-356.
35. Yao, L., Rong, M.Z., Zhang, M.Q. and Yuan, Y.C. Self-healing of thermoplastics via reversible addition-fragmentation chain transfer polymerization. *Journal of Materials Chemistry.* 2011, **21**(25), pp.9060-9065.
36. Zhao, D.L., Tang, Q., Zhou, Q., Peng, K., Yang, H.Y. and Zhang, X.Y. A photo-degradable injectable self-healing hydrogel based on star poly(ethylene glycol)-b-polypeptide as a potential pharmaceuticals delivery carrier. *Soft Matter.* 2018, **14**(36), pp.7420-7428.
37. Guo, H.S., Han, Y., Zhao, W.Q., Yang, J. and Zhang, L. Universally autonomous self-healing elastomer with high stretchability. *Nature Communications.* 2020, **11**(1), pp.1-9.
38. Warren, N.J., Mykhaylyk, O.O., Mahmood, D., Ryan, A.J. and Armes, S.P. RAFT Aqueous Dispersion Polymerization Yields Poly(ethylene glycol)-Based Diblock Copolymer Nano-Objects with Predictable Single Phase Morphologies. *Journal of the American Chemical Society.* 2014, **136**(3), pp.1023-1033.
39. Clayton, K.N., Salameh, J.W., Wereley, S.T. and Kinzer-Ursem, T.L. Physical characterization of nanoparticle size and surface modification using particle scattering diffusometry. *Biomicrofluidics.* 2016, **10**(5), 054107.

Chapter 6. Sulfanilamide Modified Polymeric Nanoparticles with Antimicrobial Activity

Abstract

Sulfanilamide-modified poly(ρ-hydroxystyrene), (poly(ρ-hydroxystyrene-sulfanilamide)) and the sulfanilamide-modified diblock copolymer poly(ρ-hydroxystyrene-sulfanilamide)-b-poly(acrylamide) were synthesised via RAFT polymerisation. Sulfanilamide potentially provides antibacterial property to the polymers. Polymer nanoparticles were created by coacervation, dissolving the polymers in dimethyl sulfoxide, added dropwise in aqueous solution with stirring. To the author's knowledge, the polymers reported are the first examples of sulfanilamide-modified polymers that can form nanoparticles in aqueous media. The produced sulfanilamide-modified polymer nanoparticles are good candidates for antimicrobial analysis in the next step.

6.1. Introduction

Antimicrobial agents have been intensely developed to prevent of microbial infection, particularly in hospitals and dental equipment [1-4]. Many antimicrobial agents may kill microorganisms or inhibit their growth in the human body but the toxicity of the antimicrobial agents directly affected human healthy [5]. Therefore, the development of non-toxic and effective antimicrobial polymers is necessary.

Sulfanilamide (SA) has a para-aminobenzene sulfonamide structure which has antimicrobial activity. However, bacteria in the human body has resistance to the antimicrobial agent SA [6-7]. Antibiotic resistance is when bacteria develops the ability to defeat the drug designed to kill them [8-9]. In order to minimise the antibiotic resistance, SA-modified polymers were developed because the action mechanisms of the polymers in human body are different from the individual antimicrobial agents [10-15]. The actions include the surface-activity properties, adsorption/absorption abilities and the bonding affinity between the polymer/copolymer and the bacterial cells [12]. Umamaheswara's group synthesised antibacterial polymers based on 4-(*N*-

acrylamido)benzenesulfonamide by copolymerisation, forming poly(4-(*N*-acrylamido)benzenesulfonamide)-*co*-acrylic acid) and poly(4-(*N*-acrylamido)benzenesulfonamide-*co*-2-hydroxyethyl acrylate) (Scheme 6.1) [16]. Both of the polymers and the 4-(*N*-acrylamido)benzenesulfonamide were tested against gram-positive bacteria *S. aureus* [16-17]. The results indicate that the antimicrobial activity of the SA-based copolymers was greater compared to the 4-(*N*-acrylamido)benzenesulfonamide [16, 18]. The polymer chains formed a cage-like structure around the microorganism which can be stabilised by ionic and hydrogen bonding between the polymer chains and the microorganism cell wall [19]. The ionic strength and the hydrophilic nature of the medium near the cell wall of the microorganism can trigger the cell wall to open [19]. The acrylic acid (AC) of poly(ABA-*co*-AC) and the 2-hydroxyethyl acrylate (HEA) of poly(ABA-*co*-HEA) increased the ionic strength of the medium next to the cell wall of the microorganism [19]. AC and HEA actively delivered SA using the system discussed above [16, 18-19].

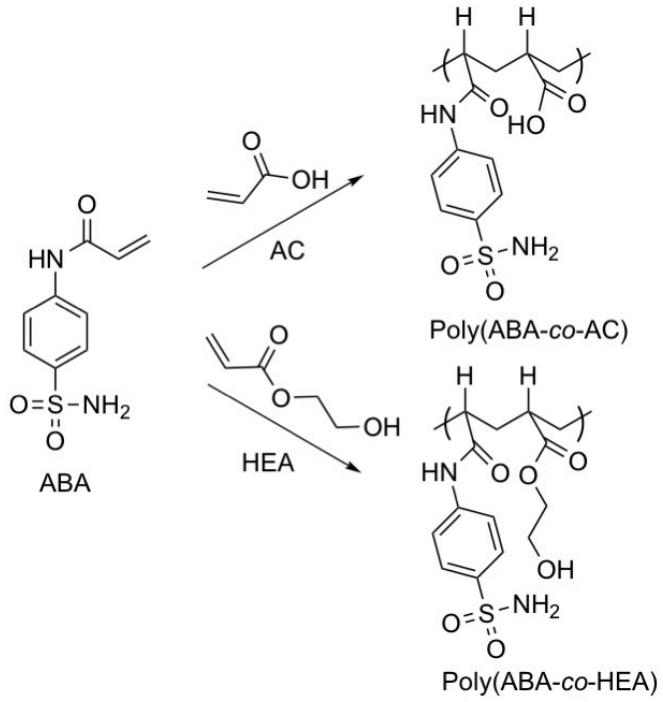

Scheme 6. 1. Synthesis of poly(ABA-*co*-AC) and poly(ABA-*co*-HEA) [16].

SA has also been applied to the synthesis of antimicrobial fibre in wound healing and biocompatible membranes for drug delivery. Mani and co-workers synthesised nanofibre which showed antibacterial activity and could be used in wound healing [20]. SA, silver

nitrate and chitosan-polyvinyl alcohol (CS-PVA) were dissolved in deionised water, isopropyl alcohol (volume ratio 4:1), acetic acid and formic acid and produced a homogeneous solution. The solution was electrospun to make nanofibres [20]. In the wound healing process, dermal and epidermal tissues were regenerated [20-21]. The rate of wound healing of the SA and silver nanoparticles loaded CS-PVA nanofibres was 91 ± 4.3 % after 7 days which was greater than the nanofibre without the SA and silver nanoparticles loaded (55 ± 3.5 % after 20 days) [20]. SA based biocompatible surfactant may be used as a cell membrane compatible niosomal drug carrier [22]. The surfactant was synthesised in a single step by conjugating deconyl chloride to SA (SA-modified deconyl chloride molecule) followed by self-micellisation to form niosomes [22-23]. The hydrophobic drug clarithromycin was loaded into the niosomes via dissolving the drug, the niosomes and cholesterol in chloroform and methanol, evaporating the organic solvents leaving a membrane powder mixture, rehydrating the powder with PBS buffer solution and sonicating the mixture [22, 24]. The drug loaded niosomes were hemocompatible and non-toxic in blood hemolysis and cytotoxicity assays (mouse embryonic fibroblast cells NIH/3T3), releasing 80 % of clarithromycin to an aqueous pH 7.4 environment after 12 hours [22].

The research in this chapter reports the creation of pH-responsive and pH-switchable SA-modified poly(*ρ*-hydroxystyrene), poly(*ρ*-hydroxystyrene)-*b*-poly(acrylamide) and poly(*ρ*-hydroxystyrene)-*co*-poly(acrylamide) nanoparticles with high SA conjugation efficiency. Nanoparticles were formed by dissolving the SA modified polymers in DMSO and adding the solution dropwise into deionised water. The pH-responsive and pH-switchable properties of the SA-modified polymers were due to protonation/ deprotonation of the sulfonamide and deprotonation of the phenol groups in aqueous acid and alkaline solutions.

6.2. Experimental

6.2.1. Synthesis of poly(acetoxystyrene) [25]

2-(((Dodecylthio)carbonothioy)thio)-2-methylpropanoic acid (72.2 mg, 0.198 mmol) and AIBN (10 mg, 0.061 mmol) were dissolved in anhydrous DMF (4 mL) under nitrogen. 4-

Acetoxystyrene (ACS) (3 mL, 19.8 mmol) was added to the reaction. The reaction was heated at 70 °C and flushed nitrogen for four hours. Then the mixture was diluted by anhydrous DMF (2 mL), precipitated in cold methanol (60 mL), centrifuged at 6000 rev/min for 10 minutes and dried in a vacuum oven at 40 °C for 24 hours. The chain length of the synthesised poly(acetoxystyrene) was 100 ($PACS_{100}$). $PACS_{50}$ was also synthesised, using the same procedure, ACS (1.5 mL, 9.90 mmol), AIBN (5 mg, 0.030 mmol) and 2-(((dodecylthio)carbonothioy)thio)-2-methylpropanoic acid (72.2 mg, 0.198 mmol). $PACS_{100}$: 2.89 g, 88.1 wt. % (pale yellow powder). APC (THF, PMMA standards): M_w= 16700 g mol^{-1}. Dispersity= 1.39. ^{1}H NMR (500 MHz, $CDCl_3$, δ, ppm): 11.93-11.62 (s, 1H, COOH), 7.12-5.80 (m, 400H, $(ArHOCOCH_3)_{100}$), 2.43-1.06 (m, 628H, $HOOCCCH_3CH_3(CH_2CHArOCOCH_3)_{100}C_{11}H_{22}$), 0.94-0.78 (t, 3H, $C_{11}H_{22}CH_3$). FTIR: ν_{max}/cm^{-1} (solid): 2924 cm^{-1} (carboxylic acid O-H stretch), 1756 cm^{-1} (aromatic ester C=O stretch), 1502 cm^{-1} (alkane C-H stretch), 1189 cm^{-1} (aromatic ester C-O stretch), 1015 cm^{-1} (C=S stretch), 843 cm^{-1} (C-H aromatic bending).

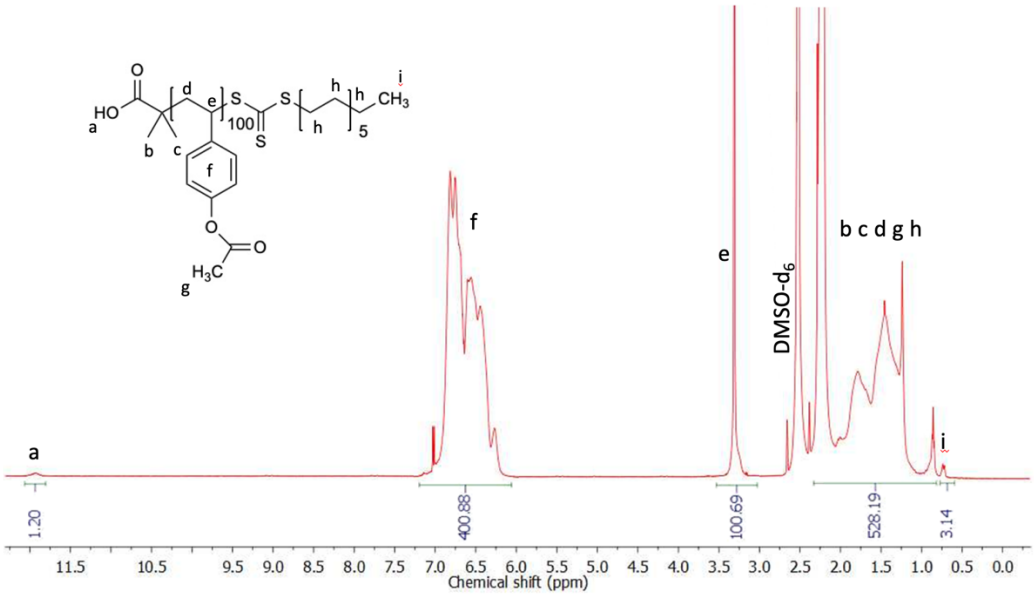

Figure 6. 1. The 500 MHz ^{1}H-NMR spectrum of $PACS_{100}$ in $CDCl_3$ at 25 °C.

$PACS_{50}$: 1.45 g, 86.5 wt. % (pale yellow powder). APC (PMMA standards): M_w= 8600 g mol^{-1}. Dispersity= 1.27. ^{1}H NMR (500 MHz, $CDCl_3$, δ, ppm): 11.84-11.69 (s, 1H, COOH), 7.16-6.22 (m, 200H, $(ArHOCOCH_3)_{50}$), 2.52-1.11 (m, 328H, $HOOCCCH_3CH_3(CH_2CHArOCOCH_3)_{50}C_{11}H_{22}$), 0.98-0.79 (t, 3H, $C_{11}H_{22}CH_3$). FTIR: ν_{max}/cm^{-1} (solid): 2922 cm^{-1} (carboxylic acid O-H stretch), 1757 cm^{-1} (aromatic ester C=O stretch),

1505 cm^{-1} (alkane C-H stretch), 1187 cm^{-1} (aromatic ester C-O stretch), 1011 cm^{-1} (C=S stretch), 842 cm^{-1} (C-H aromatic bending).

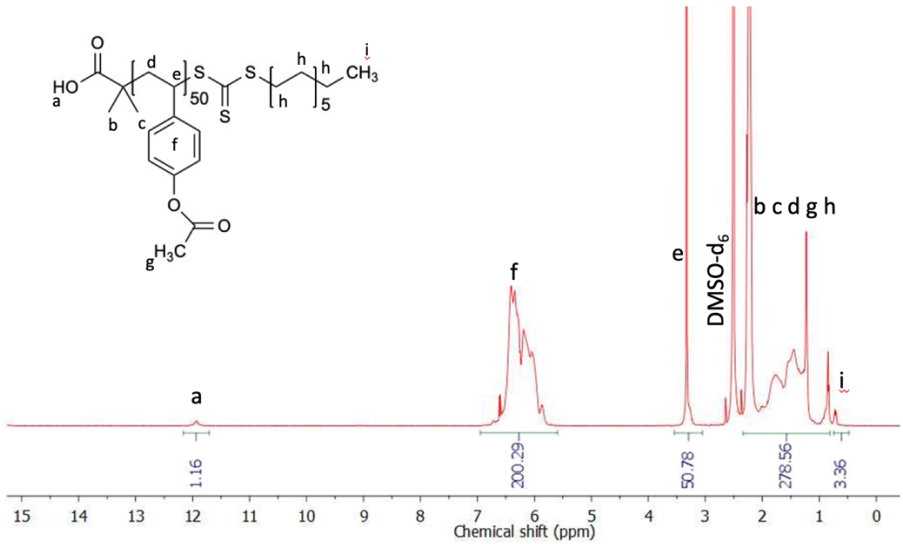

Figure 6. 2. The 500 MHz ^{1}H-NMR spectrum of $PACS_{50}$ in $CDCl_3$ at 25 °C.

6.2.2. Synthesis of poly(*ρ*-hydroxystyrene)

PACS (502 mg, 0.030 mmol) and phosphoric acid (1344 mg, 13.7 mmol) were dissolved in DMF (5 mL) and TFA (5.0 mL, 65.3 mmol). The reaction was stirred at room temperature for two days. Then the reaction mixture was precipitated in cold methanol (100 mL), centrifuged at 6000 rev/min for 10 minutes and dried in a vacuum oven at 40 °C for 24 hours. The synthesised poly(*ρ*-hydroxystyrene) has 100 units ($P\rho HS_{100}$). $P\rho HS_{50}$ was also synthesised, using the same procedure and quantity of reactants. $P\rho HS_{100}$: 0.35 g, 94.4 wt. % (pale yellow powder). APC (PMMA standards): M_w= 12600 g mol^{-1}. Dispersity= 1.31. ^{1}H NMR (500 MHz, $CDCl_3$, δ, ppm): 11.83-11.69 (s, 1H, COOH), 7.15-5.80 (m, 500H, $(ArHOH)_{100}$), 2.43-0.84 (m, 328H, $HOOCCCH_3CH_3(CH_2CHArOH)_{100}C_{11}H_{22}$), 0.84-0.69 (t, 3H, $C_{11}H_{22}CH_3$). FTIR: ν_{max}/cm^{-1} (solid): 2919 cm^{-1} (carboxylic acid O-H stretch), 2344 cm^{-1} (phenol O-H stretch), 1760 cm^{-1} (carboxylic acid C=O stretch) 1510 cm^{-1} (alkane C-H stretch), 1185 cm^{-1} (phenol C-O stretch), 1007 cm^{-1} (C=S, stretch), 839 cm^{-1} (aromatic C-H bending).

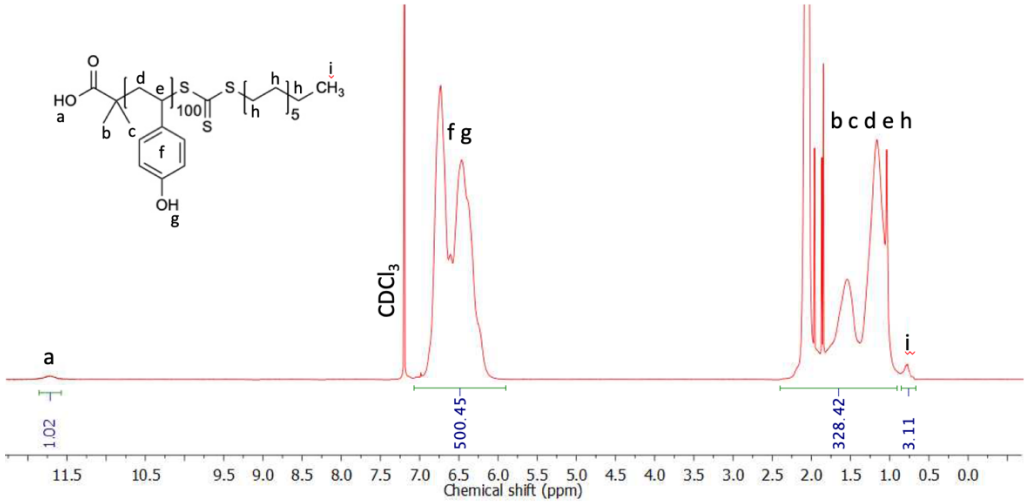

Figure 6. 3. The 500 MHz ^{1}H-NMR spectrum of PρHS$_{100}$ in $CDCl_3$ at 25 °C.

PρHS$_{50}$: 0.18 g, 94.3 wt. % (pale yellow powder). APC (PMMA standards): M_w= 6600 mol^{-1}. Dispersity= 1.22. ^{1}H NMR (500 MHz, $CDCl_3$, δ, ppm): 12.07-11.78 (s, 1H, COOH), 7.00-5.77 (m, 250H, (ArHOH)$_{50}$), 2.48-0.95 (m, 178H, HOOCCCH$_3$CH$_3$(CH$_2$CHArOH)$_{50}$C$_{11}$H$_{22}$), 0.82-0.70 (t, 3H, C$_{11}$H$_{22}$CH$_3$). FTIR: ν_{max}/cm^{-1} (solid): 2928 cm^{-1} (carboxylic acid O-H stretch), 2320 cm^{-1} (phenol O-H stretch), 1760 cm^{-1} (carboxylic acid C=O stretch), 1505 cm^{-1} (alkane C-H stretch), 1189 (phenol C-O stretch), 1016 cm^{-1} (C=S, stretch), 839 cm^{-1} (aromatic C-H bending).

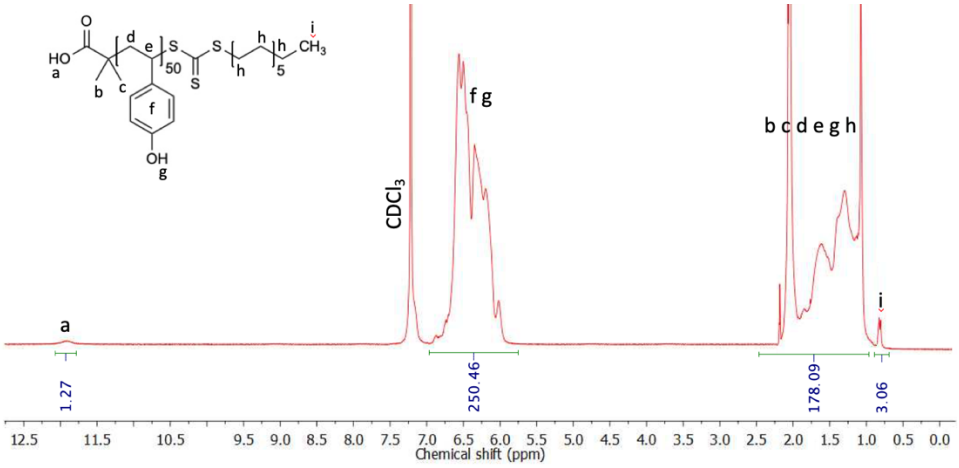

Figure 6. 4. The 500 MHz ^{1}H-NMR spectrum of PρHS$_{50}$ in $CDCl_3$ at 25 °C.

6.2.3. Synthesis of poly(ρ-hydroxystyrene-sulfanilamide)

Sodium nitrite (412.2 mg, 5.97 mmol) was dissolved in propionic acid (3.0 mL, 40.1 mmol), concentrated sulfuric acid (6.0 mL, 112.6 mmol), acetic acid (18.0 mL, 314.7 mmol). PρHS

(281.4 mg, 0.023 mmol) and SA (791.2 mg, 4.59 mmol) were dissolved in DMF (7.0 mL). The polymer solution was added dropwise into the prepared acid solution. The reaction was stirred for 24 hours at room temperature. Then the reaction was added to 300 mL of deionised water, brown precipitates were formed. The brown precipitates were washed three time by deionised water and collected via centrifuge at 6000 rev/min for 20 minutes and freeze dried for 24 hours. The synthesised polymer was P(ρHS-SA)$_{100}$. P(ρHS-SA)$_{50}$ was also produced using the same procedure and quantity of reactants. P(ρHS-SA)$_{100}$: 0.36 g, 51.0 wt. % (brown solid). APC (PMMA standards): M_w= 30800 g mol^{-1}. Dispersity= 1.25. ^{1}H NMR (500 MHz, DMSO-d$_6$, δ, ppm): 10.72-10.34 (s, 1H, COO<u>H</u>), 9.32-8.70 (s, 200H, (<u>H$_2$</u>NSO$_2$Ar)$_{100}$), 6.98-5.83 (m, 800H, (Ar<u>H</u>N$_2$Ar<u>H</u>O<u>H</u>)$_{100}$), 2.28-0.78 (m, 328H, HOOCCC<u>H$_3$</u>C<u>H$_3$</u>(C<u>H$_2$</u>C<u>H</u>)$_{100}$C$_{11}$<u>H$_{22}$</u>), 0.70-0.62 (t, 3H, C$_{11}$H$_{22}$C<u>H$_3$</u>). FTIR: ν_{max}/cm^{-1} (solid): 3309 cm^{-1} (primary amine N-H stretch), 2924 cm^{-1} (carboxylic acid O-H stretch), 1760 cm^{-1} (carboxylic acid C=O stretch), 1515 cm^{-1} (alkane C-H stretch), 1444 cm^{-1} (azo N=N stretch), 1326 cm^{-1} (S=O stretch), 1196 cm^{-1} (phenol C-O stretch), 1014 cm^{-1} (C=S, stretch), 827 cm^{-1} (aromatic C-H bending).

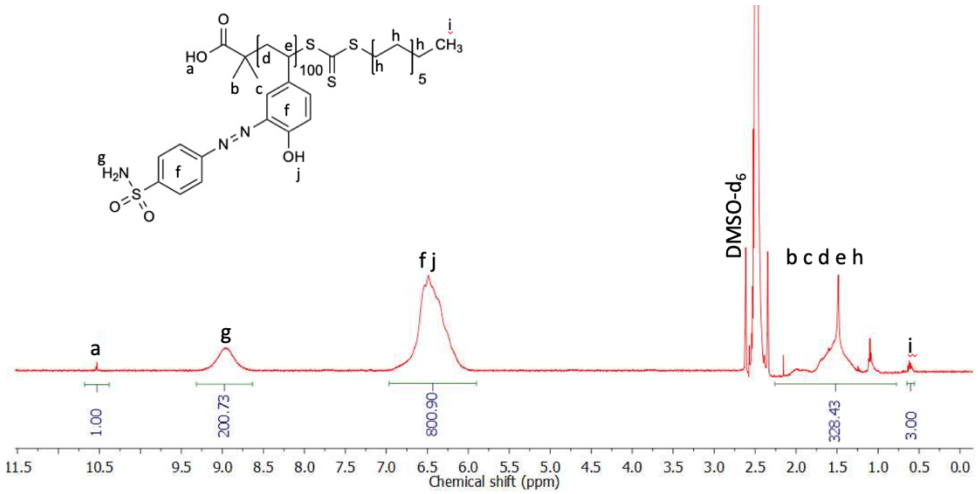

Figure 6. 5. The 500 MHz ^{1}H-NMR spectrum of P(ρHS-SA)$_{100}$ in DMSO-d$_6$ at 25 °C.

P(ρHS-SA)$_{50}$: 0.22 g, 61.7 wt. % (brown solid). APC (PMMA standards): M_w= 15700 g mol^{-1}. Dispersity= 1.33. ^{1}H NMR (500 MHz, DMSO-d$_6$, δ, ppm): 10.78-10.38 (s, 1H, COO<u>H</u>), 9.36-8.96 (s, 49H, (<u>H$_2$</u>NSO$_2$Ar)$_{50}$), 7.18-5.83 (m, 400H, (Ar<u>H</u>N$_2$Ar<u>H</u>O<u>H</u>)$_{50}$), 2.48-1.74 (m, 178H, HOOCCC<u>H$_3$</u>C<u>H$_3$</u>(C<u>H$_2$</u>C<u>H</u>)$_{50}$C$_{11}$<u>H$_{22}$</u>), 0.80-0.70 (t, 3H, C$_{11}$H$_{22}$C<u>H$_3$</u>). FTIR: ν_{max}/cm^{-1} (solid): 3309 cm^{-1} (primary amine N-H stretch), 2924 cm^{-1} (carboxylic acid O-H stretch), 1760 cm^{-1} (carboxylic acid C=O stretch), 1515 cm^{-1} (alkane C-H stretch), 1444 cm^{-1} (azo

N=N stretch), 1326 cm^{-1} (SO_2 S=O stretch), 1201 cm^{-1} (phenol C-O stretch), 1014 cm^{-1} (C=S, stretch), 833 cm^{-1} (aromatic C-H bending).

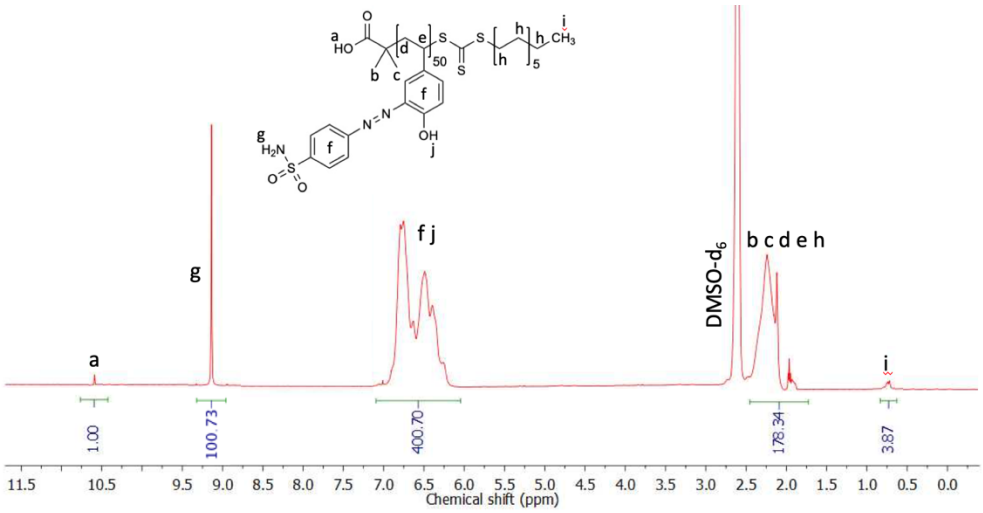

Figure 6. 6. The 500 MHz ^{1}H-NMR spectrum of P(*p*HS-SA)$_{50}$ in DMSO-d_6 at 25 °C.

6.2.4. Synthesis of poly(acetoxystyrene)-*b*-poly(acrylamide)

PACS (302.1 mg, 0.018 mmol), acrylamide (AM) (256.6 mg, 3.61 mmol), and 0.042 g of AIBN (42.8 mg, 0.261 mmol) were dissolved in anhydrous DMF (7.0 mL) with flushing nitrogen. The reaction was stirred at 70 °C for four hours under nitrogen. Then the reaction mixture was precipitated in cold diethyl ether (60.0 mL), centrifuged at 6000 rev/min for 10 minutes and dried in a vacuum oven at 40 °C for 24 hours. The synthesised polymer was poly(acetoxystyrene)$_{100}$-*b*-poly(acrylamide)$_{200}$ (PACS$_{100}$-*b*-PAM$_{200}$). PACS$_{50}$-*b*-PAM$_{100}$ and PACS$_{50}$-*b*-PAM$_{200}$ were also produced, using the same procedure and the quantity of reactants were PACS$_{50}$ (289.7 mg, 0.034 mmol) and AM (243.1 mg, 3.42 mmol); PACS$_{50}$ (290.6 mg, 0.034 mmol) and AM (484.1 mg, 6.81 mmol), respectively. PACS$_{100}$-*b*-PAM$_{200}$: 0.45 g, 81.3 wt. % (pale yellow powder). APC (PMMA standards): M_w= 30900 g mol^{-1}. Dispersity= 1.23. ^{1}H NMR (500 MHz, DMSO-d_6, δ, ppm): 12.13-11.79 (s, 1H, COOH), 7.73-6.17 (m, 800H, $(CH_2CHARH)_{100}(CHCONH_2)_{200}$), 2.28-0.99 (m, 1228H, $CH_3CH_3(CH_2CHArOCOCH_3)_{100}(CHCH_2)_{200}C_{11}H_{22}$), 0.87-0.80 (t, 3H, $C_{11}H_{22}CH_3$). FTIR: ν_{max}/cm^{-1} (solid): 3342 cm^{-1} (primary amide N-H stretch), 2929 cm^{-1} (carboxylic acid O-H stretch), 1755 cm^{-1} (aromatic ester C=O stretch), 1652 cm^{-1} (primary amide C=O stretch), 1504 cm^{-1} (alkane C-H stretch), 1191 cm^{-1} (aromatic ester C-O stretch), 1014 cm^{-1} (C=S stretch), 843 cm^{-1} (aromatic C-H bending).

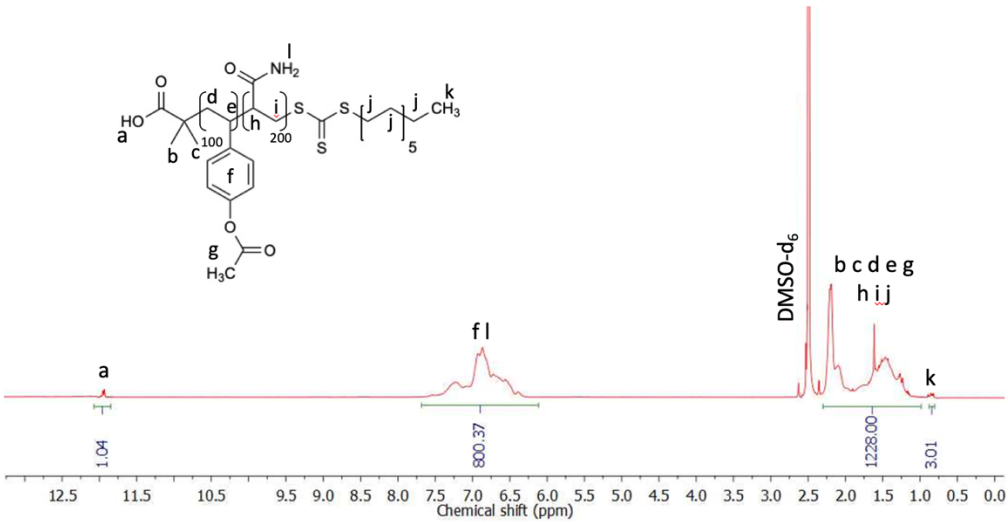

Figure 6. 7. The 500 MHz ^{1}H-NMR spectrum of $PACS_{100}$-*b*-PAM_{200} in DMSO-d_6 at 25 °C.

$PACS_{50}$-*b*-PAM_{100}: 0.42 g, 79.4 wt. % (pale yellow powder). APC (PMMA standards): M_w= 15600 g mol^{-1}. Dispersity= 1.34. ^{1}H NMR (500 MHz, DMSO-d_6, δ, ppm): 12.21-11.76 (s, 1H, COO<u>H</u>), 7.77-6.12 (m, 400H, $(CH_2CHAR\underline{H})_{50}(CHCON\underline{H_2})_{100}$), 2.27-1.11 (m, 628H, $C\underline{H_3}C\underline{H_3}(C\underline{H_2}C\underline{H}ArOCOC\underline{H_3})_{50}(C\underline{H}C\underline{H_2})_{100}C_{11}\underline{H_{22}}$), 0.90-0.74 (t, 3H, $C_{11}H_{22}C\underline{H_3}$). FTIR: ν_{max}/cm^{-1} (solid): 3337 cm^{-1} (primary amide N-H stretch), 2929 cm^{-1} (carboxylic acid O-H stretch), 1758 cm^{-1} (aromatic ester C=O stretch), 1652 cm^{-1} (primary amide C=O stretch), 1504 cm^{-1} (alkane C-H stretch), 1191 cm^{-1} (aromatic ester C-O stretch), 1014 cm^{-1} (C=S stretch), 843 cm^{-1} (aromatic C-H bending).

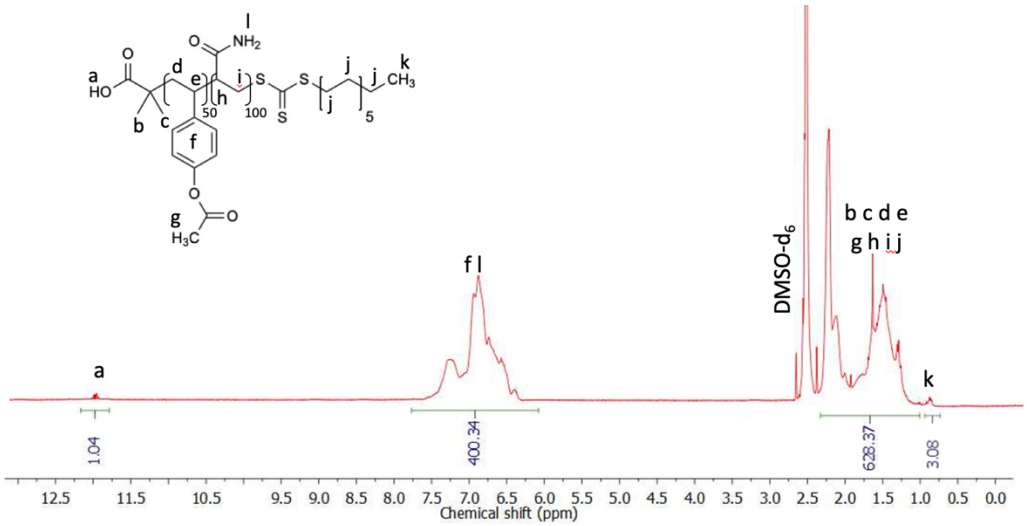

Figure 6. 8. The 500 MHz ^{1}H-NMR spectrum of $PACS_{50}$-*b*-PAM_{100} in DMSO-d_6 at 25 °C.

$PACS_{50}$-*b*-PAM_{200}: 0.63 g, 81.8 wt. % (pale yellow powder). APC (PMMA standards): M_w= 22800 g mol^{-1}. Dispersity= 1.21. ^{1}H NMR (500 MHz, DMSO-d_6, δ, ppm): 12.24-11.72 (s,

1H, COOH), 7.79-6.38 (m, 600H, $(CH_2CHARH)_{50}(CHCONH_2)_{200}$), 2.23-1.10 (m, 928H, $CH_3CH_3(CH_2CHArOCOCH_3)_{50}(CHCH_2)_{200}C_{11}H_{22}$), 0.94-0.74 (t, 3H, $C_{11}H_{22}CH_3$). FTIR: ν_{max}/cm^{-1} (solid): 3342 cm^{-1} (primary amide N-H stretch), 2932 cm^{-1} (carboxylic acid O-H stretch), 1758 cm^{-1} (aromatic ester C=O stretch), 1652 cm^{-1} (primary amide C=O stretch), 1504 cm^{-1} (alkane C-H stretch), 1191 cm^{-1} (aromatic ester C-O stretch), 1102 cm^{-1} (C=S stretch), 843 cm^{-1} (aromatic C-H bending).

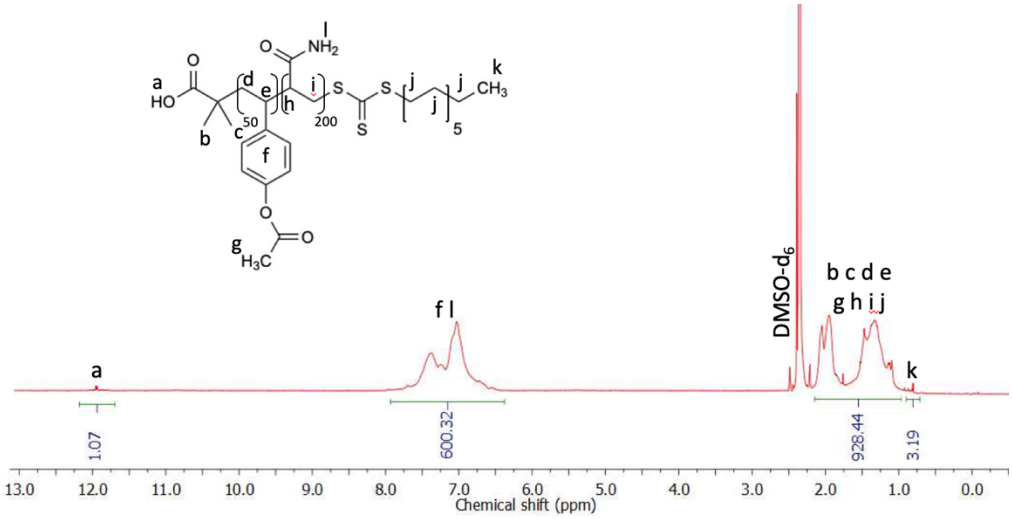

Figure 6. 9. The 500 MHz ^{1}H-NMR spectrum of $PACS_{50}$-*b*-PAM_{200} in DMSO-d_6 at 25 °C.

6.2.5. Synthesis of poly(*ρ*-hydroxystyrene)-*b*-poly(acrylamide)

PACS-*b*-PAM (414.7 mg, 0.013 mmol) and phosphoric acid (580.1 mg, 5.92 mmol) were dissolved in DMF (10.0 mL) and TFA (5.0 mL, 65.3 mmol) and stirred for two days at room temperature. Then the reaction mixture was precipitated in cold diethyl ether (100 mL), centrifuged at 6000 rev/min for 20 minutes and dried in a vacuum oven at 40 °C for two days. The synthesised polymer was P*ρ*HS_{100}-*b*-PAM_{200}. P*ρ*HS_{50}-*b*-PAM_{100} and P*ρ*HS_{50}-*b*-PAM_{200} were also produced using the same procedure and the quantity of the reactants were the same. P*ρ*HS_{100}-*b*-PAM_{200}: 0.31 g, 89.8 wt. % (pale yellow powder). APC (PMMA standards): M_w= 26700 g mol^{-1}. Dispersity= 1.29. ^{1}H NMR (500 MHz, $CDCl_3$, δ, ppm): 10.70-10.65 (s, 1H, COOH), 7.02-5.77 (m, 900H, $(CH_2CHARHOH)_{100}(H_2NCO)_{200}$), 2.35-0.75 (m, 928H, $CH_3CH_3(CH_2CH)_{100}(CHCH_2)_{200}C_{11}H_{22}$), 0.94-0.74 (t, 3H, $C_{11}H_{22}CH_3$). FTIR: ν_{max}/ cm^{-1} (solid): 3320 cm^{-1} (primary amide N-H stretch), 2929 cm^{-1} (carboxylic acid O-H stretch), 2324 cm^{-1} (phenol O-H stretch), 1647 cm^{-1} (primary amide C=O stretch), 1191 cm^{-1} (phenol C-O stretch), 1108 cm^{-1} (C=S stretch), 877 cm^{-1} (aromatic C-H bending).

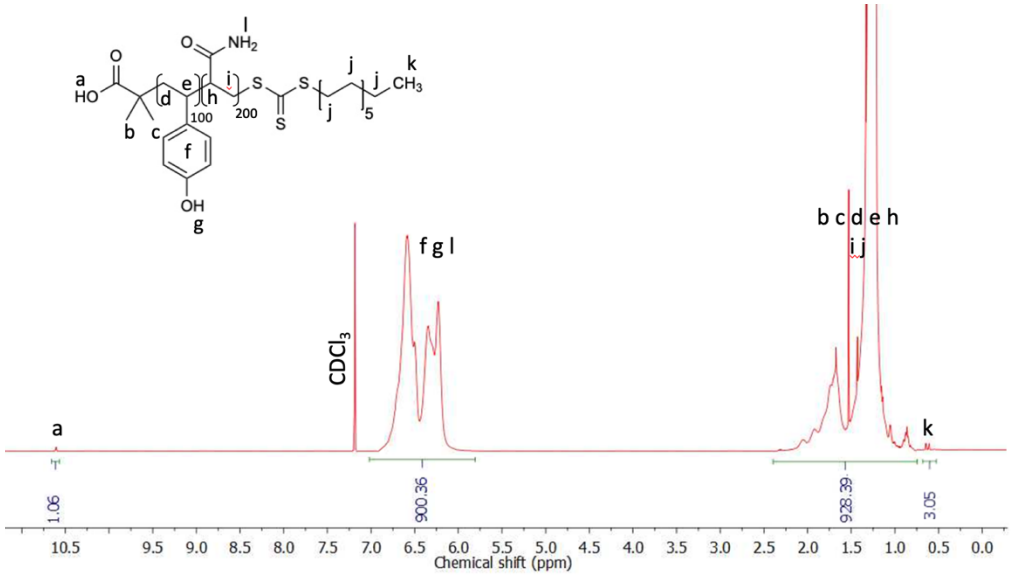

Figure 6. 10. The 500 MHz ^{1}H-NMR spectrum of PρHS$_{100}$-*b*-PAM$_{200}$ in $CDCl_3$ at 25 °C.

PρHS$_{50}$-*b*-PAM$_{100}$: 0.15 g, 85.7 wt. % (pale yellow powder). APC (PMMA standards): M_w= 13600 g mol^{-1}. Dispersity= 1.28. ^{1}H NMR of PρHS$_{50}$-*b*-PAM$_{100}$ (500 MHz, $CDCl_3$, δ, ppm): 10.72-10.41 (s, 1H, COOH), 6.97-5.76 (m, 450H, $(CH_2CHARHOH)_{50}(H_2NCO)_{100}$), 2.60-0.79 (m, 478H, $CH_3CH_3(CH_2CH)_{50}(CHCH_2)_{100}C_{11}H_{22}$), 0.81-0.68 (t, 3H, $C_{11}H_{22}CH_3$). FTIR: ν_{max}/ cm^{-1} (solid): 3386 cm^{-1} (primary amide N-H stretch), 2932 cm^{-1} (carboxylic acid O-H stretch), 2320 cm^{-1} (phenol O-H stretch), 1636 cm^{-1} (primary amide C=O stretch), 1196 cm^{-1} (phenol C-O stretch), 1120 cm^{-1} (C=S stretch), 871 cm^{-1} (aromatic C-H bending).

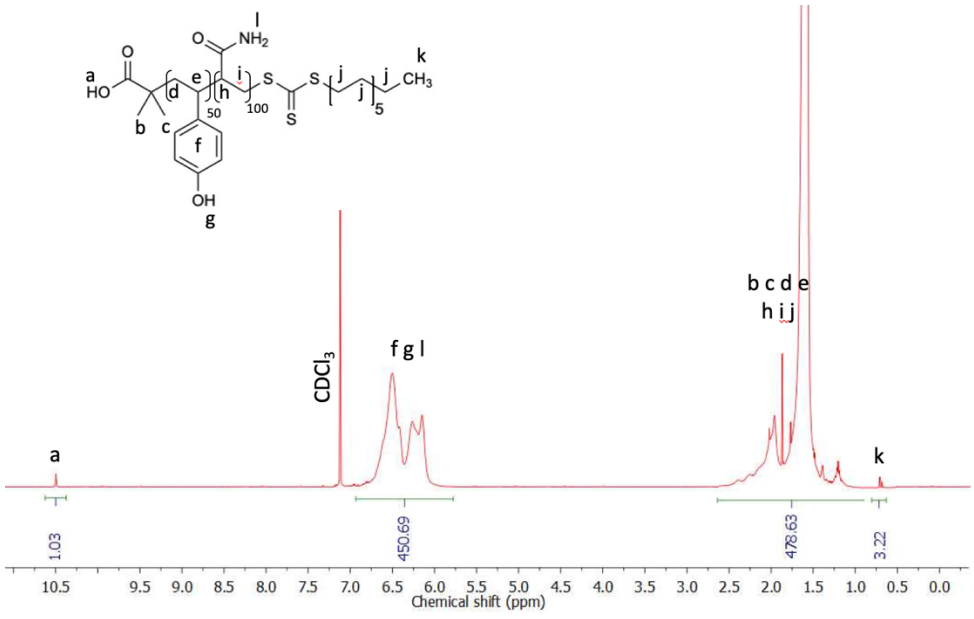

Figure 6. 11. The 500 MHz ^{1}H-NMR spectrum of PρHS$_{50}$-*b*-PAM$_{100}$ in $CDCl_3$ at 25 °C.

PρHS$_{50}$-*b*-PAM$_{200}$: 0.23 g, 86.0 wt. % (pale yellow powder). APC (PMMA standards): M_w= 20700 g mol^{-1}. Dispersity= 1.30. ^{1}H NMR (500 MHz, $CDCl_3$, δ, ppm): 10.72-10.51 (s, 1H, COO<u>H</u>), 8.19-6.20 (m, 650H, (CH$_2$CHAR<u>H</u>O<u>H</u>)$_{50}$(<u>H</u>$_2$NCO)$_{200}$), 2.47-1.21 (m, 778H, C<u>H</u>$_3$C<u>H</u>$_3$(C<u>H</u>$_2$C<u>H</u>)$_{50}$(C<u>H</u>C<u>H</u>$_2$)$_{200}$C$_{11}$<u>H</u>$_{22}$), 0.97-0.77 (t, 3H, C$_{11}$H$_{22}$C<u>H</u>$_3$). FTIR: ν_{max}/ cm^{-1} (solid): 3358 cm^{-1} (primary amide N-H stretch), 2924 cm^{-1} (carboxylic acid O-H stretch), 2319 cm^{-1} (phenol O-H stretch), 1647 cm^{-1} (primary amide C=O stretch), 1185 cm^{-1} (phenol C-O stretch), 1108 cm^{-1} (C=S stretch), 882 cm^{-1} (aromatic C-H bending).

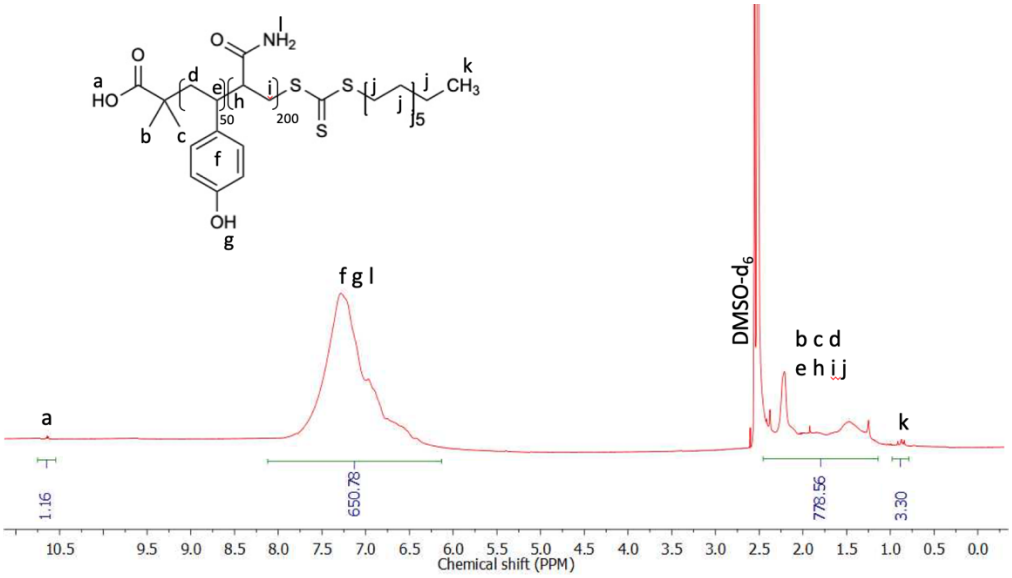

Figure 6. 12. The 500 MHz ^{1}H-NMR spectrum of PρHS$_{50}$-*b*-PAM$_{200}$ in DMSO-d$_6$ at 25 °C.

6.2.6. Sulfanilamide modification of poly(*ρ*-hydroxystyrene)-*b*-poly(acrylamide)

PρHS-*b*-PAM (153.8 mg, 0.0058 mmol) and SA (4.99 mg, 0.029 mmol) were dissolved in DMF (7 mL). Sodium nitrite (269.5 mg, 3.91 mmol) was dissolved in propionic acid (3 mL, 40.1 mmol), concentrated sulfuric acid (6 mL, 112.6 mmol) and acetic acid (18 mL, 314.7 mmol). The polymer solution was added dropwise in the acidic solution and stirred for 24 hours. Then the reaction mixture was added to acetone (100 mL), yellow precipitates were formed. The yellow precipitates were washed three times by acetone, centrifuged at 6000 rev/min for 20 minutes at 20 °C and freeze dried for 24 hours. The polymer synthesised was P(ρHS-SA)$_{100}$-*b*-PAM$_{200}$. P(ρHS-SA)$_{50}$-*b*-PAM$_{100}$ and P(ρHS-SA)$_{50}$-*b*-PAM$_{200}$ were also synthesised, using the same procedure and the same quantity of

reactants. P(ρHS-SA)$_{100}$-*b*-PAM$_{200}$: 0.16 g, 61.5 wt. % (pale brown solid). APC (PMMA standards): M_w= 45000 g mol^{-1}. Dispersity= 1.41. ^{1}H NMR (500 MHz, DMSO-d$_6$, δ, ppm): 10.76-10.58 (s, 1H, COOH), 9.30-8.72 (s, 61H, ($H_2NSO_2Ar)_{100}$), 7.74-5.78 (m, 1200H, ($CH_2CHARHOHN_2ArH)_{100}(H_2NCO)_{200}$), 2.30-0.77 (m, 928H, $CH_3CH_3(CH_2CH)_{100}(CHCH_2)_{200}C_{11}H_{22}$), 0.74-0.71 (t, 3H, $C_{11}H_{22}CH_3$). FTIR: v_{max}/ cm^{-1} (solid): 3335 cm^{-1} (primary amide N-H stretch), 2924 cm^{-1} (carboxylic acid O-H stretch), 1653 cm^{-1} (primary amide C=O stretch), 1505 cm^{-1} (alkane C-H stretch), 1444 cm^{-1} (azo N=N stretch), 1372 cm^{-1} (S=O stretch), 1196 cm^{-1} (phenol O-H stretch), 1014 cm^{-1} (C=S stretch), 827 cm^{-1} (aromatic C-H stretch).

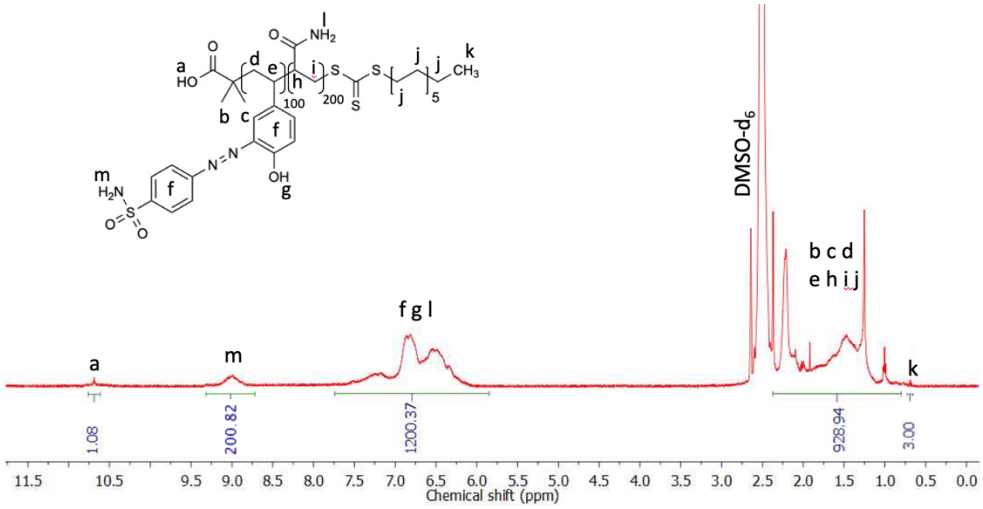

Figure 6. 13. The 500 MHz ^{1}H-NMR spectrum of P(ρHS-SA)$_{100}$-*b*-PAM$_{200}$ in DMSO-d$_6$ at 25 °C.

P(ρHS-SA)$_{50}$-*b*-PAM$_{100}$: 0.08 g, 61.0 wt. % (pale brown solid). APC (PMMA standards): M_w= 22800 g mol^{-1}. Dispersity= 1.44.^{1}H NMR (500 MHz, DMSO-d$_6$, δ, ppm): 10.70-10.49 (s, 1H, COOH), 9.41-8.68 (s, 50H, ($H_2NSO_2Ar)_{50}$), 7.37-5.69 (m, 600H, ($CH_2CHARHOHN_2ArH)_{50}(H_2NCO)_{100}$), 2.36-0.80 (m, 478H, $CH_3CH_3(CH_2CH)_{50}(CHCH_2)_{100}C_{11}H_{22}$), 0.76-0.72 (t, 3H, $C_{11}H_{22}CH_3$). FTIR: v_{max}/ cm^{-1} (solid): 3342 cm^{-1} (primary amide N-H stretch), 2924 cm^{-1} (carboxylic acid O-H stretch), 1651 cm^{-1} (primary amide C=O stretch), 1503 cm^{-1} (alkane C-H stretch), 1444 cm^{-1} (azo N=N stretch), 1372 cm^{-1} (S=O stretch), 1191 cm^{-1} (phenol O-H stretch), 1014 cm^{-1} (C=S stretch), 833 cm^{-1} (aromatic C-H stretch).

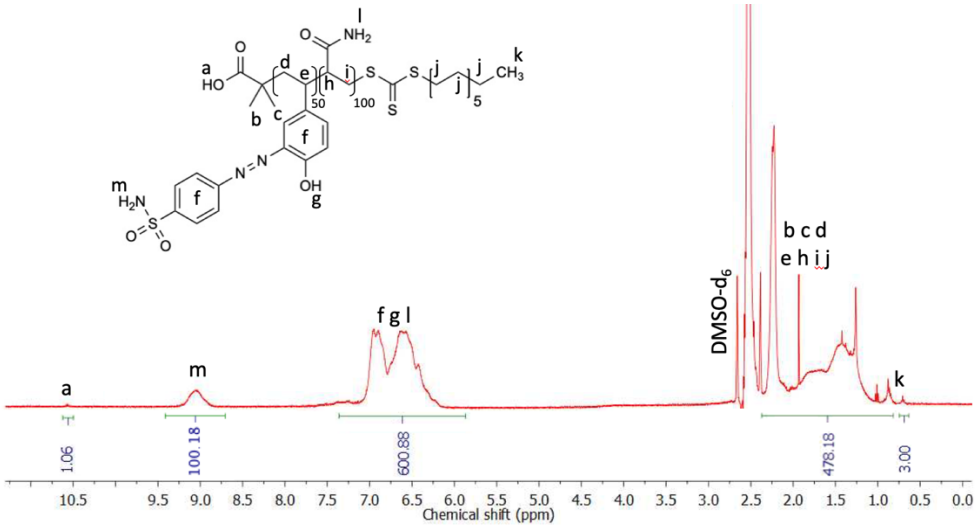

Figure 6. 14. The 500 MHz ^{1}H-NMR spectrum of P(ρHS-SA)$_{50}$-*b*-PAM$_{100}$ in DMSO-d$_6$ at 25 °C.

P(ρHS-SA)$_{50}$-*b*-PAM$_{200}$: 0.08 g, 61.0 wt. % (pale brown solid). APC (PMMA standards): M_w= 29900 g mol^{-1}. Dispersity= 1.39. ^{1}H NMR (500 MHz, DMSO-d$_6$, δ, ppm): 10.82-10.67 (s, 1H, COOH), 9.47-8.70 (s, 100H, (H_2NSO$_2$Ar)$_{50}$), 8.28-6.09 (m, 800H, (CH_2CHARHOHN$_2$ArH)$_{50}$(H_2NCO)$_{200}$), 2.29-1.06 (m, 778H, CH_3CH_3(CH_2CH)$_{50}$($CHCH_2$)$_{200}$C$_{11}H_{22}$), 0.89-0.62 (t, 3H, C$_{11}H_{22}CH_3$). FTIR: v_{max}/ cm^{-1} (solid): 3331 cm^{-1} (primary amide N-H stretch), 2941 cm^{-1} (carboxylic acid O-H stretch), 1651 cm^{-1} (primary amide C=O stretch), 1505 cm^{-1} (alkane C-H stretch), 1444 cm^{-1} (azo N=N stretch), 1366 cm^{-1} (S=O stretch), 1185 cm^{-1} (phenol O-H stretch), 1009 cm^{-1} (C=S stretch), 828 cm^{-1} (aromatic C-H stretch).

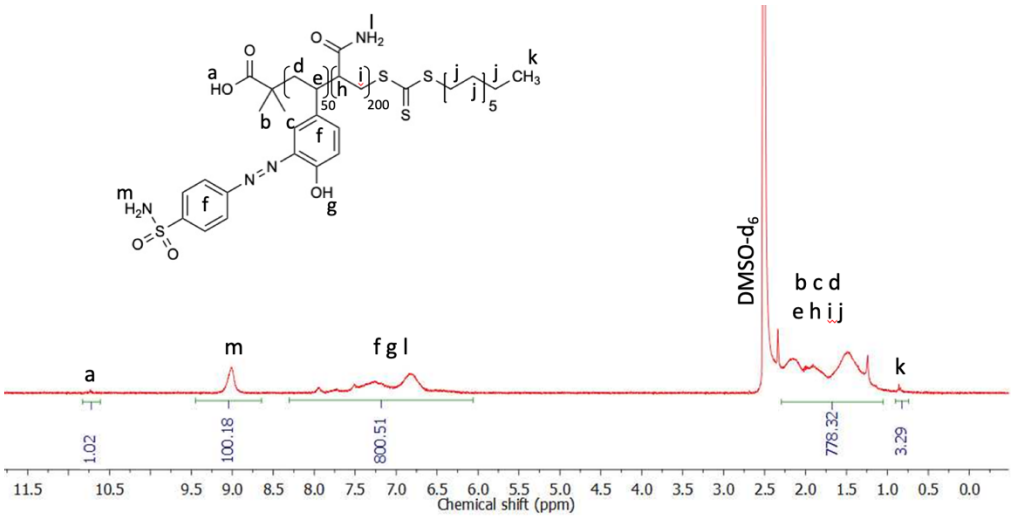

Figure 6. 15. The 500 MHz ^{1}H-NMR spectrum of P(ρHS-SA)$_{50}$-*b*-PAM$_{200}$ in DMSO-d$_6$ at 25 °C.

6.2.7. Synthesis of poly(acetoxystyrene)-*co*-poly(acrylamide)

2-(((Dodecylthio)carbonothioy)thio)-2-methylpropanoic acid (98.0 mg, 0.269 mmol), ACS (2.20g, 13.7 mmol), AM (3.83 g, 53.9 mmol), and AIBN (8.84 mg, 0.054 mmol) were dissolved in anhydrous DMF (14.0 mL) with flushing nitrogen. The reaction was stirred at 70 °C for four hours under nitrogen. Then the reaction mixture was precipitated in cold diethyl ether (60.0 mL), centrifuged at 6000 rev/min for 10 minutes and dried in a vacuum oven at 40 °C for 24 hours. The synthesised polymer was poly(acetoxystyrene)$_{50}$-*co*-poly(acrylamide)$_{200}$ (PACS$_{50}$-*co*-PAM$_{200}$). PACS$_{50}$-*co*-PAM$_{200}$: 4.61 g, 75.6 wt. % (pale yellow powder). APC (PMMA standards): M_w= 22800 g mol^{-1}. Dispersity= 1.37. ^{1}H NMR (500 MHz, DMSO-d$_6$, δ, ppm): 12.08-11.94 (s, 1H, COO<u>H</u>), 7.71-6.26 (m, 600H, (CH$_2$CHAR<u>H</u>)$_{50}$(CHCON<u>H$_2$</u>)$_{200}$), 2.32-0.99 (m, 928H, C<u>H$_3$</u>C<u>H$_3$</u>(C<u>H$_2$</u>C<u>H</u>ArOCOC<u>H$_3$</u>)$_{50}$(C<u>H</u>C<u>H$_2$</u>)$_{200}$C$_{11}$<u>H$_{22}$</u>), 0.98-0.70 (t, 3H, C$_{11}$H$_{22}$C<u>H$_3$</u>). FTIR: ν_{max}/cm^{-1} (solid): 3329 cm^{-1} (primary amide N-H stretch), 2931 cm^{-1} (carboxylic acid O-H stretch), 1752 cm^{-1} (aromatic ester C=O stretch), 1647 cm^{-1} (primary amide C=O stretch), 1509 (alkane C-H stretch), 1187 cm^{-1} (aromatic ester C-O stretch), 1099 cm^{-1} (C=S stretch), 850 cm^{-1} (aromatic C-H bending).

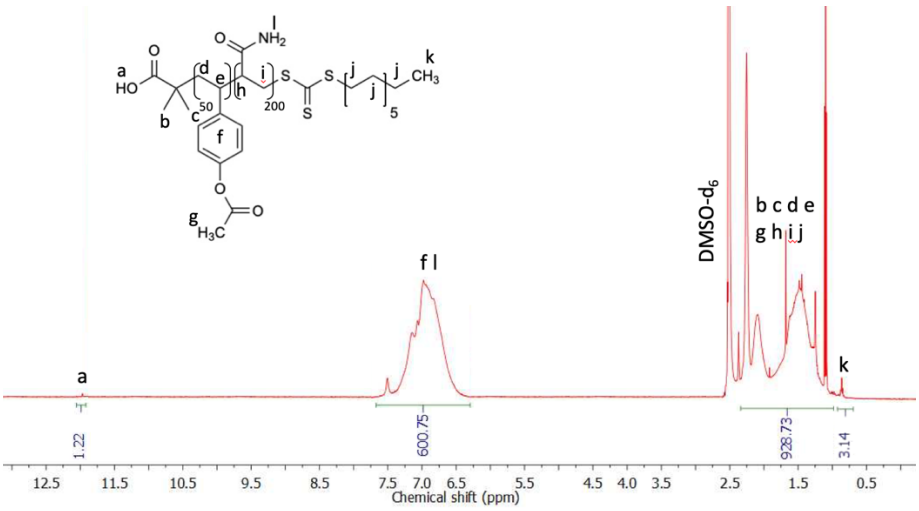

Figure 6. 16. The 500 MHz ^{1}H-NMR spectrum of PACS$_{50}$-*co*-PAM$_{200}$ in DMSO-d$_6$ at 25 °C.

6.2.8. Synthesis of poly(*ρ*-hydroxystyrene)-*co*-poly(acrylamide)

The procedures were the same as that described in 6.2.5. The quantity of the reactants were PACS$_{50}$-*co*-PAM$_{200}$ (3.23 g, 0.143 mmol), phosphoric acid (2.05 g, 20.9 mmol), TFA

(10.0 mL, 130.7 mmol), DMF (20.0 mL) and cold diethyl ether (150 mL). PρHS$_{50}$-*co*-PAM$_{200}$: 2.56 g, 87.1 wt. % (pale yellow powder). APC (PMMA standards): M_w= 20800 g mol^{-1}. Dispersity= 1.48. ^{1}H NMR (500 MHz, $CDCl_3$, δ, ppm): 10.68-10.58 (s, 1H, COOH), 7.67-6.21 (m, 650H, $(CH_2CHARHOH)_{50}(H_2NCO)_{200}$), 2.39-0.88 (m, 778H, $CH_3CH_3(CH_2CH)_{50}(CHCH_2)_{200}C_{11}H_{22}$), 0.87-0.77 (t, 3H, $C_{11}H_{22}CH_3$). FTIR: ν_{max}/ cm^{-1} (solid): 3379 cm^{-1} (primary amide, N-H, stretch), 2931 cm^{-1} (carboxylic acid, O-H, stretch), 2322 cm^{-1} (phenol, O-H, stretch), 1647 cm^{-1} (primary amide, C=O, stretch), 1110 cm^{-1} (C=S, stretch), 872 cm^{-1} (aromatic, C-H, bending).

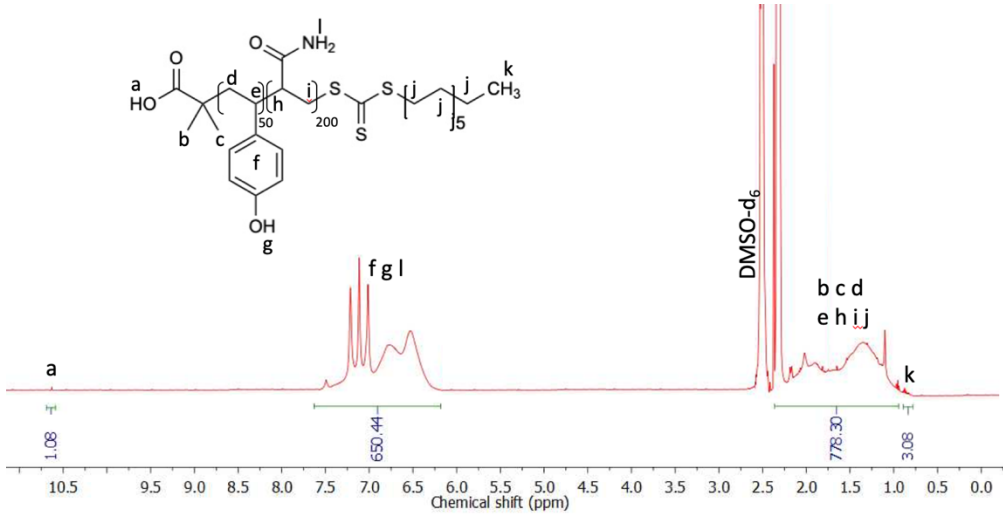

Figure 6. 17. The 500 MHz ^{1}H-NMR spectrum of PρHS$_{50}$-*co*-PAM$_{200}$ in DMSO-d$_6$ at 25 °C.

6.2.9. Sulfanilamide modification of poly(ρ-hydroxystyrene)-*co*-poly(acrylamide)

The synthesis procedures were the same as that described in 6.2.6. The quantities of the reactants were PρHS$_{50}$-*co*-PAM$_{200}$ (2.11 g, 0.103 mmol), SA (0.089 g, 0.515 mmol), sodium nitrite (269.5 mg, 3.91 mmol), propionic acid (3 mL, 40.1 mmol), concentrated sulfuric acid (6 mL, 112.6 mmol), acetic acid (18 mL, 314.7 mmol), DMF (14 mL) and acetone (200 mL). P(ρHS-SA)$_{50}$-*co*-PAM$_{200}$: 1.94 g, 63.4 wt. % (pale brown solid). APC (PMMA standards): M_w= 29900 g mol^{-1}. Dispersity= 1.46. ^{1}H NMR (500 MHz, DMSO-d$_6$, δ, ppm): 10.83-10.66 (s, 1H, COOH), 9.61-8.69 (s, 100H, $(H_2NSO_2Ar)_{50}$), 7.74-5.92 (m, 800H, $(CH_2CHARHOHN_2ArH)_{50}(H_2NCO)_{200}$), 2.38-0.94 (m, 778H, $CH_3CH_3(CH_2CH)_{50}(CHCH_2)_{200}C_{11}H_{22}$), 0.91-0.78 (t, 3H, $C_{11}H_{22}CH_3$). FTIR: ν_{max}/ cm^{-1} (solid): 3352 cm^{-1} (primary amide N-H stretch), 2931 cm^{-1} (carboxylic acid O-H stretch), 1664 cm^{-}

[1] (primary amide C=O stretch), 1444 cm^{-1} (azo N=N stretch), 1370 cm^{-1} (S=O stretch), 1193 cm^{-1} (phenol O-H stretch), 1016 cm^{-1} (C=S stretch), 833 cm^{-1} (aromatic C-H stretch).

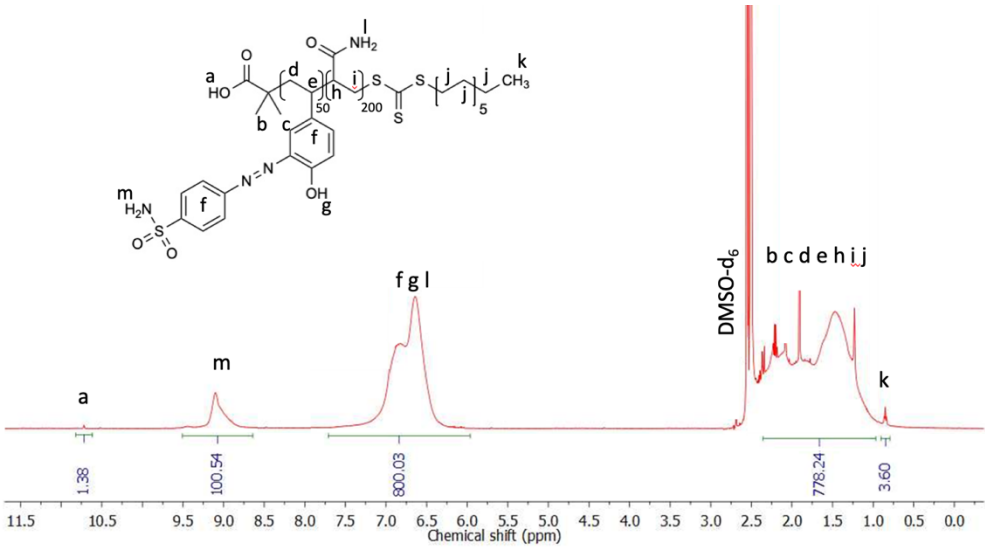

Figure 6. 18. The 500 MHz ^{1}H-NMR spectrum of P(ρHS-SA)$_{50}$-*co*-PAM$_{200}$ in DMSO-d$_6$ at 25 °C.

6.3. Results and discussion

PACS$_n$-*b*-PAM$_m$ was synthesised by RAFT polymerisation. The acetoxy group in PACS was hydrolysed by TFA and phosphoric acid to produce PρHS$_n$-*b*-PAM$_m$. SA was conjugated to PρHS$_n$-*b*-PAM$_m$ by azo coupling reaction. P(ρHS-SA)$_n$-*b*-PAM$_m$ showed red colour in acid, then changed to colourless by adding base until reached neutral environment (pH 7.4). Then more base was added in, the solution colour changed to pale yellow. The colour of the solution changed to orange red when acid was added again until pH was 0.6 (Scheme 6.2).

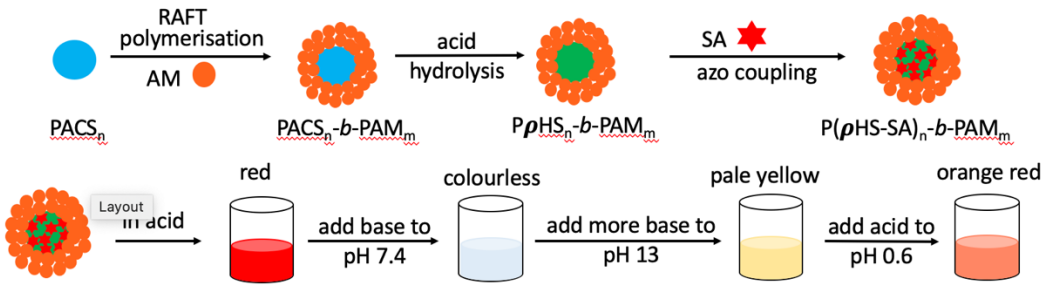

Scheme 6. 2. Reaction outline for the creation of P(ρHS-SA)$_n$-*b*-PAM$_m$ that shows red colour in acid, colourless in neutral environment, pale yellow in base, and orange red when acid adds again.

Synthesis of poly(acetoxystyrene), poly(ρ-hydroxystyrene) and poly(ρ-hydroxystyrene-sulfanilamide)

PACS was synthesised via RAFT polymerisation, using AIBN as an initiator in anhydrous DMF at 70 °C (Scheme 6.3).

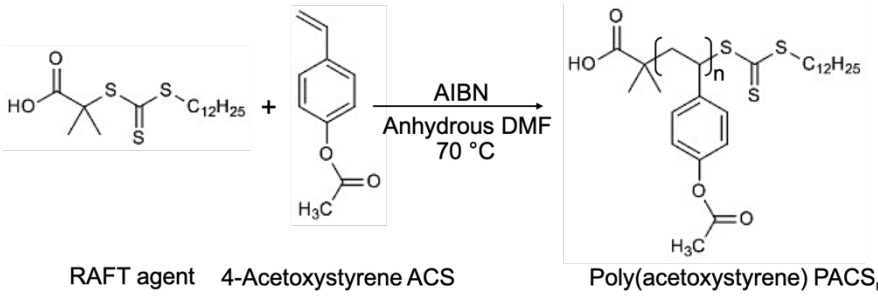

Scheme 6. 3. Synthesis of $PACS_n$.

Then the acetoxy group of PACS was hydrolysed by phosphoric acid and TFA, forming an alcohol group and the produced polymer was PρHS (Scheme 6.4).

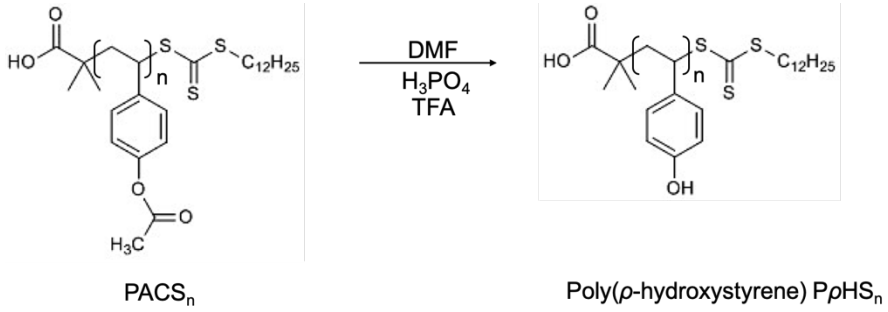

Scheme 6. 4. Synthesis of $P\rho HS_n$.

The azo coupling proceeded in strong acids, SA conjugated to PρHS via an azo bond so PρHS-SA was synthesised (Scheme 6.5). The azo coupling was considered to occur at the meta position which was close to the carboxylic acid functional group on the aromatic group. The OH group (electron donating group) shared the lone pair of electrons from the oxygen atom in the aromatic ring, contributing to the resonance structure. The OH group had a '2,4-directing effect' so the incoming group likely conjugated at 2 (meta position next to the OH group) or at 4 (opposite to the OH group) [26-27]. Conjugation at 3 (ortho position) is unlikely because the product is produced very slowly [26]. The $C_{12}H_{25}$ chain was bulky (more sterically crowded) compared to the 2-methylpropanoic acid group so less steric hindrance at the meta position close to the 2-methylpropanoic

acid group occurred compared to near the $C_{12}H_{25}$ chain. Consequently, azo coupling was considered to occur at the meta position indicated in Scheme 6.5.

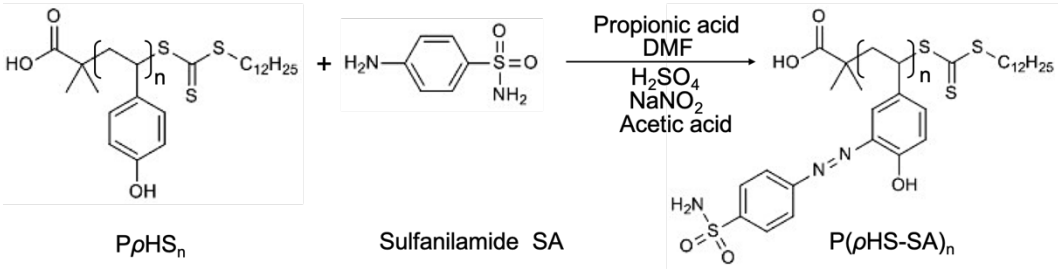

Scheme 6. 5. Synthesis of P(ρHS-SA)$_n$.

^{1}H NMR analysis revealed that the integrals corresponding to the proton environments a and i of PACS, PρHS and PρHS-SA were one and three, respectively, which were the same as the number of hydrogen atoms in each environment (Figures 6.1-6.6). The chain lengths of PACS, PρHS and PρHS-SA were measured by the integrals of the aromatic rings (environment f, f g or f j) and other proton environments (b, c, d, e, and h). The integral of each environment was consistent to the number of hydrogen atoms in each group in PACS, PρHS and PρHS-SA. In the acid hydrolysis step (acid deprotection Scheme 6.4), phosphoric acid and TFA did not destroy PρHS$_{50}$ and PρHS$_{100}$ and the chain lengths remained as 100 and 50 units (Figures 6.3-6.4). The molecular weight of PACS$_{100}$, PρHS$_{100}$, PACS$_{50}$, PρHS$_{50}$, P(ρHS-SA)$_{100}$ and P(ρHS-SA)$_{50}$ measured by APC, the theoretical and actual molecular weight are comparable (Table 6.1). The integral of the primary amine (Figures 6.5-6.6) was used to determine the amount of SA conjugated to PρHS. The integral of the primary amine of P(ρHS-SA)$_{100}$ and P(ρHS-SA)$_{50}$ were 200 and 100 which indicated the complete azo coupling. Therefore, proton NMR analysis and APC data proved that PACS$_{100}$, PρHS$_{100}$, P(ρHS-SA)$_{100}$, PACS$_{50}$, PρHS$_{50}$ and P(ρHS-SA)$_{50}$ were synthesised.

Table 6. 1. APC data revealing the average polymers molecular weight and dispersity values for $PACS_{100}$, $PACS_{50}$, $P\rho HS_{100}$, $P\rho HS_{50}$, $P(\rho HS\text{-}SA)_{100}$ and $P(\rho HS\text{-}SA)_{50}$.

Polymers	Theoretical M_w (g. mol^{-1})	Actual M_w (g. mol^{-1})	PDI
$PACS_{100}$	16564	16700	1.39
$PACS_{50}$	8464	8600	1.27
$P\rho HS_{100}$	12364	12600	1.31
$P\rho HS_{50}$	6364	6600	1.22
$P(\rho HS\text{-}SA)_{100}$	30664	30800	1.25
$P(\rho HS\text{-}SA)_{50}$	15514	15700	1.33

Carboxylic acid O-H (2924 cm^{-1}, 2922 cm^{-1}), aromatic ester C=O (1756 cm^{-1}, 1757 cm^{-1}), C-O (1189 cm^{-1}, 1187 cm^{-1}), C=S (1011 cm^{-1}, 1015 cm^{-1}) and aromatic C-H (842 cm^{-1}, 843 cm^{-1}) groups were shown in the FTIR spectra of both $PACS_{100}$ and $PACS_{50}$ (Figures 6.19-6.20 black). After acid deprotection of $PACS_{100}$ and $PACS_{50}$, the ester bonds were cleaved, revealing phenol O-H bonds (2919 cm^{-1}, 2928 cm^{-1}). The C=S (1007 cm^{-1}, 1016 cm^{-1}) and the aromatic bonds C-H (839 cm^{-1}) were also presented, confirming that $P\rho HS_{100}$ and $P\rho HS_{50}$ were produced successfully (Figures 6.19-6.20 red). Following azo coupling, primary amine N-H (3309 cm^{-1}), azo N=N (1444 cm^{-1}) and S=O (1326 cm^{-1}) bonds were observed by FTIR spectroscopy, indicating that $P(\rho HS\text{-}SA)_{100}$ and $P(\rho HS\text{-}SA)_{50}$ were synthesised (Figures 6.19-6.20 blue).

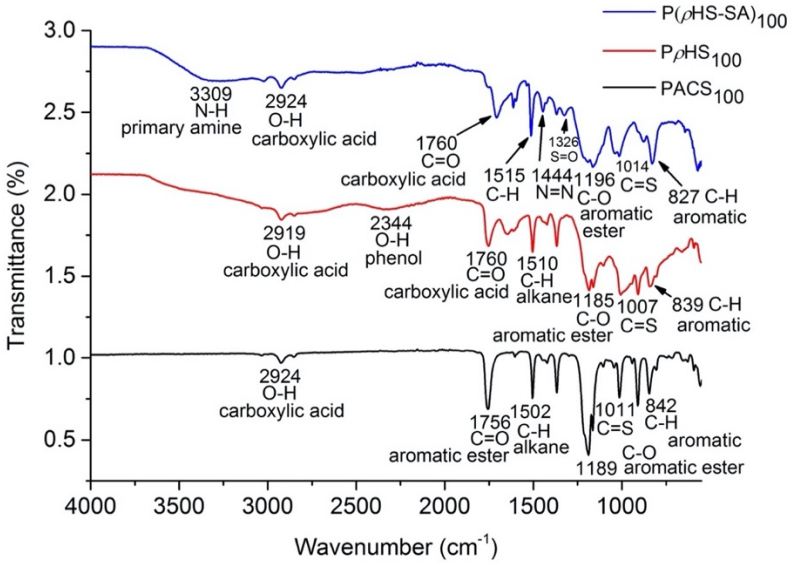

Figure 6. 19. FTIR spectra of $PACS_{100}$, $P\rho HS_{100}$, and $P(\rho HS\text{-}SA)_{100}$.

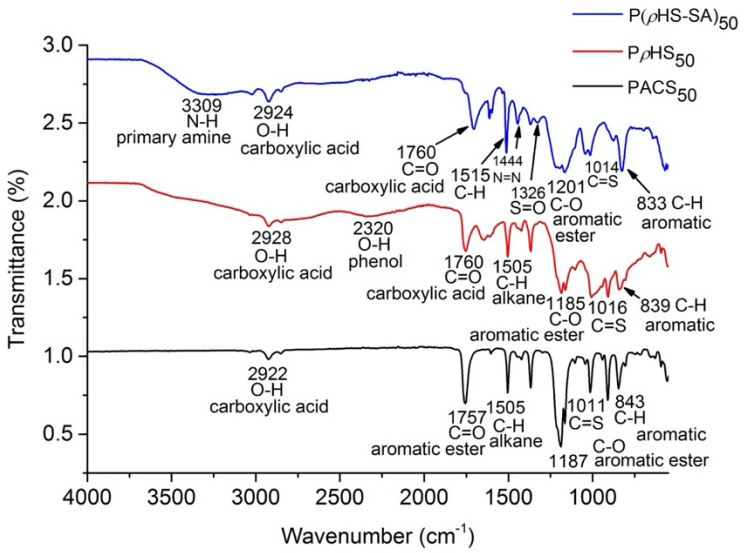

Figure 6. 20. FTIR spectra of $PACS_{50}$, $P\rho HS_{50}$, and $P(\rho HS\text{-}SA)_{50}$.

Synthesis of poly(acetoxystyrene)-*b*-poly(acrylamide), poly(*ρ*-hydroxystyrene)-*b*-poly(acrylamide) and poly(*ρ*-hydroxystyrene-sulfanilamide)-*b*-poly(acrylamide)

In order to enable the dispersion of P*ρ*HS-SA particles in aqueous solution, amphiphilic diblock copolymers P(*ρ*HS-SA)-*b*-PAM with various chain lengths were synthesised (Scheme 6.6). The method of synthesis of PACS was the same as that described in Scheme 6.3. PAM was the hydrophilic block of P(*ρ*HS-SA)-*b*-PAM.

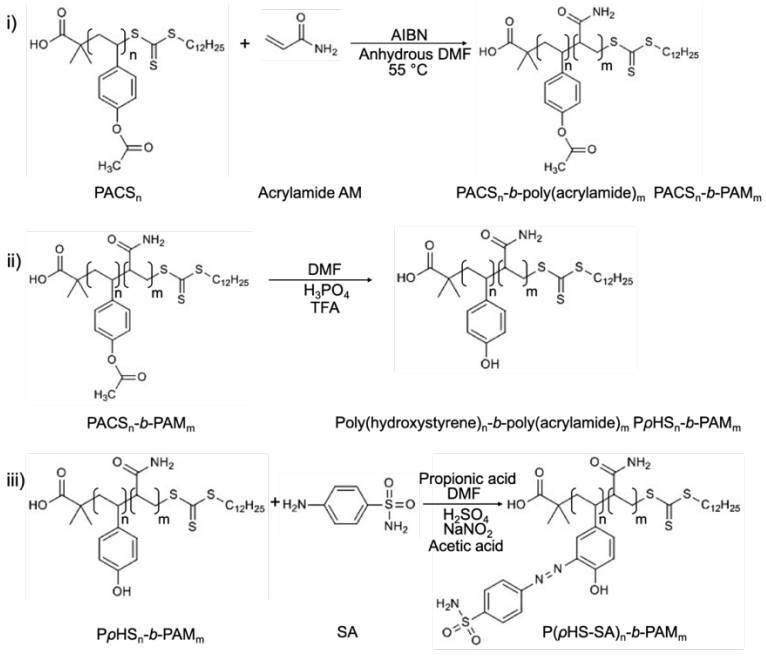

Scheme 6. 6. Synthesise of $P(\rho HS\text{-}SA)_n$-*b*-PAM_m.

^{1}H NMR analysis revealed that the integral of the carboxylic acid group O<u>H</u> (a) and the alkane $C_{11}H_{22}$-C<u>H_3</u> (k) of PACS-*b*-PAM (Figures 6.7-6.9), PρHS-*b*-PAM (Figures 6.10-6.12) and P(ρHS-SA)-*b*-PAM (Figures 6.13-6.16) were one and three, respectively, allowing the integration of the aromatic (f or f and g), the primary amide (l) and other proton environments (b, c, d, e, h, i, j, k and m) of the polymers to be measured. The chain lengths of PACS and PAM blocks was analysed by the integration of the aromatic ring (f or f and g) and the primary amide (l), respectively. The integration of the primary amine (m) from P(ρHS-SA)-*b*-PAM was employed to analyse the efficiency of azo coupling (Figure 6.13-6.15). The integrals of the other environments of PACS-*b*-PAM, PρHS-*b*-PAM and P(ρHS-SA)-*b*-PAM were utilised to confirm the chain lengths of the polymers. The molecular weight of $PACS_{100}$-*b*-PAM_{200}, PρHS_{100}-*b*-PAM_{200}, P(ρHS-SA)$_{100}$-*b*-PAM_{200}, $PACS_{50}$-*b*-PAM_{100}, PρHS_{50}-*b*-PAM_{100}, P(ρHS-SA)$_{50}$-*b*-PAM_{100}, $PACS_{50}$-*b*-PAM_{200}, PρHS_{50}-*b*-PAM_{200} and P(ρHS-SA)$_{50}$-*b*-PAM_{200} measured by APC, the theoretical and actual molecular weights are comparable (Table 6.2) which confirmed that the target polymers were synthesised.

Table 6. 2. APC data revealing the average polymers molecular weight and dispersity values for $PACS_{100}$-*b*-PAM_{200}, $PACS_{50}$-*b*-PAM_{100}, $PACS_{50}$-*b*-PAM_{200}, PρHS_{100}-*b*-PAM_{200}, PρHS_{50}-*b*-PAM_{100}, PρHS_{50}-*b*-PAM_{200}, P(ρHS-SA)$_{100}$-*b*-PAM_{200}, P(ρHS-SA)$_{50}$-*b*-PAM_{100} and P(ρHS-SA)$_{50}$-*b*-PAM_{200}.

Copolymers	Theoretical M_w (g. mol^{-1})	Actual M_w (g. mol^{-1})	PDI
$PACS_{100}$-*b*-PAM_{200}	30764	30900	1.23
$PACS_{50}$-*b*-PAM_{100}	15564	15600	1.34
$PACS_{50}$-*b*-PAM_{200}	22664	22800	1.21
PρHS_{100}-*b*-PAM_{200}	26564	26700	1.29
PρHS_{50}-*b*-PAM_{100}	13464	13600	1.28
PρHS_{50}-*b*-PAM_{200}	20564	20700	1.30
P(ρHS-SA)$_{100}$-*b*-PAM_{200}	44864	45000	1.41
P(ρHS-SA)$_{50}$-*b*-PAM_{100}	22614	22800	1.44
P(ρHS-SA)$_{50}$-*b*-PAM_{200}	29714	29900	1.39

In FTIR analysis, the primary amide N-H (3342 cm^{-1}, 3337 cm^{-1}), carboxylic acid O-H (2929 cm^{-1}, 2932 cm^{-1}), ester C=O (1755 cm^{-1}, 1758 cm^{-1}), C-O (1191 cm^{-1}), C=S (1014 cm^{-1}, 1102 cm^{-1}) and aromatic C-H (843 cm^{-1}) were shown in the FTIR spectra of $PACS_{100}$-*b*-PAM_{200} (Figure 6.21 black), $PACS_{50}$-*b*-PAM_{100} (Figure 6.22 black), and $PACS_{50}$-*b*-PAM_{200} (Figure 6.23 black). The acetoxy functional groups PACS-*b*-PAMs were cleaved under acidic conditions, yielding alcohol groups (2324 cm^{-1}, 2320 cm^{-1}, 2319 cm^{-1}) (Figures 6.21-6.23 red) and consequently P$\rho$$HS_{100}$-*b*-$PAM_{200}$, P$\rho$$HS_{50}$-*b*-$PAM_{100}$ and P$\rho$$HS_{50}$-*b*-$PAM_{200}$ were then conjugated to SA by azo coupling. The primary amide N-H (3335 cm^{-1}, 3342 cm^{-1}, 3331 cm^{-1}) C=O (1653 cm^{-1}, 1651 cm^{-1}), N=N (1444 cm^{-1}), S=O (1372 cm^{-1}, 1366 cm^{-1}), phenol C-O (1196 cm^{-1}, 1191 cm^{-1}, 1185 cm^{-1}), C=S (1014 cm^{-1}, 1009 cm^{-1}) and aromatic C-H (827 cm^{-1}, 833 cm^{-1}, 828 cm^{-1}) bonds presented in P(ρHS-SA)$_{100}$-*b*-PAM_{200} (Figure 6.21 blue), P(ρHS-SA)$_{50}$-*b*-PAM_{100} (Figure 6.22 blue) and P(ρHS-SA)$_{50}$-*b*-PAM_{200} (Figure 6.23 blue) FTIR spectra, confirming SA successfully conjugated to PρHS-*b*-PAMs. The FTIR spectra of $PACS_{100}$-*b*-PAM_{200}, P$\rho$$HS_{100}$-*b*-$PAM_{200}$, P($\rho$HS-SA)$_{100}$-*b*-$PAM_{200}$ (Figure 6.21), $PACS_{50}$-*b*-PAM_{100}, P$\rho$$HS_{50}$-*b*-$PAM_{100}$, P($\rho$HS-SA)$_{50}$-*b*-$PAM_{100}$ (Figure 6.22), $PACS_{50}$-*b*-PAM_{200}, P$\rho$$HS_{50}$-*b*-$PAM_{200}$, and P($\rho$HS-SA)$_{50}$-*b*-$PAM_{200}$ (Figure 6.23) confirmed the polymers were produced.

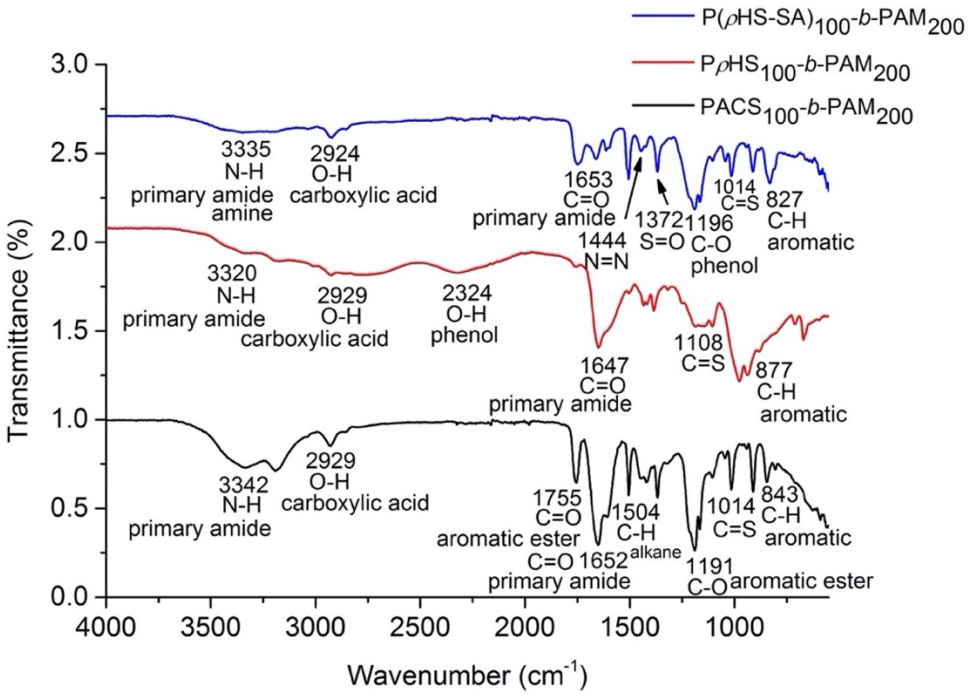

Figure 6. 21. FTIR spectra of $PACS_{100}$-*b*-PAM_{200}, P$\rho$$HS_{100}$-*b*-$PAM_{200}$, and P($\rho$HS-SA)$_{100}$-*b*-$PAM_{200}$.

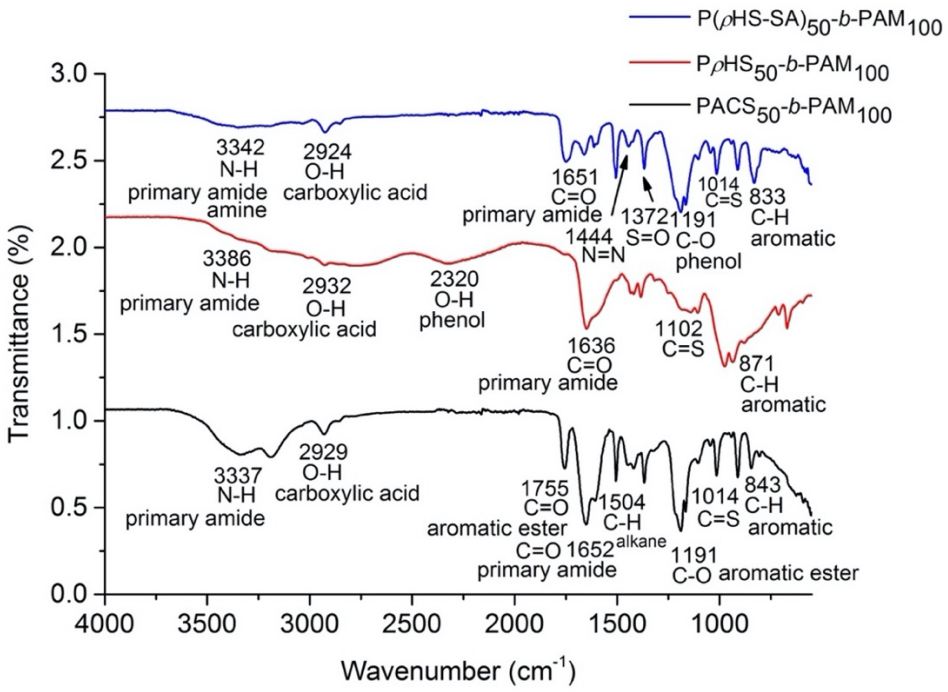

Figure 6. 22. FTIR spectra of $PACS_{50}$-*b*-PAM_{100}, $P\rho HS_{50}$-*b*-PAM_{100}, and $P(\rho HS\text{-}SA)_{50}$-*b*-$PAM_{100}$.

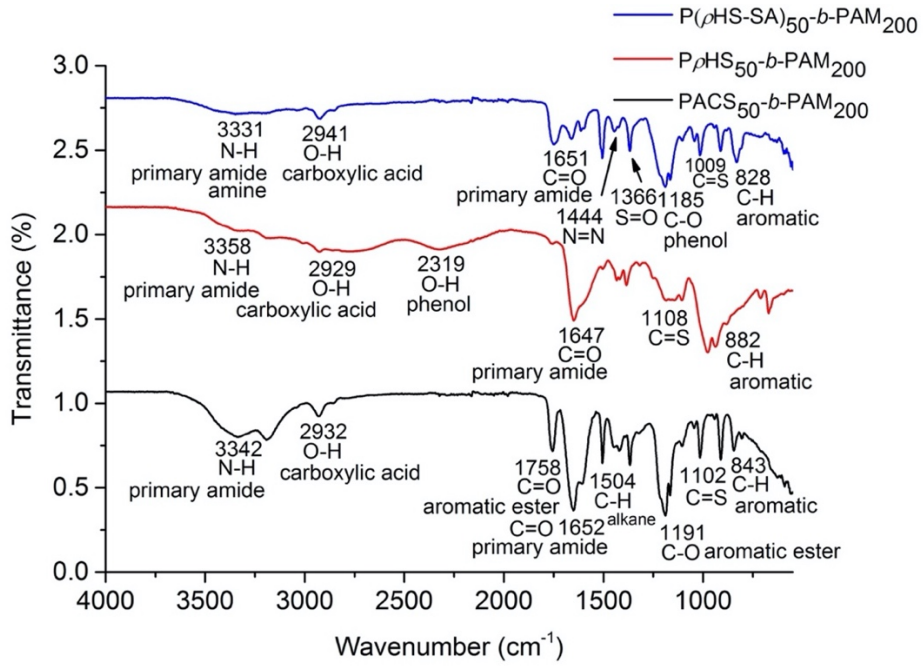

Figure 6. 23. FTIR spectra of $PACS_{50}$-*b*-PAM_{200}, $P\rho HS_{50}$-*b*-PAM_{200}, and $P(\rho HS\text{-}SA)_{50}$-*b*-$PAM_{200}$.

Synthesis of poly(*ρ*-hydroxystyrene-sulfanilamide)-*co*-poly(acrylamide)

PACS-*co*-PAM was then synthesised by ACS and AM monomers via random copolymerisation (Scheme 6.7). The acid deprotecton and the azo coupling steps were the same as that described in Scheme 6.6 ii and iii. P(ACS-SA)-*co*-PAM was expected to

disperse better in aqueous and polar solutions (compared to P(ACS-SA)-*b*-PAM), yielding an antimicrobial polymer that can be incorporated within a polar solvent and potentially deployed within hand wash or laundry detergent formulations.

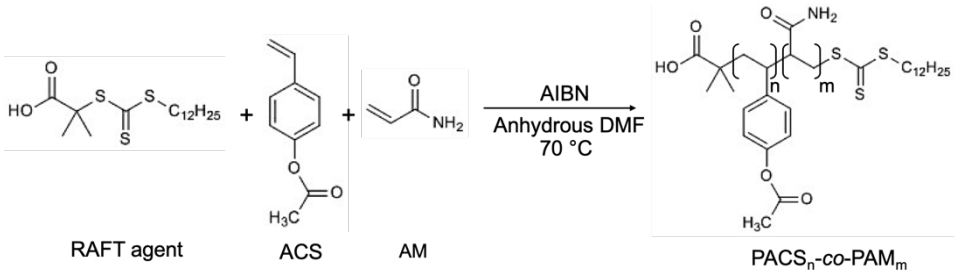

Scheme 6. 7. Synthesis of $PACS_n$-*co*-PAM_m.

^{1}H NMR analysis revealed that the integration value of the carboxylic acid COO<u>H</u> (a) and the alkane $C_{11}H_{22}C\underline{H_3}$ groups (k) were one and three, respectively. Therefore, the chain lengths of PACS-*co*-PAM, PρHS-*co*-PAM and P(ρHS-SA)-*co*-PAM were analysed via the integrals of the aromatic ring (f or f and g) and the primary amide (l) confirming the synthesised polymers were $PACS_{50}$-*co*-PAM_{200} (Figure 6.16), PρHS_{50}-*co*-PAM_{200} (Figure 6.17) and P(ρHS-SA)$_{50}$-*co*-PAM_{200} (Figure 6.18). The integration of other proton environments (b, c, d, e, h, I, j, k and m) of $PACS_{50}$-*co*-PAM_{200}, PρHS_{50}-*co*-PAM_{200} and P(ρHS-SA)$_{50}$-*co*-PAM_{200} were consistent to the number of hydrogen atoms in the environments in the polymers. The molecular weight of $PACS_{50}$-*co*-PAM_{200}, PρHS_{50}-*co*-PAM_{200} and P(ρHS-SA)$_{50}$-*co*-PAM_{200} measured by APC, the theoretical and actual molecular weights of each polymer (Table 6.3) are comparable. The repeat units of P(ρHS-SA)$_{50}$-*co*-PAM_{200} were the same as P(ρHS-SA)$_{50}$-*b*-PAM_{200} and so the antimicrobial activity of both types of polymers can be compared.

Table 6. 3. APC data revealing the average polymer molecular weight and dispersity values for $PACS_{50}$-*co*-PAM_{200}, PρHS_{50}-*co*-PAM_{200} and P(ρHS-SA)$_{50}$-*co*-PAM_{200}.

Copolymers	Theoretical M_w (g. mol^{-1})	Actual M_w (g. mol^{-1})	PDI
$PACS_{50}$-*co*-PAM_{200}	22664	22800	1.37
PρHS_{50}-*co*-PAM_{200}	20564	20800	1.48
P(ρHS-SA)$_{50}$-*co*-PAM_{200}	29714	29900	1.46

Further confirmation of $PACS_{50}$-*co*-PAM_{200}, $P\rho HS_{50}$-*co*-PAM_{200} and $P(\rho HS\text{-}SA)_{50}$-*co*-$PAM_{200}$ synthesis was provided by FTIR analysis. $PACS_{50}$-*co*-PAM_{200} was synthesised as indicated by the primary amide N-H (3329 cm^{-1}), carboxylic acid O-H (2931 cm^{-1}), ester C=O (1752 cm^{-1}), primary amide C=O (1647 cm^{-1}), C-O (1187 cm^{-1}), C=S (1099 cm^{-1}) and aromatic C-H (850 cm^{-1}) peaks in the FTIR spectrum (Figure 6.24 black). The $PACS_{50}$ block of $PACS_{50}$-*co*-PAM_{200} was hydrolysed by phosphoric acid and TFA so the ester bond disappeared and an alcohol bond (2322 cm^{-1}) formed as part of $P\rho HS_{50}$-*co*-PAM_{200} (Figure 6.24 red). The primary amide (3379 cm^{-1}), carboxylic acid (2931 cm^{-1}), primary amide (1647 cm^{-1}), C=S (1110 cm^{-1}) and aromatic (872 cm^{-1}) bonds were also represented in the FTIR spectrum of $P\rho HS_{50}$-*co*-PAM_{200} confirming that $PACS_{50}$-*co*-PAM_{200} was hydrolysed by phosphoric acid and TFA successfully. $P\rho HS_{50}$-*co*-PAM_{200} was conjugated with SA so N=N (1448 cm^{-1}), S=O (1370 cm^{-1}) bonds were formed which showed in the FTIR spectrum of $P(\rho HS\text{-}SA)_{50}$-*co*-$PAM_{200}$ (Figure 6.24 blue). Therefore, the FTIR spectra of $PACS_{50}$-*co*-PAM_{200}, $P\rho HS_{50}$-*co*-PAM_{200} and $P(\rho HS\text{-}SA)_{50}$-*co*-$PAM_{200}$ (Figure 6.24) confirmed that the desired polymers were synthesised.

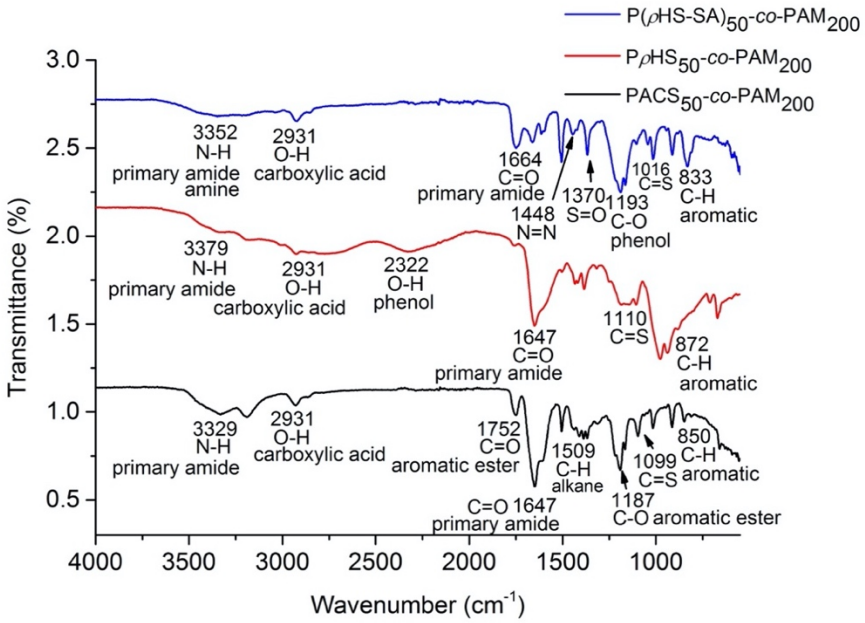

Figure 6. 24. FTIR spectra of $PACS_{50}$-*co*-PAM_{200}, $P\rho HS_{50}$-*co*-PAM_{200}, and $P(\rho HS\text{-}SA)_{50}$-*co*-$PAM_{200}$.

$PACS_{100}$, $PACS_{50}$, $P\rho HS_{100}$, $P\rho HS_{50}$, $P(\rho HS\text{-}SA)_{100}$, $P(\rho HS\text{-}SA)_{50}$, $PACS_{100}$-*b*-PAM_{200}, $PACS_{50}$-*b*-PAM_{100}, $PACS_{50}$-*b*-PAM_{200}, $P\rho HS_{100}$-*b*-PAM_{200}, $P\rho HS_{50}$-*b*-PAM_{100}, $P\rho HS_{50}$-*b*-PAM_{200}, $P(\rho HS\text{-}SA)_{100}$-*b*-$PAM_{200}$, $P(\rho HS\text{-}SA)_{50}$-*b*-$PAM_{100}$, $P(\rho HS\text{-}SA)_{50}$-*b*-$PAM_{200}$, $PACS_{50}$-*co*-PAM_{200},

PρHS$_{50}$-*co*-PAM$_{200}$ and P(ρHS-SA)$_{50}$-*co*-PAM$_{200}$ nanoparticles were produced by coacervation in aqueous solution (preparation procedure was described in Chapter 2.12, briefly 0.2 mg of polymer was dissolved in 0.5 mL of DMSO then added dropwise into 1.5 mL of deionised water with stirring) and the particle size was measured by DLS (Tables 6.4-6.6 and Figures 6.26-6.28). Particle size was analysed by intensity size distribution. The refractive index and absorption of P(ρHS-SA) cannot be found in literature. Therefore, the refractive index and absorption of polystyrene were used which were 1.592 and 0.100 [28], respectively. The volume and number size analysis need accurate refractive index and absorption of the sample but intensity size analysis depends on light scattering of the sample. Therefore, intensity size analysis of the sample is more reliable. The correlogram of P(ρHS-SA)$_{100}$ was shown in Figure 6.25. The particle size of P(ρHS-SA)$_{100}$ was (102±31) nm, therefore, the small (light) the nanoparticles, the fast they were, so the correlogram decayed quick and had a steep gradient.

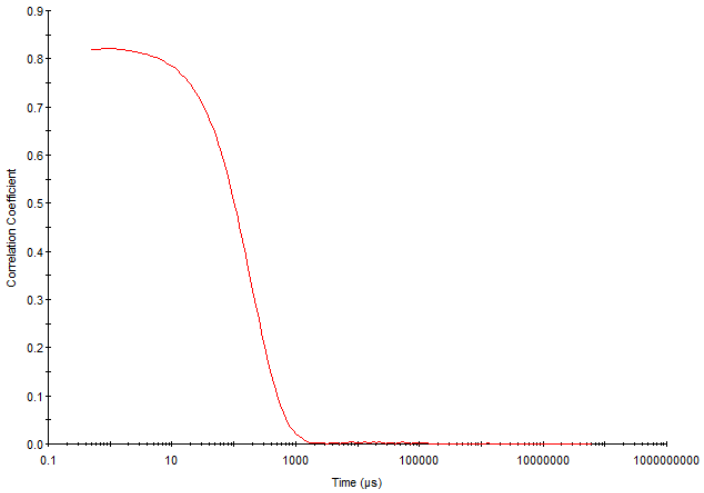

Figure 6. 25. Correlogram of P(ρHS-SA)$_{100}$ in deionised water at room temperature.

Particle size and time relationship of PACS$_{100}$, PACS$_{50}$, PρHS$_{100}$, PρHS$_{50}$, P(ρHS-SA)$_{100}$ and P(ρHS-SA)$_{50}$ after 24 hours, one week and two weeks were shown in Figure 6.26, DLS data presented in Table A6.1 and Figure A6.1. Average of the particle sizes and PDI values of newly created particles are provided in Table 6.4. PACS$_{100}$ and PACS$_{50}$ nanoparticles were measured initially, the size and the PDI values were (413±15)nm and 0.246, and (343±22)nm and 0.199, respectively (Table 6.4). PACS$_{100}$ has a longer chain length so its particle size was larger than that of PACS$_{50}$. After acid hydrolysis, PρHS$_{100}$ and PρHS$_{50}$ were produced and the particle size of the corresponding nanoparticles decreased to

(78±8)nm (PDI= 0.222) and (53±20)nm (PDI= 0.239), respectively, due to the increased polarity of the polymer, resulting in less polymer aggregation (Table 6.4). The nanoparticles of $PACS_{100}$, $PACS_{50}$, $P\rho HS_{100}$ and $P\rho HS_{50}$ were stable in water as demonstrated by PDI values of less than 0.3 in all cases. $P\rho HS_{100}$ and $P\rho HS_{50}$ were conjugated to SA, producing $P(\rho HS\text{-}SA)_{100}$ and $P(\rho HS\text{-}SA)_{50}$ and the size of the nanoparticles increased. The particle size of $P(\rho HS\text{-}SA)_{100}$ and $P(\rho HS\text{-}SA)_{50}$ were (102±31)nm and (66±12)nm (Table 6.4). The nanoparticles of $P(\rho HS\text{-}SA)_{100}$ and $P(\rho HS\text{-}SA)_{50}$ were unstable in water which was indicated by the PDI values 0.583 and 0.727 (greater than 0.3), respectively. This is likely due to the conjugation of aromatic SA to $P\rho HS_{100}$ and $P\rho HS_{50}$, promoting nanoparticle aggregation.

Table 6. 4. DLS data of $PACS_{100}$, $PACS_{50}$, $P\rho HS_{100}$, $P\rho HS_{50}$, $P(\rho HS\text{-}SA)_{100}$ and $P(\rho HS\text{-}SA)_{50}$ in deionised water with concentration of 0.1 mg mL^{-1}.

Polymers	Size (nm)	PDI
$PACS_{100}$	413 ± 15	0.246
$PACS_{50}$	343 ± 22	0.199
$P\rho HS_{100}$	78 ± 8	0.222
$P\rho HS_{50}$	53 ± 20	0.239
$P(\rho HS\text{-}SA)_{100}$	102 ± 31	0.583
$P(\rho HS\text{-}SA)_{50}$	66 ± 12	0.727

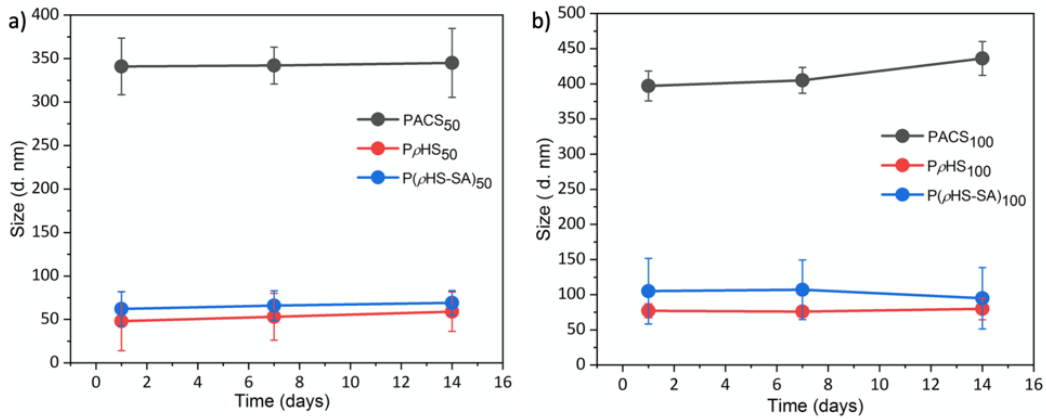

Figure 6. 26. Particle size and time relationship of a) $PACS_{50}$, $P\rho HS_{50}$ and $P(\rho HS\text{-}SA)_{50}$ and b) $PACS_{100}$, $P\rho HS_{100}$ and $P(\rho HS\text{-}SA)_{100}$.

$PACS_{100}$-*b*-PAM_{200}, $PACS_{50}$-*b*-PAM_{100} and $PACS_{50}$-*b*-PAM_{200} diblock copolymer nanoparticles were then synthesised. PAM was included as part of the copolymer in order to enhance the stability of any particles formed in aqueous/polar solution. Particle size and time relationship of $PACS_{100}$-*b*-PAM_{200}, $PACS_{50}$-*b*-PAM_{100}, $PACS_{50}$-*b*-PAM_{200}, P$\rho$$HS_{100}$-*b*-$PAM_{200}$, P$\rho$$HS_{50}$-*b*-$PAM_{100}$, P$\rho$$HS_{50}$-*b*-$PAM_{200}$, P($\rho$HS-SA)$_{100}$-*b*-$PAM_{200}$, P($\rho$HS-SA)$_{50}$-*b*-$PAM_{100}$ and P(ρHS-SA)$_{50}$-*b*-PAM_{200} measured after 24 hours, one week, and two weeks were shown in Figure 6.28, DLS data presented in Table A6.2 and Figure A6.2. Average of the particle size and PDI values were indicated in Table 6.5. The correlogram of P(ρHS-SA)$_{100}$-*b*-PAM_{200} is shown in Figure 6.27. The particle size of P(ρHS-SA)$_{100}$-*b*-PAM_{200} was (171±25) nm (small size) therefore, the correlogram decayed quick with a steep gradient.

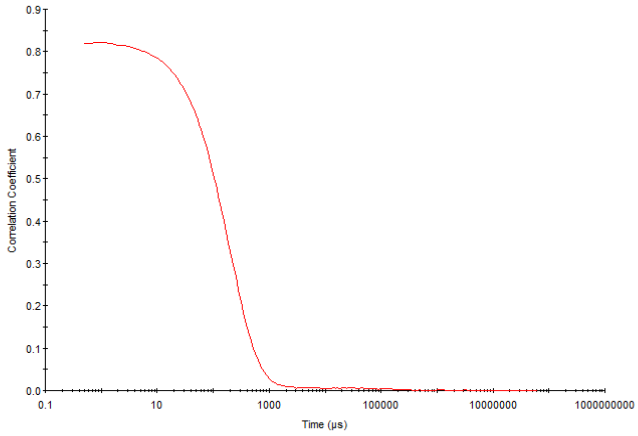

Figure 6. 27. Correlogram of P(ρHS-SA)$_{100}$-*b*-PAM_{200} in deionised water at room temperature.

The particle size of $PACS_{100}$-*b*-PAM_{200}, $PACS_{50}$-*b*-PAM_{100} and $PACS_{50}$-*b*-PAM_{200} were found to be (283±26)nm (PDI= 0.222), (199±22)nm (PDI= 0.202), and (116±17)nm (PDI= 0.166), respectively (Table 6.5). The acetoxy groups of $PACS_{100}$-*b*-PAM_{200}, $PACS_{50}$-*b*-PAM_{100} and $PACS_{50}$-*b*-PAM_{200} were hydrolysed by acids and the particle size of the resultant nanoparticles decreased to (149±30)nm (PDI= 0.269), (105±13)nm (PDI= 0.207) and (76±14)nm (PDI= 0.165), respectively. The reason of the particle size decrease was the same as that of P$\rho$$HS_{100}$ and P$\rho$$HS_{50}$: hydrolysis of the acetoxy group to alcohol group, leading to less polymer aggregation. The nanoparticles of PACS-*b*-PAM and PρHS-*b*-PAM were stable in aqueous solution as demonstrated by PDI values lower than 0.3. After azo coupling with SA, the particle size of P(ρHS-SA)$_{100}$-*b*-PAM_{200}, P(ρHS-SA)$_{50}$-*b*-PAM_{100}, and P(ρHS-SA)$_{50}$-*b*-PAM_{200} increased to (171±25)nm (PDI= 0.182), (121±15)nm (PDI= 0.191)

and (115±24)nm (PDI= 0.169), respectively. The PDI values of P(ρHS-SA)$_{100}$-*b*-PAM$_{200}$, P(ρHS-SA)$_{50}$-*b*-PAM$_{100}$, and P(ρHS-SA)$_{50}$-*b*-PAM$_{200}$ were smaller than 0.3 conforming that the nanoparticles were stable in aqueous solution. Therefore, the hydrophilic PAM chain enhanced the stability of the P(ρHS-SA)-*b*-PAM nanoparticles in aqueous solution compared to PρHS-SA (PDI>0.5).

Table 6. 5. DLS data of PACS$_{100}$-*b*-PAM$_{200}$, PACS$_{50}$-*b*-PAM$_{100}$, PACS$_{50}$-*b*-PAM$_{200}$, PρHS$_{100}$-*b*-PAM$_{200}$, PρHS$_{50}$-*b*-PAM$_{100}$, PρHS$_{50}$-*b*-PAM$_{200}$, P(ρHS-SA)$_{100}$-*b*-PAM$_{200}$, P(ρHS-SA)$_{50}$-*b*-PAM$_{100}$, and P(ρHS-SA)$_{50}$-*b*-PAM$_{200}$ in deionised water with concentration of 0.1 mg mL^{-1}.

Copolymers	Size (nm)	PDI
PACS$_{100}$-*b*-PAM$_{200}$	283 ± 26	0.222
PACS$_{50}$-*b*-PAM$_{100}$	199 ± 22	0.202
PACS$_{50}$-*b*-PAM$_{200}$	116 ± 17	0.166
PρHS$_{100}$-*b*-PAM$_{200}$	149 ± 30	0.269
PρHS$_{50}$-*b*-PAM$_{100}$	105 ± 13	0.207
PρHS$_{50}$-*b*-PAM$_{200}$	76 ± 14	0.165
P(ρHS-SA)$_{100}$-*b*-PAM$_{200}$	171 ± 25	0.182
P(ρHS-SA)$_{50}$-*b*-PAM$_{100}$	121 ± 35	0.191
P(ρHS-SA)$_{50}$-*b*-PAM$_{200}$	115 ± 24	0.169

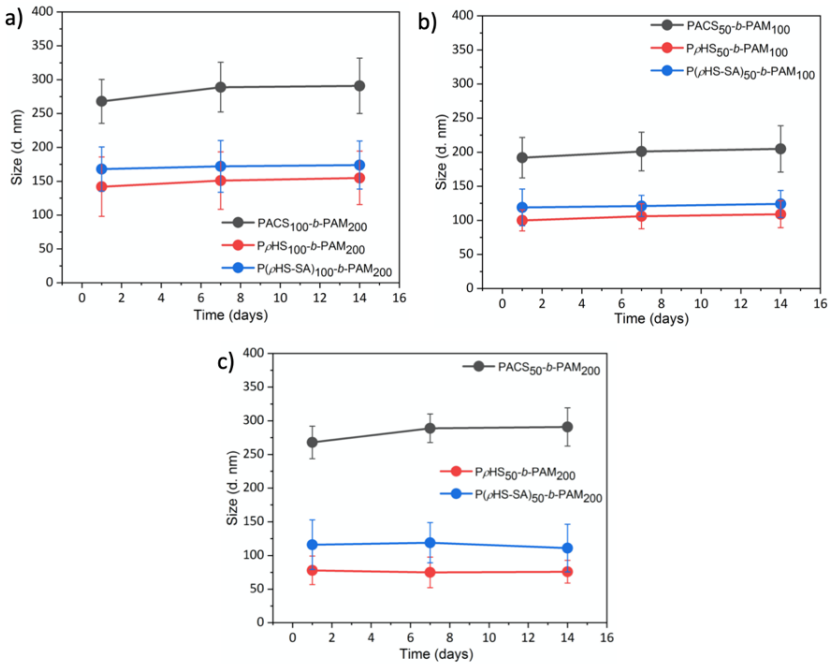

Figure 6. 28. Particle size and time relationship of a) $PACS_{100}$-*b*-PAM_{200}, PρHS_{100}-*b*-PAM_{200} and P(ρHS-SA)$_{100}$-*b*-PAM_{200}, b) $PACS_{50}$-*b*-PAM_{100}, PρHS_{50}-*b*-PAM_{100} and P(ρHS-SA)$_{50}$-*b*-PAM_{100}, and c) $PACS_{50}$-*b*-PAM_{200}, PρHS_{50}-*b*-PAM_{200} and P(ρHS-SA)$_{50}$-*b*-PAM_{200}.

Particle size and time relationship of $PACS_{50}$-*co*-PAM_{200}, PρHS_{50}-*co*-PAM_{200} and P(ρHS-SA)$_{50}$-*co*-PAM_{200} measured after 24 hours, one week, and two weeks were shown in Figure 6.30, DLS data presented in Table A6.3 and Figure A6.3. Average of the particle size and PDI values were provided in Table 6.6. The correlogram of P(ρHS-SA)$_{50}$-*co*-PAM_{200} is shown in Figure 6.29. The particle size of P(ρHS-SA)$_{50}$-*co*-PAM_{200} was (621±19)nm which was larger than P(ρHS-SA)$_{100}$-*b*-PAM_{200} (171±25) nm and P(ρHS-SA)$_{100}$ (102±31) nm. Therefore, the correlogram of P(ρHS-SA)$_{50}$-*co*-PAM_{200} decayed slower and had a shadow compared to P(ρHS-SA)$_{100}$-*b*-PAM_{200} and P(ρHS-SA)$_{100}$.

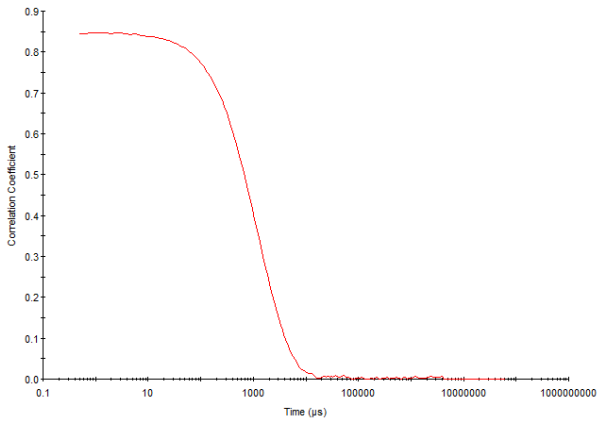

Figure 6. 29. Correlogram of P(ρHS-SA)$_{50}$-*co*-PAM_{200} in deionised water at room temperature.

The particle size of $PACS_{50}$-*co*-PAM_{200}, PρHS_{50}-*co*-PAM_{200} and P(ρHS-SA)$_{50}$-*co*-PAM_{200} were (708±15)nm, (553±26)nm and (621±19)nm, (Table 6.6) respectively which are greater values than those of $PACS_{50}$-*b*-PAM_{200} (116±17)nm, PρHS_{50}-*b*-PAM_{200} (76±14)nm, and P(ρHS-SA)$_{50}$-*b*-PAM_{200} (115±24)nm (Table 6.5). The particle size of $PACS_{50}$-*co*-PAM_{200} (708±15)nm decreased to (553±26)nm (PρHS_{50}-*co*-PAM_{200}) following acid hydrolysis of the acetoxy group to the hydroxyl group, and then increased to (621±19)nm (P(ρHS-SA)$_{50}$-*co*-PAM_{200}) after azo coupling with SA which followed the same trend as that of PACS and PACS-*b*-PAM. For $PACS_{50}$-*b*-PAM_{200}, $PACS_{50}$ was synthesised before 200 units of AM were polymerised to it, producing $PACS_{50}$-*b*-PAM_{200}. In the synthesis of $PACS_{50}$-*co*-PAM_{200}, 50 units of ACS and 200 units of AM (monomers) were polymerised via random copolymerisation, producing the random copolymer $PACS_{50}$-*co*-PAM_{200}. $PACS_{50}$-*co*-PAM_{200}, PρHS_{50}-*co*-PAM_{200} and P(ρHS-SA)$_{50}$-*co*-PAM_{200} had greater average particle sizes than $PACS_{50}$-*b*-PAM_{200}, PρHS_{50}-*b*-PAM_{200} and P(ρHS-SA)$_{50}$-*b*-PAM_{200}. The PDI values of $PACS_{50}$-*co*-PAM_{200}, PρHS_{50}-*co*-PAM_{200} and P(ρHS-SA)$_{50}$-*co*-PAM_{200} were 0.371, 0.342 and 0.480 (>0.3) (Table 6.6), respectively. $PACS_{50}$-*co*-PAM_{200}, PρHS_{50}-*co*-PAM_{200} and P(ρHS-SA)$_{50}$-*co*-PAM_{200} nanoparticles were unstable in aqueous solution.

Table 6. 6. DLS data of $PACS_{50}$-*co*-PAM_{200}, PρHS_{50}-*co*-PAM_{200} and P(ρHS-SA)$_{50}$-*co*-PAM_{200} in deionised water with concentration of 0.1 mg mL^{-1}.

Copolymers	Size (nm)	PDI
$PACS_{50}$-*co*-PAM_{200}	708 ± 15	0.371
PρHS_{50}-*co*-PAM_{200}	553 ± 26	0.342
P(ρHS-SA)$_{50}$-*co*-PAM_{200}	621 ± 19	0.480

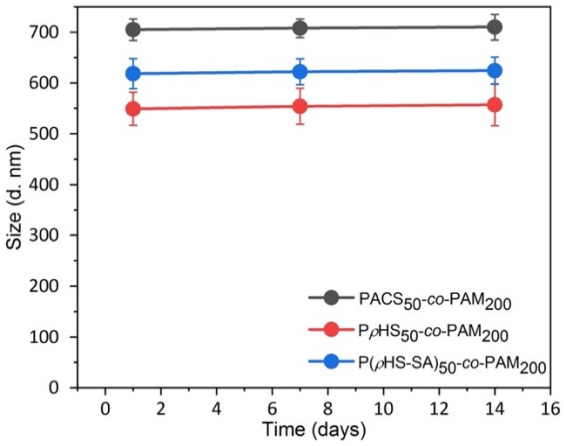

Figure 6. 30. Particle size and time relationship of a) $PACS_{50}$-*co*-PAM_{200}, $P\rho HS_{50}$-*co*-PAM_{200} and $P(\rho HS\text{-}SA)_{50}$-*co*-$PAM_{200}$.

Dr. David Green conducted SEM analysis for $P(\rho HS\text{-}SA)_{100}$-*b*-$PAM_{200}$, $P(\rho HS\text{-}SA)_{50}$-*b*-$PAM_{100}$, $P(\rho HS\text{-}SA)_{50}$-*b*-$PAM_{200}$, $P(\rho HS\text{-}SA)_{100}$ and $P(\rho HS\text{-}SA)_{50}$ nanoparticles. The PDI values of $P(\rho HS\text{-}SA)_{100}$-*b*-$PAM_{200}$, $P(\rho HS\text{-}SA)_{50}$-*b*-$PAM_{100}$ and $P(\rho HS\text{-}SA)_{50}$-*b*-$PAM_{200}$ nanoparticles (0.182, 0.191 and 0.169, respectively) were less than 0.3, and so nanoparticles from these batches were chosen for SEM analysis. Although the PDI values of $P(\rho HS\text{-}SA)_{100}$ (0.583) and $P(\rho HS\text{-}SA)_{50}$ (0.727) nanoparticles were greater than 0.3 (unstable in aqueous solution), the morphology and the particle size are different (lack of PAM chains) compared to $P(\rho HS\text{-}SA)_{100}$-*b*-$PAM_{200}$, $P(\rho HS\text{-}SA)_{50}$-*b*-$PAM_{100}$ and $P(\rho HS\text{-}SA)_{50}$-*b*-$PAM_{200}$ nanoparticles. Therefore, $P(\rho HS\text{-}SA)_{100}$-*b*-$PAM_{200}$, $P(\rho HS\text{-}SA)_{50}$-*b*-$PAM_{100}$, $P(\rho HS\text{-}SA)_{50}$-*b*-$PAM_{200}$, $P(\rho HS\text{-}SA)_{100}$ and $P(\rho HS\text{-}SA)_{50}$ nanoparticles were analysed by SEM (Figures 6.7-6.8). The samples used were the same as that analysed by DLS. All of the analysed polymeric nanoparticles were spherical. Particle size of $P(\rho HS\text{-}SA)_{100}$-*b*-$PAM_{200}$, $P(\rho HS\text{-}SA)_{50}$-*b*-$PAM_{100}$, $P(\rho HS\text{-}SA)_{50}$-*b*-$PAM_{200}$, $P(\rho HS\text{-}SA)_{100}$ and $P(\rho HS\text{-}SA)_{50}$ nanoparticles measured by statistical analysis from SEM images were (34±2)nm, (71±1)nm, (50±2)nm, (42±1)nm and (46±1)nm, respectively which were smaller than the particle size measured by DLS which were (171±25)nm, (121±35)nm, (115±24)nm, (102±31)nm, and (66±12)nm, respectively. FWHM values and R^2 values of the particle size distributions of $P(\rho HS\text{-}SA)_{100}$-*b*-$PAM_{200}$, $P(\rho HS\text{-}SA)_{50}$-*b*-$PAM_{100}$, $P(\rho HS\text{-}SA)_{100}$ and $P(\rho HS\text{-}SA)_{50}$ were (19±4)nm and 0.88 (Figure 6.31 d), (38±2)nm and 0.99 (Figure 6.31 e), (21±2)nm and 0.97 (figure 6.32 c), and (18±2)nm and 0.99 (figure 6.32 d), respectively.

For the particles size distribution of P(ρHS-SA)$_{50}$-*b*-PAM$_{200}$ (Figure 6.31 f), the counts numbers are too small to be statistically significant so it cannot be fitted with a distribution curve. It appeared to be a broad distribution from 30nm-160nm. The samples analysed by DLS were in aqueous state so hydrogen bonding interactions presented between the polymer chains (hydroxyl groups) and the aqueous solution. The SEM samples were prepared by air-drying method, the polymer nanoparticles lost hydrogen bonding interactions when dried. This might be the reason that the size of the nanoparticles decreased when analysed by SEM.

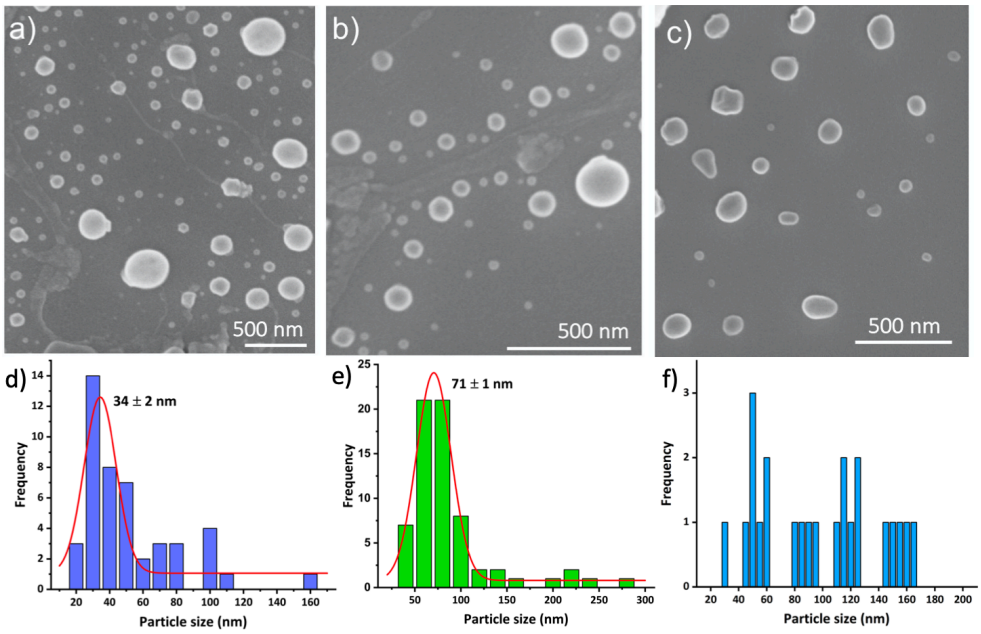

Figure 6. 31. SEM images of a) P(ρHS-SA)$_{100}$-*b*-PAM$_{200}$, b) P(ρHS-SA)$_{50}$-*b*-PAM$_{100}$ and c) P(ρHS-SA)$_{50}$-*b*-PAM$_{200}$, scale bars represent 500 nm; statistical analysis of d) P(ρHS-SA)$_{100}$-*b*-PAM$_{200}$, e) P(ρHS-SA)$_{50}$-*b*-PAM$_{100}$ and f) P(ρHS-SA)$_{50}$-*b*-PAM$_{200}$ nanoparticles determined by the SEM images.

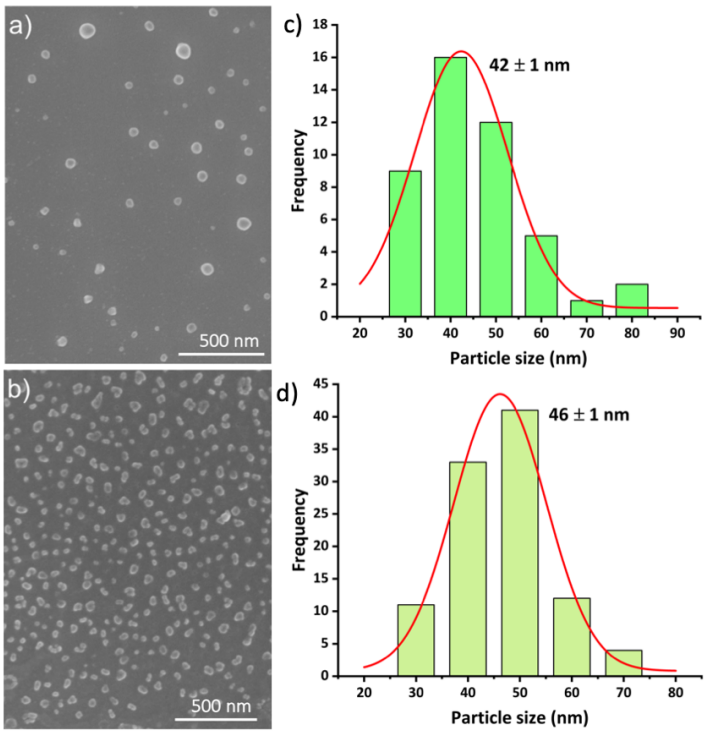

Figure 6. 32. SEM images of a) P(ρHS-SA)$_{100}$ and b) P(ρHS-SA)$_{50}$, scale bars represent 500 nm; statistical analysis of c) P(ρHS-SA)$_{100}$ and d) P(ρHS-SA)$_{50}$ nanoparticles determined by the SEM images.

P(ρHS-SA)$_{100}$, P(ρHS-SA)$_{50}$, P(ρHS-SA)$_{100}$-*b*-PAM$_{200}$, P(ρHS-SA)$_{50}$-*b*-PAM$_{100}$, P(ρHS-SA)$_{50}$-*b*-PAM$_{200}$ and P(ρHS-SA)$_{50}$-*co*-PAM$_{200}$ were not soluble in water. The colour of an azo compound may be majorly affected by its functional groups and resonance structures; minorly influenced by hydrogen bonds forming between the azo compound and a solvent that the azo compound can dissolve in [29-30]. P(ρHS-SA)$_{100}$, P(ρHS-SA)$_{50}$, P(ρHS-SA)$_{100}$-*b*-PAM$_{200}$, P(ρHS-SA)$_{50}$-*b*-PAM$_{100}$, P(ρHS-SA)$_{50}$-*b*-PAM$_{200}$ and P(ρHS-SA)$_{50}$-*co*-PAM$_{200}$ were soluble in concentrated sulfuric acid (H_2SO_4) and showed red colour. The dissociation of phenol-OH_2^+ to phenol-OH has a pKa of -6 [31] so the hydroxyl group cannot be protonated in concentrated sulfuric acid (pKa=-3). When the acid was added, the amine groups were protonated, and the resonance in sulfonamide was blocked (Scheme 6.8) [32]. Therefore, the chromophore in the polymers responsible for the colour is likely to be the resonance between phenol, azo bond and the aromatic ring conjugate to the sulfonamide, and the hydrogen bonds formed with aqueous acid [32]. Also, a number of literature reports suggest that azo compounds have a red colour because of the resonance between azo bonds and adjacent aromatic rings [32-35].

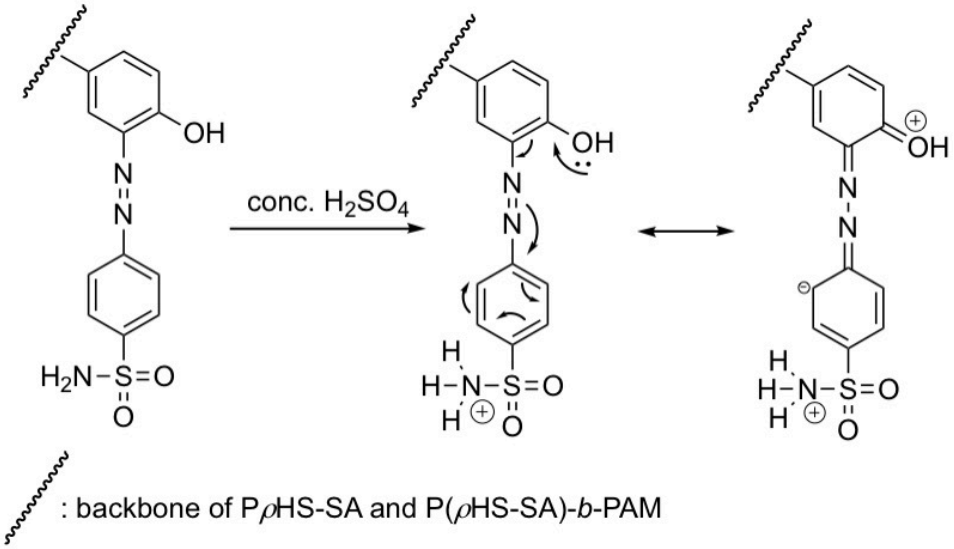

Scheme 6. 8. Sulfanilamide conjugated polymers in concentrated sulfuric acid.

Each of the SA-containing polymers was dissolved in concentrated H_2SO_4 to a concentration of 1.0 mg mL^{-1}, generating red solutions (Figure 6.33). In the UV-vis spectra, the peak maximums of P(ρHS-SA)$_{100}$, P(ρHS-SA)$_{50}$, P(ρHS-SA)$_{100}$-*b*-PAM$_{200}$, P(ρHS-SA)$_{50}$-*b*-PAM$_{200}$, P(ρHS-SA)$_{50}$-*co*-PAM$_{200}$ and P(ρHS-SA)$_{50}$-*b*-PAM$_{100}$ were 543 nm, 542 nm, 543 nm, 538 nm, 537 nm and 526 nm, respectively, which correspond to the green colour region (Figure 6.34). Visible light covers the range from approximately 400 nm to 800 nm. When white light passed through the red solution (samples), the light in the 490 nm-560 nm range was absorbed, showing the complementary colour (diametrically opposite) in human eyes which is indicated by the colour wheel (Figure 6.34) [36]. Therefore, the absorption of 490 nm-560 nm light renders a substance red. PρHS$_{100}$-SA had a stronger UV absorption than that of PρHS$_{50}$-SA because the hydroxystyrene chain of P(ρHS-SA)$_{100}$ was double that of P(ρHS-SA)$_{50}$, resulting in greater SA conjugation to PρHS$_{100}$. The UV absorption decreased from P(ρHS-SA)$_{100}$-*b*-PAM$_{200}$ to P(ρHS-SA)$_{50}$-*b*-PAM$_{200}$, P(ρHS-SA)$_{50}$-*co*-PAM$_{200}$, and P(ρHS-SA)$_{50}$-*b*-PAM$_{100}$. P(ρHS-SA)$_{100}$-*b*-PAM$_{200}$ had the longest PρHS chain (more SA conjugation and azo bonds) and consequently the most intense absorbance. P(ρHS-SA)$_{50}$-*b*-PAM$_{100}$ had the lowest UV absorption, possibly because the short PAM chains, forming less hydrogen bonds between the amide and aqueous acid solution [32].

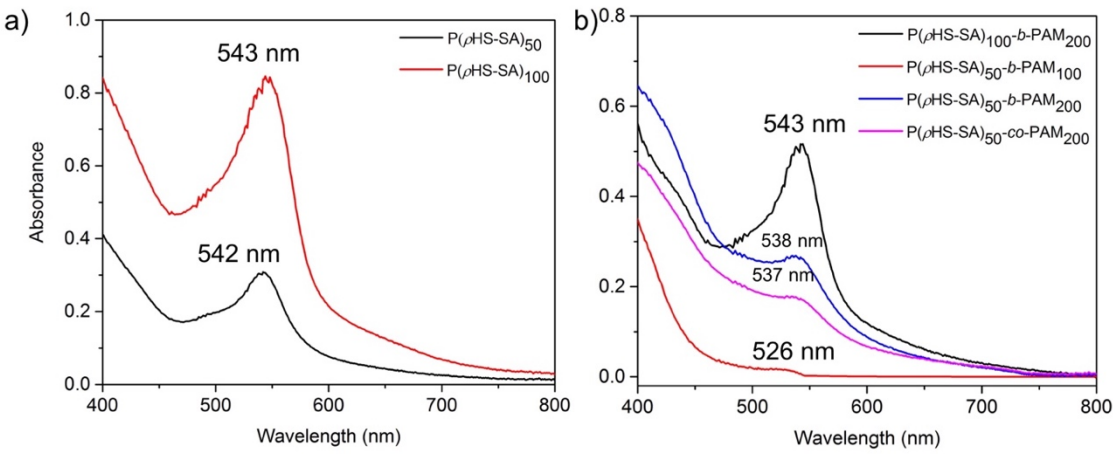

Polymers	P(ρHS-SA)$_{100}$	P(ρHS-SA)$_{50}$	P(ρHS-SA)$_{100}$-*b*-PAM$_{200}$	P(ρHS-SA)$_{50}$-*b*-PAM$_{200}$	P(ρHS-SA)$_{50}$-*co*-PAM$_{200}$	P(ρHS-SA)$_{50}$-*b*-PAM$_{100}$
Images						
pH values	0.12	0.16	0.11	0.14	0.17	0.19

Figure 6. 33. UV-vis spectra, appearances and pH values of P(ρHS-SA)$_{100}$, P(ρHS-SA)$_{50}$, P(ρHS-SA)$_{100}$-*b*-PAM$_{200}$, P(ρHS-SA)$_{50}$-*b*-PAM$_{200}$, P(ρHS-SA)$_{50}$-*co*-PAM$_{200}$ and P(ρHS-SA)$_{50}$-*b*-PAM$_{100}$ in concentrated sulfuric acid at a concentration of 1.0 mg mL^{-1}.

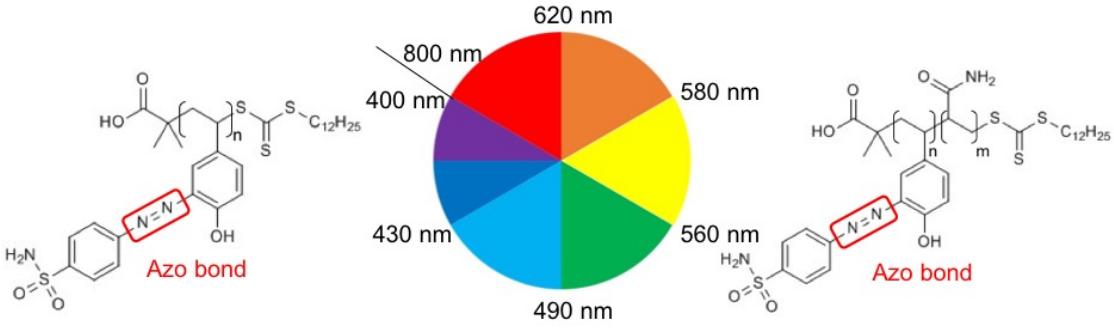

Figure 6. 34. Colour wheel and chemical structures of P(ρHS-SA)$_n$ and P(ρHS-SA)$_n$-*b*-PAM$_m$.

P(ρHS-SA)$_{100}$, P(ρHS-SA)$_{50}$, P(ρHS-SA)$_{100}$-*b*-PAM$_{200}$, P(ρHS-SA)$_{50}$-*b*-PAM$_{100}$, P(ρHS-SA)$_{50}$-*b*-PAM$_{200}$ and P(ρHS-SA)$_{50}$-*co*-PAM$_{200}$ acidic solutions (red) were neutralised with 1M potassium hydroxide (KOH) solution to pH 7.4 approximately, producing potassium sulfate, water and colourless solution [37]. For the polymers discussed above, the resonance in the sulfonamide became unblocked (Scheme 6.9) and so electrons migrated between phenol, azo bond and benzenesulfonamide functional groups. At this point, the electrons in the sulfonamide could move to the adjacent aromatic ring

(resonance), resulting in weakening the polymer solution colour and rendering the solution colourless. [29, 37].

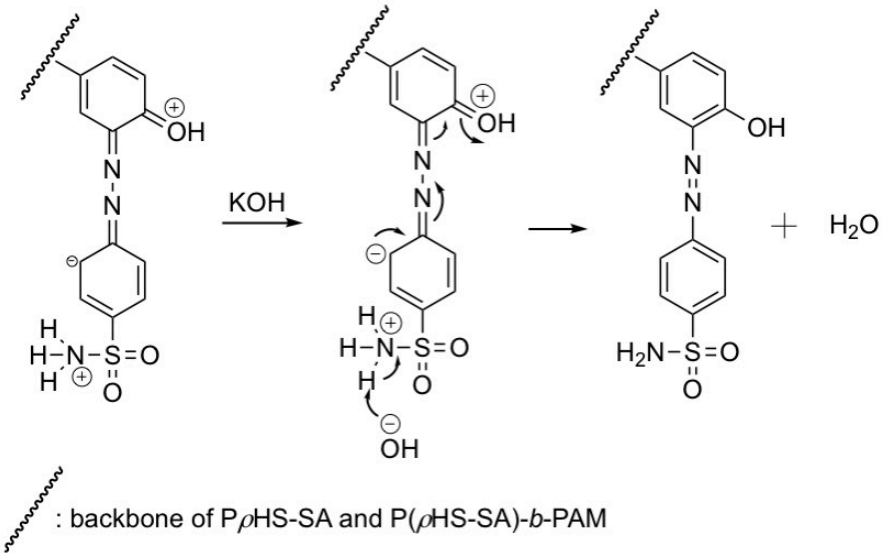

Scheme 6. 9. Sulfanilamide conjugated polymers in neutral environment.

As more of KOH solution was added until the pH value became approximately 13, the colour of the solution changed to pale yellow [38] and the UV-vis spectra revealed a limited increase in peak intensity from 400 nm to 420 nm. When excess KOH was added, there were a great amount of hydroxide ions in the solution and the amine and the hydroxyl groups were deprotonated. The resonance between the sulfonamide and the phenol groups of the polymers (Scheme 6.10) was stronger compared to that in approximately pH 7.4 solution. Therefore, the chromophore in the polymers has strong resonance between the sulfonamide and the phenol groups. The UV absorption from 400 nm to 420 nm in the violet and indigo region, the complementary colour is yellow so P(ρHS-SA)$_{100}$, P(ρHS-SA)$_{50}$, P(ρHS-SA)$_{100}$-*b*-PAM$_{200}$, P(ρHS-SA)$_{50}$-*b*-PAM$_{100}$, P(ρHS-SA)$_{50}$-*b*-PAM$_{200}$ and P(ρHS-SA)$_{50}$-*co*-PAM$_{200}$ in alkaline solution were pale yellow to human eyes.

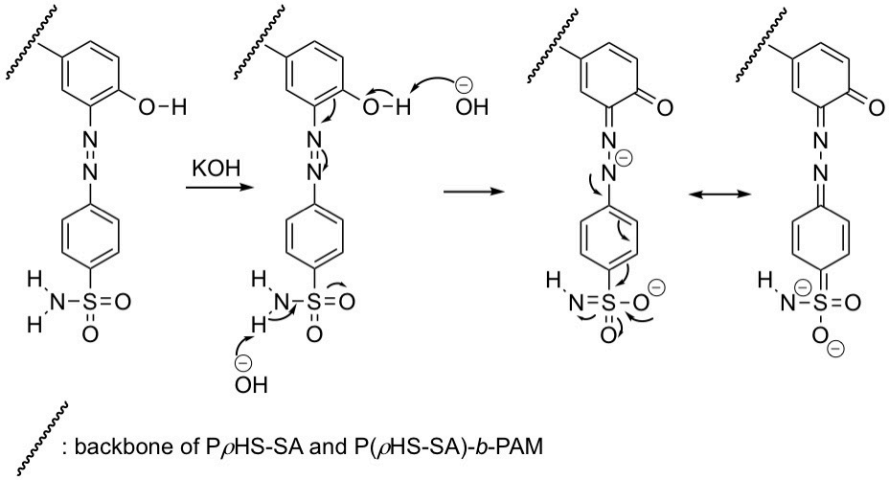

Scheme 6. 10. Sulfanilamide conjugated polymers in potassium hydroxide.

Concentrated H_2SO_4 was added again until the solution pH values became approximately pH 0.6. All of the pale yellow (alkaline) solution changed to orange red solution and absorption in the 490 nm-560 nm region appeared again on the UV-vis spectra (Figures 6.35-6.37). The UV absorbance peaks of P(ρHS-SA)$_{100}$, P(ρHS-SA)$_{50}$, P(ρHS-SA)$_{100}$-*b*-PAM$_{200}$, P(ρHS-SA)$_{50}$-*b*-PAM$_{100}$, P(ρHS-SA)$_{50}$-*b*-PAM$_{200}$ and P(ρHS-SA)$_{50}$-*co*-PAM$_{200}$ upon the polymers returning to acidic solutions were 540 nm, 528 nm, 537 nm, 524 nm, 540 nm and 540 nm, respectively. As more acid was added, the hydroxide ions (from KOH) were further neutralised and excess hydrogen ions formed in the solution, protonating the amine group. For the polymers discussed above, the resonance in the sulfonamide was blocked again (Scheme 6.11) so the chromophores of the polymers were the resonance between phenol, azo bond, the aromatic ring adjacent to the sulfonamide, and the hydrogen bond formed with concentrated H_2SO_4, the colour of the solution became to orange red.

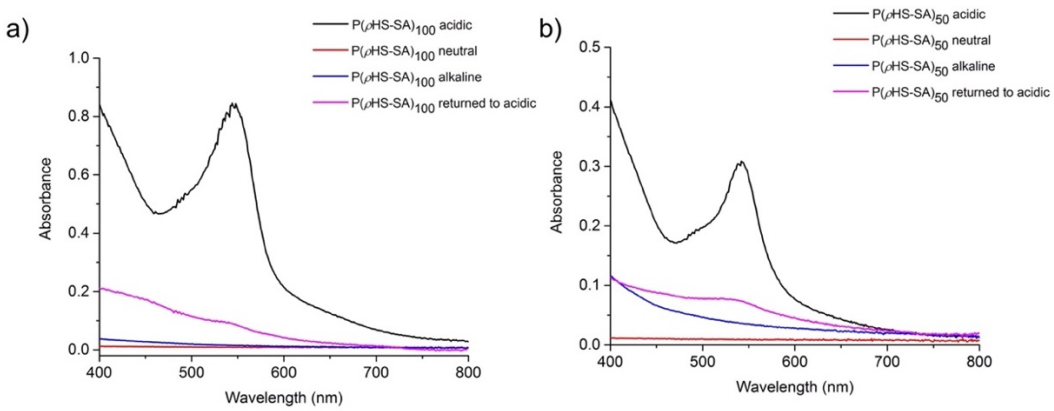

P(ρHS-SA)$_{100}$	Acidic	Neutral	Alkaline	Returned to acidic
Images				
pH values	0.12	7.35	13.33	0.60

P(ρHS-SA)$_{50}$	Acidic	Neutral	Alkaline	Returned to acidic
Images				
pH values	0.16	7.43	13.39	0.62

Figure 6. 35. UV-vis spectra, appearances and pH values of a) P(ρHS-SA)$_{100}$, b) P(ρHS-SA)$_{50}$ in the environments of acidic, neutral, alkaline and returned to acidic.

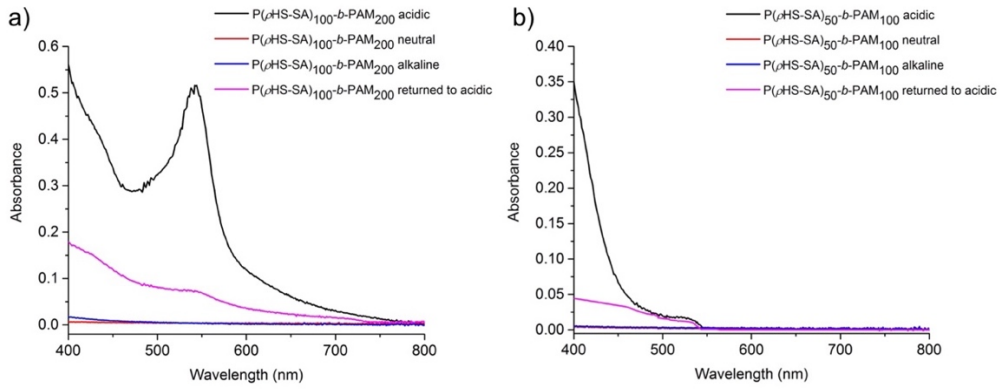

P(ρHS-SA)$_{100}$-*b*-PAM$_{200}$	Acidic	Neutral	Alkaline	Returned to acidic
Images				
pH values	0.11	7.52	13.12	0.67

P(ρHS-SA)$_{50}$-*b*-PAM$_{100}$	Acidic	Neutral	Alkaline	Returned to acidic
Images				
pH values	0.14	7.53	13.19	0.65

Figure 6. 36. UV-vis spectra, appearances and pH values of a) P(ρHS-SA)$_{100}$-*b*-PAM$_{200}$, b) P(ρHS-SA)$_{50}$-*b*-PAM$_{100}$ in the environments of acidic, neutral, alkaline and returned to acidic.

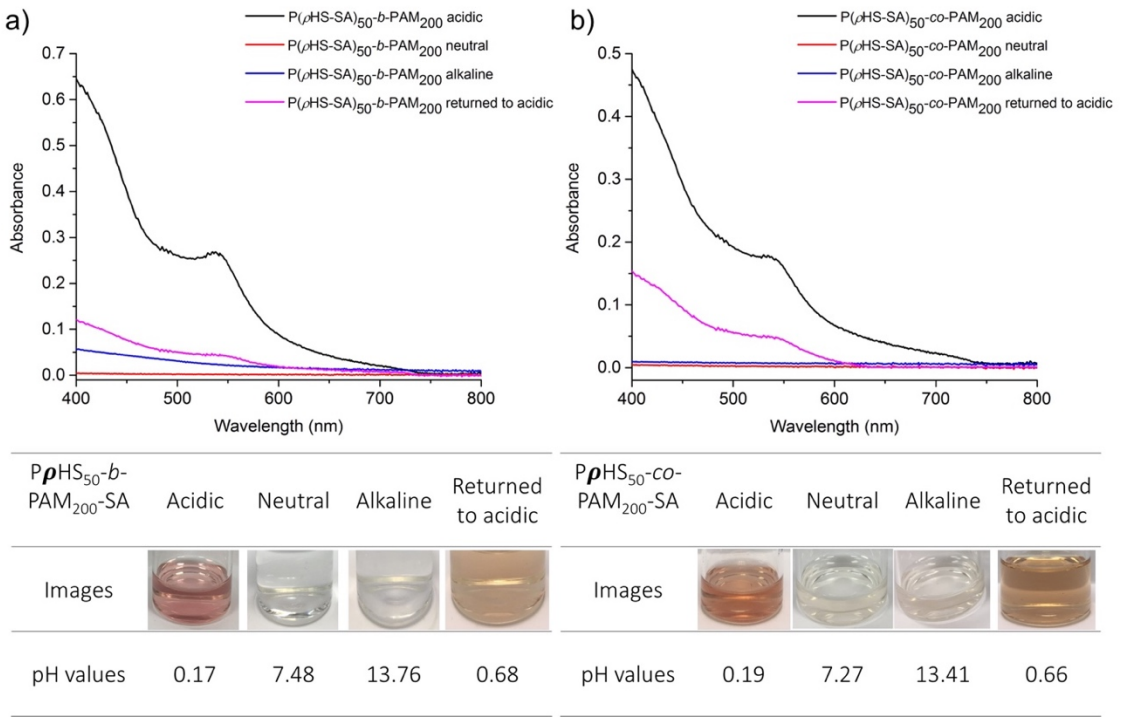

PρHS$_{50}$-*b*-PAM$_{200}$-SA	Acidic	Neutral	Alkaline	Returned to acidic
Images				
pH values	0.17	7.48	13.76	0.68

PρHS$_{50}$-*co*-PAM$_{200}$-SA	Acidic	Neutral	Alkaline	Returned to acidic
Images				
pH values	0.19	7.27	13.41	0.66

Figure 6. 37. UV-vis spectra, appearances and pH values of a) P(ρHS-SA)$_{50}$-*b*-PAM$_{200}$ and b) P(ρHS-SA)$_{50}$-*co*-PAM$_{200}$ in the environments of acidic, neutral, alkaline and returned to acidic.

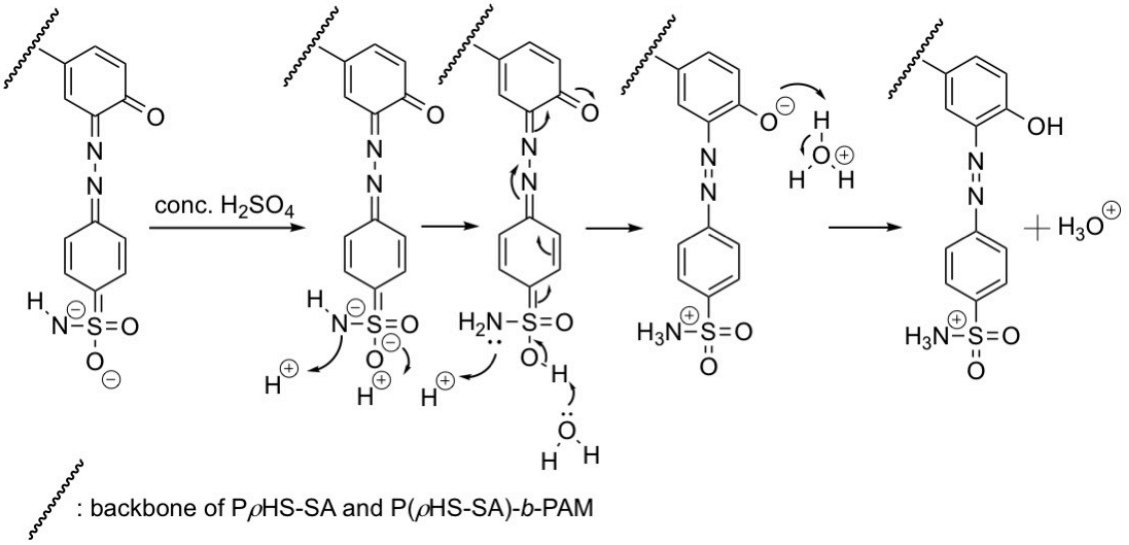

Scheme 6. 11. Sulfanilamide conjugated polymers returned to acidic environment.

These results suggest that P(ρHS-SA)$_{100}$, P(ρHS-SA)$_{50}$, P(ρHS-SA)$_{100}$-*b*-PAM$_{200}$, P(ρHS-SA)$_{50}$-*b*-PAM$_{100}$, P(ρHS-SA)$_{50}$-*b*-PAM$_{200}$ and P(ρHS-SA)$_{50}$-*co*-PAM$_{200}$ are pH-responsive (functional group (de)protonation) and pH-switchable (reversible solution colour change) due to protonation/deprotonation of the sulfonamide, deprotonation of the phenol groups and the related formation/prevention of resonance. The polymers formed a

solution of red colour in acid initially, that turned pale yellow in basic solution, and returned to an orange-red colour when the solution became acidic once more.

6.4. Conclusions

P(ρHS-SA)$_{100}$, P(ρHS-SA)$_{50}$, P(ρHS-SA)$_{100}$-*b*-PAM$_{200}$, P(ρHS-SA)$_{50}$-*b*-PAM$_{100}$, P(ρHS-SA)$_{50}$-*b*-PAM$_{200}$ and P(ρHS-SA)$_{50}$-*co*-PAM$_{200}$ were synthesised by RAFT polymerisation, subsequent acid hydrolysis of the acetoxy group of PACS to yield a hydroxyl group, and finally the azo coupling of SA to the phenol group. All of the polymers formed particles in aqueous solution. The PDI values of P(ρHS-SA)$_{100}$-*b*-PAM$_{200}$, P(ρHS-SA)$_{50}$-*b*-PAM$_{100}$ and P(ρHS-SA)$_{50}$-*b*-PAM$_{200}$ were less than 0.3 due to the hydrophilic PAM chain reducing polymer aggregation and enhancing nanoparticle stability in aqueous media. All of the polymers formed red solutions when dissolved in concentrated H_2SO_4 by protonating the amine group, the resonance in the sulfonamide was blocked. The resonance between phenol, azo bond and the adjacent aromatic ring were the chromophore responsible for the red colour. When KOH was added until the pH value was approximately 7.4, the acid was neutralised, the resonance in the sulfonamide became unblocked so electrons in sulfonamide can move to the conjugate aromatic ring, weakening the solution colour. The solution colour changed to colourless. As more of KOH added until pH value was around 13, the amine and the hydroxyl groups were deprotonated so the resonance between the phenol, the azo bond and the benzenesulfonamide became stronger compared to that at neutral state which changed the solution colour to pale yellow. When concentrated sulfuric acid was added again until pH value was approximately 0.6, the resonance in the sulfonamide was blocked. The solution colour changed to orange red due to the resonance between phenol, azo bond and the adjacent aromatic ring. The polymers are pH-responsive, demonstrating a reversible pH-mediated switch in colour due to the protonation/deprotonation of the sulfonamide, deprotonation of the phenol groups, and the related changes to the resonance present. In order to confirm the colour change is caused by the mechanism discussed above, ^{13}C NMR analysis may be performed. The SA group present may render the particles formed as being antimicrobial materials, therefore, antimicrobial studies form the next step of the research.

6.5. References

1. Wang, R., Zhou, B., Xu, D.L., Xu, H., Liang, L., Feng, X.H., Ouyang, P.K. and Chi, B. Antimicrobial and biocompatible epsilon-polylysine-gamma-poly(glutamic acid)-based hydrogel system for wound healing. *Journal of Bioactive and Compatible Polymers.* 2016, **31**(3), pp.242-259.
2. Shen, W., He, P., Xiao, C.S. and Chen, X.S. From Antimicrobial Peptides to Antimicrobial Poly(alpha-amino acid)s. *Advanced Healthcare Materials*. 2018, **7**(20), 1800354.
3. Pola, C.C., Moraes, A.R.F., Medeiros, E.A.A., Teofilo, R.F., Soares, N.F.F. and Gomes, C.L. Development and optimization of pH-responsive PLGA-chitosan nanoparticles for triggered release of antimicrobials. *Food Chemistry*. 2019, **295**, pp.671-679.
4. Wang, C.Y., Zolotarskaya, O., Ashraf, K.M., Wen, X.J., Ohman, D.E. and Wynne, K.J. Surface Characterization, Antimicrobial Effectiveness, and Human Cell Response for a Biomedical Grade Polyurethane Blended with a Mixed Soft Block PTMO-Quat/PEG Copolyoxetane Polyurethane. *Acs Applied Materials & Interfaces*. 2019, **11**(23), pp.20699-20714.
5. Alvarez-Paino, M., Munoz-Bonilla, A. and Fernandez-Garcia, M. Antimicrobial Polymers in the Nano-World. *Nanomaterials.* 2017, **7**(2), 48.
6. Timofeeva, L. and Kleshcheva, N. Antimicrobial polymers: mechanism of action, factors of activity, and applications. *Applied Microbiology and Biotechnology.* 2011, **89**(3), pp.475-492.
7. Chen, S.S., Wang, C.H., Zhang, M., Zhang, W.X., Qi, J.W., Sun, X.Y., Wang, L.J. and Li, J.S. N-doped Cu-MOFs for efficient electrochemical determination of dopamine and sulfanilamide. *Journal of Hazardous Materials.* 2020, **390**, 122157.
8. Kumar, N., Wang, W.J., Ortiz-Marquez, J.C., Catalano, M., Gray, M., Biglari, N., Hikari, K., Ling, X., Gao, J.M., van Opijnen, T. and Burch, K.S. Dielectrophoresis assisted rapid, selective and single cell detection of antibiotic resistant bacteria with G-FETs. *Biosensors & Bioelectronics.* 2020, **156**, 112123.
9. Zhao, L., Liu, Y., Zhang, Z.L., Wei, J.J., Xie, S.Z. and Li, X.H. Fibrous testing papers for fluorescence trace sensing and photodynamic destruction of antibiotic-resistant bacteria. *Journal of Materials Chemistry B.* 2020, **8**(13), pp.2709-2718.
10. Feng, T.Y., Ren, F., Fang, Q., Dai, G.C., Li, Y., Li, Q., Xi, H.M., Li, H., Hao, Y.Y. and Hu, J.H. Effects of sulfanilamide on boar sperm quality, bacterial composition, and fertility during liquid storage at 17 degrees C. *Animal Science Journal*. 2019, **90**(9), pp.1161-1169.
11. Sui, Y.F., Li, D., Wang, J., Bheemanaboina, R.R.Y., Ansari, M.F., Gan, L.L. and Zhou, C.H. Design and biological evaluation of a novel type of potential multi-targeting antimicrobial sulfanilamide hybrids in combination of pyrimidine and azoles. *Bioorganic & Medicinal Chemistry Letters*. 2020, **30**(6), 126982.
12. Timofeeva, L. and Kleshcheva, N. Antimicrobial polymers: mechanism of action, factors of activity, and applications. *Applied Microbiology and Biotechnology.* 2011, **89**(3), pp.475-492.
13. Siedenbiedel, F. and Tiller, J.C. Antimicrobial Polymers in Solution and on Surfaces: Overview and Functional Principles. *Polymers.* 2012, **4**(1), pp.46-71.
14. Engler, A.C., Wiradharma, N., Ong, Z.Y., Coady, D.J., Hedrick, J.L. and Yang, Y.Y. Emerging trends in macromolecular antimicrobials to fight multi-drug-resistant infections. *Nano Today.* 2012, **7**(3), pp.201-222.
15. Krumm, C., Harmuth, S., Hijazi, M., Neugebauer, B., Kampmann, A.L., Geltenpoth, H., Sickmann, A. and Tiller, J.C. Antimicrobial Poly(2-methyloxazoline) s with Bioswitchable Activity through Satellite Group Modification. *Angewandte Chemie-International Edition.* 2014, **53**(15), pp.3830-3834.

16. Alsughayer, A., Elassar, A.Z.A., Al Sagheer, F. and Mustafa, S. Synthesis and characterization of polysulfanilamide and its copolymers: bioactivity and drug release. *Pharmaceutical Chemistry Journal.* 2012, **46**(7), pp.418-428.
17. Esen, N., Shuffield, D., Syed, M.M. and Kiellan, T. Modulation of connexin expression and gap junction communication in astrocytes by the gram-positive bacterium S-aureus. *Glia.* 2007, **55**(1), pp.104-117.
18. Reddy, C.U., Arun, A., Amalraj, A. and Reddy, B.S.R. Polymeric drug based on sulfanilamide: synthesis, antimicrobial and drug releasing studies. *Journal of Pharmacy and Pharmacology.* 2007, **59**(9), pp.1207-1213.
19. Florea, M.G., Nedelcu, I.A., Ungureanu, C., Ficai, A., Ficai, D., Guran, C. and Andronescu, E. Alginate and Sulfanilamide Based DDS with Antibacterial Activity. *International Journal of Polymeric Materials and Polymeric Biomaterials.* 2014, **63**(2), pp.92-96.
20. Ganesh, M., Aziz, A.S., Ubaidulla, U., Hemalatha, P., Saravanakumar, A., Ravikumar, R., Peng, M.M., Choi, E.Y. and Jang, H.T. Sulfanilamide and silver nanoparticles-loaded polyvinyl alcohol-chitosan composite electrospun nanofibers: Synthesis and evaluation on synergism in wound healing. *Journal of Industrial and Engineering Chemistry*. 2016, **39**, pp.127-135.
21. Nejaddehbashi, F., Hashemitabar, M., Bayati, V., Moghimipour, E., Movaffagh, J., Orazizadeh, M. and Abbaspour, M. Incorporation of Silver Sulfadiazine into An Electrospun Composite of Polycaprolactone as An Antibacterial Scaffold for Wound Healing in Rats. *Cell Journal.* 2020, 21(4), pp.379-390.
22. Ali, I., Shah, M.R., Yousuf, S., Ahmed, A., Shah, K. and Javed, I. Hemolytic and cellular toxicology of a sulfanilamide-based nonionic surfactant: a niosomal carrier for hydrophobic drugs. *Toxicology Research*. 2018, **7**(5), pp.771-778.
23. Rathee, J., Kanwar, R., Kaushik, D., Salunke, D.B. and Mehta, S.K. Niosomes as efficient drug delivery modules for encapsulation of Toll-like receptor 7 agonists and IDO-inhibitor. *Applied Surface Science.* 2020, **505**, 144078.
24. Ozturk, A.A., Yenilmez, E. and Ozarda, M.G. Clarithromycin-Loaded Poly (Lactic-co-glycolic Acid) (PLGA) Nanoparticles for Oral Administration: Effect of Polymer Molecular Weight and Surface Modification with Chitosan on Formulation, Nanoparticle Characterization and Antibacterial Effects. *Polymers.* 2019, **11**(10), 1632.
25. Kanagasabapathy, S., Sudalai, A. and Benicewicz, B.C. Reversible addition-fragmentation chain-transfer polymerization for the synthesis of poly(4-acetoxystyrene) and poly(4-acetoxystyrene)-block-polystyrene by bulk, solution and emulsion techniques. *Macromolecular Rapid Communications.* 2001, **22**(13), pp.1076-1080.
26. Harrison, M.A.J., Barra, S., Borghesi, D., Vione, D., Arsene, C. and Olariu, R.L. Nitrated phenols in the atmosphere: a review. *Atmospheric Environment.* 2005, **39**(2), pp.231-248.
27. Warren, N.J., Mykhaylyk, O.O., Mahmood, D., Ryan, A.J. and Armes, S.P. RAFT Aqueous Dispersion Polymerization Yields Poly(ethylene glycol)-Based Diblock Copolymer Nano-Objects with Predictable Single Phase Morphologies. *Journal of the American Chemical Society.* 2014, **136**(3), pp.1023-1033.
28. Chen, X.K., Wang, H.L., Doitomi, K., Ooi, C.Y., Zheng, P.C., Liu, W.S., Guo, H., Yang, S., Song, B.A., Hirao, H. and Chi, Y.G.R. A reaction mode of carbene-catalysed aryl aldehyde activation and induced phenol OH functionalization. *Nature Communications.* 2017, **8**, pp.1-8.
29. Kumler, W.D. and Strait, L.A. The ultraviolet absorption spectra and resonance in benzene derivatives - Sulfanilamide, metanilamide, p-aminobenzoic acid, benzenesulfonamide, benzoic acid aniline. *Journal of the American Chemical Society.* 1943, **65**, pp.2349-2354.

30. Ahmed, S., Owen, C.P., James, K., Patel, C.K. and Patel, M. Acid dissociation constant, a potential physicochemical factor in the inhibition of the enzyme estrone sulfatase (ES). *Bioorganic & Medicinal Chemistry Letters.* 2001, **11**(7), pp.899-902.
31. Benkhaya, S., M'Rabet, S. and El Harfi, A. Classifications, properties, recent synthesis and applications of azo dyes. *Heliyon.* 2020, **6**(1), p.26.
32. Girard, P., Hemez, J., Silvestre, V., Labrugere, C., Lartigue, L., Duvail, J.L. and Ishow, E. Strong Color Tuning of Self-Assembled Azo-Derived Phosphonic Acids upon Hydrogen Bonding. *Chemphotochem.* 2017, **1**(1), pp.6-11.
33. Wang, Q., Liang, L.P., Xi, F.F., Tian, G.L., Mao, Q.L. and Meng, X. Adsorption of Azo Dye Acid Red 73 onto Rice Wine Lees: Adsorption Kinetics and Isotherms. *Advances in Materials Science and Engineering.* 2020, **2020**.
34. Roy, U., Das, P. and Bhowal, A. Treatment of azo dye (congo red) solution in fluidized bed bioreactor with simultaneous approach of adsorption coupled with biodegradation: optimization by response surface methodology and toxicity assay. *Clean Technologies and Environmental Policy.* 2019, **21**(8), pp.1675-1686.
35. Lark, D., Buzzo, A.J.D., Garcia, J.A.A., Correa, V.G., Helm, C.V., Correa, R.C.G., Peralta, R.A., Moreira, R., Bracht, A. and Peralt, R.M. Enzymatic degradation and detoxification of azo dye Congo red by a new laccase from Oudemansiella canarii. *Bioresource Technology.* 2019, **289**, 121655.
36. Ndjiongue, A.R., Ngatched, T.M.N. and Ferreira, H.C. APSK-CSK Systems Based on Kite and Color Wheel Constructions. *Ieee Systems Journal.* 2019, **13**(3), pp.2396-2407.
37. Wang, G.F., Satake, M. and Horita, K. Spectrophotometric determination of nitrate and nitrite in water and some fruit samples using column preconcentration. *Talanta.* 1998, **46**(4), pp.671-678.
38. Khalil, R.A., Jalil, A.H. and Abd-Alrazzak, A.Y. Application of a Schiff Base Derived from Sulfanilamide as an Acid-Base Indicator. *Journal of the Iranian Chemical Society.* 2009, **6**(2), pp.345-352.

Overall Summary and Future work

This PhD thesis has demonstrated a variety of thermoresponsive and pH-responsive polymer nanoparticles synthesised by RAFT polymerisation and NCA ROP which may be employed as drug delivery vehicles or as antimicrobial agents.

In chapter 6, polymers that have potential application as antimicrobial materials were reported. The antimicrobial activity of SA-modified P(ρHS)-*b*-PAM nanoparticles can be tested against *S. aureus* and *E. coli* as immediate future work. The azo bonds within the SA-modified P(ρHS)-*b*-PAM nanoparticles may be broken by azoreductase enzymes secreted by bacterial strains such as *Clostridium perfringens*, *Bacillus species*, *Enterococcus faecalis* and *Enterococcus faecium* (Scheme F1) [1]. Initially, SA-modified P(ρHS)-*b*-PAM nanoparticles can be prepared and tested against azoreductase and a control, non-selective, enzyme. Upon a positive result, the same nanoparticles can be tested against bacterial cultures, such as those stated above. Polymer-free bacterial cultures and sterile broths can act as positive and negative controls, respectively [2]. Details of antimicrobial tests are described in reference [2].

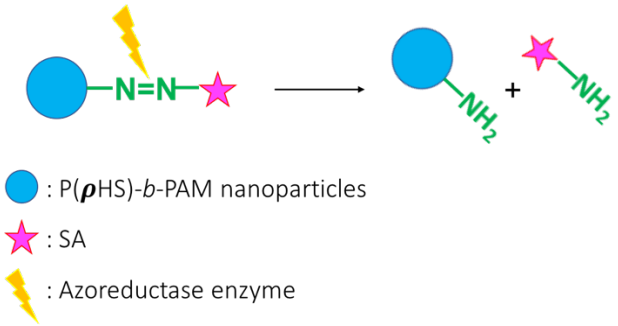

Scheme F 1. Schematic diagram of azo bond cleavage to release SA from SA-modified polymer nanoparticles.

Nanoparticles that have potential application for mouse tumour model studies are reported in chapter 3-5. For instance, aqueous Dox-loaded and without loaded $PSar_{136}$-*b*-$PHPMA_5$ and $PBLG_{26}$-*b*-PEG_{113} nanoparticles (the nanoparticles disperse in PBS buffer solution) can be injected via a mouse tail vein. An appropriate volume range is from 40μL to 100 μL, with various concentrations of nanoparticles included [3]. As mouse tumour may has a slightly higher temperature (≈41 °C) and in an acidic environment (pH 6.5),

Dox release is envisaged to occur selectively [4]; when internalised by cancer cells, Dox from $PSar_{136}$-*b*-$PHPMA_5$ and $PBLG_{26}$-*b*-PEG_{113} nanoparticles may be slowly released and kills cancer for long time tumour exposures of Dox. After Dox is released, $PSar_{136}$-*b*-$PHPMA_5$ (11600 g mol^{-1}) and $PBLG_{26}$-*b*-PEG_{113} (9142 g mol^{-1}) are break down and have sufficiently small molecular weights to enable their clearance via the kidney [4].

For fucose-$PHPMA_{100}$ nanoparticles (chapter 5), pancreatic cancer cell study can be developed further. Fucose conjugates to $PHPMA_{100}$ nanoparticles which may accumulate to pancreatic cancer cells and treat pancreatic cancer. KP4, PK-59, PK-45H, MIA PaCa-2, PANC-1 and HuCCT1 are pancreatic cell lines which can be obtained from the Riken BRC Cell Bank [5]. Free Dox can be used as a positive control. Fucose-$PHPMA_{100}$ nanoparticles are thermoresponsive and so Dox-loaded and blank fucose-$PHPMA_{100}$ nanoparticles can be assessed on KP4, PK-59, PK-45H, MIA PaCa-2, PANC-1 and HuCCT1 pancreatic cancer cells at 37 °C and 41 °C.

Murine models of cancer tumour study can be used to determine the effectiveness of Dox-loaded fucose-$PHPMA_{100}$ nanoparticles and Dox-loaded $PBLG_{26}$-*b*-PEG_{113} nanoparticles withheld in the $PHPMA_{200}$ depot. Nanoparticle/$PHPMA_{200}$ depot solutions can be intratumoral injected into murine pancreatic cancer tumour [6] and mice bearing human breast carcinoma xenografts, respectively [7]. The volume of injection can range from less than 10 μL to 100 μL [6]. In order to characterise the pancreatic and breast cancer therapy, the volume and weight of the pancreatic tumour and the breast tumour, and the weight of the mouse body and spleen can be measured at 7, 14 and 30 days for histopathologic tumour evaluation [6-7]. After Dox is released, $PHPMA_{200}$ depot (M_w=28455 g mol^{-1}) may not be metabolised and cleared from mouse body, but $PHPMA_{200}$ is biocompatible and non-toxic so it is not harmful to health. Alternatively, surgery may be used to remove the depot from the breast. For pancreas, no evidence shows the depot can be removed by surgery.

References

1. Rafii, F., Franklin, W. and Cerniglia, C.E. AZOREDUCTASE ACTIVITY OF ANAEROBIC-BACTERIA ISOLATED FROM HUMAN INTESTINAL MICROFLORA. *Applied and Environmental Microbiology.* 1990, **56**(7), pp.2146-2151.
2. Rowley JV, Wall P, Yu H, Tronci G, Devine DA, Vernon JJ, Thornton PD. Antimicrobial Dye-Conjugated Polyglobalide-Based Organogels. *ACS Applied Polymer Materials.* 2020.
3. Hillegass, J.M., Blumen, S.R., Cheng, K., MacPherson, M.B., Alexeeva, V., Lathrop, S.A., Beuschel, S.L., Steinbacher, J.L., Butnor, K.J., Ramos-Nino, M.E., Shukla, A., James, T.A., Weiss, D.J., Taatjes, D.J., Pass, H.I., Carbone, M., Landry, C.C. and Mossman, B.T. Increased efficacy of doxorubicin delivered in multifunctional microparticles for mesothelioma therapy. *International Journal of Cancer.* 2011, **129**(1), pp.233-244.
4. Eliasof, S., Lazarus, D., Peters, C.G., Case, R.I., Cole, R.O., Hwang, J., Schluep, T., Chao, J., Lin, J., Yen, Y., Han, H., Wiley, D.T., Zuckerman, J.E. and Davis, M.E. Correlating preclinical animal studies and human clinical trials of a multifunctional, polymeric nanoparticle. *Proceedings of the National Academy of Sciences of the United States of America.* 2013, **110**(37), pp.15127-15132.
5. Yoshida, M., Takimoto, R., Murase, K., Sato, Y., Hirakawa, M., Tamura, F., Sato, T., Iyama, S., Osuga, T., Miyanishi, K., Takada, K., Hayashi, T., Kobune, M. and Kato, J. Targeting Anticancer Drug Delivery to Pancreatic Cancer Cells Using a Fucose-Bound Nanoparticle Approach. *Plos One.* 2012, **7**(7), 39545.
6. Erstad, D.J., Sojoodi, M., Taylor, M.S., Ghoshal, S., Razavi, A.A., Graham-O'Regan, K.A., Bardeesy, N., Ferrone, C.R., Lanuti, M., Caravan, P., Tanabe, K.K. and Fuchs, B.C. Orthotopic and heterotopic murine models of pancreatic cancer and their different responses to FOLFIRINOX chemotherapy. *Disease Models & Mechanisms.* 2018, **11**(7).
7. Wolinsky, J.B., Colson, Y.L. and Grinstaff, M.W. Local drug delivery strategies for cancer treatment: Gels, nanoparticles, polymeric films, rods, and wafers. *Journal of Controlled Release.* 2012, **159**(1), pp.14-26.

List of publications

1. Yu, H.Y., Ingram, N., Rowley, J.V., Parkinson, S., Green, D.C., Warren, N.J. and Thornton, P.D. Thermoresponsive Polysarcosine-based Nanoparticles (vol 7, pg 4217, 2019). *Journal of Materials Chemistry B.* 2019, **7**(48), pp.7795-7795. https://pubs.rsc.org/en/content/articlelanding/2019/TB/C9TB00588A#!divAbstract
2. Yu, H.Y., Ingram, N., Rowley, J.V., Green, D.C. and Thornton, P.D. Meticulous Doxorubicin Release from pH-responsive Nanoparticles Entrapped within an Injectable Thermoresponsive Depot. *Chemistry-A European Journal*. 2020. https://chemistryeurope.onlinelibrary.wiley.com/doi/abs/10.1002/chem.202000389
3. Yu, H.Y., Rowley, J.V., Green, D.C. and Thornton, P.D. Fucose-modified thermoresponsive poly(2-hydroxypropyl methacrylate) nanoparticles for controlled doxorubicin release from an injectable depot. *Materials Advances.* 2020. https://pubs.rsc.org/en/content/articlehtml/2020/ma/d0ma00280a
4. Rowley, J.V., Exley, J., Yu, H.Y., Mircale, G.S., Hayward, A.S. and Thornton, P.D. Covalent polyester colouration by in situ chromophore creation. *Chemical Communications.* 2020, **56**(47), pp. 6360-6363. https://pubs.rsc.org/en/content/articlelanding/2020/CC/D0CC00653J#!divAbstract
5. Rowley, J.V., Wall, P., Yu, H.Y., Tronci, G., Devine, D.A., Vernon, J.J. and Thornton, P.D. Antimicrobial Dye-Conjugated Polyglobalide-Based Organogels. *Acs Applied Polymer Materials.* 2020, **2**(7), pp.2927-2933. https://pubs.acs.org/doi/10.1021/acsapm.0c00422

Appendix 3

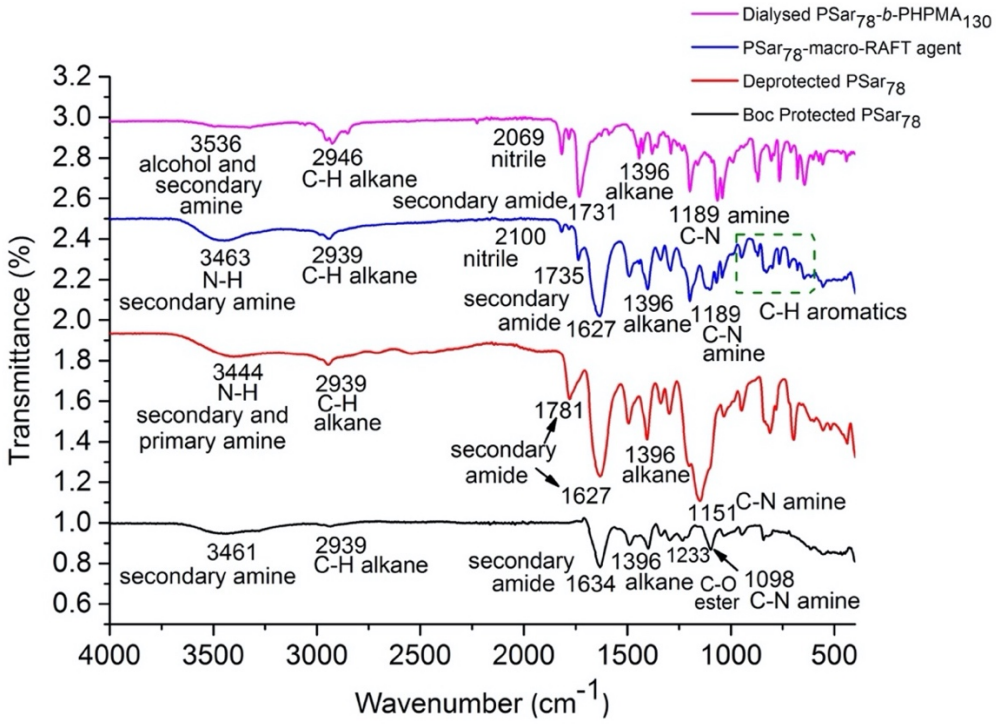

Figure A3.1. FTIR spectra of Boc-PSar$_{78}$, deprotected PSar$_{78}$, PSar$_{78}$-macro-RAFT agent and dialysed PSar$_{78}$-*b*-PHPMA$_{130}$.

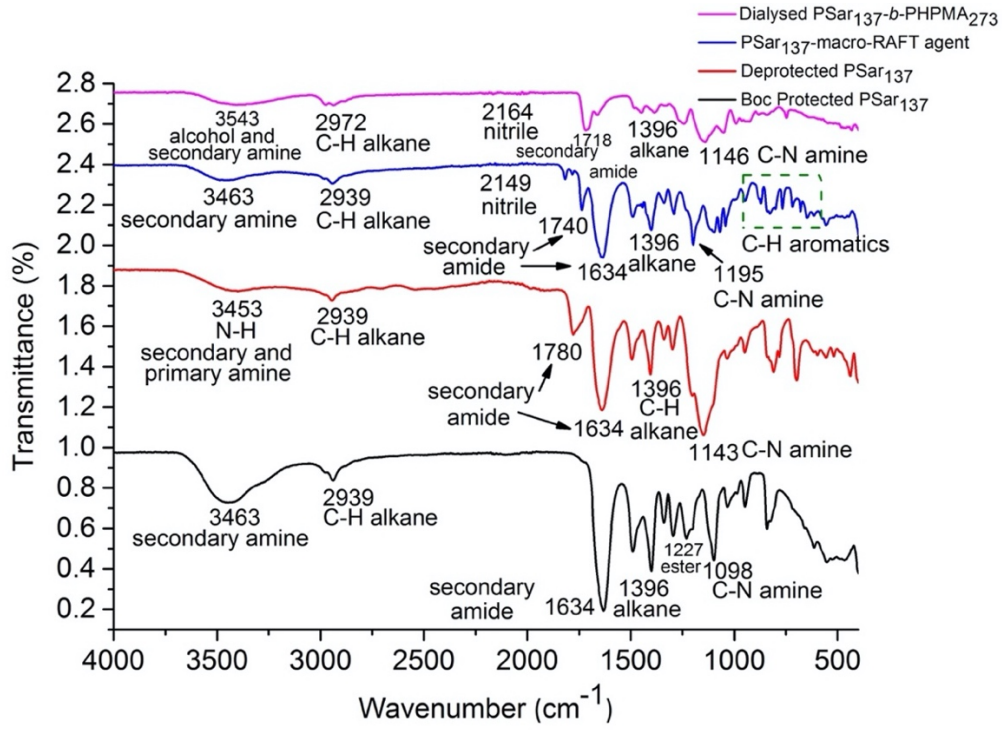

Figure A3.2. FTIR spectra of Boc-PSar$_{137}$, deprotected PSar$_{137}$, PSar$_{137}$-macro-RAFT agent and dialysed PSar$_{137}$-*b*-PHPMA$_{273}$.

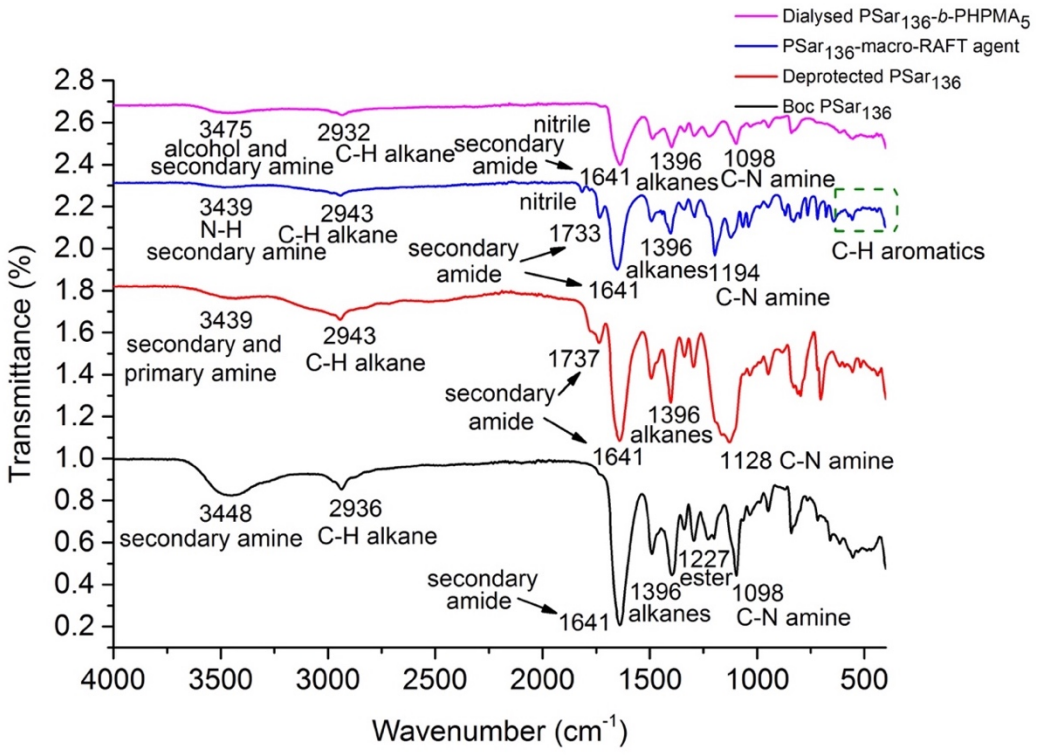

Figure A3.3. FTIR spectra of Boc protected $PSar_{136}$, deprotected $PSar_{136}$, $PSar_{136}$-macro-RAFT agent and dialysed $PSar_{136}$-*b*-$PHPMA_5$.

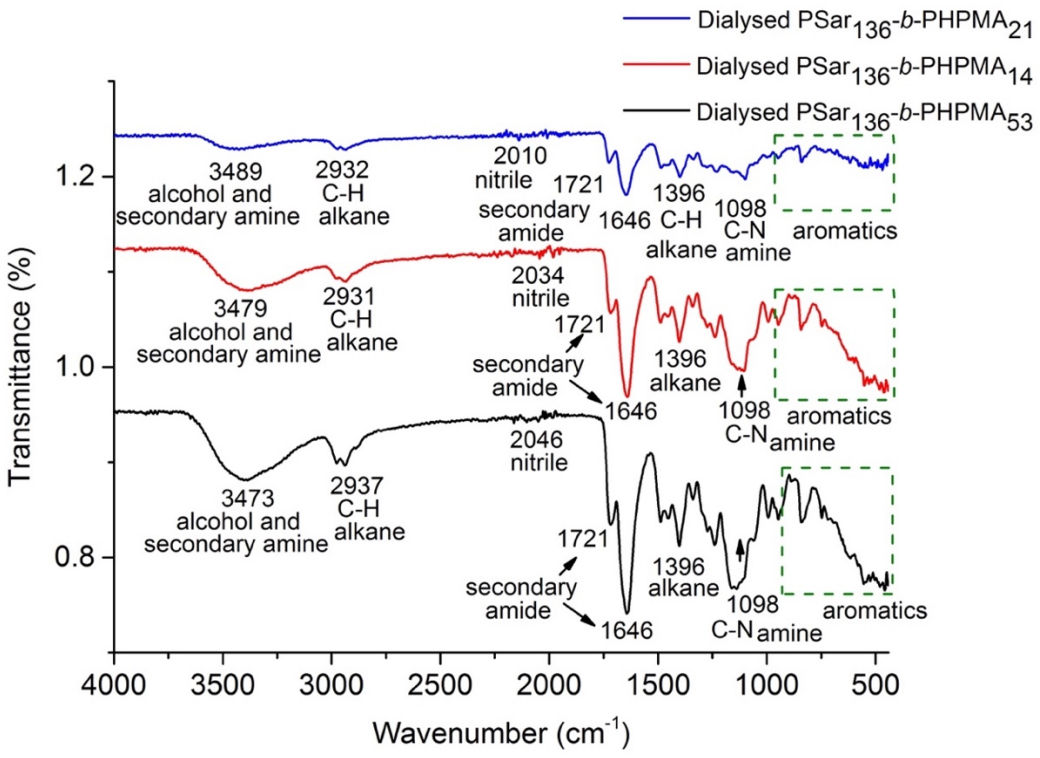

Figure A3.4. FTIR spectra of dialysed $PSar_{136}$-*b*-$PHPMA_{21}$, dialysed $PSar_{136}$-*b*-$PHPMA_{14}$ and dialysed $PSar_{136}$-*b*-$PHPMA_{53}$.

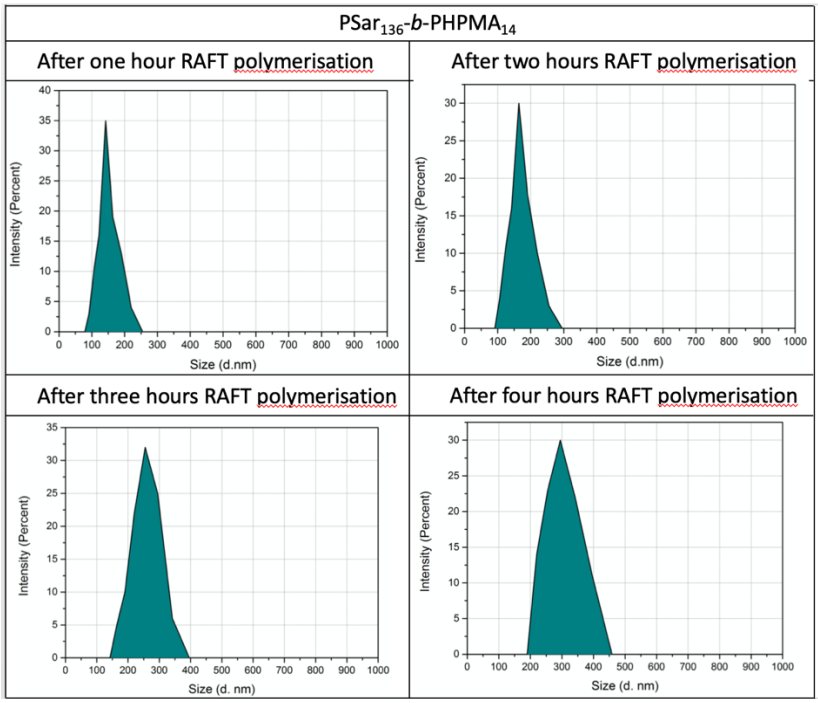

Figure A3.5. DLS distribution of $PSar_{136}$-*b*-$PHPMA_{14}$ during fours of polymerisation.

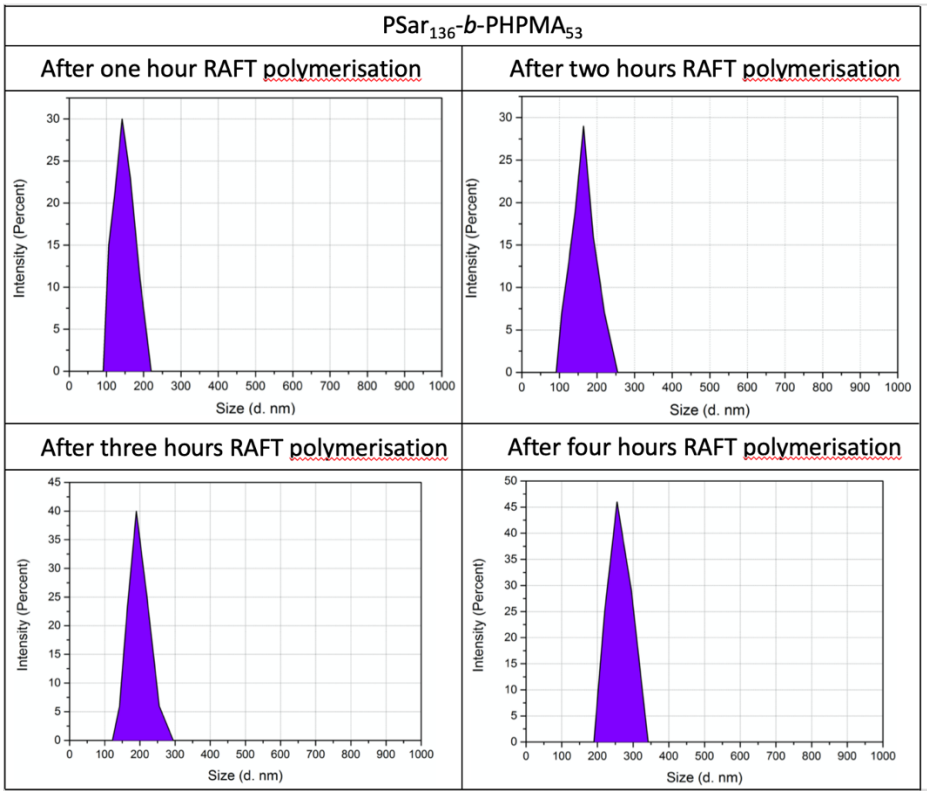

Figure A3.6. DLS distribution of $PSar_{136}$-*b*-$PHPMA_{53}$ during fours of polymerisation.

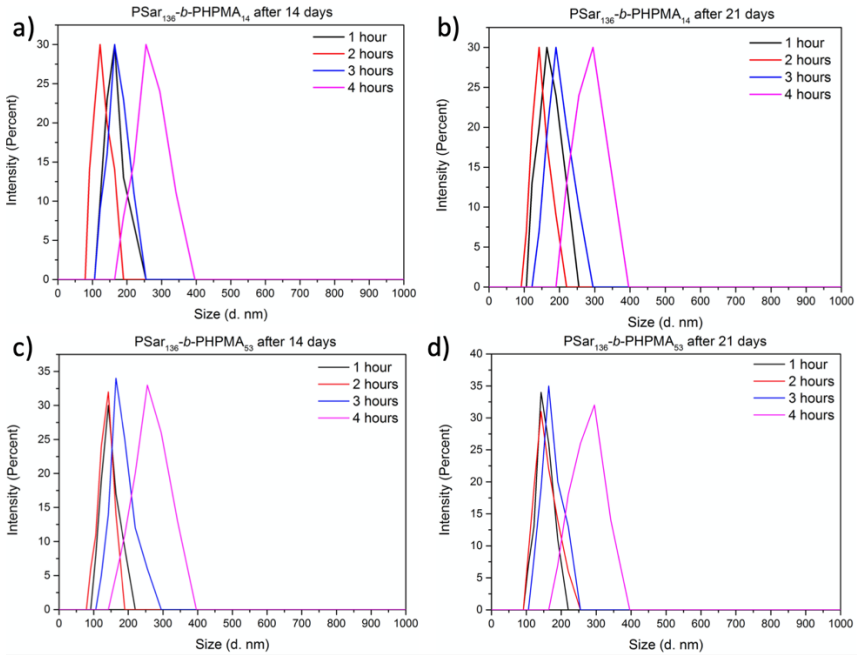

Figure A3.7. DLS analysis of a) $PSar_{136}$-*b*-$PHPMA_{14}$ after 14 days, b) $PSar_{136}$-*b*-$PHPMA_{14}$ after 21 days, c) $PSar_{136}$-*b*-$PHPMA_{53}$ after 14 days, and d) $PSar_{136}$-*b*-$PHPMA_{53}$ after 21 days, during four hours polymerisation.

Dr. Sam Parkinson performed GPC analysis for $PSar_{136}$-*b*-$PHPMA_5$ and $PSar_{136}$-*b*-$PHPMA_{21}$. The zoomed in peaks were responsible for $PSar_{136}$-*b*-$PHPMA_5$ (Figure A3.8) and $PSar_{136}$-*b*-$PHPMA_{21}$ (Figure A3.9). The peaks at approximately 21 minutes were solvent (DMF) peaks in both graphs. There were other small peaks on Figures A3.8-3.9, which might be unknown compounds stuck on GPC columns.

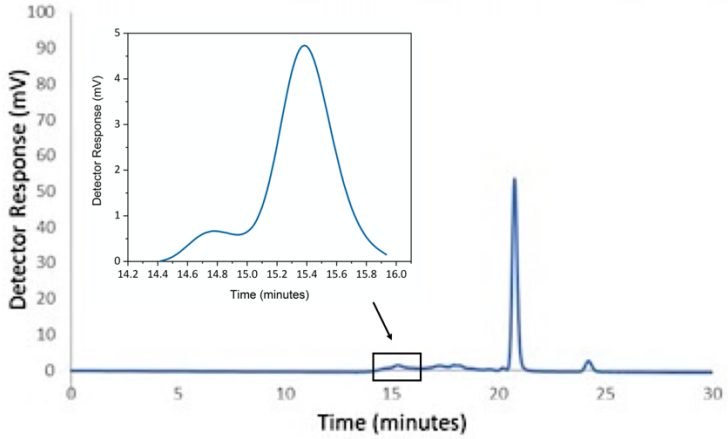

Figure A3.8. GPC chromatogram corresponding to $PSar_{136}$-*b*-$PHPMA_5$.

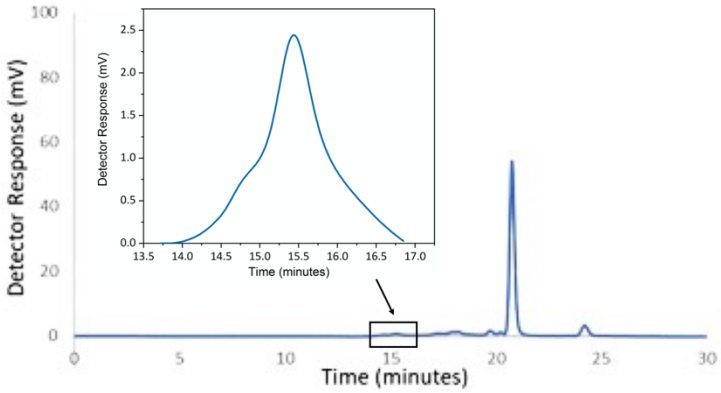

Figure A3.9. GPC chromatogram corresponding to $PSar_{136}$-*b*-$PHPMA_{21}$.

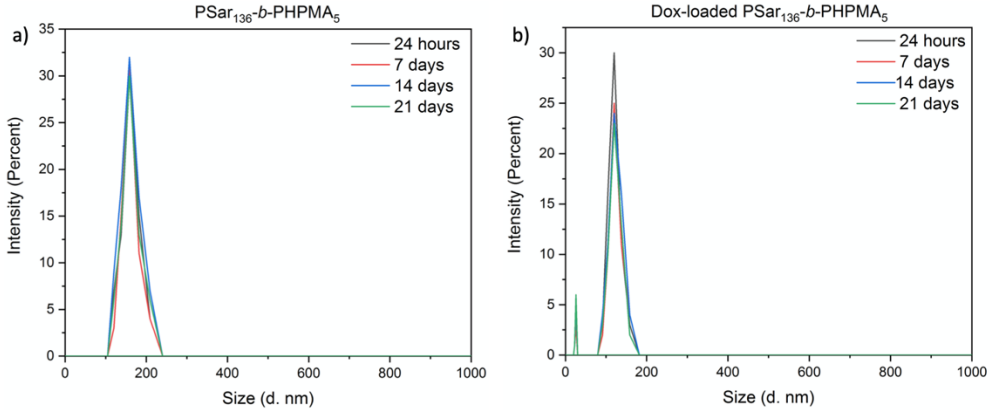

Figure A3.10. DLS analysis of a) $PSar_{136}$-*b*-$PHPMA_5$ and Dox-loaded $PSar_{136}$-*b*-$PHPMA_5$ nanoparticles in deionised water after 24 hours, 7 days, 14 days and 21 days.

Table A3.1. A comparison of Dox-loaded and unloaded $PSar_{136}$-*b*-$PHPMA_5$ nanoparticle sizes at room temperature, 37 °C and 50 °C.

Polymer	Size (nm)	PDI
$PSar_{136}$-*b*-$PHPMA_5$ without Dox loaded at room temperature	166 ± 14	0.218
At 37 °C	164 ± 19	0.261
At 50 °C	132 ± 16	0.215
$PSar_{136}$-*b*-$PHPMA_5$ with Dox loaded at room temperature	161 ± 22	0.240
At 37 °C	130 ± 28	0.389
At 50 °C	91 ± 25	0.468

Dox Loading of Nanoparticles

3.0 mg of Dox was dissolved in 20.0 µL of triethylamine and 3.0 mL of chloroform, and stirred for 4 hours in dark (bright red solution). 2.0 mg of $PSar_{136}$-*b*-$PHPMA_5$ was

dissolved in 1.0 mL of DMF (colourless solution). The polymer solution was then added dropwise into 9.78 mL of PBS buffer or acetate buffer (pH 5) (colourless solution). Dox solution was added dropwise into the polymer solution to yield a final volume of 10.8 mL (bright red solution).

The Dox concentration for each sample was

$$\frac{3.0\ mg}{10.8\ mL} \approx 0.2778\ mg\ mL^{-1}$$

After six days dialysis for each sample, the concentration for $PSar_{136}$-*b*-$PHPMA_5$ in PBS buffer was 0.272 mg mL^{-1}, as measured by UV-vis spectroscopy.

For $PSar_{136}$-*b*-$PHPMA_5$ in acetate buffer pH 5, the concentration was 0.269 mg mL^{-1}. Therefore, the percentage that was encapsulated by the polymer $PSar_{136}$-*b*-$PHPMA_5$ was,

$$At\ pH\ 7.4, \frac{0.272}{0.2778} \times 100\ \% \approx 97.9\ \%,$$

The mass of Dox in the above sample was $0.272\ mg\ mL^{-1} \times 10.8\ mL \approx 2.94\ mg$

$$At\ pH\ 5, \frac{0.269}{0.2778} \times 100\ \% \approx 96.8\ \%$$

Mass of Dox in the above sample was $0.269\ mg\ mL^{-1} \times 10.8\ mL \approx 2.91\ mg$

For $PSar_{136}$-*b*-$PHPMA_{21}$, after six days dialysis the Dox concentration of the sample prepared in PBS was 0.270 mg mL^{-1}, and the Dox concentration of the sample prepared in acetate buffer was 0.268 mg mL^{-1}.

Therefore, the percentage that was encapsulated by the polymer $PSar_{136}$-*b*-$PHPMA_{21}$ was,

$$At\ pH\ 7.4, \frac{0.270}{0.2778} \times 100\ \% \approx 97.2\ \%$$

Mass of Dox in the above sample was $0.270\ mg\ mL^{-1} \times 10.8\ mL \approx 2.92\ mg$

$$At\ pH\ 5, \frac{0.268}{0.2778} \times 100\ \% \approx 96.5\ \%$$

Mass of Dox in the above sample was $0.268\ mg\ mL^{-1} \times 10.8\ mL \approx 2.89\ mg$

Appendix 4

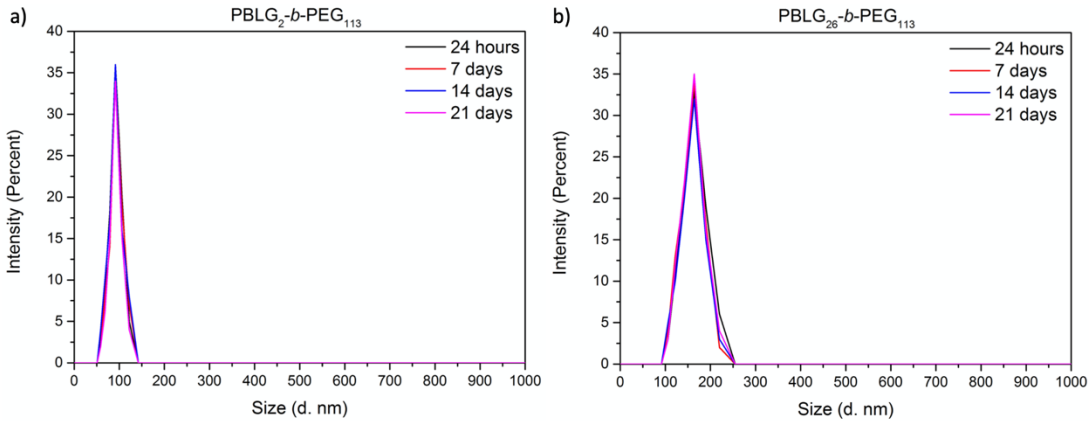

Figure A4.1. DLS analysis of $PBLG_2$-*b*-PEG_{113} and $PBLG_2$-*b*-PEG_{113} in deionised water after 24 hours, 7 days, 14 days and 21 days.

Dox loading of $PBLG_2$-*b*-PEG_{113} Nanoparticles

12.0 mg of Dox was dissolved in 20 µL of triethylamine and 3.0 mL of chloroform, and stirred for 4 hours in dark (bright red solution). 2.0 mg of $PBLG_2$-*b*-PEG_{113} was dissolved in 1.0 mL of DMF (colourless solution). The polymer solution was then added dropwise into 35.0 mL of PBS buffer or acetate buffer (pH 6.5) (colourless solution). Dox solution was added dropwise into the polymer solution to yield a final volume of 36.0 mL (red solution). $PBLG_2$-*b*-PEG_{113} only has two repeat units of PBLG so more Dox was used for loading in because only a small amount of Dox can be loaded in theoretically.

The Dox concentration for each sample was

$$\frac{12.0\ mg}{36.0\ mL} \approx 0.3333\ mg\ mL^{-1}$$

After three days dialysis for each sample, the concentration for $PBLG_{26}$-*b*-PEG_{113} in PBS buffer was 0.0165 mg mL^{-1}, as measured by UV-vis spectroscopy.

Therefore, the percentage that was encapsulated by the polymer $PBLG_{26}$-*b*-PEG_{113} was,

$$\text{At pH 7.4, } \frac{0.0165}{0.3333} \times 100\% \approx 4.95\ \%\ ,$$

The mass of Dox in the above sample was 0.0165 mg mL^{-1} × 36.0 mL = 0.594 mg

Dox loading of $PBLG_{26}$-*b*-PEG_{113} Nanoparticles

1.0 mg of Dox was dissolved in 20 µL of trimethylamine and 3.0 mL of chloroform, and stirred for 4 hours in dark (bright red solution). 2.0 mg of $PBLG_{26}$-*b*-PEG_{113} was dissolved in 1.0 mL of DMF (colourless solution). The polymer solution was then added dropwise

into 35.0 mL mL of PBS buffer or acetate buffer (pH 6.5) (colourless solution). Dox solution was added dropwise into the polymer solution to yield a final volume of 36.0 mL (red solution).

The Dox concentration for each sample was

$$\frac{1.0\ mg}{36.0\ mL} \approx 0.0278\ mg\ mL^{-1}$$

After three days dialysis for each sample, the concentration for $PBLG_{26}$-*b*-PEG_{113} in PBS buffer was 0.0122 mg mL^{-1}, as measured by UV-vis spectroscopy.

Therefore, the percentage that was encapsulated by the polymer $PBLG_{26}$-*b*-PEG_{113} was,

$$\text{At pH 7.4, } \frac{0.0122}{0.0278} \times 100\% \approx 43.9\ \%\ ,$$

The mass of Dox in the above sample was 0.0122 mg mL^{-1} × 36.0 mL = 0.4392 mg

All the Dox release samples were prepared in PBS buffer.

Dox release from the $PBLG_2$-*b*-PEG_{113} and $PBLG_{26}$-*b*-PEG_{113} nanoparticles

2.0 mL of solution containing Dox loaded $PBLG_2$-*b*-PEG_{113} was added to dialysis tubes (MWCO = 2,000 Da). The dialysis tubes were independently immersed in a beaker containing either 70.0 mL PBS buffer solution or pH 6.5 acetate buffer solution. The beakers were covered with aluminium foil and maintained at 37 °C in a water bath before the temperature was increased to 41 °C. 2.0 mL of buffer solution was periodically removed for analysis by UV-vis spectroscopy, before being returned to the beaker. The same procedure was conducted to measure Dox release from $PBLG_2$-*b*-PEG_{113} nanoparticles.

Loading of Dox encapsulated $PBLG_{26}$-*b*-PEG_{113} nanoparticles in PHPMA gel

0.0007 g freeze dried Dox encapsulated $PBLG_{26}$-*b*-PEG_{113} nanoparticles were dissolved in 0.8 mL of DMSO. 0.5585 g of $PHPMA_{200}$ gel was dissolved in the DMSO solution. 0.05 mL of the red mixture was injected in 14.0 mL of PBS solution and pH 6.5 acetate buffer solutions, producing Dox loaded $PBLG_{26}$-*b*-PEG_{113} nanoparticles in PHPMA gels depot. The same procedure was applied to free dox loaded PHPMA gels.

The mass of Dox for each sample was

$$\frac{0.7\ mg \times 44\%}{16} = 0.01925\ mg$$

Dox release from $PBLG_{26}$-*b*-PEG_{113} nanoparticles embedded within the $PHPMA_{200}$ depot:

Nanoparticle-loaded $PHPMA_{200}$ depot (35 mg) was added to either 2.0 mL PBS buffer solution or pH 6.5 acetate buffer solution within separate dialysis tubes (MWCO = 2,000 Da). The dialysis tubes were independently immersed in a beaker containing either 70.0 mL PBS buffer solution or 70.0 mL pH 6.5 acetate buffer solution. The beakers were covered with aluminium foil and maintained either in a water bath at 37 °C or in a fumehood at 20 °C. 2.0 mL of buffer solution was periodically removed for analysis by UV-vis spectroscopy, before being returned to the beaker.

Statistical Tests

Cytotoxicity of $PBLG_{26}$-*b*-PEG_{113} (Figure 4.8). Using fitted curves, a comparison of Log IC_{50} values between the data sets using an extra Sum-of-Squares F test was performed, where alpha = 0.05. The null hypothesis is that the Log IC_{50} value is the same for all the data sets.

F ratio = F-ratio is the ratio of the between group variance to the within group variance. It can be compared to a critical F-ratio, which is determined by rejecting or accepting the null hypothesis, which determines whether there are no differences between groups.

DFn = degrees of freedom for the numerator of the F ratio

DFd = degrees of freedom for the denominator of the F ratio

MCF-7 F(DFn,DFd) = 21.71 (2,110) $p < 0.0001$, the null hypothesis is rejected

MDA-MB-231 F(DFn,DFd) = 18.10 (2,109) $p < 0.0001$, the null hypothesis is rejected

MDA-MB-453 F(DFn,DFd) = 90.23 (2,116) $p < 0.0001$, the null hypothesis is rejected

In conclusion, the difference in IC_{50} values between the polymer, Dox-loaded nanoparticles, and free Dox are significantly different for each cell line.

Appendix 5

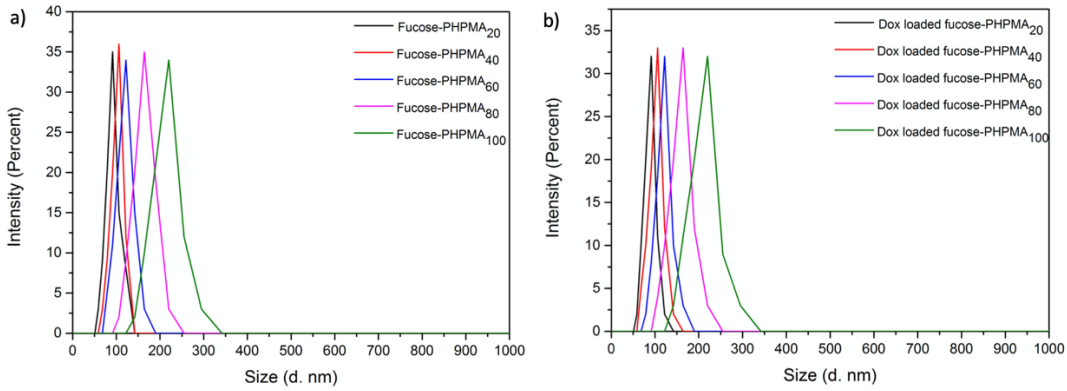

Figure A5. 1 DLS analysis of a) fucose-PHPMA with 20, 40, 60, 80 and 100 chain lengths in deionised water at room temperature, b) Dox-loading fucose-PHPMA with 20, 40, 60 80 and 100 chain lengths in deionised water at room temperature.

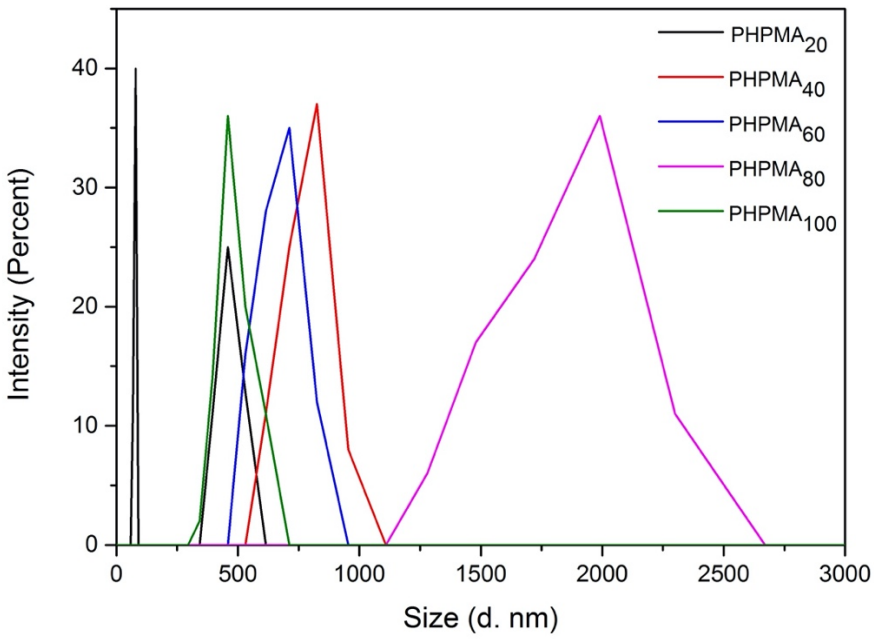

Figure A5.2. DLS analysis of PHPMA with 20, 40, 60 80 and 100 chain lengths in deionised water at room temperature.

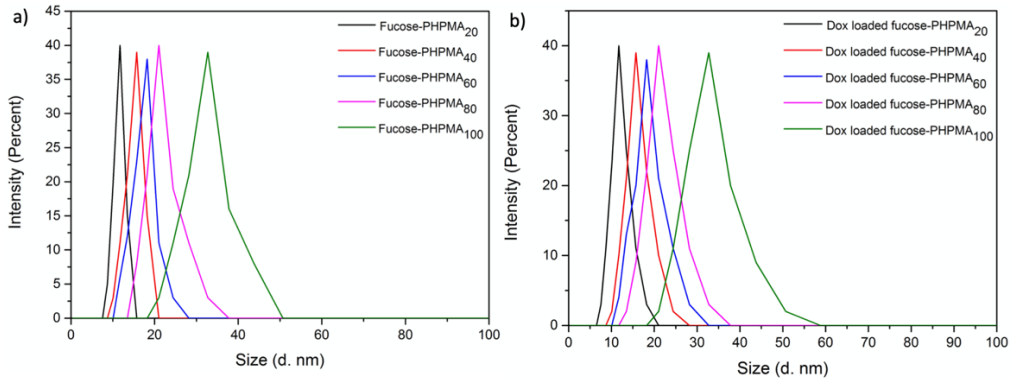

Figure A5.3. DLS analysis of a) fucose-PHPMA with 20, 40, 60, 80 and 100 chain lengths in deionised water at 37 °C, b) Dox-loaded fucose-PHPMA with 20, 40, 60, 80 and 100 chain lengths in deionised water at 37 °C.

Dox loading of fucose-PHPMA$_{100}$ Nanoparticles

2.5 mg of Dox was dissolved in 20 µL of triethylamine and 3.0 mL of chloroform, and stirred for 4 hours in dark (bright red solution). 3.0 mg of fucose-PHPMA$_{100}$ was dissolved in 1.0 mL of DMF (colourless solution). The polymer solution was then added dropwise into 7.0 mL mL of PBS buffer (colourless solution). Dox solution was added dropwise into the polymer solution to yield a final volume of 8.0 mL (bright red solution).

The Dox concentration for each sample was

$$\frac{2.5\ mg}{8.0\ mL} \approx 0.3125\ mg\ mL^{-1}$$

After three days dialysis for each sample, the concentration for fucose-PHPMA$_{100}$ in PBS buffer solution was 0.2562 mg mL^{-1}, as measured by UV-vis spectroscopy.

Therefore, the percentage that was encapsulated by the polymer fucose-PHPMA$_{100}$ was,

$$\text{At pH 7.4, } \frac{0.2562}{0.3125} \times 100\% \approx 82.0\ \%\ ,$$

The mass of Dox in the above sample was 0.2562 mg mL^{-1} × 8.0 mL = 2.0496 mg

All the Dox release samples were prepared in PBS buffer.

The same Dox loading procedures were applied to fucose-PHPMA$_{20}$, fucose-PHPMA$_{40}$, fucose-PHPMA$_{60}$ and fucose-PHPMA$_{80}$ nanoparticles.

Loading Dox fucose-PHPMA$_{100}$ nanoparticles in PHPMA$_{200}$ Depot

0.0005 g freeze dried Dox encapsulated fucose-PHPMA$_{100}$ was dissolved in 0.8 mL of DMSO. 0.550 g of PHPMA$_{200}$ gel was dissolved in the DMSO solution. 0.05 mL of the red

mixture was syringed and injected in 14.0 mL of PBS buffer solution, producing Dox fucose-PHPMA$_{100}$ in PHPMA$_{200}$ gel.

The mass of Dox for each sample was

$$\frac{0.5\ mg \times 82\%}{16} \approx 0.0256\ mg$$

Appendix 6

Table A6.1. DLS data of PACS$_{100}$, PACS$_{50}$, PρHS$_{100}$, PρHS$_{50}$, P(ρHS-SA)$_{100}$, P(ρHS-SA)$_{50}$ in deionised water with concentration of 0.1 mg mL^{-1}, after 24 hours, one week and two weeks.

Polymers	Size (nm)	PDI
PACS$_{100}$ after 24 hours	397±15	0.162
PACS$_{100}$ after one week	405±13	0.342
PACS$_{100}$ after two weeks	436±17	0.233
PACS$_{50}$ after 24 hours	341±23	0.242
PACS$_{50}$ after one week	342±15	0.247
PACS$_{50}$ after two weeks	345±28	0.108
PρHS$_{100}$ after 24 hours	77±7	0.162
PρHS$_{100}$ after one week	76±5	0.270
PρHS$_{100}$ after two weeks	80±11	0.233
PρHS$_{50}$ after 24 hours	48±24	0.195
PρHS$_{50}$ after one week	53±19	0.281
PρHS$_{50}$ after two weeks	59±16	0.241
P(ρHS-SA)$_{100}$ after 24 hours	105±33	0.626
P(ρHS-SA)$_{100}$ after one week	107±30	0.548
P(ρHS-SA)$_{100}$ after two weeks	95±31	0.575
P(ρHS-SA)$_{50}$ after 24 hours	62±14	0.725
P(ρHS-SA)$_{50}$ after one week	66±12	0.844
P(ρHS-SA)$_{50}$ after two weeks	69±10	0.612

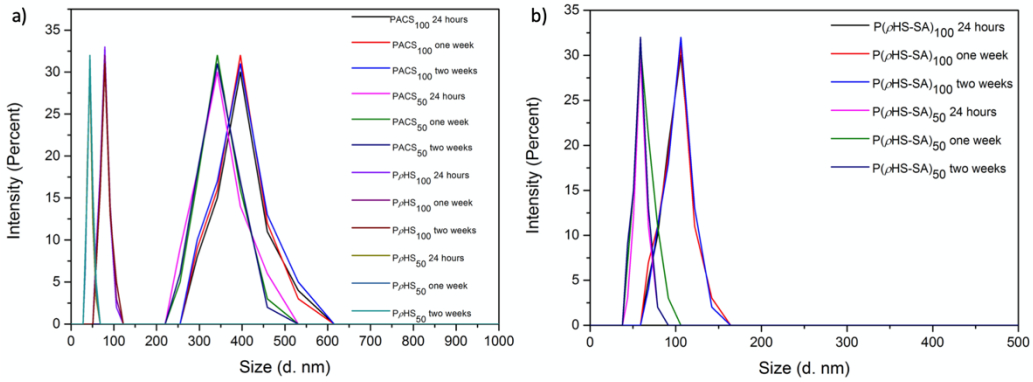

Figure A6.1. DLS analysis of a) $PACS_{100}$, $PACS_{50}$, $P\rho HS_{100}$, $P\rho HS_{50}$, and b) $P(\rho HS\text{-}SA)_{100}$, $P(\rho HS\text{-}SA)_{50}$ in deionised water after 24 hours, one week and two weeks.

Table A6.2. DLS data of $PACS_{100}$-*b*-PAM_{200}, $PACS_{50}$-*b*-PAM_{100}, $PACS_{50}$-*b*-PAM_{200}, $P\rho HS_{100}$-*b*-PAM_{200}, $P\rho HS_{50}$-*b*-PAM_{100}, $P\rho HS_{50}$-*b*-PAM_{200}, $P(\rho HS\text{-}SA)_{100}$-*b*-$PAM_{200}$, $P(\rho HS\text{-}SA)_{50}$-*b*-$PAM_{200}$, $P(\rho HS\text{-}SA)_{50}$-*b*-$PAM_{200}$ in deionised water with concentration of 0.1 mg mL^{-1}, after 24 hours, one week and two weeks.

Copolymers	Size (nm)	PDI
$PACS_{100}$-*b*-PAM_{200} after 24 hours	268±23	0.269
$PACS_{100}$-*b*-PAM_{200} after one week	289±26	0.260
$PACS_{100}$-*b*-PAM_{200} after two weeks	291±29	0.136
$PACS_{50}$-*b*-PAM_{100} after 24 hours	192±21	0.229
$PACS_{50}$-*b*-PAM_{100} after one week	201±20	0.235
$PACS_{50}$-*b*-PAM_{100} after two weeks	205±24	0.142
$PACS_{50}$-*b*-PAM_{200} after 24 hours	268±17	0.269
$PACS_{50}$-*b*-PAM_{200} after one week	289±15	0.260
$PACS_{50}$-*b*-PAM_{200} after two weeks	291±20	0.136
$P\rho HS_{100}$-*b*-PAM_{200} after 24 hours	142±31	0.267
$P\rho HS_{100}$-*b*-PAM_{200} after one week	151±30	0.257
$P\rho HS_{100}$-*b*-PAM_{200} after two weeks	155±28	0.283
$P\rho HS_{50}$-*b*-PAM_{100} after 24 hours	100±11	0.248
$P\rho HS_{50}$-*b*-PAM_{100} after one week	106±13	0.261
$P\rho HS_{50}$-*b*-PAM_{100} after two weeks	109±14	0.111
$P\rho HS_{50}$-*b*-PAM_{200} after 24 hours	78±15	0.166
$P\rho HS_{50}$-*b*-PAM_{200} after one week	75±16	0.148

PρHS$_{50}$-*b*-PAM$_{200}$ after two weeks	76±12	0.181
P(ρHS-SA)$_{100}$-*b*-PAM$_{200}$ after 24 hours	168±23	0.182
P(ρHS-SA)$_{100}$-*b*-PAM$_{200}$ after one week	172±27	0.158
P(ρHS-SA)$_{100}$-*b*-PAM$_{200}$ after two weeks	174±25	0.205
P(ρHS-SA)$_{50}$-*b*-PAM$_{100}$ after 24 hours	119±19	0.095
P(ρHS-SA)$_{50}$-*b*-PAM$_{100}$ after one week	121±11	0.271
P(ρHS-SA)$_{50}$-*b*-PAM$_{100}$ after two weeks	124±14	0.207
P(ρHS-SA)$_{50}$-*b*-PAM$_{200}$ after 24 hours	116±26	0.170
P(ρHS-SA)$_{50}$-*b*-PAM$_{200}$ after one week	119±21	0.172
P(ρHS-SA)$_{50}$-*b*-PAM$_{200}$ after two weeks	111±25	0.165

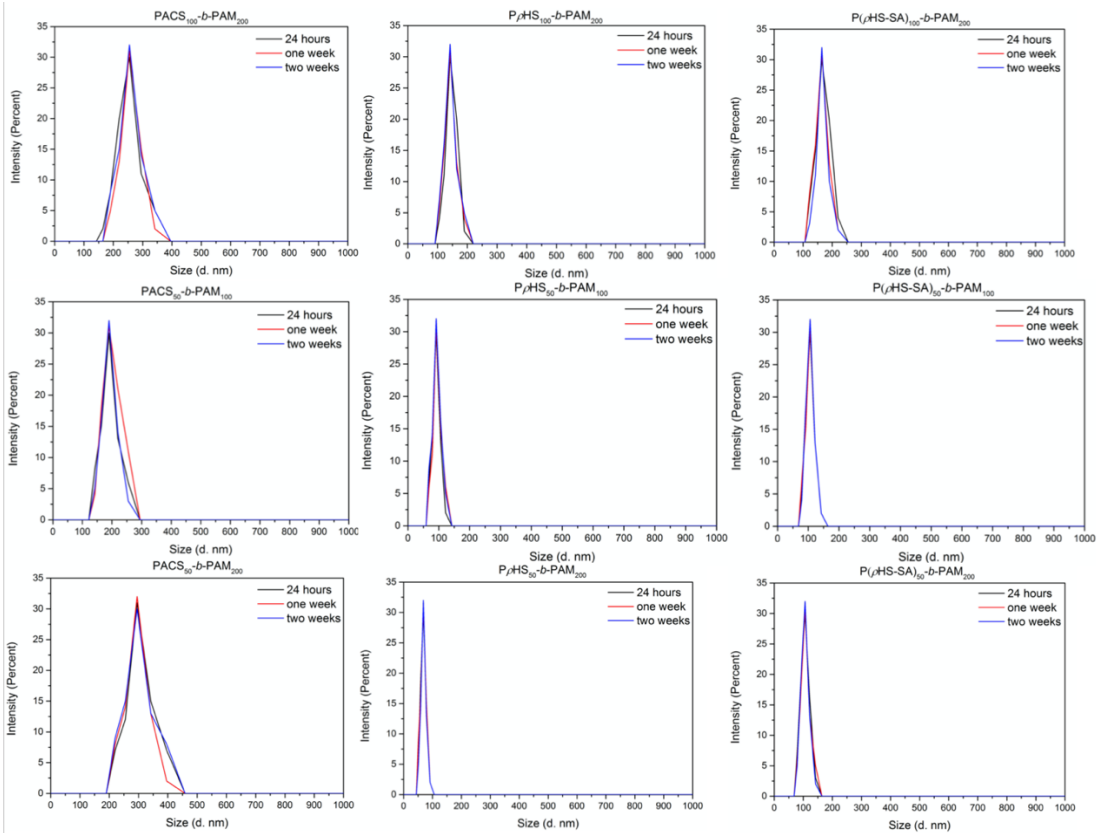

Figure A6.2. DLS data of PACS$_{100}$-*b*-PAM$_{200}$, PACS$_{50}$-*b*-PAM$_{100}$, PACS$_{50}$-*b*-PAM$_{200}$, PρHS$_{100}$-*b*-PAM$_{200}$, PρHS$_{50}$-*b*-PAM$_{100}$, PρHS$_{50}$-*b*-PAM$_{200}$, P(ρHS-SA)$_{100}$-*b*-PAM$_{200}$, P(ρHS-SA)$_{50}$-*b*-PAM$_{200}$, P(ρHS-SA)$_{50}$-*b*-PAM$_{200}$ in deionised deionised water after 24 hours, one week and two weeks.

Table A6. 3. DLS data of $PACS_{50}$-*co*-PAM_{200}, $P\rho HS_{50}$-*co*-PAM_{200}, $P(\rho HS\text{-}SA)_{50}$-*co*-$PAM_{200}$ in deionised water with concentration of 0.1 mg mL^{-1}, after 24 hours, one week and two weeks.

Copolymers	Size (nm)	PDI
$PACS_{50}$-*co*-PAM_{200} after 24 hours	705±15	0.379
$PACS_{50}$-*co*-PAM_{200} after one week	708±13	0.361
$PACS_{50}$-*co*-PAM_{200} after two weeks	710±18	0.373
$P\rho HS_{50}$-*co*-PAM_{200} after 24 hours	549±23	0.309
$P\rho HS_{50}$-*co*-PAM_{200} after one week	554±25	0.356
$P\rho HS_{50}$-*co*-PAM_{200} after two weeks	557±29	0.362
$P(\rho HS\text{-}SA)_{50}$-*co*-$PAM_{200}$ after 24 hours	618±21	0.671
$P(\rho HS\text{-}SA)_{50}$-*co*-$PAM_{200}$ after one week	622±18	0.386
$P(\rho HS\text{-}SA)_{50}$-*co*-$PAM_{200}$ after two weeks	624±19	0.383

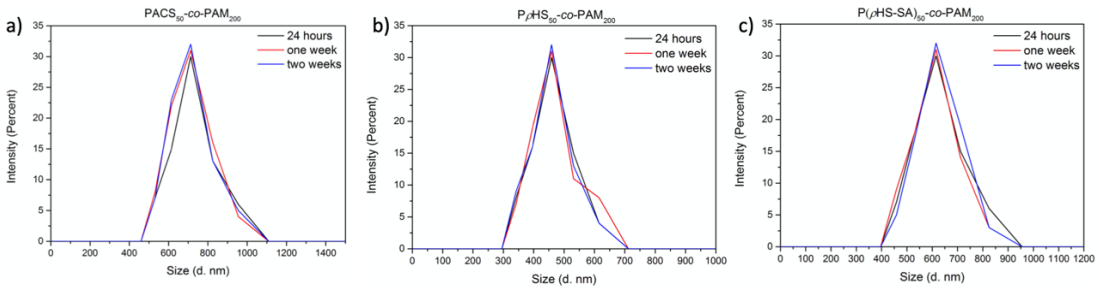

Figure A6.3. DLS analysis of $PACS_{50}$-*co*-PAM_{200}, $P\rho HS_{50}$-*co*-PAM_{200}, $P(\rho HS\text{-}SA)_{50}$-*co*-$PAM_{200}$ in deionised water after 24 hours, one week and two weeks.